



**HAL**  
open science

# Study, characterisation and modelling of residual stresses in fiber-reinforced composite laminates

Aboubakar Sédick Ibrahim Mamane

► **To cite this version:**

Aboubakar Sédick Ibrahim Mamane. Study, characterisation and modelling of residual stresses in fiber-reinforced composite laminates. Mechanical engineering [physics.class-ph]. Université de Haute Alsace - Mulhouse, 2022. English. NNT : 2022MULH4487 . tel-03833704

**HAL Id: tel-03833704**

**<https://theses.hal.science/tel-03833704v1>**

Submitted on 28 Oct 2022

**HAL** is a multi-disciplinary open access archive for the deposit and dissemination of scientific research documents, whether they are published or not. The documents may come from teaching and research institutions in France or abroad, or from public or private research centers.

L'archive ouverte pluridisciplinaire **HAL**, est destinée au dépôt et à la diffusion de documents scientifiques de niveau recherche, publiés ou non, émanant des établissements d'enseignement et de recherche français ou étrangers, des laboratoires publics ou privés.

UNIVERSITÉ DE HAUTE ALSACE  
UNIVERSITÉ DE STRASBOURG

Année 2022

**Thèse**

Présentée pour l'obtention du grade de

**Docteur de l'Université de Haute-Alsace**

École Doctorale : Mathématiques, Sciences de l'Information et de l'Ingénieur (ED 269)

Discipline : **Mécanique**

Présentée et soutenue publiquement

par

**Aboubakar Sédick IBRAHIM  
MAMANE**

Le 07 Juillet 2022

---

**Study, characterisation and modelling of residual  
stresses in fiber-reinforced composite laminates**

Sous la direction de Gildas L'HOSTIS, Marie-José PAC et Sylvain GILJEAN

---

Jury :

Pr.	Nahiene HAMILA	Ec Nat Ingénieurs Brest	Rapporteur
Dr.	Fabrice RICHARD	Université Besançon Franche-Comté	Rapporteur
Pr.	Damien SOULAT	ENS Arts Indust Text Roubaix	Examineur
Pr.	Gildas L'HOSTIS	Université de Mulhouse, Haute-Alsace	Directeur de thèse
Pr.	Marie-José PAC	Université de Mulhouse, Haute-Alsace	Co-directrice de thèse
Dr.	Sylvain GILJEAN	Université de Mulhouse, Haute-Alsace	Co-encadrant de thèse



---

## Abstract

This thesis focuses on the measurement of the residual stress profile in fiber-reinforced composites by the incremental hole drilling method. The objective is to develop numerical and experimental tools adapted to the measurement of residual stresses and to study the thermal, chemical and mechanical behaviors of the composites during the drilling. A thorough and comprehensive understanding of the incremental hole drilling method is required to reliably determine the gradient of residual stresses in the composite. This method consists of drilling a small hole incrementally through the thickness of the material and measuring the induced relaxation strains for all increments. These relaxation strains are then converted into stresses using coefficients called calibration coefficients. The calibration coefficients are calculated by finite element simulations. Thus, this work can be summarized into a numerical and experimental part.

In the numerical part, a configurable numerical model based on Abaqus Scripting is developed to automate the calculation of the calibration coefficients. This configurable model was also used to perform parametric simulations of the incremental hole drilling method to assess the sensitivity of the method to experimental errors. This allow to identify the critical stages of the experimental protocol and to propose solutions to minimize errors.

In the experimental part, the device developed to measure the relaxation strains is presented. This device is developed in such a way as to minimize errors such as errors on increment depth, misalignment of the gages with respect to the fibers and eccentricity of the hole. The residual stresses of samples manufactured under different conditions are determined. The response of the gages to the heat induced by the drilling and the consequences on the local chemical properties of the resin are studied.

## Résumé

Cette thèse se concentre sur la mesure des contraintes résiduelles dans les composites à renforts fibreux par la méthode du trou incrémental. L'objectif est de développer des outils numériques et expérimentaux adaptés à la mesure des contraintes résiduelles et d'étudier les comportements thermiques, chimiques et mécaniques des composites lors du perçage. Une compréhension approfondie et complète de la méthode du trou incrémental est nécessaire pour déterminer de façon fiable le gradient des contraintes résiduelles dans le composite. Cette méthode consiste à percer un petit trou incrément par incrément à travers l'épaisseur du matériau et à mesurer les déformations de relaxation induites pour

---

chaque incrément. Ces déformations de relaxation sont ensuite converties en contraintes en utilisant des coefficients appelés coefficients de calibration. Les coefficients de calibration sont calculés par des simulations par éléments finis. Ainsi, ce travail peut être résumé en une partie numérique et expérimentale.

Dans la partie numérique, un modèle numérique configurable basé sur du Abaqus Scripting est développé pour automatiser le calcul des coefficients de calibration. Ce modèle configurable a également été utilisé pour effectuer des études paramétriques afin d'évaluer la sensibilité de la méthode du trou incrémental aux erreurs expérimentales. Cela a permis d'identifier les étapes critiques du protocole expérimental et de proposer des solutions pour minimiser les erreurs.

Dans la partie expérimentale, le dispositif développé pour mesurer les déformations de relaxation est présenté. Ce dispositif est développé de manière à minimiser les erreurs telles que les erreurs sur la profondeur d'incrément, le mauvais alignement des jauges par rapport aux fibres et l'excentricité du trou. Les contraintes résiduelles d'échantillons fabriqués dans différentes conditions sont déterminées. La réponse des jauges à la chaleur induite par le perçage et les conséquences sur les propriétés locales de la résine sont étudiées.



---

*"Le paradoxe qui fait qu'une fin n'est en réalité qu'un autre début est très certainement ce qui rend la recherche passionnante."*

Aboubakar Sédick IBRAHIM MAMANE

*Je dédie ce travail à mes parents.*

*Comment ne pas le dédier à ces piliers qui m'ont porté, qui me portent et qui m'ont toujours pousser vers l'excellence.*



# Remerciements

Comme l'a si bien dit Hans Christian Andersen "La reconnaissance est la mémoire du coeur". Je tiens donc à remercier toutes les personnes qui ont contribué à l'aboutissement de ce travail.

Je remercie tout d'abord mon équipe encadrante Sylvain GILJEAN, Marie-José PAC et Gildas L'HOSTIS qui m'ont suivi pendant cette thèse. Je les remercie pour leur confiance, leurs conseils et leurs assistances précieuses sur le fond et la forme de mon travail.

J'aimerais ensuite remercier Christian PIDANCIER pour sa contribution à la réalisation du banc expérimental, Cyril MARSQUET et Brice SENN pour leurs diverses aides notamment pour la calibration du banc expérimental.

Je remercie le Laboratoire de Photochimie et d'Ingénierie Macromoléculaires (LPIM) et particulièrement Benoît GACHET pour tous les tests de calorimétrie différentielle à balayage et d'analyse mécanique dynamique. Je remercie également Mahmoud Hussein pour son assistance dans la réalisation des tests de caractérisation des champs thermiques.

Je tiens à remercier le Groupe G.MAGYAR pour la fabrication des échantillons de composite étudiés, ainsi que Fabrice LAURENT et Bernard DURAND pour leur aide dans l'interprétation et la compréhension des résultats expérimentaux.

J'adresse mes remerciements à Peng WANG, Gilles ARNOLD, Gregory COVAREL pour toutes les discussions scientifiques souvent informelles qui m'ont fait avancer dans mes réflexions et mes idées.

Merci à tous les doctorants et membres du Laboratoire de Physique et Mécanique Textiles (LPMT).



# Contents

List of figures	xx
List of tables	xxii
General Introduction	1
<b>1 Generality on residual stresses</b>	<b>5</b>
1.1 Introduction	7
1.2 Origins of residual stresses	7
1.2.1 Mechanisms occurring during processing of thermoset laminates	7
1.2.2 Chemically-induced residual stresses	9
1.2.3 Thermally-induced residual stresses	10
1.3 Influences of residual stresses on material properties and minimization techniques	14
1.3.1 Influences of residual stresses on composite laminates properties	14
1.3.1 - a Effects of residual stresses on the matrix properties	14
1.3.1 - b Effects of residual stresses on the fiber-matrix interface	15
1.3.1 - c Defects due to residual stresses	15
1.3.1 - d Effects of residual stresses on the structure of composite laminates	18
1.3.1 - e Effects of residual stresses on the mechanical properties of composite laminates	20
1.3.2 Residual stress minimization techniques	24
1.3.2 - a Modification of the cure cycle	24
1.3.2 - b Relaxation of residual stresses by annealing	26
1.3.2 - c Relaxation of residual stresses by water absorption	26
1.3.2 - d Molecular additive insertion in the resin	27
1.4 Methods for measuring and predicting residual stresses	28
1.4.1 Residual stress prediction methods	28
1.4.1 - a Micro-mechanical level	28
1.4.1 - b Macro-mechanical level	29
1.4.2 Experimental methods for measuring residual stresses	32
1.4.2 - a Non-destructive methods	33
1.4.2 - b Destructive methods	36
1.4.2 - c Methods using embedded strain sensors	38
1.5 Conclusion	41
<b>2 Formulation of the incremental hole drilling method</b>	<b>43</b>
2.1 Introduction	45



2.2	Historical evolution of the hole drilling method . . . . .	45
2.3	Theoretical formulation of the hole drilling and the incremental hole drilling methods . . . . .	46
2.3.1	Case of thin structures: HDM . . . . .	46
2.3.1 - a	Isotropic materials . . . . .	46
2.3.1 - b	Orthotropic materials . . . . .	51
2.3.2	Case of thick structures: IHDM . . . . .	51
2.3.2 - a	Thick isotropic materials . . . . .	51
2.3.2 - b	Composite laminates . . . . .	56
2.4	Calculation of calibration coefficients using finite element simulations . . .	60
2.4.1	Calibration coefficients for thin structures . . . . .	60
2.4.1 - a	Isotropic materials . . . . .	60
2.4.1 - b	Orthotropic materials . . . . .	63
2.4.2	Calibration coefficients for thick structures . . . . .	66
2.4.2 - a	Thick isotropic materials . . . . .	66
2.4.2 - b	Composite laminates . . . . .	68
2.5	Development of a configurable numerical model . . . . .	71
2.5.1	About Python scripts in Abaqus . . . . .	71
2.5.2	Configurable numerical model using Python scripts . . . . .	72
2.5.3	Analysis of the influence of the mesh on the calibration coefficients . . .	75
2.6	Conclusion . . . . .	77
<b>3</b>	<b>Numerical study of the influence of experimental errors on calibration coefficients and development of the experimental procedure</b>	<b>79</b>
3.1	Introduction . . . . .	80
3.2	Study of the influence of experimental errors on calibration coefficients . .	80
3.2.1	Errors on increment depth . . . . .	82
3.2.2	Angular deviation of the gages from their theoretical position . . .	85
3.2.3	Hole eccentricity errors . . . . .	87
3.3	Numerical correction of the calibration coefficients . . . . .	89
3.3.1	Presentation of the numerical correction method . . . . .	89
3.3.2	Numerical validation of the correction method . . . . .	93
3.4	Development of the experimental device . . . . .	94
3.4.1	General description of the experimental device . . . . .	94
3.4.2	Bonding protocol for gages . . . . .	95
3.4.3	Perpendicularity of the milling cutter with respect to the surface of the sample . . . . .	97
3.4.4	Optical centering of the milling cutter . . . . .	98
3.4.5	Detection of the drilling reference . . . . .	100
3.5	Conclusion . . . . .	101
<b>4</b>	<b>Tests campaign: results and discussion</b>	<b>103</b>
4.1	Introduction . . . . .	105
4.2	Materials manufacturing and experimental methods . . . . .	105
4.2.1	Manufacturing process . . . . .	105
4.2.2	Sample preparation . . . . .	107
4.2.3	Experimental methods . . . . .	107
4.3	Analysis of the raw acquisition data of relaxation strains . . . . .	110

4.3.1	Presentation of the raw acquisition data . . . . .	110
4.3.2	Thermal and mechanical contributions of drilling on raw acquisition data . . . . .	111
4.4	Thermal effects of the drilling on the local chemical and mechanical properties of the raw resin . . . . .	119
4.4.1	Differential Scanning Calorimetry (DSC) tests . . . . .	119
4.4.1 - a	Principle of the DSC . . . . .	119
4.4.1 - b	Sample preparation and experimental parameters . . . . .	119
4.4.1 - c	Results and discussion . . . . .	120
4.4.2	Dynamique Mechanical Analysis (DMA) tests . . . . .	122
4.4.2 - a	Principle of the DMA . . . . .	122
4.4.2 - b	Sample preparation and experimental parameters . . . . .	122
4.4.2 - c	Results and discussion . . . . .	123
4.5	Determination of the residual stress profile . . . . .	125
4.5.1	Measurement of relaxation strains . . . . .	125
4.5.2	Calculation of residual stresses . . . . .	126
4.6	Discussion and Conclusion . . . . .	129
<b>General Conclusion &amp; Perspectives</b>		<b>131</b>
<b>Résumé en Français</b>		<b>135</b>
	Introduction générale . . . . .	135
	Chapitre 1 : généralité sur les contraintes résiduelles (CR) . . . . .	137
	C1.1 Introduction . . . . .	137
	C1.2 Origines des contraintes résiduelles . . . . .	138
	C1.3 Influence des contraintes résiduelles sur les propriétés des matériaux et techniques de minimisation . . . . .	138
	C1.4 Méthodes de mesure et de prédiction des contraintes résiduelles . . . . .	139
	C1.5 Conclusion . . . . .	140
	Chapitre 2 : Formulation de la méthode du trou incrémental . . . . .	140
	C2.1 Introduction . . . . .	140
	C2.2 Formulation théorique de la méthode du trou incrémental . . . . .	141
	C2.3 Calcul des coefficients de calibration par simulations par éléments finis . . . . .	142
	C2.4 Développement d'un modèle numérique paramétrable . . . . .	146
	C2.5 Conclusion . . . . .	147
	Chapitre 3 : Etude numérique de l'influence des erreurs expérimentales sur les coefficients de calibration et développement du protocole expérimental . . . . .	148
	C3.1 Introduction . . . . .	148
	C3.2 Etude de l'influence des erreurs expérimentales sur les coefficients de calibration . . . . .	149
	C3.3 Correction numérique des coefficients de calibration . . . . .	151
	C3.4 Développement du dispositif expérimental . . . . .	151
	C3.5 Conclusion . . . . .	152
	Chapitre 4 Campagne de tests : résultats et discussions . . . . .	153
	C4.1 Introduction . . . . .	153
	C4.2 Matériaux . . . . .	154
	C4.3 Analyse des données d'acquisition brutes des déformations de relaxation . . . . .	154
	C4.4 Effets thermiques du perçage sur les propriétés locales de la résine . . . . .	156
	C4.5 Détermination du profil de contraintes résiduelles . . . . .	159

C.6 Discussion et Conclusion . . . . .	162
Conclusion générale . . . . .	163
<b>References</b>	<b>167</b>
<b>A Expressions of coefficients <math>k_p^{ij}</math> and <math>K_p^{ij}</math></b>	<b>181</b>
<b>B Numerical relaxation strains (<math>\epsilon_k^i</math>), calibration coefficients (<math>c_{ijgs}</math>) and <math>[S_{ii}]</math> matrices used for the numerical validation of the correction method (presented in section 3.3 of chapter 3)</b>	<b>187</b>
<b>C Influence of rotational speed on the damage of the hole surface</b>	<b>193</b>
<b>D Influence of the withdrawal speed of the milling cutter on the shape of the raw acquisition data</b>	<b>195</b>
<b>E Calibration coefficients used to calculate the residual stresses in section 4.5.2 of chapter 4</b>	<b>197</b>

# List of figures

- 1.1 Relevant stages of the recommended cure cycle for thermoset laminates (AS4/8552 carbon/epoxy laminates, [5]) . . . . . 8
- 1.2 (a) Evolution of the degree of cure and the glass transition temperature during the cure cycle of a AS4/8552 carbon/epoxy composite, (b) Evolution of the strain through the cure cycle [6] . . . . . 8
- 1.3 Progress of the degree of cure for different cure temperature of the second dwell for an IM6/3100 graphite/bismaleimide composite [9] . . . . . 10
- 1.4 Formation of residual stresses at the micro-mechanical level [10] . . . . . 11
- 1.5 Formation of residual stresses at the ply-to-ply level [10] . . . . . 12
- 1.6 Formation of residual stresses at macro-mechanical level [10] . . . . . 12
- 1.7 (a) Glass/polyester and graphite/epoxy cure cycle , (b) Temperature distributions due to the exotherm of the reaction in unidirectional glass/polyester for different thicknesses at 164 minutes of the cure cycle [8] . . . . . 13
- 1.8 Fiber-matrix interfacial bonding mechanisms: (a) molecular entanglement due to interdiffusion, (b) electrostatic adhesion, (c) chemical bonding and (d) mechanical interlocking [20] . . . . . 15
- 1.9 Crack initiation along fiber–matrix interfaces in a carbon fiber polyphenylene-sulfide laminate [15] . . . . . 16
- 1.10 Transverse cracks in surface plies of 0<sub>3</sub>/90<sub>9</sub>/0<sub>3</sub> carbon fiber polyetherimide laminate [15] . . . . . 17
- 1.11 (a) Residual stress induced microcracking in the 45°plies of a 32-ply quasi-isotropic laminate and (b) residual stress induced delamination in a 32-ply cross-ply laminate [28] . . . . . 17
- 1.12 Micrograph of a composite laminate showing fiber waviness [15] . . . . . 18
- 1.13 Distorted glass fiber fabric reinforced polyetherimide laminate due to non-uniform cooling of the hot platen press [15] . . . . . 19

1.14 Schematic of the spring-forward phenomenon: (a) before consolidation, in-plane contraction is represented by the dotted arrows, and out-of-plane contraction by the solid arrows, (b) after consolidation and cooling from the processing temperature [15] . . . . .	20
1.15 A comparison of the stress-strain curves of an annealed and un-annealed $((+/- 45^\circ)_2)_s$ IM6/PEEK laminate cooled at $50^\circ/min$ [15] . . . . .	21
1.16 Kink-band formation of localized buckling [2]. . . . .	22
1.17 Effect of longevity on the fatigue life of 50 MPa prestressed woven composite (E-glass/polyester) [42] . . . . .	23
1.18 Modification of the cure cycle to reduce residual stresses: three-step curing with an intermediate dwell [45] . . . . .	25
1.19 Conventional cure cycle and modified cure cycle proposed by Kim et al. [46] in their work . . . . .	25
1.20 Micro-scale model used to predict micro residual stresses: finite element representation of the fiber, the matrix and the interphase [2] . . . . .	28
1.21 Effect of different fiber arrangements on micro residual stresses: (a) The 3 arrangements studied , (b) Obtained residual stresses for each arrangement [2] . . . . .	29
1.22 Isothermal Differential Scanning Calorimetry (DSC) [45] . . . . .	31
1.23 (a) Comparison between numerically predicted [2] and experimentally determined [68] evolution of degree of cure, (b) Comparison between numerically predicted [2] and experimentally determined [68] interlaminar stress . . . . .	33
1.24 Example of Moiré patterns depicting relaxed displacements due to hole drilling [76] . . . . .	35
1.25 Compressive strain induced shift of $2660\text{ cm}^{-1}$ Raman peak in AS4 carbon fiber embedded in a PEEK matrix [79] . . . . .	36
1.26 Example of curvature induced by layer removal [82] . . . . .	37
1.27 Principle of the incremental hole drilling method: (a) Measurement of the relaxation strains [85], (c) Load cases to apply through the thickness for the calculation of the calibration coefficients [86] . . . . .	37
1.28 Principle of the compliance method [90] . . . . .	38
1.29 (a) Schematic representation of the EFPI sensor working principle [94], (b) Different components of an EFPI sensor [73] . . . . .	39

1.30	Principle of residual stresses measurement in composite materials using X-Ray Diffraction [98]: (A) Representation of diffraction conditions, (B) Direction of strain masurement with respect to laminate axes . . . . .	40
2.1	Strain gage rosette used to measure the relaxation strains . . . . .	47
2.2	Gage coordinates referenced to stress direction [87] . . . . .	48
2.3	Strain as the radial distance between gage circle and ellipse for uniaxial stress along (a) the x-axis, (b) the y-axis. (c) is the strain propotional to $K(\alpha)$ in rectangular coordiantes [87] . . . . .	48
2.4	Experimental measurement of the relaxation strains using a strain gage rosette [85] . . . . .	49
2.5	Superposition principle [114]:difference between the stress field of a plate (a) and that of a drilled plate (b) . . . . .	49
2.6	Presentation of the hole depth h and the integration variable z that corresponds to the current depth . . . . .	52
2.7	Discrete representation of the cumulative depth of the increments: example of a hole corresponding to 3 increments ( $i=3, 1 \leq j \leq i$ ) . . . . .	53
2.8	Representation of the discrete residual stresses for a hole corresponding to 3 increments ( $i=3, 1 \leq j \leq i$ ) . . . . .	54
2.9	correspondence between the continuous and discrete writing of the calibration coefficients: example of a hole corresponding to 3 increments ( $i=3, 1 \leq j \leq i$ ) . . . . .	55
2.10	Matrix form of equation 2.25: expansion for 3 increments, for the rosette orientation presented in Fig. 2.11 . . . . .	55
2.11	Orientation of gage 1 in the fiber direction: $\alpha_1 = 0^\circ$ , $\alpha_2 = -135^\circ$ and $\alpha_3 = 90^\circ$ . . . . .	55
2.12	(a) Writing of coefficients $A_{ij}$ and $B_{ij}$ in the form of a lower triangular matrix for 3 increments, (b) Increment corresponding to each calibration coefficient . . . . .	56
2.13	(a) Expansion of the relation between residual stresses and relaxation strains for three increments, (b) correspondence between increments and calibration coefficients . . . . .	58
2.14	Contribution of the residual stresses of each layer to the total strains measured on the surface of the material: $\{\sigma_s^j\}$ are the residual stresses, $\{\epsilon_g^i\}$ are the total relaxation strains and $\{\epsilon_g^i\}_{incrementj}$ is the contribution of increment j to the total relaxation strains . . . . .	59

2.15	Modelling of the strain gages as rectangular partitions . . . . .	61
2.16	Features of the used gages . . . . .	61
2.17	Strain field (E11) obtained for the calculation of coefficient B (load case $\sigma_x = -\sigma_y = \sigma_0 = 20MPa$ ) . . . . .	62
2.18	Associated deformations of the material: (a) associated deformation for $\sigma_x$ , (b) associated deformation for $\sigma_{xy}$ and (c) associated deformation for $\sigma_y$ .	64
2.19	Strain field (E11) for a longitudinal uni-axial tensile stress $\sigma_x = 20MPa$ . .	65
2.20	(a) Lower triangular matrix writing of coefficients $A_{ij}$ and $B_{ij}$ , (b) Principle of calculation of the calibration coefficients $A_{ij}$ or $B_{ij}$ depending on whether load case 1 or load case 2 is considered . . . . .	67
2.21	Cutaway view of the 3D composite model (quarter of the model) . . . . .	68
2.22	Mesh strategy: (a) Partitions used for the mesh, (b) distribution of nodes on the edges (seed edge), (c) Mesh refinement area and gage positions, (d) Mesh in the thickness . . . . .	69
2.23	(a) Expansion of the relation between residual stresses and relaxation strains for three increments, (b) Load cases to calculate the different matrices of calibration coefficients $[C_{31gs}]$ ( $\sigma_0$ is the magnitude of the load cases) . . . .	70
2.24	Load case to be applied to calculate coefficients $c_{31gs}$ (Cutaway view of the model) . . . . .	71
2.25	Interaction between the different types of commands and the kernel [118] .	72
2.26	Example of a simple model generated by a script . . . . .	72
2.27	The different steps of the configurable numerical model for custom calcu- lation of calibration coefficients . . . . .	73
3.1	Studied errors: (a) Illustration of error on increment depth, (b) Angular deviation of the gages from their theoretical position, (c) Radial ( $e_c$ ) and angular ( $\alpha_c$ ) eccentricity of the hole . . . . .	82
3.2	Variation of the calibration coefficients $c_{11gs}$ (a) and the coefficients $K_p^{11}$ (b) for different errors on increment depth $\delta d_{model}$ ranging from $-10\%$ to $50\%$ of the desired increment depth $d_{model}$ . . . . .	84
3.3	Variation of the calibration coefficients $c_{44gs}$ (a) and the coefficients $K_p^{44}$ (b) for different errors on increment depth $\delta d_{model}$ ranging from $-15\%$ to $50\%$ of the desired increment depth $d_{model}$ at the 0/90 interface . . . . .	85
3.4	Variation of coefficients $c_{11gs}$ (a) and $K_p^{11}$ (b) for different angular deviations in the counter-clockwise direction . . . . .	86

3.5	Radial eccentricities: variation of coefficients $c_{11gs}$ (a) and $K_p^{11}$ (b), Angular eccentricities: variation of coefficients $c_{11gs}$ (c) and $K_p^{11}$ (d) . . . . .	88
3.6	Numerical correction of the calibration coefficients by a configurable experimental-numerical coupling . . . . .	90
3.7	General presentation of the experimental device used to measure the relaxation strains . . . . .	95
3.8	Bonding protocol for gages: presentation of the device used to minimize angular offset between gage 1 and the fibers . . . . .	96
3.9	(a) Alignment of composite fibers and grids of gage 1 of the rosette, (b) Verification of the quality of the orientation after bonding . . . . .	96
3.10	Schematic representation of the perpendicularity error of the milling cutter with respect to the surface of the sample . . . . .	97
3.11	Adjustment of the perpendicularity: (a) perpendicularity of the milling cutter with respect to the surface of the sample holder, (b) perpendicularity of the z-axis translation with respect to the plane of the composite (yz plane). . . . .	98
3.12	Centering of the milling cutter with respect to the strain gage rosette using a camera . . . . .	99
3.13	Image processing of the strain gage rosette to determine its center: (a) picture of the strain gage rosette, (b) central pattern contour detection and center coordinates extraction, (c) schematic representation of the dx and dy translations needed to center the camera with respect to the rosette . . . . .	99
3.14	Determination of the center of the rosette in case of incomplete detection of the contour of the central pattern of the rosette: (a) fitting method and (b) circumscribed circle method . . . . .	100
3.15	Determination of the center of the rosette if the contour of the central pattern of the rosette is not detected clean: (a) fitting method and (b) circumscribed circle method . . . . .	100
4.1	3D model of the mould used to manufacture composite plates by filament winding method . . . . .	106
4.2	3D model of the counter-moulds used to fix the thickness of the composite and to ensure the sealing of the mould during curing . . . . .	106
4.3	Thickness of plate 3 determined by scanning . . . . .	107
4.4	(a) Cut of samples from plate 3 in the areas where the thickness gradient is low, (b) Sample identification method as a matrix. For example, sample 1-3 is the sample for which $p=1$ and $q=3$ . . . . .	108



4.5	(a) Raw acquisition data obtained for sample 1-3 of plate 3, (b) detail for one increment cycle . . . . .	110
4.6	Thermal strains recorded for the composite (sample 2-3) after applying a heat flow at the rosette location . . . . .	111
4.7	Thermal strains recorded for the resin (plate 3) after applying a heat flow at the rosette location . . . . .	112
4.8	Variation of the thermal field (measured using an IR camera) during an increment cycle: thermal field (a) at the end of the previous increment, (b) during the drilling step, (c) during the relaxation and (d) at the end of the relaxation time . . . . .	113
4.9	Locations of the selected points to plot the variation of the temperature throughout the IHDM . . . . .	114
4.10	Variation of the temperature throughout the IHDM at the gage and the intermediate point locations: (a) for gage1, (b) for gage 2 and (c) for gage 3	115
4.11	(a) Different steps of an increment cycle, (b) Variation of the temperatures during the increment cycle . . . . .	116
4.12	Differences between the first and last increments: (a) Whole test data, example among the (b) first and (b) last increments . . . . .	117
4.13	Modulates DSC tests results: cold extracted samples for (a) plate 1, (c) plate 2 and (e) plate 3. Samples extracted by drilling for (b) plate 1, (b) plate 2 and (f) plate 3. "Enthalpy" corresponds to the enthalpy of the reaction and "Midpoint" to the glass transition temperature. . . . .	121
4.14	DMA sample dimensions . . . . .	122
4.15	DMA results for (a) plate 1, (b) plate 2 and (c) plate 3 . . . . .	124
4.16	Measuring area for relaxation strains . . . . .	125
4.17	Typical relaxation strains measurement curves: (a) raw acquisition data, (b) strains at the end of the relaxation time (strains used to calculate the residual stresses) . . . . .	126
4.18	Relaxation strains measured for the three plates (means and dispersions are determined from 3 tests): results obtained for (a) gage 1, (b) gage 2 and (c) gage 3 . . . . .	127
4.19	Residual stresses determined for the three plates: (a) $\sigma_x$ ( $\sigma_x$ of plate 2 is hidden by that of plate 3 at the first increment), (b) $\sigma_y$ and (c) $\sigma_{xy}$ . . . . .	128
4.20	Déformée associée au cas de charge : (a) $\sigma_x$ , (b) $\sigma_{xy}$ and (c) $\sigma_y$ . . . . .	143

4.21	Champ de déformation (E11) correspondant à une traction longitudinale uni-axiale de $\sigma_x = 20MPa$ . . . . .	144
4.22	Vue en coupe du modèle 3D du composite (quart du modèle) . . . . .	144
4.23	Stratégie de maillage: (a) Partitions utilisées pour le maillage, (b) Distribution des noeuds sur les arêtes (seed edge), (c) Zone d'affinage du maillage et positions des jauges, (d) Maillage suivant l'épaisseur . . . . .	145
4.24	Les différentes étapes du modèle numérique configurable pour un calcul personnalisé des coefficients de calibration . . . . .	146
4.25	Variation des coefficients de calibration $c_{11gs}$ pour différentes erreurs sur la profondeur des incréments $\delta d_{model}$ allant de $-10\%$ à $50\%$ de la profondeur d'incrément souhaitée $d_{model}$ . . . . .	149
4.26	Variation des coefficients de calibration $c_{11gs}$ pour différentes excentricité du trou dans le sens radial suivant l'axe de la jauge 1 . . . . .	150
4.27	Variation des coefficients de calibration $c_{11gs}$ pour différentes déviations angulaires dans le sens anti-horaire . . . . .	150
4.28	Présentation générale du dispositif experimental utilisé pour mesurer les déformations de relaxation . . . . .	152
4.29	(a) Données brutes d'acquisition obtenues pour la plaque 3, (b) détails pour un cycle d'incrément . . . . .	155
4.30	Variation du champ thermique (mesuré en utilisant une caméra thermique) pour un incrément : champ thermique (a) à la fin du précédent incrément , (b) pendant le perçage, (c) pendant la relaxation et (d) à la fin du temps de relaxation . . . . .	156
4.31	Résultats des tests de DSC modulés : échantillons extraits à froid (a) de la plaque 1, (c) de la plaque 2 et (e) de la plaque 3. Echantillons extraits par perçage (b) de la plaque 1, (b) de la plaque 2 et (f) de la plaque 3. "Enthalpy" correspond à l'enthalpie de la réaction et "Midpoint" à la temperature de transition vitreuse. . . . .	158
4.32	Relaxation strains measured for the three plates (means and dispersions are determined from 3 tests): results obtained for (a) jauge 1, (b) jauge 2 and (c) jauge 3 . . . . .	160
4.33	CR déterminées pour les 3 plaques : (a) $\sigma_x$ ( $\sigma_x$ de la plaque 2 est caché par celui de la plaque 3 au 1er incrément), (b) $\sigma_y$ and (c) $\sigma_{xy}$ . . . . .	161
C.1	Damage on the surface of the hole as function of the rotation speed: (a) 20000 rpm , (b) 16000 rpm, (c) 12000 rpm, (d) 8000 rpm, (e) 5000 rpm . .	193

D.1 Study of the influence of the withdrawal speed on the raw acquisition data:  
v1 = 5 mm/s, v2 = 1 mm/s, v3 = 0.5 mm/s, v4 = 0.1 mm/s, v5 = 10  
mm/s, v6 = 2 mm/s and v7 = 5 mm/s . . . . . 195

# List of Tables

- 2.1 Features of the used gages . . . . . 60
- 2.2 Comparison of the calibration coefficients obtained in this work with those obtained in the literature for a thin isotropic material:  $E=200$  GPa and  $\nu=0.3$  . . . . . 63
- 2.3 Comparison of the calibration coefficients obtained in this work with those obtained in the literature for a thin orthotropic material . . . . . 65
- 2.4 Material properties used for the application [117] . . . . . 70
- 2.5 Example of a simple script: modelling of a parallepiped . . . . . 73
- 2.6 Influence of the size of the mesh elements in the area of the gage on the value of the first increment calibration coefficients. The average calculation time is the average of the calculation time of the 3 simulations corresponding to the 3 load cases. The considered material is the composite laminate presented in section 2.4.2 - b . . . . . 76
- 2.7 Influence of the model size (length and width) on the value of the first increment calibration coefficients. . . . . 76
- 2.8 Influence of the shape function of the mesh elements on the value of the first increment calibration coefficients . . . . . 77
- 3.1 variation of the calibration coefficients  $c_{11gs}$  for different errors on increment depth  $\delta d_{model}$  (increment depth  $d_{model} = 100\mu m$ ). . . . . 83
- 3.2 variation of the calibration coefficients  $c_{11gs}$  for different angular deviations in the counter-clockwise direction . . . . . 86
- 3.3 variation of the calibration coefficients  $c_{11gs}$  for different radial eccentricities 87
- 3.4 variation of the calibration coefficients  $c_{11gs}$  for different angular eccentricities 89

3.5	Numerical validation of the proposed correction method: comparison between the reference residual stresses, the corrected residual stresses and residual stresses with an eccentric hole obtained by numerical simulations of the incremental hole drilling for the considered initial residual stress profile. . . . .	93
4.1	Curing cycles used to manufacture the composite plates . . . . .	107
4.2	Experimental parameters and conditions of the incremental hole drilling test	111
4.3	Experimental parameters for Modulated DSC . . . . .	120
4.4	Experimental parameters and conditions for DMA . . . . .	122
4.5	Cycles de cuisson utilisés pour fabriquer les plaques de composite . . . . .	154
4.6	Conditions et paramètres expérimentaux du test de trou incrémental . . .	154
4.7	Paramètres expérimentaux des tests de DSC modulé . . . . .	157
B.1	Numerical relaxation strains and $[S_{ii}]$ matrices used for the numerical validation of the correction method (section 3.3 of chapter 3) . . . . .	188
B.2	Calibration coefficients ( $c_{ijijkl}$ ) used for the numerical validation of the correction method (Table 6 of the paper). . . . .	189
B.3	Comparison between the reference residual stresses, the corrected residual stresses and residual stresses with an angular deviation of the gages obtained by numerical simulations of the incremental hole drilling for the initial residual stress profile 1 (stress profile used in Table 6 of the paper). .	190
B.4	Comparison between the reference residual stresses, the corrected residual stresses and residual stresses with an eccentric hole obtained by numerical simulations of the incremental hole drilling for the initial residual stress profile 2. . . . .	191
B.5	Comparison between the reference residual stresses, the corrected residual stresses and residual stresses with an eccentric hole obtained by numerical simulations of the incremental hole drilling for the initial residual stress profile 3. . . . .	192

# General Introduction

Rapid advances in high technology and the ecological emergency have attracted particular interest in advanced materials research. This includes research on new materials and optimization of existing materials to improve their in-used performances and reduce their carbon footprint and that of the systems in which they are used. In response to the ecological emergency, several countries are putting in place strategies that include: the massive use of electromobility, alternative fuels (biogas, biofuels, hydrogen, etc.), controlling the growth of transport demand, improved vehicle performance (lower fuel consumption per km). For the latter, a solution is the reduction of the total mass of the vehicles. For several decades, a lot of research has been carried out in this direction, with the aim of developing new materials capable of meeting this need. Composites, which are materials with good specific properties, are thus experiencing a strong development and are increasingly used to lighten the structure of CO<sub>2</sub>-emitting transport modes. This is particularly effective in the case of heavy vehicles such as airplanes and tankers for which the weight gain is considerable.

In this way, Fiber Reinforced Composite Laminates are good candidates. However, due to their heterogeneous nature and their manufacturing process with complex chemical reactions and thermomechanical stresses, they are subject to significant residual internal stresses with consequences often harmful to their geometry and/or performance in their operating conditions of use. Therefore, the residual stresses are important data to consider when sizing composite parts and predicting their behavior.

Many works exist in the literature on several techniques to minimize residual stresses in thermosetting and thermoplastic composites mainly. However, these techniques very often have detrimental effects on the mechanical properties of the composites. Another important problem is the measurement of the residual stresses, whose techniques lead to many questions on the value to be given to the results (local measurements, measurements themselves inducing stresses, ...). That is why, composite internal stresses measurement and the validity of the results are the main objective of this study. Among the existing techniques, this work focuses on the incremental hole drilling method.

This work is part of a broad research carry out on the laboratory in which the manufacture and behavior of composites are the main topic. In this theme, a project called "Light Tank" (ADEME project UHA/Magyar) aims to manufacture tank trucks with composite reservoirs for the transport of dangerous liquids. One of their problems is the measurement and control of the internal stresses in order to be able in a longer-term to establish a correlation between the manufacturing parameters of various types of composites and the induced residual stresses. Thus, the first objective of this work is to summarize the multi-physical mechanisms and matrix/fibrous reinforcement interactions that lead to the formation of residual stresses in composites. The second objective is to develop experimental and numerical tools adapted to the measurement of residual stresses by the incremental hole drilling method. The third objective is to develop expertise in the measurement of residual stresses by the incremental hole method and to provide answers on some aspects which are not or very little studied in the literature such as a detailed explanation of the raw acquisition data or the influence of the drilling on the local chemical properties of the resin.

In the first chapter, the problem of residual stresses is presented in detail. The origins of residual stresses, their influence on the properties of composites laminates, the most common minimization techniques such as the modification of the curing cycle are presented. Methods for predicting and measuring residual stresses are also described in this chapter.

In the second chapter, the incremental hole drilling is presented step by step. The theoretical formulation of the method is presented in detail not only for composite laminates but also for the other configurations (thin and thick isotropic materials, thin orthotropic materials) to allow a global comprehension of the method. An important part of this chapter is the calculation of the calibration coefficients using finite element simulations. A good comprehension of these numerical calculations is necessary to understand the determination of the residual stress gradient through the material thickness. The configurable numerical model coded in Python and based on Abaqus that is used to simulate the incremental hole drilling method is described.

In the third chapter, the configurable aspect of the model is used to perform parametric study and numerically evaluate the sensitivity of the incremental hole drilling method to experimental errors. This allowed to propose a correction method for the calibration coefficients and identify the critical tasks in the experimental protocol. The experimental device developed to measure the relaxation strains and the solutions proposed to minimize

experimental errors are presented.

In the fourth chapter, the studied material is presented and the experimental procedure is described step by step. A typical acquisition curve of the relaxation strain is presented and explained in detail. A focus is done on the effect of the drilling on the local chemical and mechanical properties of the resin. For that, thermal measurements are carried out to characterize the thermal field during and after the drilling. Then, Differential Scanning Calorimetry (DSC) and Dynamic Mechanical Analysis (DMA) are carried out to characterize the local properties of the resin. The residual stresses of samples manufactured under different curing conditions are presented and compared.

Then, a conclusion will summarize the main results and the questions raised. They will be the subject of the perspectives to be given to this work.





# Chapter 1

## Generality on residual stresses

### Sommaire

---

<b>1.1</b>	<b>Introduction</b>	<b>7</b>
<b>1.2</b>	<b>Origins of residual stresses</b>	<b>7</b>
1.2.1	Mechanisms occurring during processing of thermoset laminates	7
1.2.2	Chemically-induced residual stresses	9
1.2.3	Thermally-induced residual stresses	10
<b>1.3</b>	<b>Influences of residual stresses on material properties and minimization techniques</b>	<b>14</b>
1.3.1	Influences of residual stresses on composite laminates properties	14
1.3.1 - a	Effects of residual stresses on the matrix properties	14
1.3.1 - b	Effects of residual stresses on the fiber-matrix interface	15
1.3.1 - c	Defects due to residual stresses	15
1.3.1 - d	Effects of residual stresses on the structure of composite laminates	18
1.3.1 - e	Effects of residual stresses on the mechanical properties of composite laminates	20
1.3.2	Residual stress minimization techniques	24
1.3.2 - a	Modification of the cure cycle	24
1.3.2 - b	Relaxation of residual stresses by annealing	26
1.3.2 - c	Relaxation of residual stresses by water absorption	26
1.3.2 - d	Molecular additive insertion in the resin	27
<b>1.4</b>	<b>Methods for measuring and predicting residual stresses</b>	<b>28</b>
1.4.1	Residual stress prediction methods	28
1.4.1 - a	Micro-mechanical level	28

---

1.4.1 - b Macro-mechanical level . . . . .	29
1.4.2 Experimental methods for measuring residual stresses . . . . .	32
1.4.2 - a Non-destructive methods . . . . .	33
1.4.2 - b Destructive methods . . . . .	36
1.4.2 - c Methods using embedded strain sensors . . . . .	38
<b>1.5 Conclusion . . . . .</b>	<b>41</b>

---

## 1.1 Introduction

This first chapter aims to introduce the problem of residual stresses in general. The different stages of residual stresses formation during processing of fiber reinforced composites are presented in detail to allow a global comprehension of this work. Understanding the influence of these process-induced residual stresses on materials and, in particular, on thermoset and thermoplastic composite laminates is necessary to apprehend the stakes of such a study. For many applications, the residual stresses need to be optimized in order to improve the properties and the life of the fabricated composites. For that purpose, techniques frequently used to reduce residual stresses are presented in this chapter. The most commonly used prediction models and measurement methods of residual stresses are also presented.

## 1.2 Origins of residual stresses

Composite laminates are heterogeneous materials composed of resin, fibers and sometimes fillers and additives. Processing of fiber reinforced composites requires high temperature curing and cooling to room temperature. This causes complex chemical, mechanical and thermal mechanisms which are not yet fully understood and are the subject of much research [1], [2], [3]. The properties of the final composite part are highly dependent on the processing parameters mainly temperature, pressure and time. These properties also depend on the matrix, the type of fibers, the volume fraction of fibers and the cross-link density [4].

### 1.2.1 Mechanisms occurring during processing of thermoset laminates

The recommended cure cycle for thermoset resins consists of 2 isothermal stages (Fig. 1.1)[5].

During stage I, from a limit temperature that correspond to the initiation of cross-linking (60°C in Fig. 1.1), the viscosity increases, resin starts lightly to consolidate and to contract (cure shrinkage). In stage II, cure shrinkage continues, the internal energy increases due to the exotherm of the reaction and degree of cure ( $\alpha$ ) spread within the material (Fig. 1.2a).

The mechanisms linked to the cure reaction, namely the cross-linking, the exotherm, the cure shrinkage and the degree of cure ( $\alpha$ ) continue up to the end of stage V (where the resin is almost fully cured). In stages III and IV, there is a thermal expansion caused by the augmentation of temperature. The gelation point occurs between these two stages.

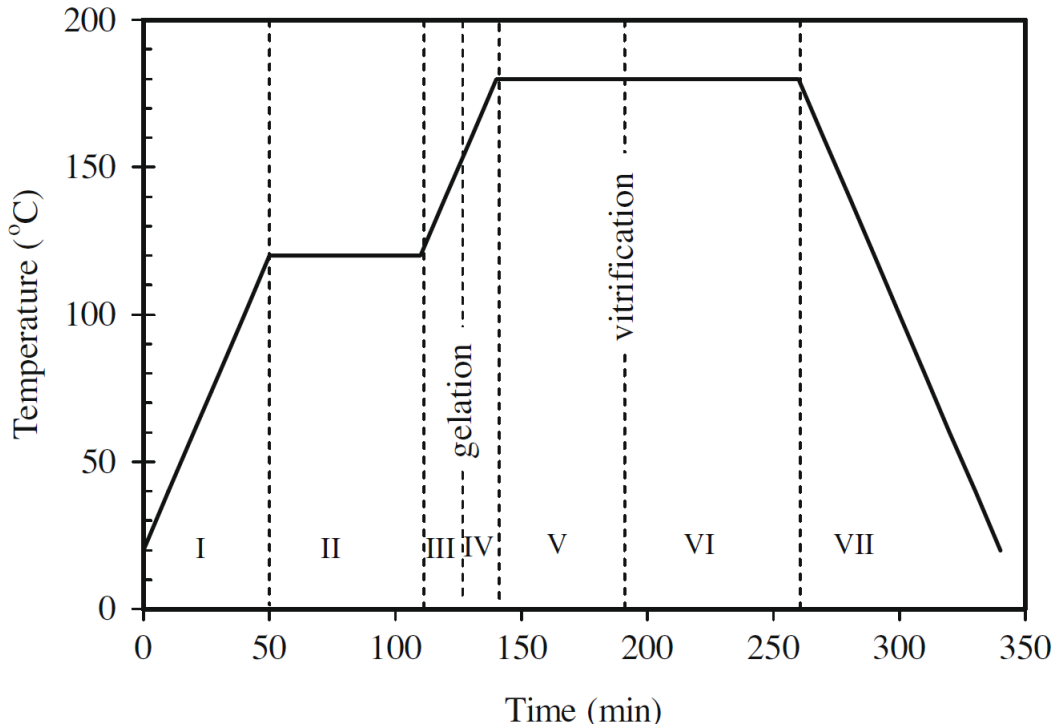


Figure 1.1 – Relevant stages of the recommended cure cycle for thermoset laminates (AS4/8552 carbon/epoxy laminates, [5])

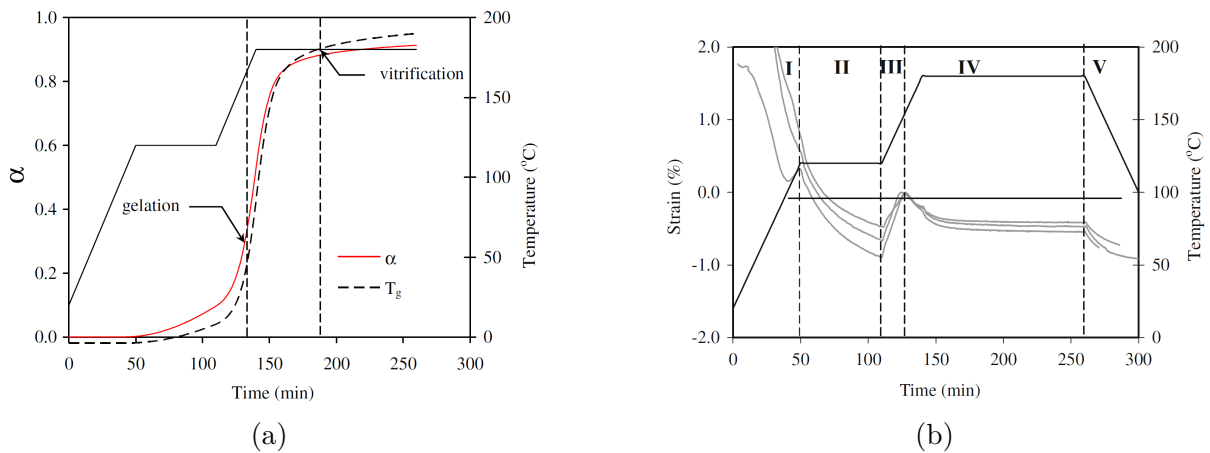


Figure 1.2 – (a) Evolution of the degree of cure and the glass transition temperature during the cure cycle of a AS4/8552 carbon/epoxy composite, (b) Evolution of the strain through the cure cycle [6]

It corresponds to the point from which the resin changes from a liquid state to a gel state due to the formation of an infinite cross-linked network. From the gelation point, the properties of the resin develop until the end of the reaction. The vitrification (end of stage V) corresponds to the point where the instantaneous glass transition temperature ( $T_g$ ) reaches the cure temperature ( $T_c$ ). In stage VI, the degree of cure reaches an asymptote (Fig. 1.2a), the resin is almost fully cured and the reaction slows down considerably. During stage VII there is a thermal contraction caused by the cooling to room temperature. It is important to note that if the resin is cured above its ultimate

glass transition temperature ( $T_{g\infty}$ ), there is only gelation (because the glass transition temperature cannot reach the cure temperature). However, there is vitrification during the cooling process, when  $T_c$  reaches  $T_{g\infty}$  [7].

### 1.2.2 Chemically-induced residual stresses

The properties of fibers are generally assumed to be independent of the cure while resin's properties and dimensions are very cure-dependent. The volumetric shrinkage of the resin, due to the cross-linking, compresses the fibers and induces residual stresses in the laminate. Bogetti and Gillespie [8] obtained a total volumetric resin shrinkage of 6% for a unidirectional glass/polyester composite under isothermal cure at 100 °C. Most of the chemical shrinkage takes place between gelation ( $\alpha = 0.33$ ) and vitrification ( $\alpha = 0.88$ ) for thermoset resins (see Fig. 1.2a). The mechanical properties of the resin also develop in this interval, consequently residual stresses cannot develop before the gelation since the resin is in a viscous liquid state. The through-the-thickness strain is an important parameter in the formation of residual stresses. Ersoy et al. [6] found a through-the-thickness strain of about  $0.48 \pm 0.06\%$  for unidirectional laminates and  $0.98 \pm 0.13\%$  for cross-ply laminates. This difference is explained by the fact that both longitudinal and transverse contraction of the resin in a cross-ply laminate are constrained by fibers, there by, contraction mainly takes place in the thickness.

The amplitude of residual stresses depends on the nature of the resin. A high rubbery modulus and shrinkage polymer such as low molar mass acrylate develops more residual stresses than resin such as epoxy [4]. Lange et al [4] have shown that the cross-linking density is an important parameter in the development of residual stresses. They found that the chemical residual stresses are less than 1% of the total residual stresses for a lightly cross-linked epoxy and more than 30% for a densely cross-linked epoxy. The level of residual stresses also depends on the curing strategy. White et Hahn [9] showed that the higher the second dwell temperature of the cure cycle, the higher the degree of cure and the shorter the cure time (Fig. 1.3). However, elevated cure temperatures induce severe degree of cure gradients causing residual stresses.

For thermoplastic matrix, it is recommended to consider a processing temperature above  $T_{g\infty}$ . At this temperature, the matrix is in an amorphous state, the composite behaves visco-elastically and residual stresses relaxation is still possible [10]. Below  $T_{g\infty}$ , the matrix is in a glassy state, the composite behave thermo-elastically and residual stresses cannot relax anymore.

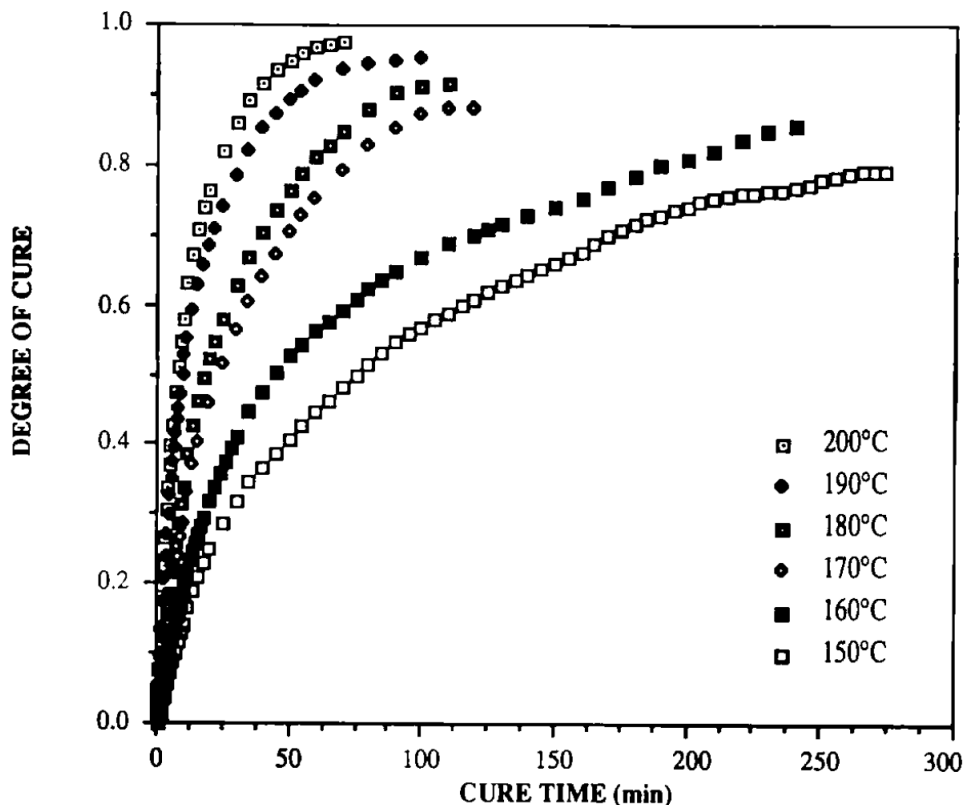


Figure 1.3 – Progress of the degree of cure for different cure temperature of the second dwell for an IM6/3100 graphite/bismaleimide composite [9]

### 1.2.3 Thermally-induced residual stresses

Thermal residual stresses are caused by the difference in coefficient of thermal expansion between fibers and matrix and they represent 70% up to 99% of the overall residual stresses [4]. Thermally-induced residual stresses build-up during the cooling procedure and are very dependent to the cooling rate. The resin is viscoelastic at elevated temperature and approaches elastic behavior at low temperature (for a curing below  $T_{g\infty}$  Fig. 1.2a) [8]. Thus, the lower the cooling rate, the lower the residual stresses as they simply have more time to relax at high temperatures (this is not true for certain semi-crystalline matrices, see the explanation at macro-mechanical level below). Fig. 1.3 shows that higher cure temperatures give higher degree of cure, however they also induce more important thermal residual stresses (for a constant cooling rate) since the temperature differential is higher during cooling to room temperature.

Thermally-induced residual stresses can be analysed at three different scales:

- Micro-mechanical level:

The mismatch in coefficient of thermal expansion between fibers and matrix is the governing parameter of the build-up of residual stresses at micro-mechanical level (micro-stresses). Consider, for example, a carbon fiber embedded in an epoxy matrix

(Fig. 1.4). For a decrease,  $\Delta T$ , of the temperature, the matrix contracts more than the fiber (approximately 6.4 times in the transverse direction of the fiber). Furthermore, the coefficient of thermal expansion of the fiber is negative in the longitudinal direction, i.e. it expands in this direction during the cooling process. There by, assuming continuity of displacements at the fiber/matrix interface, the fiber is in a state of compression and the matrix in a state of traction (Fig. 1.4).

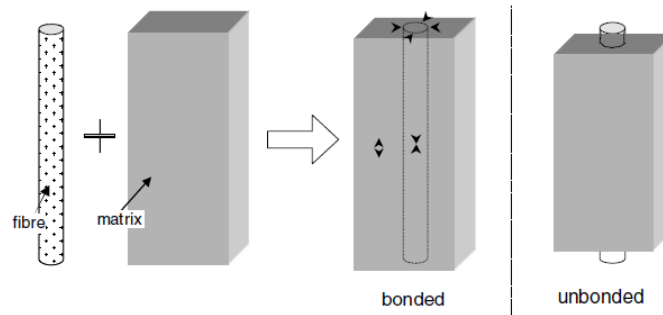


Figure 1.4 – Formation of residual stresses at the micro-mechanical level [10]

Barnes et al [11] estimated the compressive residual stresses on a single carbon fiber in an infinite PEEK matrix to be of the order of 10 MPa in the radial direction [11]. In the longitudinal direction of the fibers, they have been estimated to be of the order of 34 MPa [12]. The micro residual stresses also depend on the Young's modulus of the matrix and the fiber-matrix interface [10]. Residual stresses increase if the Young's modulus of the matrix is higher [10] and if the fiber-matrix interfacial bond is stronger [13].

- Ply-to-ply level:

The thermal contraction of a ply depends on the orientation of the fibers (Fig. 1.5).

The contraction in the fibers direction is less important than the contraction in the transverse direction. This anisotropic thermal behavior of a ply depending of the fibers orientation leads inevitably to the build-up of residual stresses at the ply-to-ply level (assuming continuity of displacements at the ply/ply interfaces). These stresses result in a curvature of the composite in the case of non-symmetrical stratification and unbalanced cooling (if the faces of the composite are subjected to the different thermal boundary conditions during cooling) [10]. Schwarz et al. [14] found that the shear residual stresses at the ply-to-ply level were maximum at fiber angles of  $\pm 30^\circ$  with respect to the main direction of the composite.

- Macro-mechanical level:

At the part scale, residual stresses build-up due to the gradient of temperature that occur in the thickness of the composite during cooling. For thick composites,



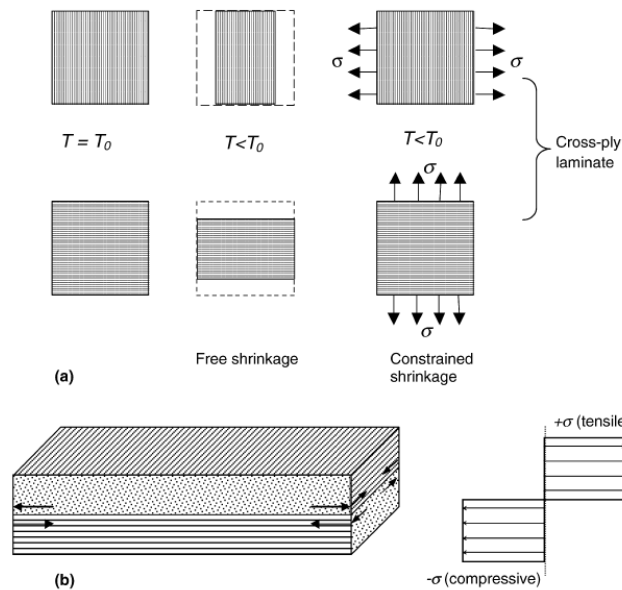


Figure 1.5 – Formation of residual stresses at the ply-to-ply level [10]

the layers closest to the surface cool faster than the central ones, resulting in a parabolic distribution of residual stresses through the thickness (Fig. 1.6). For thermoset composites, high cooling rates induce high residual stresses. However, for semi-crystalline thermoplastic composites such as PEEK, it is more complicated. The residual stresses also depend on the crystallisation kinetics of the crystalline part of the matrix. The higher the crystallinity levels, the higher the crystallisation shrinkage and the higher residual stresses. Thus, during cooling, two competing mechanisms happen: slow cooling rate, for example, leads to low residual stresses in the amorphous part of the matrix (since there is more time for relaxation) and to high residual stresses in the crystalline part of the matrix (high crystallisation shrinkage since there is enough time for crystals to form) [15]. The final stress state depends on the crystallisation kinetics. At the macro-mechanical level, the distribution of residual stresses can be symmetrical through the thickness if the lay-up is symmetrical and if the cooling is balanced [15].

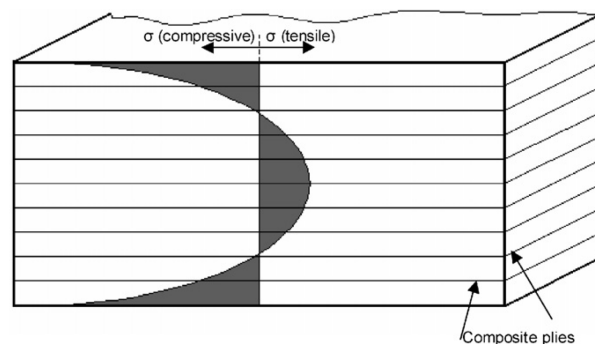


Figure 1.6 – Formation of residual stresses at macro-mechanical level [10]

Thermally-induced residual stresses are, generally, supposed to build-up exclusively during the cooling process. In other words, the thermal residual stresses are assumed to be zero at the end of the cure. However, one may wonder about the legitimacy of such an assumption for thermoset resins for which cross-linking is exothermic. Ochi et al [16] showed that the total residual stress level depend on the exotherm of the reaction. During the second dwell of the recommended cure cycle, thermal residual stresses are considered to be zero because the curing temperature is constant. However, the temperature in the thickness of the composite is not uniform because of the exotherm cross-linking. Bogetti et Gillespi [8] showed that the temperature gradient due to the exotherm has a parabolic distribution through the thickness for unidirectional glass/polyester laminates. In Fig. 1.7a, one can see that the temperature of the lower and upper surface is equal to  $90^{\circ}\text{C}$  which corresponds to the cure temperature at 164 minutes (Fig. 1.7b). It is important to note that the temperature distribution depends not only on the thickness but also on the progress of the reaction since the distribution varies over time.

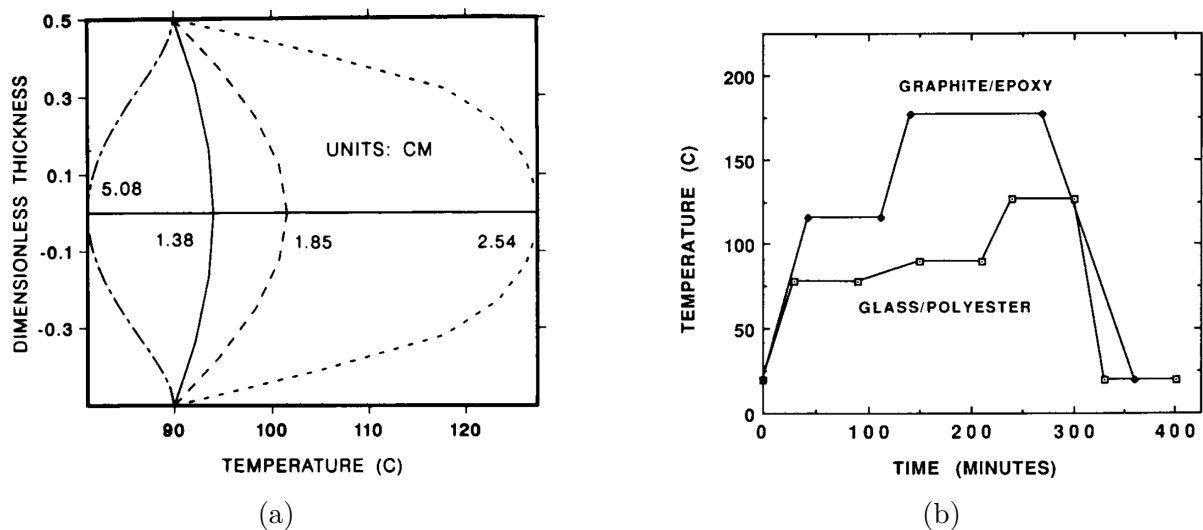


Figure 1.7 – (a) Glass/polyester and graphite/epoxy cure cycle , (b) Temperature distributions due to the exotherm of the reaction in unidirectional glass/polyester for different thicknesses at 164 minutes of the cure cycle [8]

## 1.3 Influences of residual stresses on material properties and minimization techniques

### 1.3.1 Influences of residual stresses on composite laminates properties

#### 1.3.1 - a Effects of residual stresses on the matrix properties

As detailed in section 1.2, the differences between the matrix and the fibers properties result in a state of residual tensile strain in the matrix. The induced residual stresses have a significant influence on the ultimate glass transition temperature of the matrix ( $T_{g\infty}$ ) [17]. The  $T_{g\infty}$  is increased by compressive internal stresses and decreased by tensile and shear internal stresses [17]. This was evidenced experimentally by comparing the  $T_{g\infty}$  of a carbon fiber reinforced polyetherimide (PEI) and a pure PEI [15, 17]. D'Amore et al. [17] found a decrease in  $T_{g\infty}$  of 30°C for an 8-ply quasi-isotropic laminate, while Parlevliet et al. [15] found a decrease of only 6°C for a 3 crossed ply laminate. It is essential to assess the influence of residual stresses on the  $T_{g\infty}$  given that it is an important factor in the service resistance of composite parts.

D'Amore et al [17] also showed that residual stresses have effects on the physical aging of thermoset and thermoplastic matrix. The physical aging correspond to the different relaxation mechanisms that occur when an amorphous polymer (or the amorphous part of a semicrystalline polymer) goes from a non-equilibrium to an equilibrium state. In fact, when the polymer is above its  $T_{g\infty}$ , it is a viscoelastic rubber in thermodynamic equilibrium. When the polymer is cooled below its  $T_{g\infty}$ , it becomes a non-equilibrium glass. The polymer undergoes a very slow structural rearrangement due to the relaxation of the polymer chains until it reaches the equilibrium state. The time scale of this relaxation is considerably larger than the time scale of the composites manufacturing process. This relaxation time scale can be reduced to the laboratory time scale by annealing at temperatures lower but close to  $T_{g\infty}$ . These mechanisms of relaxation or physical aging result in enthalpy recovery and changes in mechanical properties such as increased modulus and yield strength [15]. D'Amore et al. [17] found that the carbon fiber reinforced polyetherimide (PEI) aged faster than the plain matrix, which suggests that tensile residual stresses have a positive effect on matrix aging properties. It is important to note that isothermal aging has a detrimental effect on the fracture energy, the toughness and the flexural strength particularly for long aging time [18].

It is well known that moisture uptake lead to a relaxation of the residual stresses in the

matrix. However, the residual stresses also affect the moisture absorption property of the matrix. Sims and Broughton [19] reported that the rate of moisture uptake is accelerated under tensile stresses. The higher the residual stresses, the higher the moisture uptake [19].

### 1.3.1 - b Effects of residual stresses on the fiber-matrix interface

The fiber-matrix interface bonding mechanisms in composite materials generally include inter-diffusion, electrostatic adhesion, chemical reactions and mechanical interlocking which are presented in Fig. 1.8 [20]. The residual stresses have an influence on the mechanical interlocking that occurs at the fiber-matrix interface in thermoplastic composites. As explained in section 1.2.3, the matrix compresses the fibers because of the micro-mechanical residual stresses. This has a beneficial effect on the mechanical interlocking by improving the fiber-matrix interfacial shear strength. However, interfacial debonding may occur in the axial direction of the fibers due to residual stresses if the fiber-matrix bond strength is weak [21]. Interactively, the fiber-matrix bond strength influences the residual stresses magnitude. Greater bond strength lead to greater residual stresses. It is also suggested that in semi-crystalline composites such as carbon fiber reinforced polyetheretherketone (PEEK), micro-mechanical residual stresses can cause strain-induced crystallisation [22].

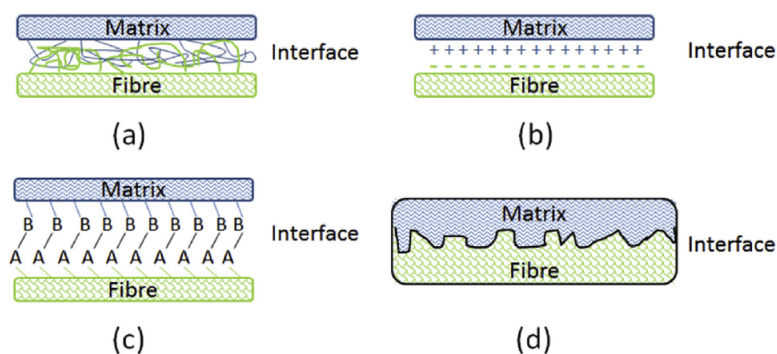


Figure 1.8 – Fiber-matrix interfacial bonding mechanisms: (a) molecular entanglement due to interdiffusion, (b) electrostatic adhesion, (c) chemical bonding and (d) mechanical interlocking [20]

### 1.3.1 - c Defects due to residual stresses

#### Micro-cracks:

Residual stresses can locally be higher than the matrix yield strength and/or the fiber-matrix bond strength [23]. This results in micro-cracking of the matrix and fiber-matrix

interfacial debonding. The micro-cracking can propagate in 2 different ways. If the fiber-matrix strength is weak, a transverse crack initiated in the matrix can join a fiber-matrix interface and propagate parallel to the fiber. If the fiber-matrix interfacial bonding is strong, transverse cracks continue to propagate through the matrix [24]. It is also possible that multiple fiber-matrix debonding join through matrix cracking and result in a failure initiation [25] (Fig. 1.9).

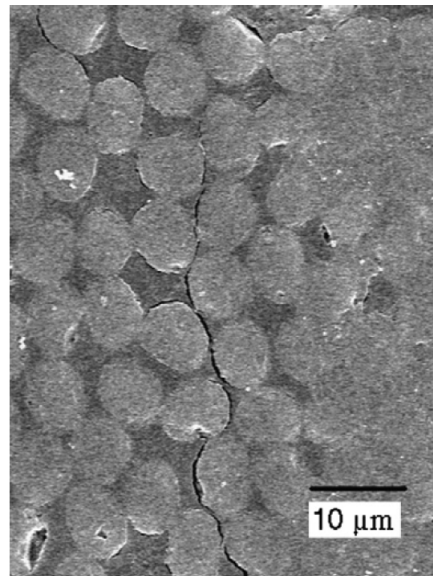


Figure 1.9 – Crack initiation along fiber–matrix interfaces in a carbon fiber polyphenylene-sulfide laminate [15]

Parlevliet et al [15] have summarised the different stages of transverse cracking in 4 points:

- fiber–matrix debonding/matrix cracking.
- Growing of matrix cracks/fiber–matrix debonds to form microcracks.
- Microcracks may grow into transverse ply cracks.
- Transverse ply cracks form initiations to delamination and subsequent failure of the laminate.

In the most severe cases, residual stresses can reach values so elevated that they can cause premature transverse ply crack during or just after processing [26] (Fig. 1.10, 1.11a). This is more frequent for brittle matrices such as thermoset matrices [24]. These cracks depend on the thickness of the ply [10] and often propagate from the free edges where the value of the residual stresses can be very high [27]. In general, the higher the residual stresses the higher the micro-cracks density within the composite laminates [27].

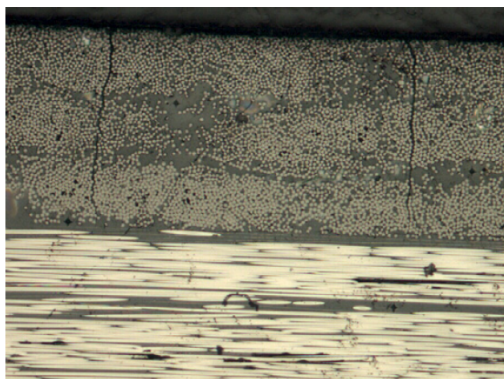


Figure 1.10 – Transverse cracks in surface plies of  $0_3/90_9/0_3$  carbon fiber polyetherimide laminate [15]

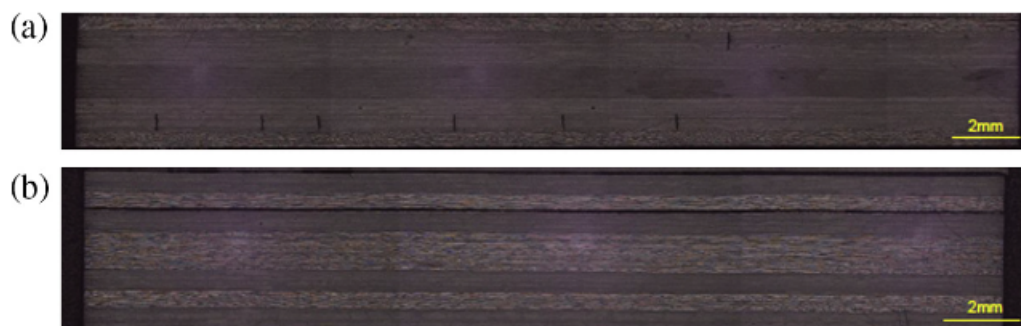


Figure 1.11 – (a) Residual stress induced microcracking in the  $45^\circ$ plies of a 32-ply quasi-isotropic laminate and (b) residual stress induced delamination in a 32-ply cross-ply laminate [28]

In their literature review, Parlevliet et al. [15], listed a certain number of transverse cracks effects on composite properties:

- A decrease of the elastic moduli and stiffness of composites, particularly for a quasi-isotropic lay-up.
- A decrease of the flexural modulus
- Reduced in-plane shear modulus and strength.
- A decrease of the transverse mechanical properties.
- A decrease of the Poisson's ratio.
- Lower values of Modes I and II interlaminar fracture toughness.
- Initiation of delamination sites during fatigue loading.
- An increase of deformation during creep loading.

- Enhanced moisture absorption. Cracks act as diffusion paths.
- Lower chemical resistance. Cracks act as entries for corrosive liquids.
- A decrease of the transverse electrical conductivity of carbon fiber reinforced laminates.

#### **Delamination:**

In a multilayered composite laminate, if the interlaminar residual stresses (ply-to-ply level, see section 1.2.3) are higher than the ply-ply bonding strength this will result in delamination (Fig. 1.11b). This is more frequent in cross-ply laminates for which the discontinuities of the interlaminar residual stresses between 0 degrees and the 90 degrees plies can be important [29, 30]. Generally, delamination occur around any stress concentration areas such as free-edges (free-edge effect), holes, cut-outs, section variations [15]. Internal delaminations can also occur in the structure of laminates due to compressive residual stresses. Acoustic emissions, electrical and electromagnetic methods are use, among others, to detected internal delaminations (as well as micro-cracks) [31].

#### **1.3.1 - d Effects of residual stresses on the structure of composite laminates**

##### **Fiber waviness:**

In fiber reinforced composite laminates, the fibers are not designed to sustain axial compressive loads. Thus, during the processing, microbuckle can occur due to the axial compressive residual stresses as a result of the consolidation of the matrix. This mechanism takes place if the matrix transverse stiffness is weak to support the fibers [32]. The microbuckles lead to fiber waviness (Fig. 1.12).

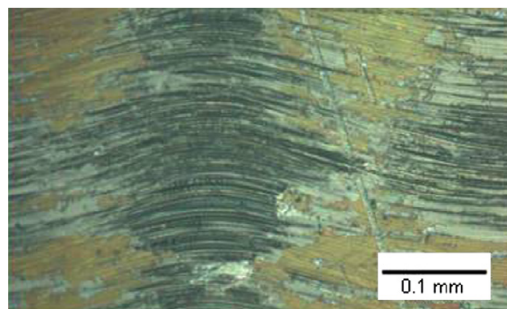


Figure 1.12 – Micrograph of a composite laminate showing fiber waviness [15]

In their work, Kugler and Moon [33] showed that the build up of fiber waviness depends on the material of the surface of the mould with which the composite is in contact and on cooling rate and length. In fact, the difference in coefficient of thermal expansion between the tool and the part as well as the cooling rate cause residual stresses. These residual stresses are responsible of the fiber waviness. Macro-residual stresses due to a

high gradient of temperature in the thickness can also generate fiber waviness [15]. Fiber waviness can weaken the compressive strength of the composite laminates [34]. Several techniques for estimating the mechanical properties of composites use strain gages. The strain gages are generally oriented with respect to the fibers. Fiber waviness can be very disturbing for such technics and introduce errors in the estimation of the mechanical properties.

### **Curvature:**

Interlaminar residual stresses are known to cause curvatures in non-symmetrical composite laminates [15]. This is due to the forced thermal deformations of adjacent layers with different fiber orientations. These residual stress-induced warpage particularly affect thin non-symmetrical laminates. However, even symmetrical laminates can experience curvatures if the macro-residual stresses are non-symmetrical through the thickness. Non-symmetrical residual stresses are mainly due to an unbalanced cooling and tool-part interaction [10]. In addition, a gradient of temperature in the tool itself (press-plates or moulds) can also generate warpage [15] (Fig. 1.13).

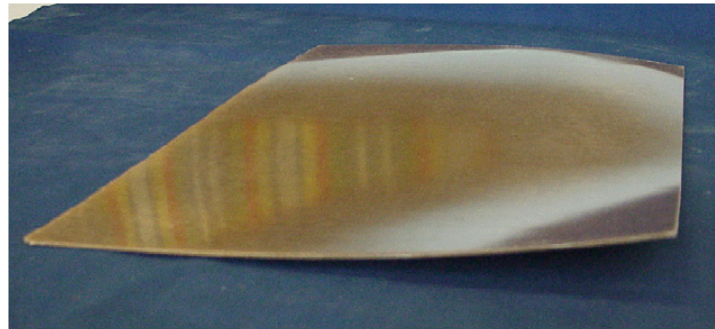


Figure 1.13 – Distorted glass fiber fabric reinforced polyetherimide laminate due to non-uniform cooling of the hot platen press [15]

For crossply laminates, the effect of interlaminar residual stresses on the curvature of parts are believed to be more important than that of macro-residual stresses [35] (through the thickness). For a 20-ply glass fiber reinforced PEI unidirectional laminate, curvatures due to unbalanced macro-residual stresses was found to be more important in the transverse direction [35]. The curvature radius of the parts depend on the residual stresses magnitude, but it also depends on defects such as micro-cracks that can lower it [15]. According to the classical stratified theory, the shape of the curved parts corresponds to a hyperbolic paraboloid (saddle shape). However, Hyer [36] showed that in the case of thin laminates, the theory is not respected. He showed through his experiments that thin laminates deform cylindrically. He has also shown that the deformation of this type of laminate is repeatable and is little affected by the difference in curing process or by the difference in materials used. Hyer hypothesized geometric instability to explain these



anomalies. He stated that the curvature of the laminates depends on the ratios “thickness over length” and “width over length”.

#### Effects on the composite global structure:

One of the most frequent effect of residual stresses on thin angled and curved composite products is the "spring-in effect" (Fig. 1.14). The out-of-plane contraction (solid arrows in Fig. 1.14) are generally more important than the in-plane contraction [15] (dotted arrows in Fig. 1.14). At the demoulding, the relaxation of the residual stresses deforms the parts so that the two sides of the curved part come closer to each other, thus reducing the enclosed angle. This is called the "spring-in effect" [37].

The machining of composite products can be affected by residual stresses. When material is removed from parts subjected to residual stresses, a local redistribution of stresses occurs. This redistribution causes relaxation strains that are very disturbing for machining because they can induce geometric instability of the part.

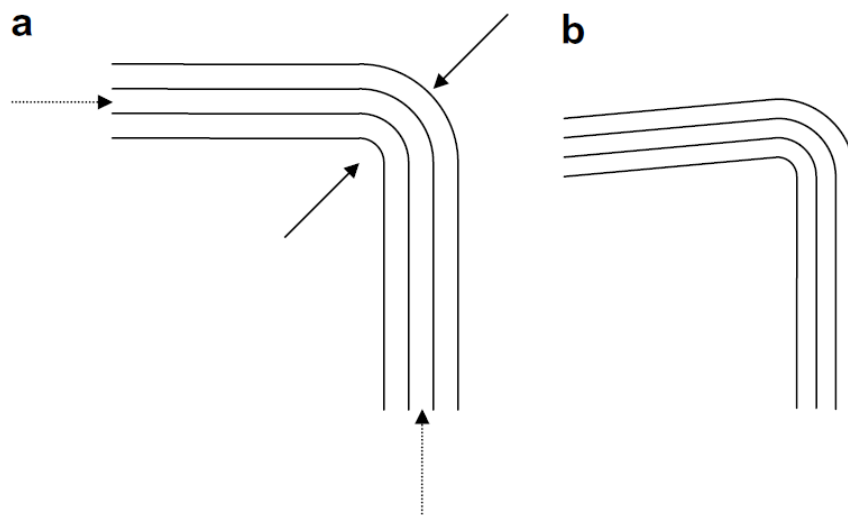


Figure 1.14 – Schematic of the spring-forward phenomenon: (a) before consolidation, in-plane contraction is represented by the dotted arrows, and out-of-plane contraction by the solid arrows, (b) after consolidation and cooling from the processing temperature [15]

#### 1.3.1 - e Effects of residual stresses on the mechanical properties of composite laminates

Residual stresses can reduce or increase the maximum load that composite parts can withstand depending on whether they are of the same sign or opposite sign to external loads. In either case, residual stresses are important data to consider when sizing composite parts.

#### Tensile:

During the processing of fiber reinforced composites, the fibers experience compressive

residual stresses (section 1.2.3). This compressive residual stress state is believed to enhance the tensile strength of composite laminates. Cantwell et al. [38] studied the effect of residual stresses on the tensile properties of  $((+/-45^\circ)_2)_s$  IM6/PEEK laminates. They compared samples cooled at  $50^\circ/min$ , annealed at  $270^\circ$  for 4h with un-annealed samples. They found a significant difference between the obtained stress-strain curves. The average strain to failure obtained for the un-annealed specimens was about 18% greater than that of the annealed specimens (Fig. 1.15). They also found that annealing altered the stiffness of the specimens. It is explained by the fact that compressive residual stresses enhance the tensile strength of the laminate, consequently, the relaxation of these compressive residual stresses, due to the annealing, altered the tensile response of the composite. The compressive residual stresses are also believed to increase the tensile failure strain [39]. Prior to loading, the plies experience a compressive strain. The total strain necessary to reach the failure of the part corresponds to the failure strain plus the initial compressive strain (due to residual stresses). Compressive stresses can be beneficial for the tensile strength of composites, but they can generate micro-cracks which reduce the properties of the parts (section 1.3.1 - c).

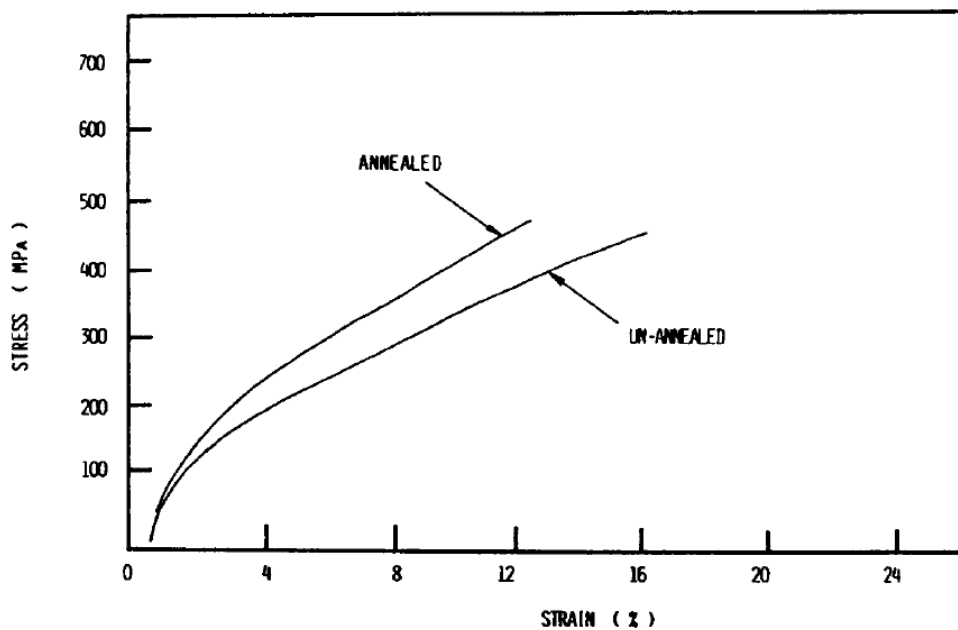


Figure 1.15 – A comparison of the stress-strain curves of an annealed and un-annealed  $((+/-45^\circ)_2)_s$  IM6/PEEK laminate cooled at  $50^\circ/min$  [15]

#### Flexural:

The process-induced residual stresses cause curvatures (section 1.3.1 - d) in composites that have non-symmetric stratifications or have experienced unbalanced cooling. These curvatures are due to the residual bending moments [9] and can considerably decrease the flexural strength of composite laminates. Guillén and Cantwell [40] reported that residual

stresses can reach 37% to 45% of the 90° flexural strength (26 MPa).

Another mechanism that has a great influence on the flexural strength is the physical aging (section 1.3.1 - a). Middleton et al. [18] studied the effect of isothermal aging on Polymer core composite conductor specimens (epoxy resin, carbon and glass fibers). They found a decrease of 20% of the flexural failure load for specimens aged at 140° and over 60% for specimens aged at 180° after 90 days of aging. There was not subsequent reduction after three months and even one year of aging for the specimens maintained at 140°. However, for the specimens aged at 180°, the flexural failure load has decreased by 75% after a year of aging. They concluded that higher temperature (while remaining below  $T_{g\infty}$ ) induce increased physical aging and suggested that this was due to the free volume reduction which cause a higher state of residual stress.

#### Compression and shear:

One of the most common compressive failure mode in composite materials is by kink-band formation. Yuan et al.[2] have divided the kink-band formation into 4 stages: uniform deformation, elastic buckle, kink-band and shear failure (Fig. 1.16). The compressive strength of a composite depends, among other, on the tranverse strength of the matrix, the fiber fraction volume, the stacking (the support provided by adjacent layers), the structure imperfection such as fiber misalignment. It was reported in section 1.3.1 - d that residual stresses can cause fiber waviness and curvatures. These residual stress-induced structure imperfections can be very detrimental for the compressive strength of composite laminates. Jensen [41] studied the effect of residual stresses on the compressive failure of unidirectional composites by the kink-band mechanism. The kink-band development depend mainly on the shear modulus of the matrix material. Jensen found that residual stresses affect the tangent shear modulus of the matrix and thereby influence (hasten or delay) the onset of the failure.

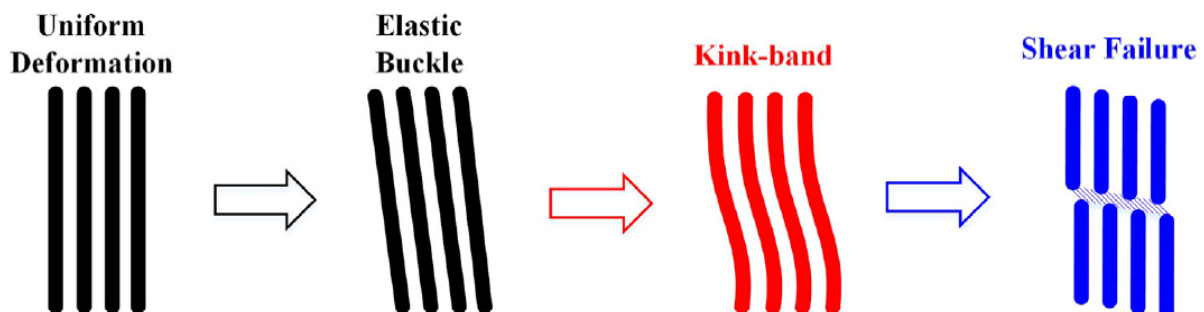


Figure 1.16 – Kink-band formation of localized buckling [2].

#### Long-term mechanical properties: fatigue and creep

The fatigue life of composite laminates depend on their residual stress state. Thus, the relaxation of residual stresses directly affects the fatigue behavior of composite, positively

or detrimentally depending on whether the stresses are of the same or opposite sign to the fatigue loads. In their work, Mostafa et al. [42] have shown the effect of residual stresses on prestressed E-glass/polyester woven composites (positive effect in their work). 50 MPa biaxial load was applied to the woven fabric before and during the curing. After the processing, the biaxial load was released and acted as residual stresses. The matrix was in a state of compression and the woven in a state of tension. The residual stresses were relaxed and tension fatigue tests were performed at various relaxation states. They found that the induced-residual stresses decreased by 27% throughout 110-130 days and became almost time-independent (Fig. 1.17). A 14% decrease was obtained between the fatigue life of the newly manufactured specimens and that of specimens that experienced 110-130 days of stress relaxation. This is explained by the fact that the sign of residual stresses of the matrix (compressive) is opposite to the fatigue load sign (tension).

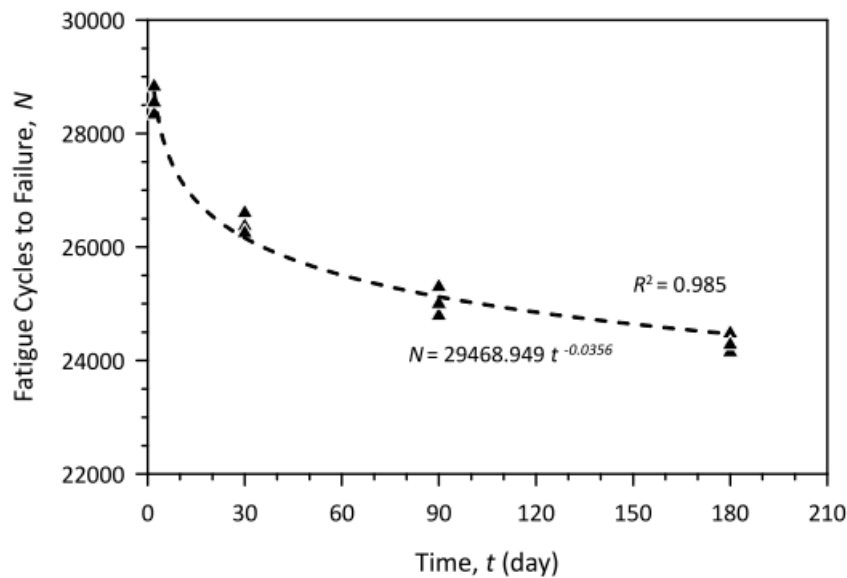


Figure 1.17 – Effect of longevity on the fatigue life of 50 MPa prestressed woven composite (E-glass/polyester) [42]

Residual stresses also affect the creep behavior of composite laminates. When a composite is subjected to residual stresses, the viscosity of the matrix [15] and the physical aging may induce relaxation or creep. For cross-ply IM6 carbon fiber PEEK laminates, the faster the composite are cooled, the higher the residual stresses and the more significant the creep behavior at room temperature [38].

#### Modes I and II fracture toughness:

Nairn [43] studied the effects of residual stresses on the fracture toughness of unidirectional graphite/polysulfone composites (thermoplastic). He considered mode I and mode II fracture tests and compared the results obtained for the composite and for neat resin. He found a much lower toughness for the graphite/polysulfone composite compared to the neat resin. Nairn suggested that the observed loss of toughness was due to the high level

of constraint imposed on the matrix by the fibers, in other words, because of the residual stresses. However, he found no significant effect on the transverse fracture properties of the composite. One can also cite the work of Gillespie and Chapman [44] who studied the influence of residual stresses on mode I interlaminar fracture of double cantilever beam testing of graphite/PEEK composites. They considered unidirectional and cross-ply samples cooled below  $30^{\circ}\text{C}/\text{s}$ . Compared to the results obtained with a cooling rate of  $0.2^{\circ}\text{C}/\text{s}$  (lower residual stresses), no significant variations were found for the unidirectional samples. However, a drop of 35% of the apparent toughness were observed for the cross-ply samples. From these works, one can conclude that residual stresses must be taken into account in numerical and/or analytical fracture toughness prediction models to have good agreement with the experimental results and accurate predictions.

#### 1.3.2 Residual stress minimization techniques

The minimization of residual stresses (or rather their optimization to be more rigorous) is an important issue in the manufacture of high-performance composites. Several authors have investigated different methods for minimizing residual stresses in composite laminates.

##### 1.3.2 - a Modification of the cure cycle

As detailed in section 1.2, residual stresses are directly linked to the process parameters. In certain studies, these parameters have been modified to decrease the level of residual stresses. White et Hahn [45] reduced the residual stress level in a graphite/BMI composite by decreasing the second dwell temperature by  $22^{\circ}\text{C}$ . However, to retain the mechanical properties they increased the dwell time by 160 min. They also showed that an intermediate dwell at low temperatures ( $160^{\circ}\text{C}$  and  $149^{\circ}\text{C}$ , see Fig. 1.18) in a three-step curing allows to reduce in a similar way the residual stresses without additional cure time.

Kim et al. [46] proposed a modified cure cycle to reduce the process-induced residual stresses in thick-walled carbon fabric phenolic composite cylinders. They modified the conventional cure cycle by adding a cooling and reheating stage during the second increase of temperature (Fig. 1.19). They measured the effect of the new cure cycle on the composite parts by using the radial-cut-cylinder-bending method. They found a reduction of 30% of the residual stresses compared to the conventional cure cycle.

With the increasing power of numerical tools, finite element simulations and numerical optimization have been extensively used to optimize the cure cycle of polymers and composite materials [47, 48, 49]. Shah et al. [47] used finite elements simulations and the genetic algorithms with Latin hypercube sampling to optimize the cure cycle of thin

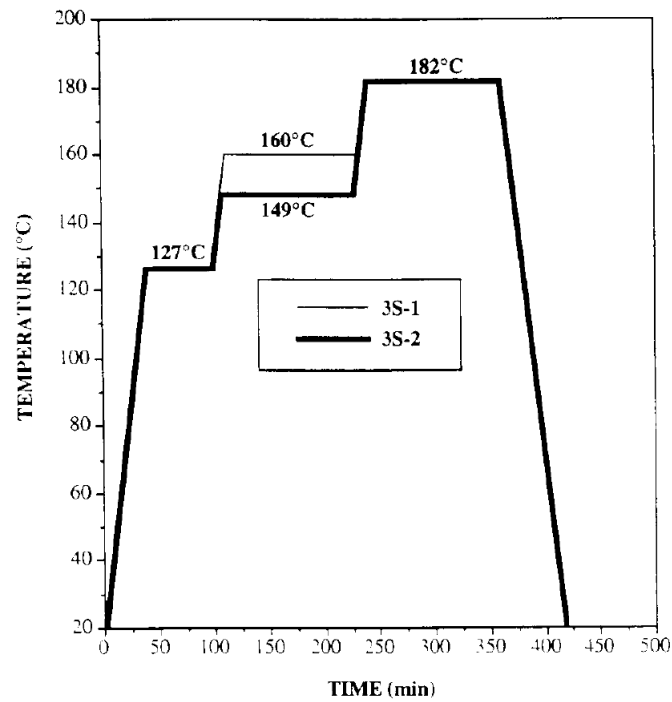


Figure 1.18 – Modification of the cure cycle to reduce residual stresses: three-step curing with an intermediate dwell [45]

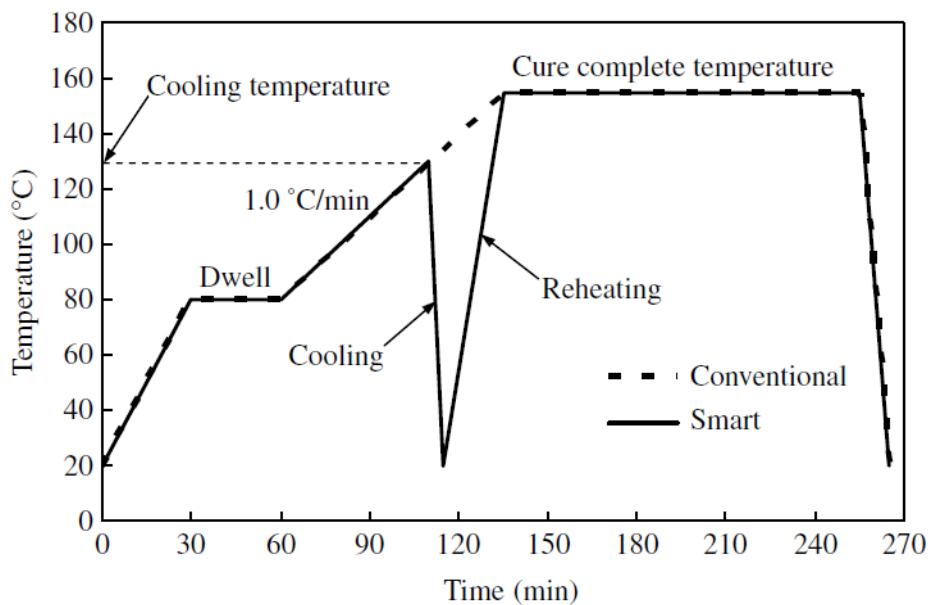


Figure 1.19 – Conventional cure cycle and modified cure cycle proposed by Kim et al. [46] in their work

(span/thickness = 125) and thick (span/thickness = 12.5) asymmetric fiber reinforced composite laminates. The objectives of the optimization was to minimize the curvature, the cure cycle time and the residual stresses, to maximise transverse modulus of the composite and finally to achieve a complete and uniform curing (avoid degree of cure gradients). Different results were found and can be considered in practice according to

the user needs. For example, in comparison the manufacturer's recommended cure cycle, they found, for the thick laminate, a reduction of 47% of the residual stresses and of 1h of the total cure cycle. For thin laminates, the optimization result reduces the curvature by 13% but increases the total time of 2.4h.

#### 1.3.2 - b Relaxation of residual stresses by annealing

Annealing is a common process used to improve the crystallinity (for crystalline or semi-crystalline materials) or to reduce residual stresses in different types of material [10, 50, 51]. Composite laminates can be annealed by raising their temperature above the glass transition temperature and by letting the residual stresses relax. Annealing can be very effective for macro-mechanical residual stresses (section 1.2.3) but it does not significantly relax micro-mechanical and interlaminar (ply-to-ply level) residual stresses [10, 26].

At the macro-mechanical level, the effect of annealing on the residual stresses depend on the type of the matrix. For amorphous matrices, a raise of the temperature above the glass transition temperature induces a visco-elastic relaxation of the residual stresses which can alter the stress-free temperature [52, 53]. For semi-crystalline matrice, If the annealing is performed below the glass transition temperature, the residual stresses will relax without significant change in the crystallinity level [10]. If the annealing is performed above the glass transition temperature, the crystallinity will increase inducing a higher shrinkage (crystallisation shrinkage) and higher residual stresses depending on the crystallinity kinetics of the matrix [10]. Two competing mechanisms occur during the annealing: a relaxation of the residual stresses in the amorphous part of the matrix and an increase of the residual stresses in the crystalline part of the matrix. The final result (relaxed or increased residual stresses) depend on the crystallinity kinetics of the matrix.

#### 1.3.2 - c Relaxation of residual stresses by water absorption

Composite materials (both the matrices and the fibers) have the ability to absorb moisture when manufactured or stored in a humid environment. The absorbed moisture induces expansion strains in the matrix by swelling [54]. These expansion strains counterbalance the process-induced thermal strains. Consequently, the residual stresses are partially relaxed due to the moisture absorption. However, moisture softens the matrix and lowers the glass transition temperature [54]. In addition, moisture can alter the time-dependent behavior of the matrix which induces in return changes in moisture absorption kinetics of the matrix [55] and certain mechanical properties [56]. Harper and Weitsman [54] carried out cycles of moisture absorption and drying on antisymmetric cross-ply graphite/epoxy composites in order to study the effect on the residual stresses. They found a relaxation

of the process-induced curvatures with moisture absorption. They reported that drying of saturated specimens results in tensile stresses which, under certain conditions are higher than the tensile strength. This generates matrix cracking and fiber/matrix debonding which give new paths for moisture absorption. Thus, cycle after cycle, the moisture absorption increases, resulting in higher swelling strains, until a critical level is reached.

Gentz et al. [57] performed shear tests on woven graphite/polyimide composites after hygrothermal cycles. They found that moisture can significantly relax residual stresses at room temperature. No significant effect on the shear strengths was found. During processing at high temperature, the evaporation of the water contained in the fibers can create voids in the matrix. It is, therefore, important to dry fibers before the processing particularly natural fibers that can be very hydrophilic [58].

### 1.3.2 - d Molecular additive insertion in the resin

As explained in section 1.2.2, the chemical residual stresses are caused by the volumetric shrinkage of the cure. Some authors have worked on reducing the chemical shrinkage in order to reduce residual stresses. One can cite Penn et al [59] who combined an epoxy resin with a monomeric additive to reduce shrinkage. They evaluated the effect of the additive by comparing the curvature due to residual stresses in an unsymmetrical composite with and without the additive. They obtained a decrease of the residual stresses as expected but no effect on damage accumulation of the composite was noticed. They explained this lack of effect by an increased fracture sensitivity due to the molecular additive. Another solution to reduce residual stresses is to decrease the cross-linking density. Lange et al [4] showed that the lower the cross-linking, the lower the residual stresses build-up. However, lightly cross-linked resins have low modulus, low glass transition temperature and poor solvent resistance [59].

In addition to the minimization techniques presented in this section, residual stresses can be reduced by adjusting design parameters such as fiber volume fraction, number of off-axis plies and thickness [15].



## 1.4 Methods for measuring and predicting residual stresses

### 1.4.1 Residual stress prediction methods

#### 1.4.1 - a Micro-mechanical level

The most recent micro-mechanical residual stress prediction methods are based on finite element simulations. In their work, Yuan et al. [2], developed a multi-scale model to predict the micro-mechanical residual stresses. They considered a single fiber embedded in a matrix as the representative volume element. They modelled the matrix, the fiber and the inter-phase between them (Fig. 1.20) and considered a viscoelastic behavior (the equations are detailed in the next section) for the matrix and elastic behavior for both the fiber and the inter-phase. The resin shrinkage and mechanical strain history were also taken into account.

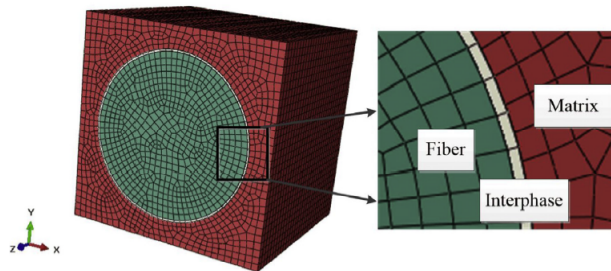


Figure 1.20 – Micro-scale model used to predict micro residual stresses: finite element representation of the fiber, the matrix and the interphase [2]

The two key steps of such an approach are the application of boundary conditions and the spatial distribution of fibers which must be as realistic as possible. The multi-scale aspect of their model allowed Yuan et al. [2] to apply their boundary conditions on the base of the information obtained locally from the macro-scale model. In order to study the influence of the fiber arrangement, they considered 3 different arrangements by assuming a periodic spatial distribution: square, hexagonal and diamond fiber arrangements (Fig. 1.21a). They found that the maximum micro residual stresses were higher in the diamond fiber arrangements (Fig. 1.21b). In practice, the fiber distribution is far from being periodic, thus, the assumption of a regular (periodic) distribution can be a source of error in the micro residual stress predictions. Fletcher and Oakeshott [60] showed in a previous study that a random distribution of the fiber (in finite element simulations) leads to higher residual stresses in the matrix compared to a regular distribution. Vaughan and McCarthy [61] proposed a method to reproduce the real (measured) fiber distribution in the finite element model. This method consists in experimentally measuring the fiber

volume fraction, the fiber diameter and the statistical distributions describing the fiber arrangement. From these experimental data, an algorithm was developed which reproduce the fiber arrangement in the finite element micro-model.

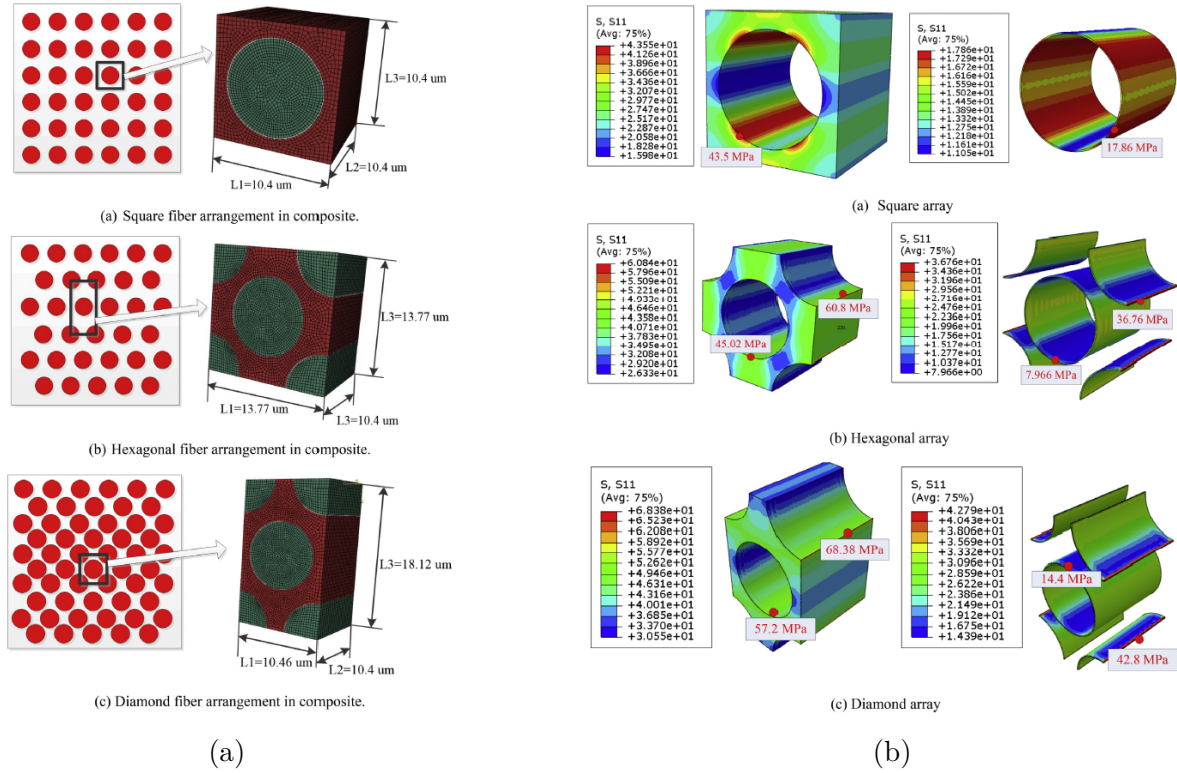


Figure 1.21 – Effect of different fiber arrangements on micro residual stresses: (a) The 3 arrangements studied , (b) Obtained residual stresses for each arrangement [2]

### 1.4.1 - b Macro-mechanical level

In the earlier studies on modelling residual stress build-up, chemically-induced residual stresses have been neglected [62], [63], [64], because of their assumed complexity, and because they were supposed to relax completely at elevated temperature. Thus, the laminates were assumed to be stress-free at the end of the curing. However, the chemically-induced stresses cannot be considered as completely relaxed [4]. The resin's properties, its shrinkage and therefore residual stresses depend on the degree of cure of the reaction. Adams [65] proposed the following phenomenological relation (equation 1.1) to describe the reaction rate for glass/polyester laminates:

$$\frac{d\alpha}{dt} = K(1 - \alpha)^n \alpha^m \quad (1.1)$$

Where  $\frac{d\alpha}{dt}$  is the cure rate,  $\alpha$  is the degree of cure, n and m are two constants to be determined. The constant K is a cure kinetic parameter given by the Arrhenius law:

$$K = A * \exp\left(\frac{-\Delta E}{RT}\right) \quad (1.2)$$

Where A is the frequency factor, R is the universal gas constant,  $\Delta E$  is the activation energy and T is the absolute temperature.

Loos et Springer [66] showed that for graphite/epoxy, the cure rate is described by equations 1.3a and 1.3b.

$$\frac{d\alpha}{dt} = (K_1 + K_2\alpha)(1 - \alpha)(0.47 - \alpha) \quad \text{for } \alpha \leq 0.3 \quad (1.3a)$$

$$\frac{d\alpha}{dt} = K_3(1 - \alpha) \quad \text{for } \alpha > 0.3 \quad (1.3b)$$

Where  $K_1$ ,  $K_2$  and  $K_3$  are constants given by the Arrhenius law (equation 1.2).

The degree of cure at any time, for a given temperature history, is obtained by integrating the cure rate:

$$\alpha = \int_t^0 \frac{d\alpha}{dt} dt \quad (1.4)$$

To determine the cure kinetic parameters K, n and m, the degree of cure and the cure rate must be measured using thermal analysis techniques such as isothermal Differential Scanning Calorimetry (DSC). For a isothermal DSC (Fig. 1.22), the degree of cure and the cure rate are given by equations 1.5 and 1.6 respectively.

$$\alpha = \frac{H}{H_T + H_R} \quad (1.5)$$

$$\frac{d\alpha}{dt} = \frac{dH/dt}{H_T + H_R} \quad (1.6)$$

Where H is the heat of the reaction up to time t,  $H_T$  is the total heat of the reaction and  $H_R$  is the residual heat of the reaction.

The development of the mechanical properties of the resin from the gelation point depends on the degree of cure of the reaction. Bogetti et Gillepsi [8] used the equation 1.7 to determine the instantaneous isotropic resin modulus  $E_m$ .

$$E_m = (1 - \alpha_{mod})E_m^0 + \alpha_{mod}E_m^\infty + \gamma\alpha_{mod}(1 - \alpha_{mod})(E_m^\infty - E_m^0) \quad (1.7)$$

Where

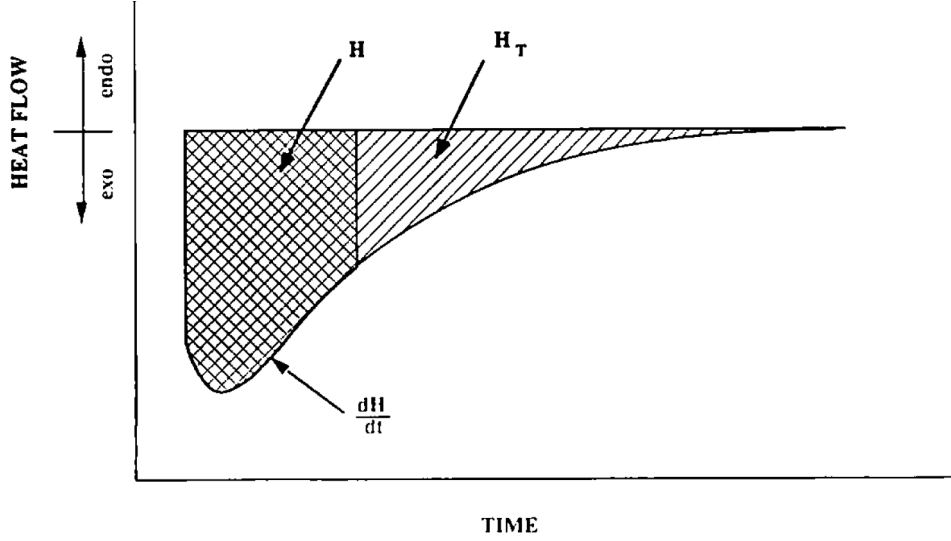


Figure 1.22 – Isothermal Differential Scanning Calorimetry (DSC) [45]

$$\alpha_{mod} = \frac{\alpha - \alpha_{gel}^{mod}}{\alpha_{diff}^{mod} - \alpha_{gel}^{mod}} \text{ and } -1 < \gamma < 1$$

$\alpha_{gel}^{mod}$  is the degree of cure at the onset of the gelation and is assumed to be zero.  $\alpha_{diff}^{mod}$  is the degree of cure at the end of the cure and is assumed to be equal to 1.  $E_m^0$  and  $E_m^\infty$  are the fully uncured and the fully cured resin moduli respectively and they are assumed to be constant. At low degree of cure, the increase in modulus is more exponential for a greater parameter  $\gamma$ . The shear modulus  $G_r$  and poisson's ratio  $\nu_r$  of the matrix can be expressed as follow [2]:

$$G_m = \frac{E_m}{2(1 + \nu_m)} \quad (1.8)$$

$$\nu_m = \frac{E_m^\infty - E_m^0(1 - 2\nu_m^\infty)}{2(1 + E_m^\infty)} \quad (1.9)$$

The build-up of residual stresses during processing can be predicted using the following linear viscoelastic constitutive equation [67]:

$$\sigma_i(t) = \int_{-\infty}^t C_{ij}(\alpha, T, t - \tau) \frac{\partial \epsilon_j^{eff}}{\partial \tau} d\tau \quad (1.10)$$

Where  $C_{ij}$  is the material stiffness tensor,  $\sigma_i$  is the stress tensor,  $\epsilon_j^{eff}$  is the total strain tensor,  $\alpha$  is the degree of cure,  $T$  is the current temperature,  $t$  and  $\tau$  are the current time and the past time respectively. The indices  $i, j$  both varying from 1 to 6 are used in order to write equation 1.10 in its contracted form. The total strain tensor  $\epsilon_j^{eff}$  is composed of mechanical  $\epsilon_j$  and non-mechanical (thermal  $\epsilon_{th}$  and chemical  $\epsilon_{ch}$ ).

$$\epsilon_j^{eff} = \epsilon_j - \epsilon_{th} - \epsilon_{ch} \quad (1.11)$$

The incremental thermal strain is given by:

$$\Delta\epsilon_{th} = CTE_j \Delta T \quad (1.12)$$

Where  $CTE_j$  is the thermal expansion coefficient of the matrix.

The incremental chemical shrinkage is given by [8]:

$$\Delta\epsilon_r = \sqrt[3]{1 + \Delta\nu_r} - 1 \quad (1.13a)$$

$$\Delta\nu_r = \Delta\alpha_{shr} * \nu_{sh}^T \quad (1.13b)$$

Where

$$\alpha_{shr} = \frac{\alpha}{\alpha_{diff}^{shr}}$$

$\nu_{sh}^T$  is the total cure shrinkage of the resin.  $\Delta\epsilon_r$  and  $\Delta\nu_r$  are respectively the incremental shrinkage strain and the specific volume change of the resin for an incremental degree of cure  $\Delta\alpha_{shr}$ .

For more details on the development of equation 1.10, the formulation and the approximation used for the stiffness tensor, the reader is referred to references [67, 2]. Once the equations which govern the various chemical, thermal and mechanical mechanisms (equations 1.1-1.13) are implemented in a numerical model, it is then possible to predict the curing, the evolution of the mechanical properties and the formation of the residual stresses through the processing. Yuan et al. [2] developed a macro-scale models to predict the curing reaction and residual stresses. They compared their predictions to experimental data provided by Kim and White [68] and found very good agreement (Fig. 1.23).

## 1.4.2 Experimental methods for measuring residual stresses

There are many experimental methods for measuring residual stresses. These methods can be classified following several criteria. Here, they are divided into 3 categories: destructive methods, non-destructive methods and methods using embedded strain sensors. The following descriptions of the methods are a presentation of their principles, the reader is referred to the cited references for more detail.

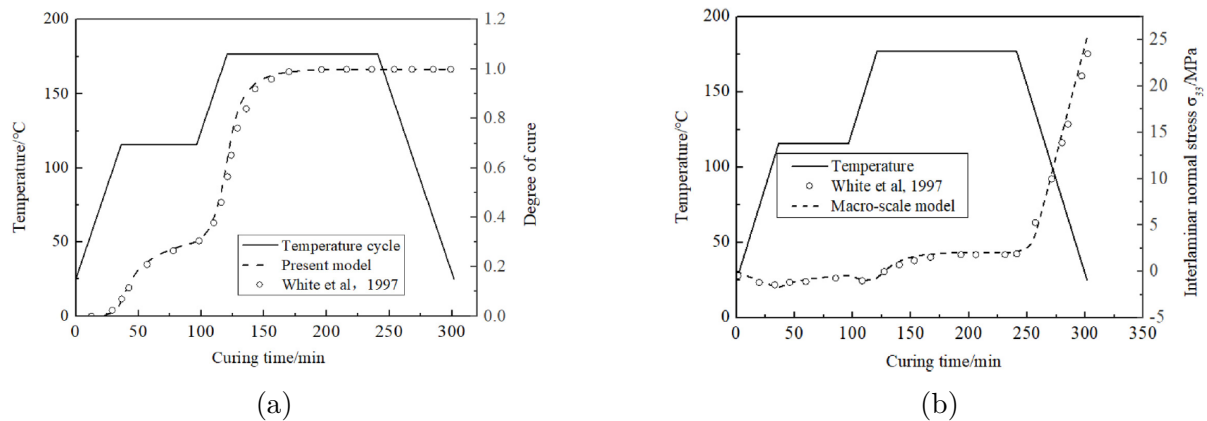


Figure 1.23 – (a) Comparison between numerically predicted [2] and experimentally determined [68] evolution of degree of cure, (b) Comparison between numerically predicted [2] and experimentally determined [68] interlaminar stress

#### 1.4.2 - a Non-destructive methods

- Curvature method:

As reported in section 1.3.1 - d, residual stresses may cause curvature in non-symmetrical laminates or in laminates which experienced an unbalanced cooling. A common technique consisting in measuring the process-induced curvature in order to estimate the residual stress state [69, 70, 71]. Many techniques exist for measuring the specimens curvature. For example, Hyer [36] measured the out-of-plane shape of the laminates by mounting a dial gage in the head of a vertical milling machine. The specimen were fixed on the machine's table which can be moved in the x-y plane allowing the measurement of the shape by the gage. Nowadays, tools such as 3D scanner are used to precisely reconstruct the specimens shape and to accurately measure the curvature. The curvature is directly related to the residual stresses through the classical laminate theory [69].

The stresses in a laminate can be obtained from the following elastic relation [69]:

$$\sigma_i = Q_{ij}(\epsilon_j - e_j^c - e_j^T) \quad (1.14)$$

Where  $\sigma_i$  are the stresses,  $Q_{ij}$  the lamina stiffness and  $\epsilon_j$  are the strains.  $e_j^c$  and  $e_j^T$  are the non-mechanical strains, chemical strains and the thermal strains respectively.

$\epsilon_j$  are given by:

$$\epsilon_j = \epsilon_j^0 + zk_j \quad (1.15)$$

Where  $\epsilon_j^0$  are the mid-plane strains,  $k_j$  are the curvatures and  $z$  is the position from

the mid-plane.

For example, considering a cross-ply laminate, the longitudinal and transverse stresses in each ply are given by the classical laminate theory [69]:

$$\sigma_1^0 = \overline{Q}_{11}(\epsilon_1 - e_1^c - e_1^T) + \overline{Q}_{12}(\epsilon_2 - e_2^c - e_2^T) \quad (1.16)$$

$$\sigma_2^0 = \overline{Q}_{12}(\epsilon_1 - e_1^c - e_1^T) + \overline{Q}_{22}(\epsilon_2 - e_2^c - e_2^T) \quad (1.17)$$

$$\sigma_1^{90} = \overline{Q}_{22}(\epsilon_1 - e_2^c - e_2^T) + \overline{Q}_{12}(\epsilon_2 - e_1^c - e_1^T) \quad (1.18)$$

$$\sigma_2^{90} = \overline{Q}_{12}(\epsilon_1 - e_2^c - e_2^T) + \overline{Q}_{11}(\epsilon_2 - e_1^c - e_1^T) \quad (1.19)$$

Where the superscripts 0 and 90 correspond to the orientation of the ply ( $0^\circ$  or  $90^\circ$ ). The subscripts 1 and 2 correspond to the direction of the fibers and the direction perpendicular to the fibers respectively. White and Hahn [69] used the overbars to represent the material symmetry axis system.

- Interferometry based methods:

These methods are based on the interference phenomenon that occur when light waves are reflected from a sample. This interference creates visual patterns that can be precisely related to the in-plane and out-of-plane displacements of the samples. Several interferometry based techniques exist. One can cite holographic interferometry [72], Shearography [73], speckle correlation interferometry [74], but one of the most known and most used technique is the Moiré interferometry [75, 76]. In the Moiré interferometry technique, 2 gratings are used to obtain the interference pattern when the reflected light passes through them. one of the gratings is applied on the material surface, thus, any displacement results in patterns change and can be accurately recorded. Xing et al. [75] used an electron beam lithography to fabricate a very fine grid (up to 10 000 lines/mm) on the specimen surface. They used a scanning electron microscope to produce the Moiré patterns with a sensitivity lower than a micron. For the measurement of out-of-plane displacements, there is no need to apply the grating on the specimen surface, it can be projected onto the surface at a given angle to the direction of the camera [73, 77].

These approaches based on interferometry are more techniques than methods since they can be combined with the curvature method (to measure the curvature) or the incremental hole drilling (to measure the relaxation strains, Fig. 1.24) for example.

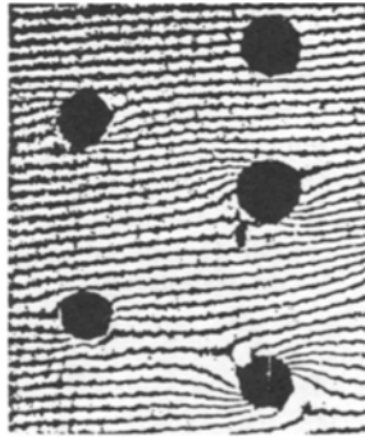


Figure 1.24 – Example of Moiré patterns depicting relaxed displacements due to hole drilling [76]

- Micro-Raman spectroscopy:

Scattering of photons can happen with (Raman scattering, only a small percentage of photons) or without (Rayleigh scattering) energy variation (loss or gain). The variation of energy in the case of Raman scattering corresponds to the vibration energy of the scattering molecule [73]. The micro-Raman Spectroscopy method is based on the strain sensitivity of most Raman vibrational modes of crystalline phases [78]. A Raman spectrum corresponds to a plot of the scattered light intensity versus its energy variation. The positions of certain peaks of the Raman spectrum depend on the strain state of the sample. Thus, this variation of Raman peak variation is related to the magnitude of residual strains. For that purpose a calibration Raman spectrum must be realised with the fibers alone in the air and compared to Raman spectrum in situ [79](Fig. 1.25). One limitation of this method is that for amorphous fibers such as glass fibers, the Raman response is too weak [78].

- Electrical conductivity of carbon fibers:

An intrinsic material property that can be used to estimate residual stress is the electrical conductivity of some fibers such as carbon fiber. The electrical resistance of conductive materials can be modified when they are subjected to strain. This property is well known and is used with strain gages, for example, to measure the deformation of material. Similarly, the principle of the method presented here, consist on measuring difference of the electrical resistance of the carbon fibers before and after the manufacturing in order to measure the process-induced strains and to calculate the residual stresses [73]. However, relating the resistance variation to the residual strains must be achieved under adequate conditions since damage and temperature also affect the electrical resistance [53].

- Photo-elasticity:



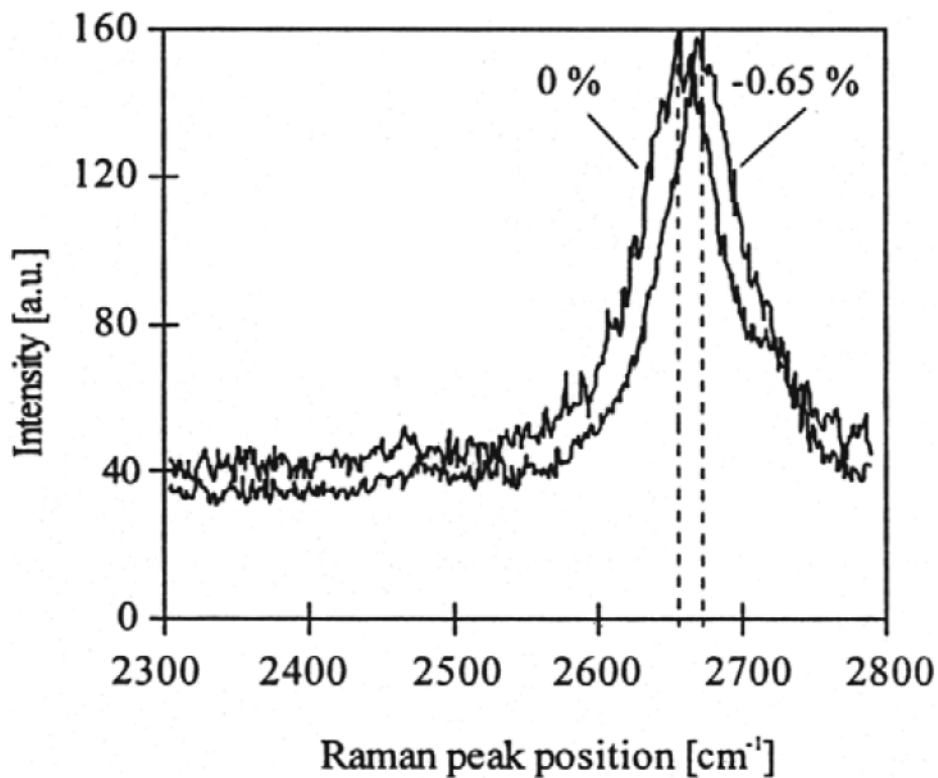


Figure 1.25 – Compressive strain induced shift of  $2660\text{ cm}^{-1}$  Raman peak in AS4 carbon fiber embedded in a PEEK matrix [79]

The optical properties of polymer materials changes under mechanical loads (photo-elasticity). When the polymer experiences a deformation, the molecular orientation distribution is modified, consequently, the photo-elasticity is affected [80]. The measurement of the residual stresses from the photo-elasticity property requires a transparent or translucent matrix [73]. The principle of this method consist on measuring the difference of phase (retardation) between two light waves that propagate in the matrix at different speeds. This difference of phase is used with the stress-optic law (Brewster's law) to calculate the residual stresses [81].

#### 1.4.2 - b Destructive methods

- Layer removal:

The layer removal method is similar to the curvature method. It consists on removing one or more layers from a balanced laminate so as to induce curvatures due to the redistribution of the residual stresses [82]. These curvatures are then measured and the residual stresses are evaluated using the same approach than the curvature method. This method allows to determine the profile of residual stresses through the thickness. The principle is summerized in Fig. 1.26.

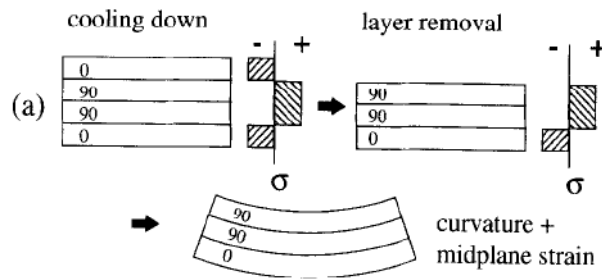


Figure 1.26 – Example of curvature induced by layer removal [82]

The layers are generally removed by milling or abrasion [83, 84]. One of the limitations of this method is the difficulty of measuring the thickness of the layers and controlling the thickness removed. This has a direct impact on the observed curvatures. In addition, the different defects and the heating generated by the milling or the abrasion induces stress relaxations which disturb the accuracy of the measurements. To overcome these limitations, Manson and Seferis [83] used separation films between the layers to facilitate the layer removal. However, one can legitimately wonder if the introduction of films, even thin ones, between the layers does not disturb the residual stress state and the inter-ply interface behavior of the laminate.

- Incremental Hole drilling method:

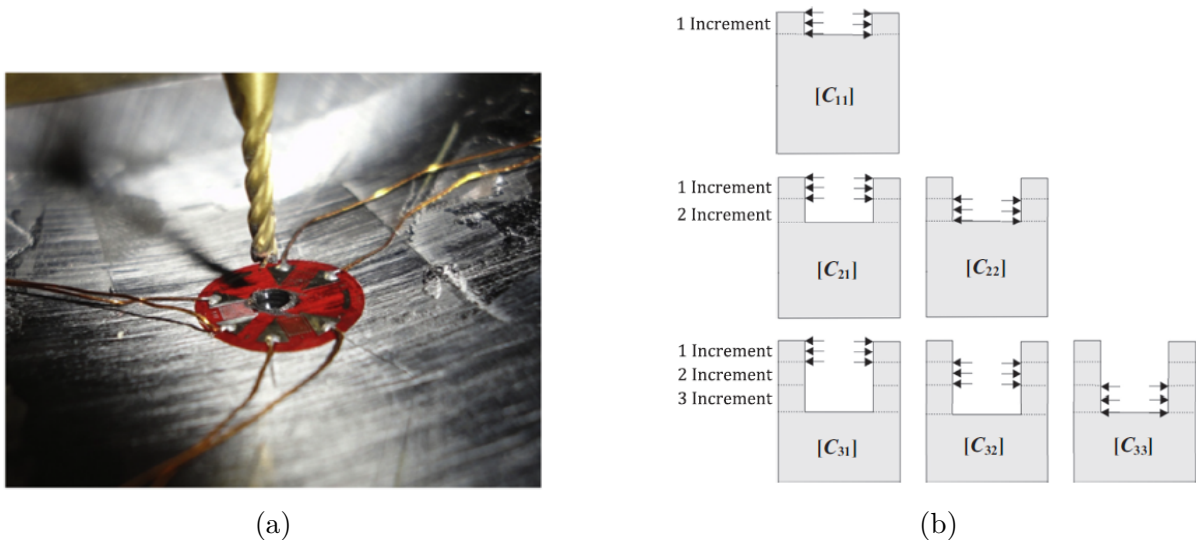


Figure 1.27 – Principle of the incremental hole drilling method: (a) Measurement of the relaxation strains [85], (c) Load cases to apply through the thickness for the calculation of the calibration coefficients [86]

The incremental hole drilling consist on drilling a hole increment by increment through the thickness of the material (Fig. 1.27). Due to the material removal, there is a local redistribution of the residual stresses. The redistribution results in

relaxation strains [87, 88]. The relaxation strains are measured using strain gages or optical measurements [72]. These strains are converted into stresses using a matrix of coefficients called calibration coefficients. The calibration coefficients are calculated by finite element simulations [89, 85, 86]. The incremental approach of the method allows to determine the non-uniform distribution of the residual stresses through the thickness (gradient of residual stresses). Drilling the hole generates heating and can cause defects that can disturb the measurements.

- Compliance method:

The principle of this method is similar to the incremental hole drilling. A thin cut is used instead of a hole. The cut is incrementally realised with increasing depth, the residual stresses are relaxed along the plane of the cut and the resulting strain are measured using strain gages (Fig. 1.28). The strains are related to the stresses by the mean of compliance functions. These compliance functions are calculated using finite element simulations. As with the layer removal and the incremental hole drilling methods, the compliance method generates heating and can induce local defects.

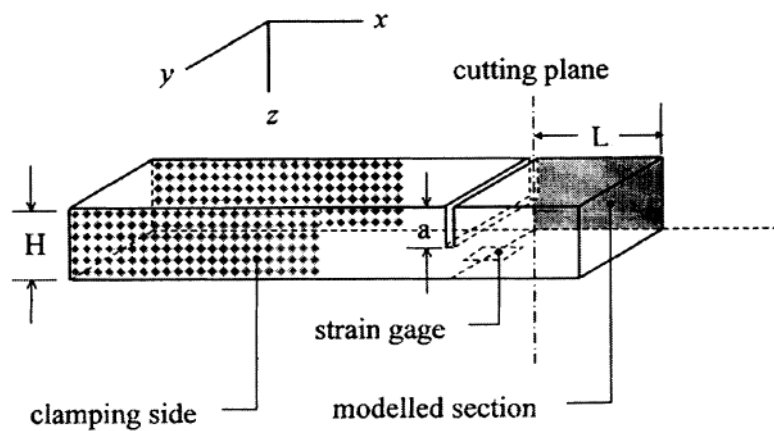


Figure 1.28 – Principle of the compliance method [90]

#### 1.4.2 - c Methods using embedded strain sensors

- Embedded strain gages:

This method consists of placing a gage inside the composite and following its deformation throughout the manufacturing process. This allows to measure the thermal and crystallisation (for semi-crystalline polymers) strains. One limitation of this method has long been the non-optimal resistance of the strain gages to the high processing temperatures [73]. However, nowadays high-temperature resistant strain gages which can sustain temperature up to 200 degrees exist [91]. Kanerva et al [91]

used embedded strain gages to measure the thermal expansion of a hybrid laminate. They found that the accuracy of the results was acceptable when thermal output (false strain indication) is compensated by applying appropriate error compensation functions. It is still questionable whether the presence of the strain gages (and electrical wires) within the material is not disruptive to the residual stress state.

- Embedded fiber optic sensors:

In this method, a fiber optic is embedded in the composite material to measure the process-induced strains. The most often used fiber optics are the extrinsic Fabry-Perot interferometric (EFPI) and the fiber Bragg grating (FBG) [73]. The EFPI sensor is composed of a cavity inside which there is 2 optical fibers separated by the cavity length (for light reflection, see Fig. 1.29b) [73]. The EFPI working principle is based on the multi-reflection of an incident light traveling inside the fiber core. This multi-reflection occurs when light passes through two interfaces: the interface between the fiber and the air, and the interface between the air and the reflection surface [92] (Fig. 1.29a). The light reflected from the first interface interferes with the light reflected from the second. When the EFPI sensor experiences residual strain, there a change of the cavity length, that can be monitored and used to calculate the corresponding strains. However the EFPI sensors have a relative large diameter and their weak mechanical resistance limits their use for measuring residual stresses. FBG sensors are increasingly used because of their accuracy and because they are more robust due to their small diameter [73]. The working principle of FBG is explained in reference [93].

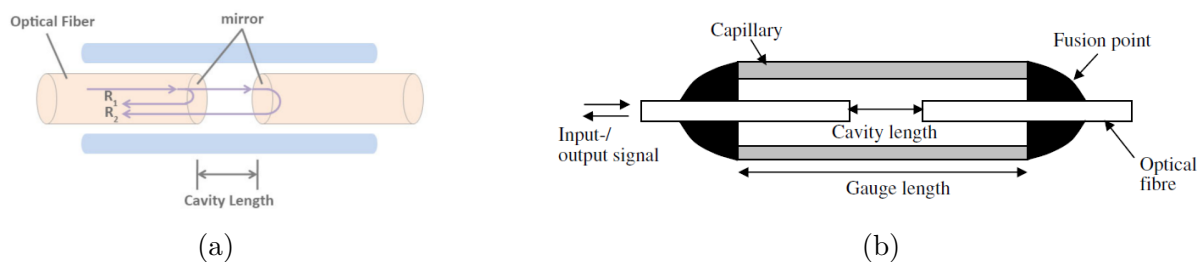


Figure 1.29 – (a) Schematic representation of the EFPI sensor working principle [94], (b) Different components of an EFPI sensor [73]

- X-Ray diffraction (embedded particles):

X-Ray diffraction is a commonly used method to measure residual stresses in metallic materials [95, 96, 97]. X-Ray diffraction requires materials with crystalline structure. For composite laminates, which are amorphous or semi-crystalline, researchers [98, 99, 100] used crystalline filler particles (embedded in the composite) to allow residual stresses measurement by X-Ray diffraction (Fig. 1.30). In their work, Predecki and Barrett [98] used Silver (Ag), Niobium (Nb) and Cadmium

Oxide (CdO) particles for their sharp diffraction peak to measure residual stresses in graphite/epoxy laminates with the X-Ray diffraction method. The crystalline filler particles are placed between prepreg plies. After processing, the X-Ray beam is diffracted and the Bragg relation ( $\lambda = 2d\sin(\theta)$ ,  $\lambda$  is the wavelength,  $\theta$  is the Bragg angle of diffraction and  $d$  is the interplanar spacing) is used to calculate the interplanar spacing. The reference interplanar spacing ( $d_u$ ) is calculated by the same method when the particles are unstressed (in the air). The 3 principal strains (the 2 in the plane and the one perpendicular to the plane) can be calculated from equations 1-3 of reference [98].

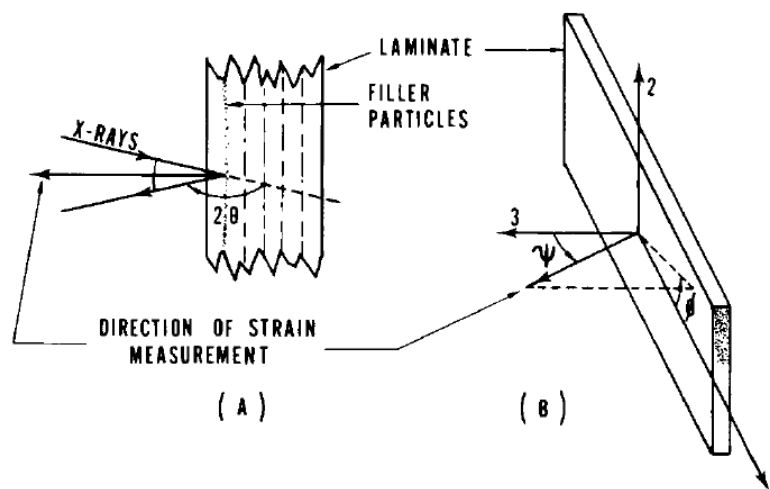


Figure 1.30 – Principle of residual stresses measurement in composite materials using X-Ray Diffraction [98]: (A) Representation of diffraction conditions, (B) Direction of strain measurement with respect to laminate axes

## 1.5 Conclusion

In heterogeneous and anisotropic materials such as fiber reinforced composite laminates, residual stresses are unavoidable. These stresses are mainly due to the complex chemical, mechanical and thermal mechanisms that occur during the manufacturing process. Residual stresses also exist in parts obtained by 3D printed and even in certain biological structures. They can alter the mechanical, chemical and electrical in-used properties of composite laminates and decrease the global quality of the parts. Many techniques exist to minimize or rather to optimize the residual stress state. However, very often, the means used to reduce the residual stresses have a detrimental effect on some mechanical properties of the composite or need supplementary resources. Complex thermo-visco-elastic formulations are more and more implemented in finite element models to predict the mechanisms occurring during processing as well as the induced micro and macro residual stresses. Thanks to the continuous improvement of numerical tools and the growing experience of researchers, the prediction models are more and more accurate. The most recent models use numerical optimization loops to find the best processing parameters. Experimentally, many methods have been developed to assess the residual stress state in composite laminates. The most commonly used methods are presented in this chapter. In the rest of this work, the experimental calculation of the residual stresses will be done using the incremental hole drilling method. This method is used, among other things, because of its good capability to determine the residual stress gradients through the thickness even in symmetrical and balanced specimens. The formulations of the incremental hole drilling method is detailed in the next chapter.



# Chapter 2

## Formulation of the incremental hole drilling method

### Sommaire

---

<b>2.1</b>	<b>Introduction</b>	<b>45</b>
<b>2.2</b>	<b>Historical evolution of the hole drilling method</b>	<b>45</b>
<b>2.3</b>	<b>Theoretical formulation of the hole drilling and the incremental hole drilling methods</b>	<b>46</b>
2.3.1	Case of thin structures: HDM	46
2.3.1 - a	Isotropic materials	46
2.3.1 - b	Orthotropic materials	51
2.3.2	Case of thick structures: IHDM	51
2.3.2 - a	Thick isotropic materials	51
2.3.2 - b	Composite laminates	56
<b>2.4</b>	<b>Calculation of calibration coefficients using finite element simulations</b>	<b>60</b>
2.4.1	Calibration coefficients for thin structures	60
2.4.1 - a	Isotropic materials	60
2.4.1 - b	Orthotropic materials	63
2.4.2	Calibration coefficients for thick structures	66
2.4.2 - a	Thick isotropic materials	66
2.4.2 - b	Composite laminates	68
<b>2.5</b>	<b>Development of a configurable numerical model</b>	<b>71</b>
2.5.1	About Python scripts in Abaqus	71
2.5.2	Configurable numerical model using Python scripts	72



---

2.5.3	Analysis of the influence of the mesh on the calibration coefficients	75
<b>2.6</b>	<b>Conclusion</b>	<b>77</b>

---

## 2.1 Introduction

The hole-drilling method (HDM) is one of the most widely used method for measuring residual stresses because of its reliability, good accuracy and the availability of standard test procedure [101]. The HDM is a semi-destructive method which consists of drilling a hole through the thickness of the material and measuring relaxation strains around the hole. These strains are then converted into residual stresses using coefficients called calibration coefficients. The calibration coefficients are calculated using finite element simulations. The HDM is therefore a combination between an experimental part which consists in measuring the relaxations strains (discussed in chapter 4) and a numerical part which consists in determining the calibration coefficients (discussed in section 2.4 of this chapter). For thick structures, the hole is drilled increment by increment (Incremental Hole-Drilling Method: IHDM) through the thickness of the material to allow the determination of the gradient of residual stresses.

The aim of this chapter, is to explain in detail the theoretical formulations of the HDM and the IHDM and to present the numerical calculations of the calibration coefficients for different types of materials. One of the important tasks of the thesis project was to develop a configurable model based on scripts to automate the calculation of the calibration coefficients and to allow parametric studies. This configurable model is presented in the last section of this chapter.

## 2.2 Historical evolution of the hole drilling method

The HDM was originally proposed by Josef Mathar [102] in 1933 for isotropic materials. Mathar used mechanical extensometer to measure deformations in the vicinity of the hole. This severely limited the accuracy and reliability of the method. In 1950, Soete and Vancrombrugge [103] introduced the use of strain gages in the application of the HDM. This improved the measurement of deformations around the hole. They also proposed an incremental approach that takes into account the non-uniformity of residual stresses in material thickness. In 1966, Rendler and Vigness [87] standardized the IHDM by adopting a precise geometry of the strain gages and defining calibration coefficients to link the relaxation deformations to the residual stresses. They showed that the residual stress calculation was repeatable. Their work later served as the basis for ASTM E837. In 1968, Bert and Thomson [104] used a similar method to calculate the residual stresses in orthotropic materials.

In the IHDM so far used, residual stresses were considered uniform in a given increment regardless of the geometric variation of the hole. In 1978, Bijak-Zochowski [105] proposed a method called "integral method", which allows to take into account the variation of resid-

ual stresses in the same increment when the depth of the hole increases. This method was initially poorly exploited because of the complexity of experimentally determining calibration coefficients for each increment. In 1981, Schajer [89] showed that it was possible to use finite element simulations to reliably calculate calibration coefficients. He proposed the «power series method» which is an approximation of the integral method. With the evolution of finite element simulations, authors such as Niku-Lari et al. [106] and Flaman and Manning [107] have contributed (in 1985) to the improvement of the integral method. In 1994, Schajer and Yang [108] showed, unlike Bert and Thomson [104], that it was not possible to extend the equations of Rendler and Vigness [87] to orthotropic materials. They proposed a new approach that takes into account the orthotropy of the material. The first numerical models used to determine calibration coefficients [89] were axisymmetric models. In 2002, Aoh and Wei [109] used a 3D numerical model to calculate calibration coefficients. Among other things, they showed the influence of the thickness of the model on the values of the calibration coefficients. They concluded that a 3D model was more representative of reality than an axisymmetric model. In 2003, Sicot et al [30] adapted Bert and Thomson's approach to the integral method and extended it to the calculation of residual stresses in laminated composites. In 2007, Shokrieh and Ghasemi [110] used the integral form of Schajer and Yang's approach, to determine residual stresses in laminated composites. More recently, in 2016, Ghasemi and Mohammadi [86] used the same method to determine residual stresses in fiber-metal laminates. The IHDM continues to be the subject of several researches which make it increasingly optimal. Barsanti et al. [111] proposed a solution to counter the effect of hole eccentricity for isotropic materials, Blödorn et al. [112] studied the effect of hole bottom geometry on residual stresses. In 2020, Schajer [113] introduced a compact form of the calibration data to facilitate their use and reduce computation time.

## **2.3 Theoretical formulation of the hole drilling and the incremental hole drilling methods**

### **2.3.1 Case of thin structures: HDM**

#### **2.3.1 - a Isotropic materials**

In early uses of the HDM, residual stresses were assumed to be constant in the materials. Thus, a through-the-thickness hole was drilled. Such an assumption is only acceptable for thin materials, for which the thickness is less than 1.2 times the mean diameter (the mean radius is presented Fig. 2.1) of the rosette used [110].

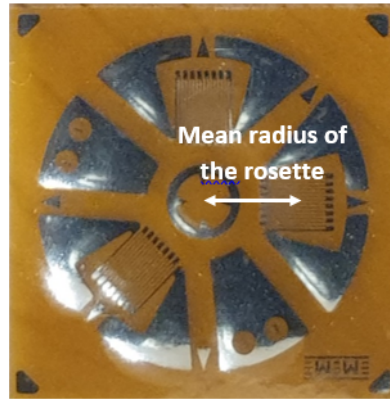


Figure 2.1 – Strain gage rosette used to measure the relaxation strains

When a hole is drilled in materials subject to residual stresses, strains are released in the vicinity of the hole. To model these released strains, Rendler et Vigness [87] suggested the following theoretical approach:

$$\epsilon(\alpha) = K(\alpha)\sigma \quad (2.1)$$

Considering the principal stresses, equation 2.1 becomes:

$$\epsilon(\alpha) = K(\alpha)\sigma_{max} + K(\alpha + 90^\circ)\sigma_{min} \quad (2.2)$$

Where:

$\alpha$  is the angle between a given radial direction and the maximum principal stress direction (Fig. 2.2).  $\epsilon(\alpha)$  is the radial strain for  $\alpha$ .  $\sigma_{max}$  and  $\sigma_{min}$  are the maximum and minimum principal stress respectively.  $K(\alpha)$  is a strain distribution function (Fig. 2.3). It corresponds to the strain measured for a unit load at a given angle  $\alpha$ .

Rendler et Vigness showed that  $K(\alpha)$  is a function that can be written as follows:

$$K(\alpha) = \sum_n A_n \cos(2n\alpha) \quad (2.3)$$

with  $n=0,1,2,3,4\dots$

By approximation only the first two terms are considered.  $K(\alpha)$  is then written:

$$K(\alpha) = A + B \cos(2\alpha) \quad (2.4)$$

Equation 2.2 becomes:

$$\epsilon(\alpha) = [A + B \cos 2(\theta - \beta)]\sigma_{max} + [A - B \cos 2(\theta - \beta)]\sigma_{min} \quad (2.5)$$

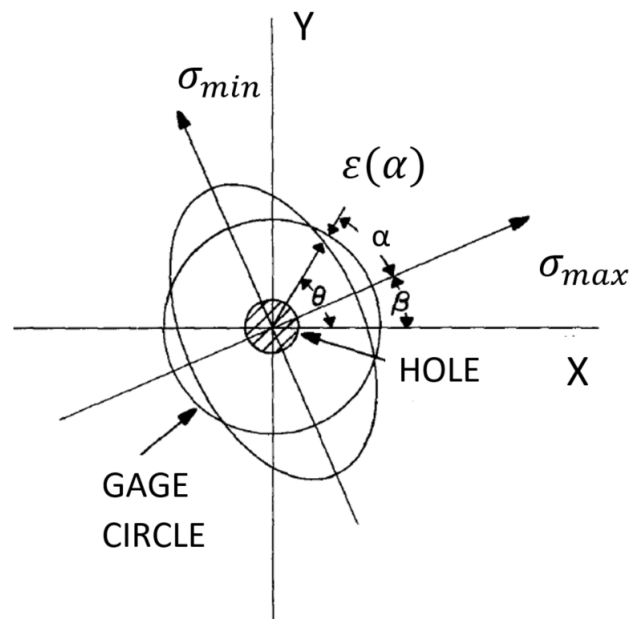


Figure 2.2 – Gage coordinates referenced to stress direction [87]

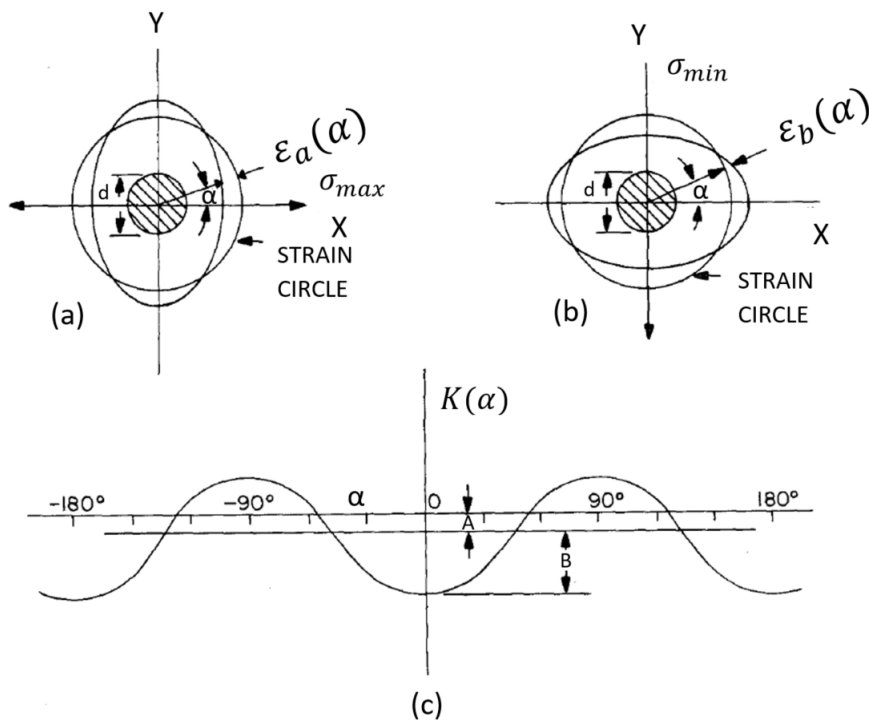


Figure 2.3 – Strain as the radial distance between gage circle and ellipse for uniaxial stress along (a) the x-axis, (b) the y-axis. (c) is the strain proportional to  $K(\alpha)$  in rectangular coordinates [87]

Where:  $\alpha = \theta - \beta$ ,  $\theta$  is the angle between a given radial direction and the x-axis direction,  $\beta$  is the maximum principal stress direction with respect to the x-axis direction.

Equation 2.5 is used to calculate the residual stresses  $\sigma_{max}$ ,  $\sigma_{min}$  and their direction  $\beta$ . To this end, the relaxation strains  $\epsilon(\alpha)$  are experimentally measured using three gages

(Fig. 2.4) and the calibration coefficients A and B are numerically or experimentally calculated.

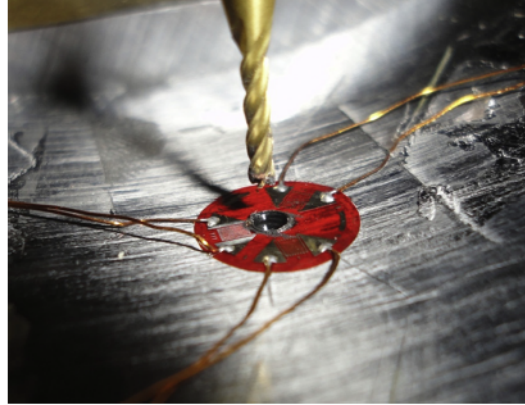


Figure 2.4 – Experimental measurement of the relaxation strains using a strain gage rosette [85]

Equation 2.5 can be obtained analytically using the superposition principle by making the difference between the stress field of a plate and that of a drilled plate (through-hole, see Fig. 2.5).

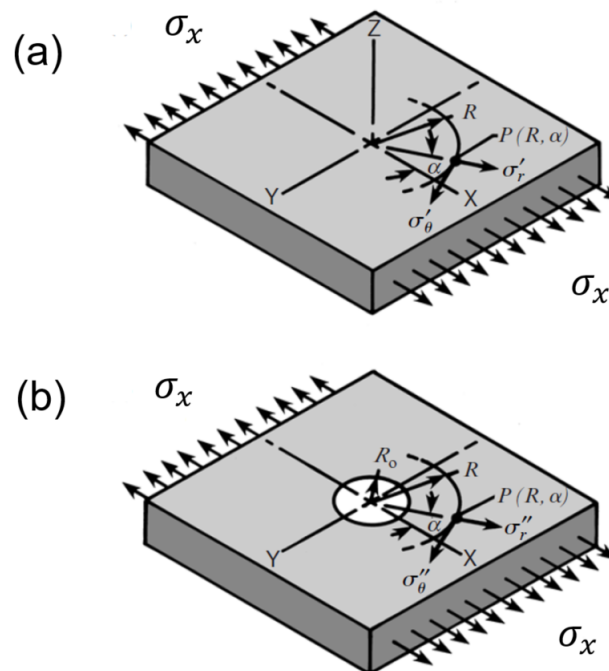


Figure 2.5 – Superposition principle [114]: difference between the stress field of a plate (a) and that of a drilled plate (b)

The radial stress field,  $\sigma_r$ , at any point  $P(R, \alpha)$  of a thin plate, loaded in longitudinal uni-axial tensile stress,  $\sigma_x$ , is given by equation 2.6.  $\beta = 0$  and  $\alpha = \theta$ .

$$\sigma_r = \frac{\sigma_x}{2}(1 + \cos 2\alpha) \quad (2.6)$$

The radial stress field at any point  $P(R, \alpha)$  of a drilled thin plate, loaded in uni-axial tensile stress, is given by equation 2.7:

$$\sigma_r^{drilled} = \frac{\sigma_x}{2}\left(1 - \frac{1}{r^2}\right) + \frac{\sigma_x}{2}\left(1 + \frac{3}{r^4} - \frac{4}{r^2}\right)\cos 2\alpha \quad (2.7)$$

Where:  $r = \frac{R}{R_0}$ ,  $R_0$  is the radius of the hole,  $(R, \alpha)$  are the polar coordinate of P (see Fig. 2.5).

The difference between the 2 stress fields gives the relaxed stress  $\Delta\sigma_r$  (equation 2.8). If the material's mechanical behavior is linear, the Hooke's law is used to obtain the radial relaxation strains (equation 2.9 and 2.10).

$$\Delta\sigma_r = \sigma_r^{drilled} - \sigma_r \quad (2.8)$$

$$\epsilon_r^x = -\frac{\sigma_x(1 + \nu)}{2E}\left[\frac{1}{r^2} - \frac{3}{r^4}\cos 2\alpha + \frac{4}{r^2(1 + \nu)}\cos 2\alpha\right] \quad (2.9)$$

E is the Young's modulus and  $\nu$  is the Poisson's ratio of the material.  $\epsilon_r^x$  is the radial strain corresponding to a longitudinal uni-axial tensile load. Equation 2.9 can be written as follows:

$$\epsilon_r^x = \sigma_x(A + B \cos 2\alpha) \quad (2.10)$$

Where the calibration coefficients A and B are given by equations 2.11 and 2.12.

$$A = -\frac{1 + \nu}{2E}\left(\frac{1}{r^2}\right) \quad (2.11)$$

$$B = -\frac{1 + \nu}{2E}\left[\left(\frac{4}{r^2(1 + \nu)}\right) - \frac{3}{r^4}\right] \quad (2.12)$$

For a transverse uni-axial tensile stress, one obtains:

$$\epsilon_r^y = \sigma_y(A - B \cos 2\alpha) \quad (2.13)$$

The sum of  $\epsilon_r^x$  (equation 2.10) and  $\epsilon_r^y$  (equation 2.13) yields the radial relaxation strain corresponding to a bi-axial tensile load. This allows to find the expression of equation 2.5.

$$\epsilon_r = \epsilon_r^x + \epsilon_r^y = \sigma_x(A + B \cos 2\alpha) + \sigma_y(A - B \cos 2\alpha) \quad (2.14)$$

### 2.3.1 - b Orthotropic materials

Bert and Thompson [104] argued that since calibration coefficients can be expressed as a function of material elasticity constants, then equation 2.5 can be extended to orthotropic materials. They used the following equation:

$$\epsilon(\alpha) = [A + B \cos 2\alpha]\sigma_{11} + [A - B \cos 2\alpha]\sigma_{22} + [C \sin 2\alpha]\sigma_{12} \quad (2.15)$$

Where:  $\sigma_{11}$ ,  $\sigma_{22}$  and  $\sigma_{12}$  are the longitudinal, transverse and shear residual stresses, respectively. A, B and C are the calibration coefficients.

However, Schajer et Yang [108] showed that for orthotropic materials, strain could not be represented by a trigonometric relationship as simple as equation 2.15 which is only valid for isotropic materials. For example, the coefficient A can be calculated numerically, from equation 2.14, by applying an equi-bi-axial tensile load ( $\sigma_x = \sigma_y$ ):  $A = \epsilon(\alpha)/2\sigma_x$ . For an isotropic material, there is only one solution A, because whatever the gage chosen, the radial strain  $\epsilon(\alpha)$  is the same. However, there are more than one solution for an orthotropic material because the radial strain  $\epsilon(\alpha)$  depends on the gage chosen. Therefore, more than one coefficient A is required in equation 2.15 to describe the relationship between the relaxation strains and the residual stresses. Schajer et Yang proposed a more complete relationship (2.16) with 9 coefficients instead of 3 to link residual stresses and released strains for orthotropic materials.

$$\frac{1}{\sqrt{E_x E_y}} \begin{bmatrix} c_{11} & c_{12} & c_{13} \\ c_{21} & c_{22} & c_{23} \\ c_{31} & c_{32} & c_{33} \end{bmatrix} \begin{Bmatrix} \sigma_x \\ \sigma_{xy} \\ \sigma_y \end{Bmatrix} = \begin{Bmatrix} \epsilon_1 \\ \epsilon_2 \\ \epsilon_3 \end{Bmatrix} \quad (2.16)$$

Where:  $c_{ij}$  are the calibration coefficients.  $E_x$  and  $E_y$  are Young's moduli following the main directions of the material.  $\epsilon_1$ ,  $\epsilon_2$  and  $\epsilon_3$  are the relaxation strains.  $\sigma_x$ ,  $\sigma_y$  and  $\sigma_{xy}$  and the residual stresses.

## 2.3.2 Case of thick structures: IHDM

### 2.3.2 - a Thick isotropic materials

For thick structures, the residual stresses distribution through the thickness is not uniform. The integral method (Eq. 2.17) is used to take into account this non-uniformity. In the integral method, the total relaxed strain,  $\epsilon(h, \alpha_g)$ , measured on the surface of the material



### 2.3. THEORETICAL FORMULATION OF THE HOLE DRILLING AND THE INCREMENTAL HOLE DRILLING METHODS

---

by a given gage oriented at  $\alpha_g$ , for a hole depth  $h$ , is the integral of the infinitesimal strains  $d\epsilon(z)$  for a depth  $z$  varying from 0 to  $h$ , where 0 corresponds to the surface of the material and  $h$  to the bottom of the hole. The hole depth  $h$  and the variable  $z$  (current depth) are presented in Fig 2.6.

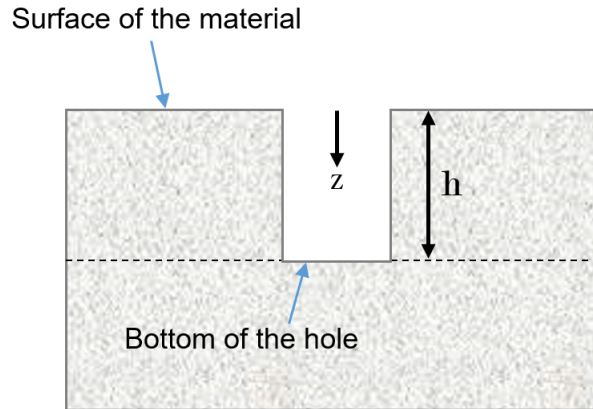


Figure 2.6 – Presentation of the hole depth  $h$  and the integration variable  $z$  that corresponds to the current depth

The relationship between the relaxation strains and the residual stresses is given by equation 2.17.

$$\epsilon(h, \alpha_g) = \int_0^h A(z, h)[\sigma_x(z) + \sigma_y(z)] dz + \int_0^h B(z, h)[\sigma_x(z) - \sigma_y(z)] \cos 2\alpha_g dz \quad (2.17)$$

Where  $0 \leq z \leq h$  and  $1 \leq g \leq 3$

Equation 2.17 is the integral form of equation 2.5.  $\alpha_g$  are the angles of the 3 gages with respect to the maximum principal stress direction.  $A(z, h)$  and  $B(z, h)$  are the calibration coefficients,  $\sigma_x(z)$  and  $\sigma_y(z)$  are the residual stresses for the current depth  $z$ . Experimentally, the IHDM is used to determine the gradient of residual stresses. The IHDM consists in drilling a hole incrementally through the thickness of the material. The residual stresses are assumed to be uniform in a same increment. The strains around the hole are measured for each increment using three gages. Since the measurement is not continuous, equation 2.17 can be written in discrete form. 2 indexes, "i" and "j", are used through this transformation from continuous to discrete. "i" is the number of increments to which the hole depth corresponds. "j" corresponds to 1 increment depth and ranges from 1 to "i" (Fig. 2.7). The cumulative depth of the increments can be written as  $h_j(1 \leq j \leq i)$  as presented in Fig. 2.7. Thus, the hole depth always corresponds to  $h_i$ .

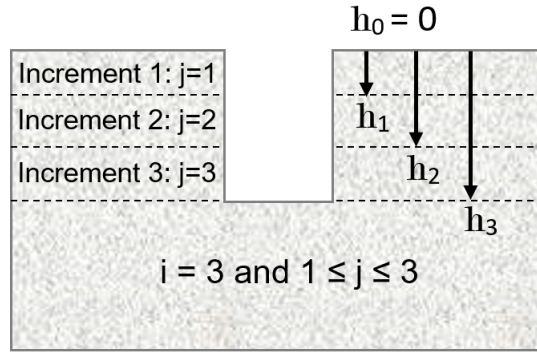


Figure 2.7 – Discrete representation of the cumulative depth of the increments: example of a hole corresponding to 3 increments ( $i=3, 1 \leq j \leq i$ )

The discrete writings of the residual stresses are given by equations 2.18a and 2.18b.

$$\sigma_x(z) = \sum_{j=1}^{j=i} \sigma_{xj} U_j(z) \quad 0 \leq z \leq h \quad (2.18a)$$

$$\sigma_y(z) = \sum_{j=1}^{j=i} \sigma_{yj} U_j(z) \quad 0 \leq z \leq h \quad (2.18b)$$

$$U_j(z) = \begin{cases} 1 & h_{j-1} \leq z \leq h_j \\ 0 & z < h_{j-1}, z > h_j \end{cases} \quad (2.19)$$

For example, for three increments,  $\sigma_x(z)$  becomes:

$$\sigma_x(z) = \sigma_{x1} U_1(z) + \sigma_{x2} U_2(z) + \sigma_{x3} U_3(z) \quad (2.20)$$

From the definition of equation 2.19, one can write:

$$\sigma_x(z) = \begin{cases} \sigma_{x1} & 0 \leq z \leq h_1 \\ \sigma_{x2} & h_1 \leq z \leq h_2 \\ \sigma_{x3} & h_2 \leq z \leq h_3 \end{cases} \quad (2.21)$$

Equation 2.21 is illustrated in Fig. 2.8. It is important to note that the residual stresses are not cumulative. For example,  $\sigma_{x2}$  is not the sum of the residual stresses of the first and second increment but only the residual stress of the second increment. It is also important to note that the residual stress is assumed to be constant in the same increment.

### 2.3. THEORETICAL FORMULATION OF THE HOLE DRILLING AND THE INCREMENTAL HOLE DRILLING METHODS

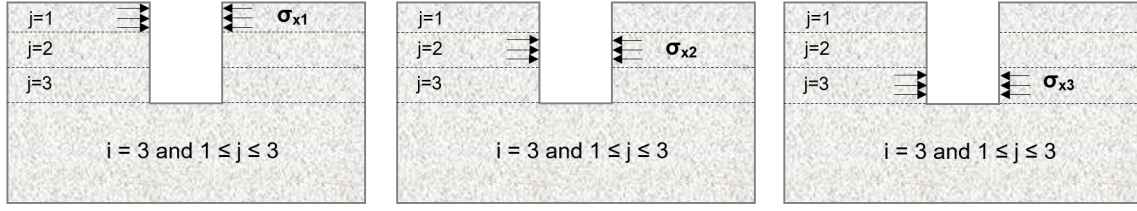


Figure 2.8 – Representation of the discrete residual stresses for a hole corresponding to 3 increments ( $i=3, 1 \leq j \leq i$ )

By replacing equations 2.18a and 2.18b in equation 2.17 , one obtains:

$$\epsilon(h_i, \alpha_g) = \int_0^{h_i} A(z, h_i) \left[ \sum_{j=1}^{j=i} (\sigma_{xj} + \sigma_{yj}) U_j(z) \right] dz + \int_0^{h_i} B(z, h_i) \left[ \sum_{j=1}^{j=i} (\sigma_{xj} - \sigma_{yj}) U_j(z) \right] \cos 2\alpha_g dz \quad (2.22)$$

$$\epsilon(h_i, \alpha_g) = \sum_{j=1}^{j=i} (\sigma_{xj} + \sigma_{yj}) \int_0^{h_j} A(z, h_i) U_j(z) dz + \sum_{j=1}^{j=i} (\sigma_{xj} - \sigma_{yj}) \cos 2\alpha_g \int_0^{h_j} B(z, h_i) U_j(z) dz \quad (2.23)$$

From the definition of equation 2.19, one can change the limits of integration and rewrite equation 2.23 as follow:

$$\epsilon(h_i, \alpha_g) = \sum_{j=1}^{j=i} (\sigma_{xj} + \sigma_{yj}) \int_{h_{j-1}}^{h_j} A(z, h_i) dz + \sum_{j=1}^{j=i} (\sigma_{xj} - \sigma_{yj}) \cos 2\alpha_g \int_{h_{j-1}}^{h_j} B(z, h_i) dz \quad (2.24)$$

Finally, this equation can be written in index form:

$$\epsilon(h_i, \alpha_g) = \sum_{j=1}^{j=i} (\sigma_{xj} + \sigma_{yj}) A_{ij} + \sum_{j=1}^{j=i} (\sigma_{xj} - \sigma_{yj}) B_{ij} \cos 2\alpha_g \quad (2.25)$$

Where:  $A_{ij} = \int_{h_{j-1}}^{h_j} A(z, h_i) dz$  and  $B_{ij} = \int_{h_{j-1}}^{h_j} B(z, h_i) dz, 1 \leq j \leq i$

$\epsilon(h_i, \alpha_g)$  is the strain given by gage "g" when the depth of the hole corresponds to "i" increments.  $\sigma_{xj}$  and  $\sigma_{yj}$  are the residual stresses in the  $j^{th}$  increment.  $A_{ij}$  and  $B_{ij}$  are the calibration coefficients of the  $j^{th}$  increment when the total number of drilled increments is "i". The correspondence between the continuous and discrete writing of the calibration coefficients is shown in Fig. 2.9.

If the gages of the rosette are aligned so that  $\alpha_1 = 0^\circ, \alpha_2 = -135^\circ$  and  $\alpha_3 = 90^\circ$  (Fig. 2.11), equation 2.25 can be written in matrix form (Fig. 2.10).

To facilitate the use of the calibration coefficients, they can be written in lower triangular matrices form as presented in Fig. 2.12. In the literature,  $a_{ij}$  and  $b_{ij}$ , given by equations 2.26 and 2.27 are, generally, used [115].

$$a_{ij} = \frac{2E}{1 + \nu} A_{ij} \quad (2.26)$$

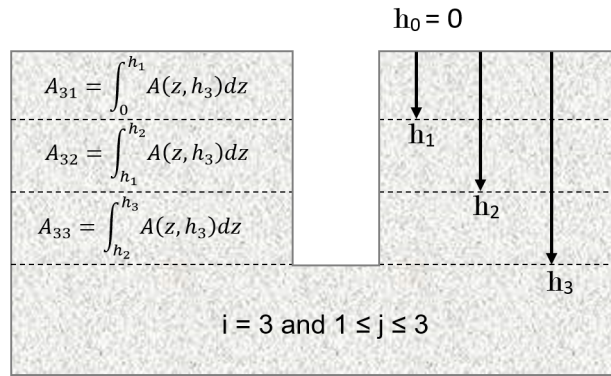


Figure 2.9 – correspondence between the continuous and discrete writing of the calibration coefficients: example of a hole corresponding to 3 increments ( $i=3, 1 \leq j \leq i$ )

$$\begin{Bmatrix} \varepsilon(h_1, \alpha_1) \\ \varepsilon(h_1, \alpha_2) \\ \varepsilon(h_1, \alpha_3) \end{Bmatrix} = \begin{bmatrix} A_{11} + B_{11} & A_{11} - B_{11} \\ A_{11} & A_{11} \\ A_{11} - B_{11} & A_{11} + B_{11} \end{bmatrix} \begin{Bmatrix} \sigma_{x1} \\ \sigma_{y1} \end{Bmatrix} \quad \text{increment 1}$$

$$\begin{Bmatrix} \varepsilon(h_2, \alpha_1) \\ \varepsilon(h_2, \alpha_2) \\ \varepsilon(h_2, \alpha_3) \end{Bmatrix} = \begin{bmatrix} A_{21} + B_{21} & A_{21} - B_{21} \\ A_{21} & A_{21} \\ A_{21} - B_{21} & A_{21} + B_{21} \end{bmatrix} \begin{Bmatrix} \sigma_{x1} \\ \sigma_{y1} \end{Bmatrix} + \begin{bmatrix} A_{22} + B_{22} & A_{22} - B_{22} \\ A_{22} & A_{22} \\ A_{22} - B_{22} & A_{22} + B_{22} \end{bmatrix} \begin{Bmatrix} \sigma_{x2} \\ \sigma_{y2} \end{Bmatrix} \quad \text{increment 2}$$

$$\begin{Bmatrix} \varepsilon(h_3, \alpha_1) \\ \varepsilon(h_3, \alpha_2) \\ \varepsilon(h_3, \alpha_3) \end{Bmatrix} = \begin{bmatrix} A_{31} + B_{31} & A_{31} - B_{31} \\ A_{31} & A_{31} \\ A_{31} - B_{31} & A_{31} + B_{31} \end{bmatrix} \begin{Bmatrix} \sigma_{x1} \\ \sigma_{y1} \end{Bmatrix} + \begin{bmatrix} A_{32} + B_{32} & A_{32} - B_{32} \\ A_{32} & A_{32} \\ A_{32} - B_{32} & A_{32} + B_{32} \end{bmatrix} \begin{Bmatrix} \sigma_{x2} \\ \sigma_{y2} \end{Bmatrix} + \begin{bmatrix} A_{33} + B_{33} & A_{33} - B_{33} \\ A_{33} & A_{33} \\ A_{33} - B_{33} & A_{33} + B_{33} \end{bmatrix} \begin{Bmatrix} \sigma_{x3} \\ \sigma_{y3} \end{Bmatrix} \quad \text{increment 3}$$

Figure 2.10 – Matrix form of equation 2.25: expansion for 3 increments, for the rosette orientation presented in Fig. 2.11

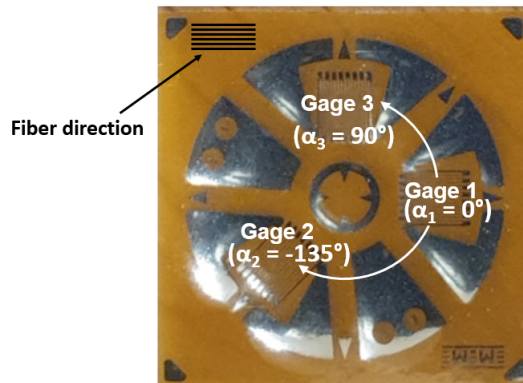


Figure 2.11 – Orientation of gage 1 in the fiber direction:  $\alpha_1 = 0^\circ$ ,  $\alpha_2 = -135^\circ$  and  $\alpha_3 = 90^\circ$

$$b_{ij} = 2E * B_{ij} \quad (2.27)$$

It can be seen in Fig. 2.12, that, for increment 2, 2 coefficients  $A_{ij}$  ( $A_{21}$  and  $A_{22}$ ) and 2 coefficients  $B_{ij}$  ( $B_{21}$  and  $B_{22}$ ) are needed. For increment 3, 3 coefficients  $A_{ij}$  and 3 coefficients  $B_{ij}$  are needed. In general, for  $i$  increments drilled,  $i$  coefficients  $A_{ij}$  and  $i$

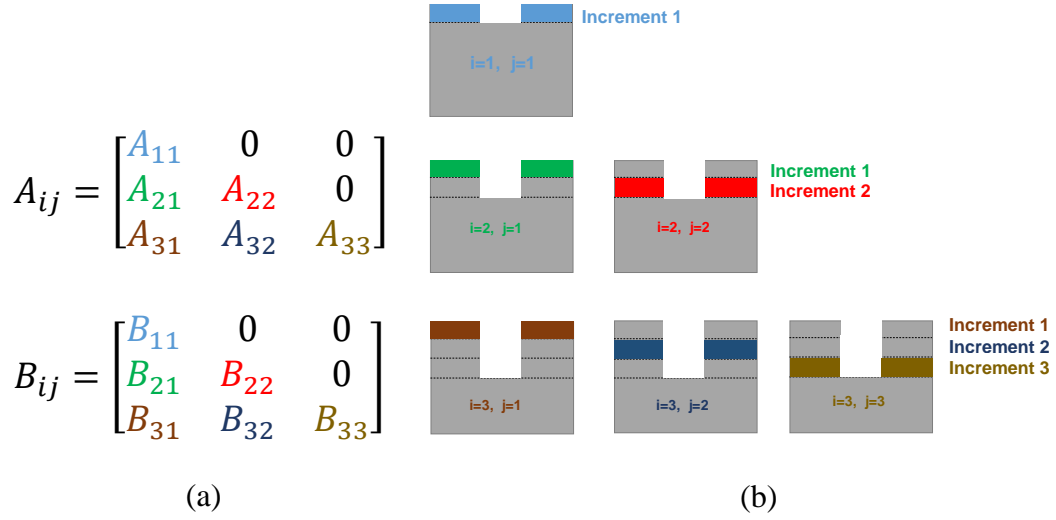


Figure 2.12 – (a) Writing of coefficients  $A_{ij}$  and  $B_{ij}$  in the form of a lower triangular matrix for 3 increments, (b) Increment corresponding to each calibration coefficient

coefficients  $B_{ij}$  are needed. This is due to the fact that it is experimentally not possible to separate the contribution of each increment in the total measured strains by the gages at the surface. To achieve the decoupling (i.e. the determination of the contribution of increment  $i$  in the total strains measured), the different calibration coefficients of the increments  $j$  (when the total hole depth corresponds to  $i$  increments) are required. For example, in Fig. 2.12, the coefficient  $B_{31}$  is needed to estimate the contribution of increment ( $i=3, j=1$ ) in the total strains measured at the surface. This decoupling process is necessary to allow the determination of the residual stress gradient by the IHDM whatever the type of material. This is detailed at the end of section 2.3.2 - b.

### 2.3.2 - b Composite laminates

Laminated composites are composed of several layers that are individually considered as orthotropic materials. Thus, the case of thick orthotropic materials can be assimilated to a particular case of composite laminates (unidirectional composite laminates). To determine the gradient of the residual stresses through the thickness of composites, the integral method [85], based on the approach of Schajer and Yang, is used. However, the reasoning remains similar to the integral method presented in the previous section (for isotropic materials [116]): the relaxation deformation measured on the surface is the sum of all infinitesimal deformations going from the surface to the bottom of the hole.

$$\epsilon(h_i, \alpha_g) = \int_0^{h_i} \sum_{s=1}^3 C_{gs}(z, h_i) \sigma_s(z) dz \quad 1 \leq g \leq 3 \quad 1 \leq s \leq 3 \quad (2.28)$$

Where:  $\epsilon(h_i, \alpha_g)$  is the strain measured by gage "g" for a hole depth  $h_i$ .  $z$  expresses

the variation of the depth.  $\sigma_s$  are the residual stresses ( $s, 1 \leq s \leq 3$ , corresponds to the stress component,  $\sigma_1 = \sigma_x$ ,  $\sigma_2 = \sigma_{xy}$  and  $\sigma_3 = \sigma_y$ ).  $C_{gs}$  is a strain distribution function and corresponds to the calibration coefficients as presented below.

In practice, residual stresses are determined incrementally. Thus, equations are used in their discrete forms.

$$\sigma_s(z) = \sum_{j=1}^i \sigma_s^j U_j(z) \quad 0 \leq z \leq h_i \quad (2.29)$$

Where

$$U_j(z) = \begin{cases} 1 & h_{j-1} \leq z \leq h_j \\ 0 & z < h_{j-1} \text{ or } z > h_j \end{cases} \quad (2.30)$$

By replacing equation 2.29 in equation 2.28, one obtains:

$$\epsilon(h_i, \alpha_g) = \int_0^{h_i} \sum_{s=1}^3 C_{gs}(z, h_i) \sum_{j=1}^i \sigma_s^j U_j(z) dz \quad (2.31)$$

$$\epsilon(h_i, \alpha_g) = \sum_{s=1}^3 \sum_{j=1}^i \sigma_s^j \int_0^{h_j} C_{gs}(z, h_i) U_j(z) dz \quad (2.32)$$

$$\epsilon(h_i, \alpha_g) = \sum_{s=1}^3 \sum_{j=1}^i \sigma_s^j C_{ijgs} \quad (2.33)$$

To simplify the writing,  $\epsilon_g^i$  is used for the relaxation strains with  $\epsilon_g^i = \epsilon(h_i, \alpha_g)$ . For example,  $\epsilon_3^2 = \epsilon(h_2, \alpha_3)$ . Thus, equation 2.33 becomes:

$$\epsilon_g^i = \sum_{s=1}^3 \sum_{j=1}^i \sigma_s^j C_{ijgs} \quad (2.34)$$

Where:  $C_{ijgs} = \int_0^{h_j} C_{gs}(z, h_i) U_j(z) dz = \int_{h_{j-1}}^{h_j} C_{gs}(z, h_i) dz$

$C_{ijgs}$  is the matrix of calibration coefficients related to the increment "j" when the total number of drilled increments is "i". Physically, it corresponds to the strain measured by gage "g" when unit loads are applied to increment "j" for a total depth corresponding to "i" increments.

Equation 2.34 can be written in matrix form:

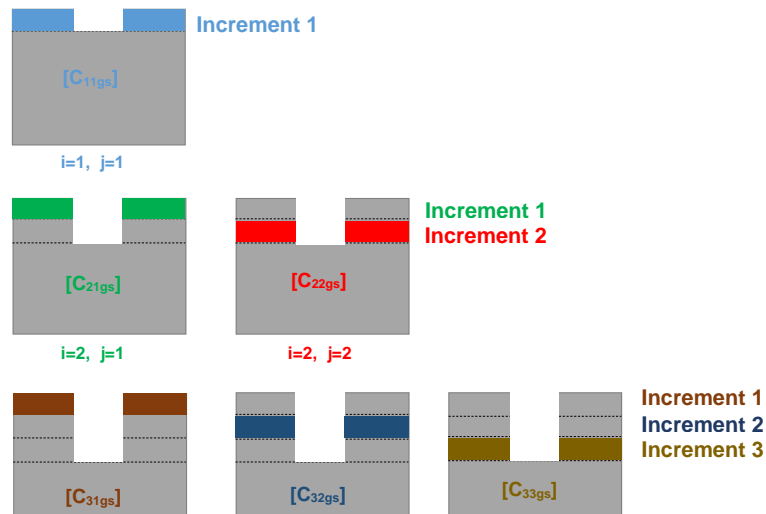
### 2.3. THEORETICAL FORMULATION OF THE HOLE DRILLING AND THE INCREMENTAL HOLE DRILLING METHODS

$$\frac{1}{\sqrt{E_x E_y}} \begin{bmatrix} c_{ij11} & c_{ij12} & c_{ij13} \\ c_{ij21} & c_{ij22} & c_{ij23} \\ c_{ij31} & c_{ij32} & c_{ij33} \end{bmatrix} \begin{Bmatrix} \sigma_x^j \\ \sigma_{xy}^j \\ \sigma_y^j \end{Bmatrix} = \begin{Bmatrix} \epsilon_1^i \\ \epsilon_2^i \\ \epsilon_3^i \end{Bmatrix} \quad (2.35)$$

Equation 2.35 is the incremental form of equation 2.16 proposed by Schajer and Yang [108] for thin orthotropic materials. The expansion of equation 2.35 for three increments is presented in Fig. 2.13.

$$\begin{Bmatrix} \epsilon_1^1 \\ \epsilon_2^1 \\ \epsilon_3^1 \\ \epsilon_1^2 \\ \epsilon_2^2 \\ \epsilon_3^2 \\ \epsilon_1^3 \\ \epsilon_2^3 \\ \epsilon_3^3 \end{Bmatrix} = \begin{bmatrix} [C_{1111} & C_{1112} & C_{1113}] & \begin{bmatrix} 0 & 0 & 0 \\ 0 & 0 & 0 \\ 0 & 0 & 0 \end{bmatrix} & \begin{bmatrix} 0 & 0 & 0 \\ 0 & 0 & 0 \\ 0 & 0 & 0 \end{bmatrix} \\ [C_{2111} & C_{2112} & C_{2113}] & \begin{bmatrix} C_{2211} & C_{2212} & C_{2213} \\ C_{2221} & C_{2222} & C_{2223} \\ C_{2231} & C_{2232} & C_{2233} \end{bmatrix} & \begin{bmatrix} 0 & 0 & 0 \\ 0 & 0 & 0 \\ 0 & 0 & 0 \end{bmatrix} \\ [C_{3111} & C_{3112} & C_{3113}] & \begin{bmatrix} C_{3211} & C_{3212} & C_{3213} \\ C_{3221} & C_{3222} & C_{3223} \\ C_{3231} & C_{3232} & C_{3233} \end{bmatrix} & \begin{bmatrix} C_{3311} & C_{3312} & C_{3313} \\ C_{3321} & C_{3322} & C_{3323} \\ C_{3331} & C_{3332} & C_{3333} \end{bmatrix} \end{bmatrix} \begin{Bmatrix} \sigma_x^1 \\ \sigma_{xy}^1 \\ \sigma_y^1 \\ \sigma_x^2 \\ \sigma_{xy}^2 \\ \sigma_y^2 \\ \sigma_x^3 \\ \sigma_{xy}^3 \\ \sigma_y^3 \end{Bmatrix}$$

(a)



(b)

Figure 2.13 – (a) Expansion of the relation between residual stresses and relaxation strains for three increments, (b) correspondence between increments and calibration coefficients

It is important to note that, in the IHDM, the residual stresses of all increments "j" ( $1 \leq j \leq i$ ) contribute to the total strain measured. This is schematically represented in Fig. 2.14 and mathematically expressed by equations 2.36, 2.37 and 2.38.

$$\{\sigma_s^1\} = [C_{11gs}]^{-1} \{\epsilon_g^1\} \quad \text{first layer} \quad (2.36)$$

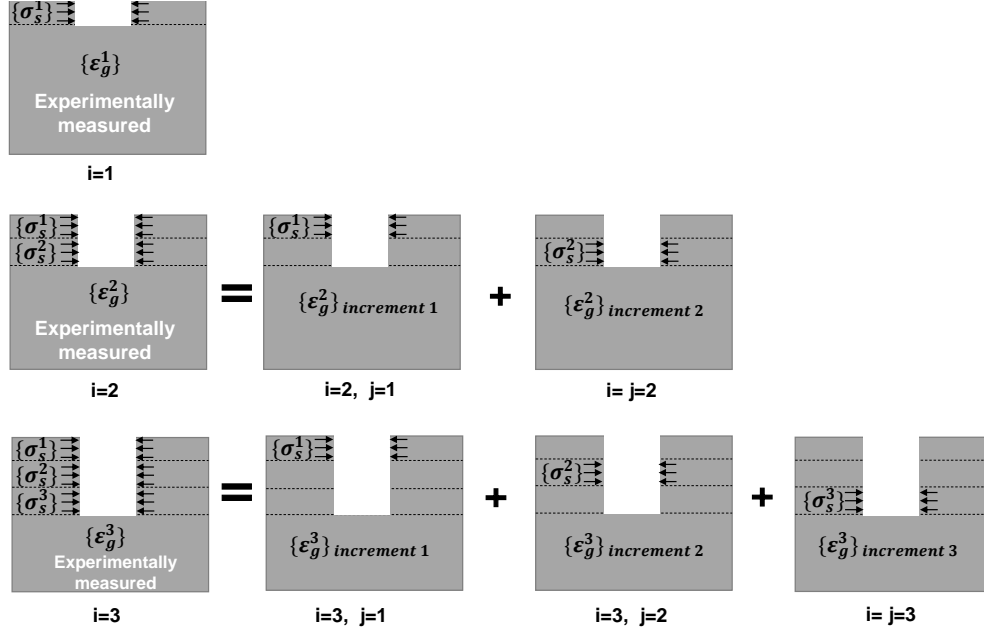


Figure 2.14 – Contribution of the residual stresses of each layer to the total strains measured on the surface of the material:  $\{\sigma_s^j\}$  are the residual stresses,  $\{\epsilon_g^i\}$  are the total relaxation strains and  $\{\epsilon_g^i\}_{increment j}$  is the contribution of increment  $j$  to the total relaxation strains

$$\begin{aligned}
 \{\sigma_s^2\} &= [C_{22gs}]^{-1} \{\epsilon_g^2\}^{increment 2} \\
 &= [C_{22gs}]^{-1} (\{\epsilon_g^2\} - \{\epsilon_g^2\}^{increment 1}) \\
 &= [C_{22gs}]^{-1} (\{\epsilon_g^2\} - [C_{21gs}] \{\sigma_s^1\}) \quad \text{second layer}
 \end{aligned} \tag{2.37}$$

$$\begin{aligned}
 \{\sigma_s^3\} &= [C_{33gs}]^{-1} \{\epsilon_g^3\}^{increment 3} \\
 &= [C_{33gs}]^{-1} (\{\epsilon_g^3\} - \{\epsilon_g^3\}^{increment 1} - \{\epsilon_g^3\}^{increment 2}) \\
 &= [C_{33gs}]^{-1} (\{\epsilon_g^3\} - [C_{31gs}] \{\sigma_s^1\} - [C_{32gs}] \{\sigma_s^2\}) \quad \text{third layer}
 \end{aligned} \tag{2.38}$$

In equation 2.37, the terms  $[C_{21gs}] \{\sigma_s^1\}$  is the contribution of the residual stresses of the first increments to the total strain measured at the surface  $\epsilon_g^2$ . Physically, it means that when the second increment is drilled, even if there are no residual stress at that increment, additional strains will be recorded due to the change in hole geometry. In equation 2.38, the terms  $[C_{31gs}] \{\sigma_s^1\}$  and  $[C_{32gs}] \{\sigma_s^2\}$  are respectively the contribution of the residual stresses of the first and second increments to the total strain measured at the surface  $\epsilon_g^3$ .



## 2.4. CALCULATION OF CALIBRATION COEFFICIENTS USING FINITE ELEMENT SIMULATIONS

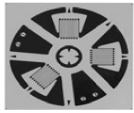
gage pattern and designation	Resistance in Ohms	Dimensions (mm)					
		gage Length	Mean radius	Hole diameter		Matrix	
				Min.	Max.	Length	Width
EA-06-062RE-120 	$120 \pm 0.2 \%$	1.57	2.56	1.5	2.0	10.7	10.7

Table 2.1 – Features of the used gages

## 2.4 Calculation of calibration coefficients using finite element simulations

The equations used to calculate residual stresses are detailed in section 2.3. The required calibration coefficients are calculated using finite element simulations of the IHDM. The principle is to numerically apply a known stress field as residual stresses, to extract the corresponding radial strains in the areas of the gage (numerical relaxation strains) and to directly calculate the calibration coefficients. These coefficients depend on the radius of the hole and the geometry of the gages used. If any of these parameters change, the model must be readjusted and the calibration coefficients must be recalculated. The commercial finite element software ABAQUS 2018 is used throughout this work. For each case study presented below, the modelling step, the meshing, the boundary conditions and the load cases are explained. The model is then validated by comparing the obtained results to recognized references and/or international standards.

### 2.4.1 Calibration coefficients for thin structures

#### 2.4.1 - a Isotropic materials

- Modelling and meshing:

Thin structures (thickness less than 1.2 times the diameter of the rosette [110]) are modelled as 2D planar deformable shell. Isotropic behavior is assigned to the model. The gages are modelled as 3 rectangular partitions on the upper surface (Fig 2.15). EA-06-062RE-120 strain gages, designed by Micro-Measurements, are used. The mean radius of the strain-gage rosette is  $r_m = 2.57$  mm and its nominal length is 1.59 mm (Table 2.1 and Fig. 2.16). 8-node biquadratic plane stress quadrilateral, reduced-integration elements (CPS8R) are used to mesh the model.

- Boundary conditions and load cases:

The boundaries of the model are fixed in the x and y directions. The appropriate

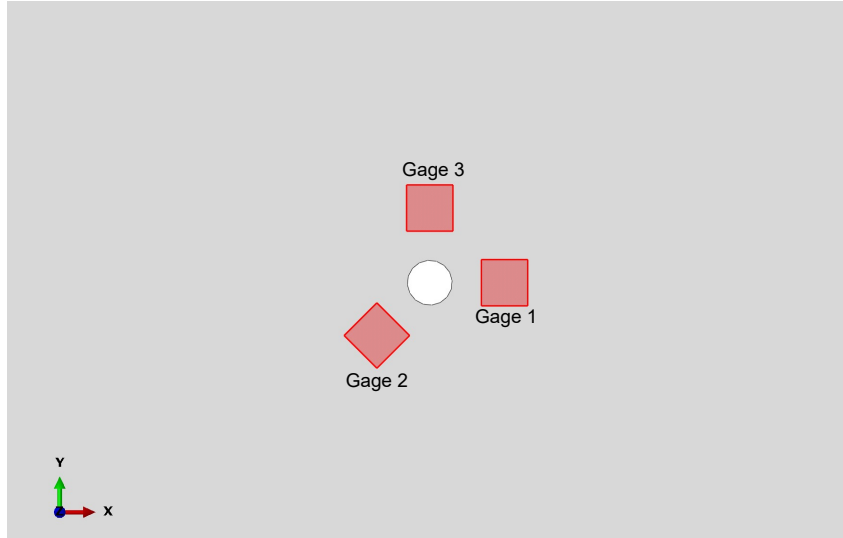


Figure 2.15 – Modelling of the strain gages as rectangular partitions

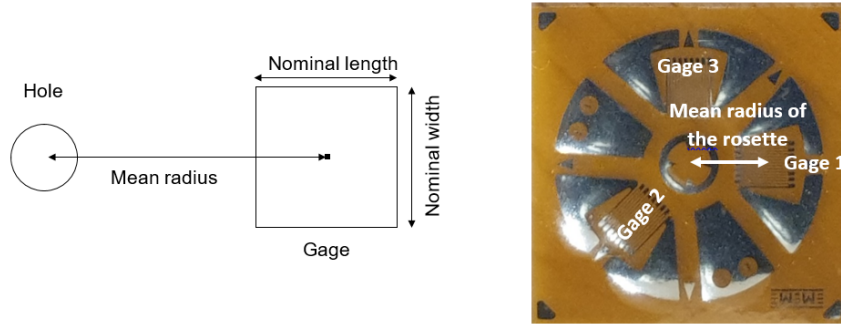


Figure 2.16 – Features of the used gages

load cases are applied to the model. Equation 2.5 ( $\epsilon(\alpha) = [A + B \cos 2(\theta - \beta)]\sigma_{max} + [A - B \cos 2(\theta - \beta)]\sigma_{min}$ ) can be rewritten as follows:

$$\epsilon(\alpha) = (\sigma_x + \sigma_y)A + (\sigma_x - \sigma_y)B \cos 2(\alpha) \quad (2.39)$$

The coefficient A is calculated from equation 2.39 by applying the following load case on the hole (equi-biaxial tensile load):

$$\sigma_x = \sigma_y = \sigma_0 \Rightarrow A = \frac{\epsilon(\alpha)}{2\sigma_0} \quad (2.40)$$

Here,  $\sigma_0$  is the magnitude of the load and it can be chosen randomly as long as it is below the yield strength of the material.

The coefficient B is calculated from equation 2.39 by applying the following load case:

$$\sigma_x = -\sigma_y = \sigma_0 \Rightarrow B = \frac{\epsilon(\alpha)}{2\sigma_0 \cos 2(\alpha)} \quad (2.41)$$

The loads are applied on the wall of the hole. A change from Cartesian coordinate system to cylindrical is therefore necessary.

$$\begin{cases} \sigma_{rr} = \sigma_x(\cos \alpha)^2 + \sigma_y(\sin \alpha)^2 \\ \sigma_{\alpha r} = \sigma_x \cos(\alpha) \sin(\alpha) - \sigma_y \cos(\alpha) \sin(\alpha) \end{cases} \quad (2.42)$$

**Load 1:**  $\sigma_x = \sigma_y = \sigma_0$

$$\begin{cases} \sigma_{rr} = \sigma_0 \\ \sigma_{\alpha r} = 0 \end{cases} \quad (2.43)$$

**Load 2:**  $\sigma_x = -\sigma_y = \sigma_0$

$$\begin{cases} \sigma_{rr} = \sigma_0 \cos(2\alpha) \\ \sigma_{\alpha r} = \sigma_0 \sin(2\alpha) \end{cases} \quad (2.44)$$

The calibration coefficients A and B are easily calculated by performing a finite element simulation and by extracting the relaxation strains ( $\epsilon(\alpha)$ ) in the measurement areas. These measurement areas correspond to the red grids on Fig 2.17 (gage 1, gage 2 and gage 3). The strain of a given gage is the average of the strains extracted on the Gauss points of the elements composing the gage. Equations 2.40 and 2.41 can , then, be used to calculate the coefficients A and B.

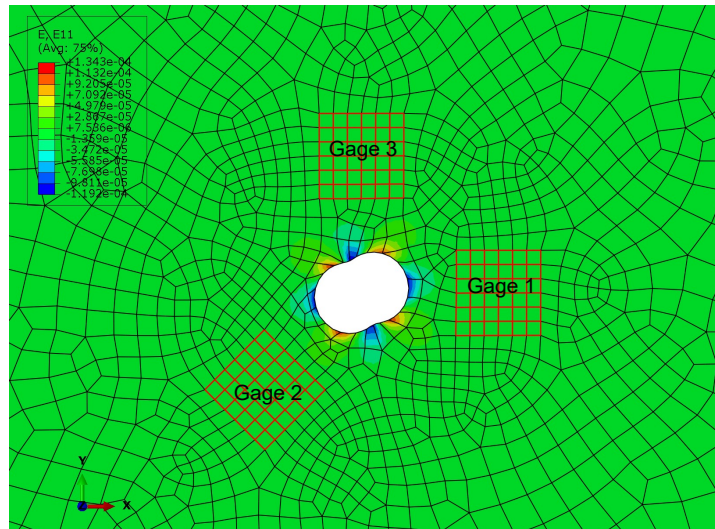


Figure 2.17 – Strain field (E11) obtained for the calculation of coefficient B (load case  $\sigma_x = -\sigma_y = \sigma_0 = 20MPa$ )

- Validation of the model:

Coefficients A and B have been calculated for different hole diameters and compared to those obtained by Shokrieh et Ghasemi [110] and those given by the ASTM standard [101] (Table 2.2).

Hole radius/ $r_m$	ASTM [101]		Shokrieh et Ghasemi [110]		This work	
	A	B	A	B	A	B
0.3	-2.89E-07	-6.93E-07	-2.89E-07	-6.95E-07	-2.89E-07	-6.96E-07
0.4	-5.13E-07	-1.13E-06	-5.13E-07	-1.14E-06	-5.14E-07	-1.13E-06

Table 2.2 – Comparison of the calibration coefficients obtained in this work with those obtained in the literature for a thin isotropic material: E=200 GPa and  $\nu=0.3$

### 2.4.1 - b Orthotropic materials

- Modelling and meshing:

2D planar deformable shell is used. Orthotropic behavior is assigned to the material. As in the case of thin isotropic material, EA-06-062RE-120 strain gages are modelled as strain measuring areas. 8-node biquadratic plane stress quadrilateral, reduced-integration elements (CPS8R) are used to mesh the model.

- Boundary conditions and load cases:

The hole is assumed infinitely far from the edges of the material. To take this into account, the 4 edges of the model are fixed in x and y direction.

The calibration coefficients are calculated from Eq. 2.16 (the expression of the equation is recalled below) using 3 different load cases.

$$\frac{1}{\sqrt{E_x E_y}} \begin{bmatrix} c_{11} & c_{12} & c_{13} \\ c_{21} & c_{22} & c_{23} \\ c_{31} & c_{32} & c_{33} \end{bmatrix} \begin{Bmatrix} \sigma_x \\ \sigma_{xy} \\ \sigma_y \end{Bmatrix} = \begin{Bmatrix} \epsilon_1 \\ \epsilon_2 \\ \epsilon_3 \end{Bmatrix}$$

If gage 1 is oriented in on-axis direction of the material then  $c_{12}$  and  $c_{32}$  are always equal to zero [108].

Load 1: longitudinal uni-axial tensile stress to determine  $c_{11}$ ,  $c_{21}$  and  $c_{31}$  (Fig. 2.18a):

$$\frac{1}{\sqrt{E_x E_y}} \begin{bmatrix} c_{11} & c_{12} & c_{13} \\ c_{21} & c_{22} & c_{23} \\ c_{31} & c_{32} & c_{33} \end{bmatrix} \begin{Bmatrix} \sigma_x \\ 0 \\ 0 \end{Bmatrix} = \begin{Bmatrix} \epsilon_1 \\ \epsilon_2 \\ \epsilon_3 \end{Bmatrix} \quad (2.45)$$

$$c_{11} = \sqrt{E_x E_y} \frac{\epsilon_1}{\sigma_x} \quad c_{21} = \sqrt{E_x E_y} \frac{\epsilon_2}{\sigma_x} \quad \text{and} \quad c_{31} = \sqrt{E_x E_y} \frac{\epsilon_3}{\sigma_x}$$

Load 2: shear stress to determine  $c_{12}$ ,  $c_{22}$  and  $c_{32}$  (Fig. 2.18b):

$$\frac{1}{\sqrt{E_x E_y}} \begin{bmatrix} c_{11} & c_{12} & c_{13} \\ c_{21} & c_{22} & c_{23} \\ c_{31} & c_{32} & c_{33} \end{bmatrix} \begin{Bmatrix} 0 \\ \sigma_{xy} \\ 0 \end{Bmatrix} = \begin{Bmatrix} \epsilon_1 \\ \epsilon_2 \\ \epsilon_3 \end{Bmatrix} \quad (2.46)$$

Load 3: transverse uni-axial tensile stress to determine  $c_{13}$ ,  $c_{23}$  and  $c_{33}$  (Fig. 2.18c):

$$\frac{1}{\sqrt{E_x E_y}} \begin{bmatrix} c_{11} & c_{12} & c_{13} \\ c_{21} & c_{22} & c_{23} \\ c_{31} & c_{32} & c_{33} \end{bmatrix} \begin{Bmatrix} 0 \\ 0 \\ \sigma_y \end{Bmatrix} = \begin{Bmatrix} \epsilon_1 \\ \epsilon_2 \\ \epsilon_3 \end{Bmatrix} \quad (2.47)$$

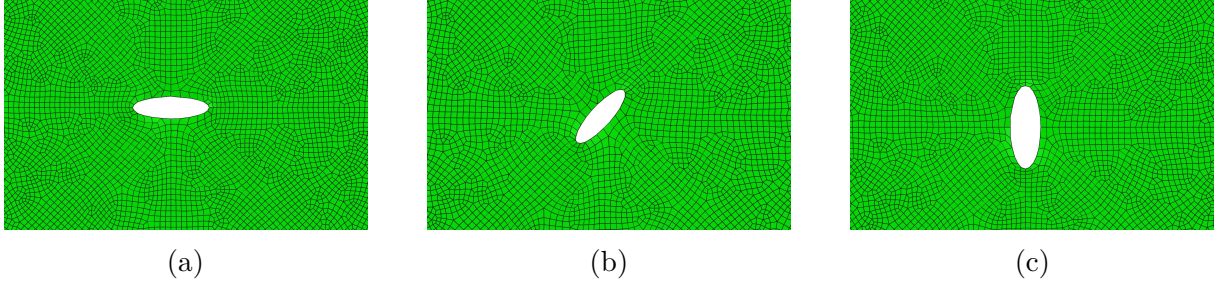


Figure 2.18 – Associated deformations of the material: (a) associated deformation for  $\sigma_x$ , (b) associated deformation for  $\sigma_{xy}$  and (c) associated deformation for  $\sigma_y$

The three loads are applied to the wall of the hole. A change from Cartesian coordinate system to cylindrical is necessary.

$$\begin{cases} \sigma_{rr} = \sigma_x (\cos \alpha)^2 + \sigma_y (\sin \alpha)^2 + \sigma_{xy} \sin(2\alpha) \\ \sigma_{\alpha r} = \frac{\sigma_y - \sigma_x}{2} \sin(2\alpha) + \sigma_{xy} \cos(2\alpha) \end{cases} \quad (2.48)$$

**Load 1:**  $\sigma_x = \sigma_0; \sigma_y = \sigma_{xy} = 0$

$$\begin{cases} \sigma_{rr} = \sigma_0 (\cos \alpha)^2 \\ \sigma_{\alpha r} = -\sigma_0 \sin(\alpha) \cos(\alpha) \end{cases} \quad (2.49)$$

Where  $\sigma_0$  is the magnitude of the load.

**Load 2:**  $\sigma_{xy} = \sigma_0; \sigma_x = \sigma_y = 0$

$$\begin{cases} \sigma_{rr} = \sigma_0 \sin(2\alpha) \\ \sigma_{\alpha r} = \sigma_0 \cos(2\alpha) \end{cases} \quad (2.50)$$

**Load 3:**  $\sigma_y = \sigma_0; \sigma_x = \sigma_{xy} = 0$

$$\begin{cases} \sigma_{rr} = \sigma(\sin \alpha)^2 \\ \sigma_{\alpha r} = \sigma \sin(\alpha) \cos(\alpha) \end{cases} \quad (2.51)$$

The simulation is carried out and the relaxation strains (see example of the radial strain in x-direction for the load case 1 on Fig. 2.19) are extracted on the Gauss points of the elements of the gages.

- Validation of the model:

The simulation is done for a material with the following elastic moduli:  $E_x = 200GPa$ ,  $E_y = 50GPa$ ,  $G_{xy} = 40GPa$  and  $\nu = 0.25$ . gage 1 is oriented at 0 degrees, gage 2 at -135 degrees and gage 3 at 90 degrees with respect to the on-axis direction of the material.

The calibration coefficients are calculated and compared with those obtained by Schajer et Yang [108] and Shokrieh et Ghasemi [110] (Table 2.3).

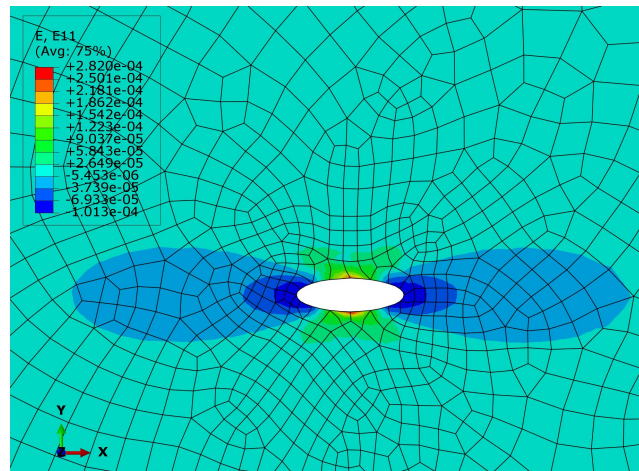


Figure 2.19 – Strain field (E11) for a longitudinal uni-axial tensile stress  $\sigma_x = 20MPa$

Authors	Calibration coefficients						
	$c_{11}$	$c_{21}$	$c_{31}$	$c_{22}$	$c_{13}$	$c_{23}$	$c_{33}$
Schajer et Yang [108]	-0.291	-0.073	0.228	0.728	0.183	-0.196	-0.659
Shokrieh et Ghasemi [110]	-0.277	-0.084	0.198	0.659	0.150	-0.193	-0.635
This work	-0.271	-0.085	0.186	0.644	0.144	-0.191	-0.621

Table 2.3 – Comparison of the calibration coefficients obtained in this work with those obtained in the literature for a thin orthotropic material

## 2.4.2 Calibration coefficients for thick structures

### 2.4.2 - a Thick isotropic materials

- Modelling and meshing:

3D deformable solid is used to model thick Materials. Axisymmetric models can also be used [89]. Isotropic behavior is assigned to the model. EA-06-062RE-120 strain gages are modelled as strain extraction areas. The hole is drilled increment by increment. For each increment, the appropriate load cases are applied, the simulations are performed and the corresponding calibration coefficients are calculated. For the mesh, 8-node linear brick isoparametric elements (C3D8R) are used.

- Boundary conditions and load cases:

The external boundaries of the model are fixed in the x and y directions. To facilitate understanding of load cases, equation 2.25 ( $\epsilon(h_i, \alpha_g) = \sum_{j=1}^{j=i} (\sigma_{xj} + \sigma_{yj}) A_{ij} + \sum_{j=1}^{j=i} (\sigma_{xj} - \sigma_{yj}) B_{ij} \cos 2\alpha_g$ ) can be rewritten as follow:

$$\epsilon_i(\alpha_g) = (\sigma_{xj} + \sigma_{yj}) A_{ij} + (\sigma_{xj} - \sigma_{yj}) B_{ij} \cos 2\alpha_g \quad (2.52)$$

With  $1 \leq j \leq i$

Coefficients  $A_{ij}$  and  $B_{ij}$  can be calculated using the following load cases.

**Load case 1:**  $\sigma_{xj} = \sigma_{yj} = \sigma_0$

$$A_{ij} = \frac{\epsilon_i(\alpha_g)}{2\sigma_0} \quad (2.53)$$

Where  $\sigma_0$  is the magnitude of the load applied to the increments.

**Load case 2:**  $\sigma_{xj} = -\sigma_{yj} = \sigma_0$

$$B_{ij} = \frac{\epsilon_i(\alpha_g)}{2\sigma_0 \cos 2(\alpha_g)} \quad (2.54)$$

As previously shown, a change from Cartesian coordinate system to cylindrical must be performed.

For an increment "i", "i" coefficients A and "i" coefficients B are required. These coefficients can be gathered in 2 lower triangular matrices. An example for 3 increments is given in Fig. 4.20a and 4.20b. To calculate the coefficient  $A_{31}$ , for example, the load case 1 must be applied to the increment j=1 when the total number of increments drilled is i=3 (Fig. 4.20)

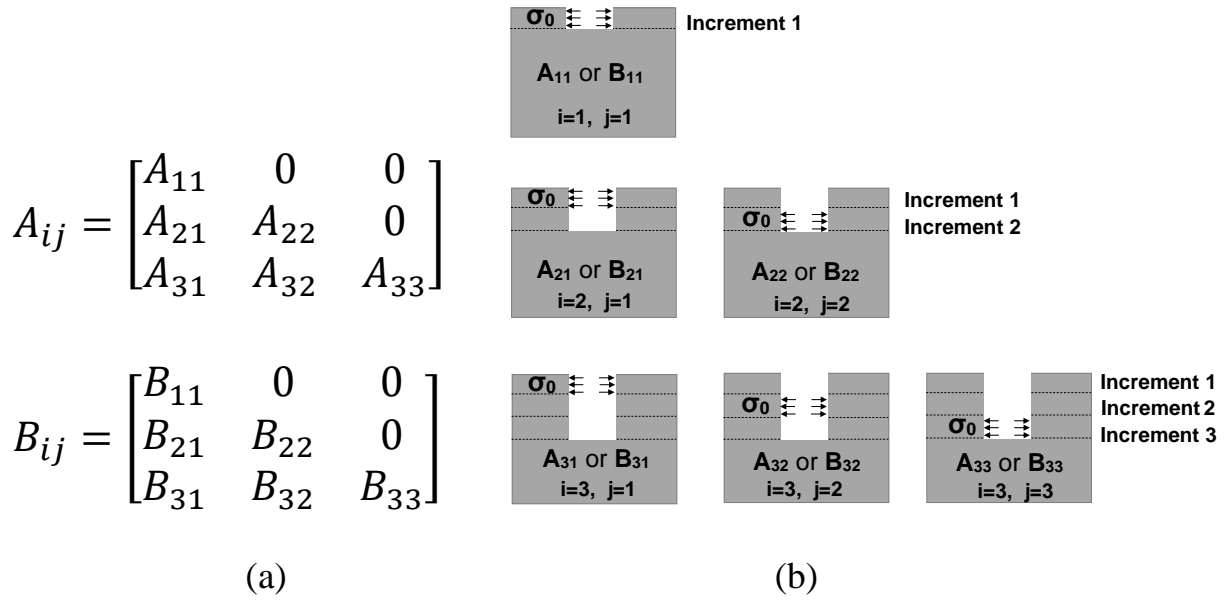


Figure 2.20 – (a) Lower triangular matrix writing of coefficients  $A_{ij}$  and  $B_{ij}$ , (b) Principle of calculation of the calibration coefficients  $A_{ij}$  or  $B_{ij}$  depending on whether load case 1 or load case 2 is considered

In the literature, coefficients  $a_{ij}$  ( $a_{ij} = \frac{2E}{1+\nu}A_{ij}$ ) and  $b_{ij}$  ( $b_{ij} = 2E*B_{ij}$ ) are generally used in their cumulative form. The cumulative form of a given coefficient is the sum of all the coefficients of the same row (same "i"), for example:  $a_{22}^{cumulative} = a_{21} + a_{22}$ . The cumulative form of a coefficient  $a_{ij}$  or  $b_{ij}$  corresponds to the total relaxation strain of the increment "ij".

- Validation of the model:

Coefficients  $a_{ij}$  and  $b_{ij}$  have been calculated in their cumulative forms for 3 increments and compared to those obtained by Aoh et Wei [109]. A material with a Young's modulus of 72 GPa and Poisson's ratio of 0.33 is modelled. The dimensionless hole radius is 0.3 ( $\frac{radius}{r_m} = 0.3$ ) and the depth of the increments is 0.128 mm.

The results obtained in this work are given bellow:

$$a_{ij} = \begin{bmatrix} -0.0121 & 0 & 0 \\ -0.0163 & -0.0290 & 0 \\ -0.0185 & -0.0343 & -0.0456 \end{bmatrix} \quad b_{ij} = \begin{bmatrix} -0.0255 & 0 & 0 \\ -0.0234 & -0.0518 & 0 \\ -0.0373 & -0.0720 & -0.0994 \end{bmatrix} \quad (2.55)$$

The results obtained by Aoh et Wei are the following.



$$a_{ij} = \begin{bmatrix} -0.0123 & 0 & 0 \\ -0.0153 & -0.0287 & 0 \\ -0.0180 & -0.0346 & -0.0481 \end{bmatrix} \quad b_{ij} = \begin{bmatrix} -0.0288 & 0 & 0 \\ -0.0323 & -0.0628 & 0 \\ -0.0356 & -0.0702 & -0.1013 \end{bmatrix} \quad (2.56)$$

### 2.4.2 - b Composite laminates

- Modelling and meshing:

The composite is modelled as a 3D deformable solid. As for the previous models, EA-06-062RE-120 strain gages are considered. The model is partitioned so that each partition corresponds to an increment (Fig. 2.21). If  $x$  increments per layer are drilled then a layer corresponds to  $x$  partitions. In Fig. 2.21 a layer corresponds to 2 partitions. Each layer of the composite is considered as an orthotropic material. The adequate material orientation is then assigned to each layer according to the desired stratification. Gage 1 is oriented at 0 degrees, gage 2 at -135 degrees and gage 3 at 90 degrees with respect to the on-axis direction of the first layer

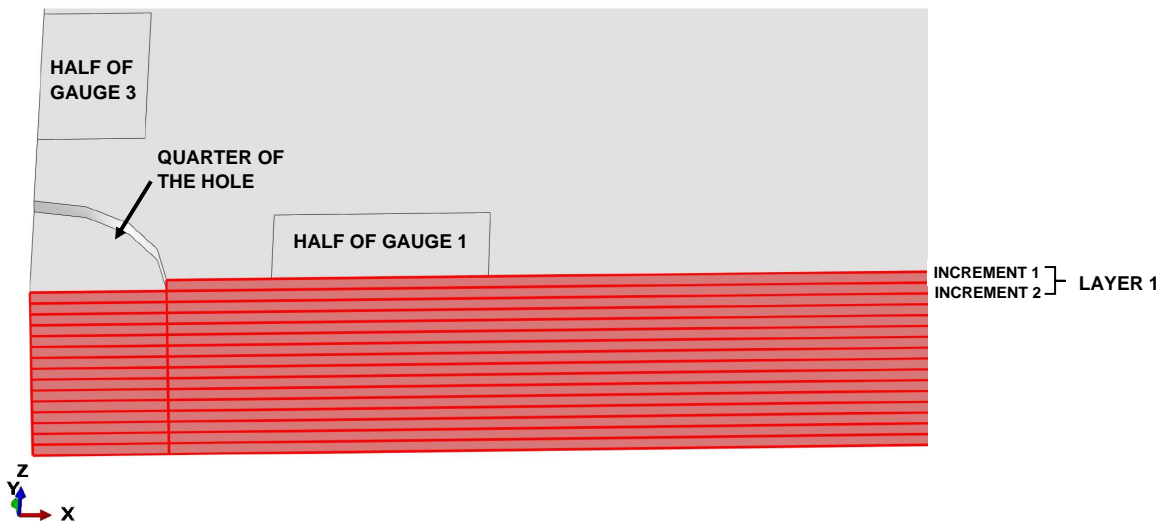


Figure 2.21 – Cutaway view of the 3D composite model (quarter of the model)

Meshing is a key step of the simulation. The better the mesh, the more accurate the results. The model is meshed with 8-node linear brick isoparametric elements (C3D8R). The mesh is configured in such a way as to guarantee its quality whatever the geometric parameters. To have the most uniform mesh, the model is partitioned along its diagonals and its two axes of symmetry (Fig. 2.22a and 2.22b). The elements sizes depend on the geometric parameters of the model. In addition, a circular

partition around the hole delimits an area of interest where the mesh is refined (Fig. 2.22c). In the thickness, the elements size is defined by the choice of the number of elements per increment (Fig. 2.22d).

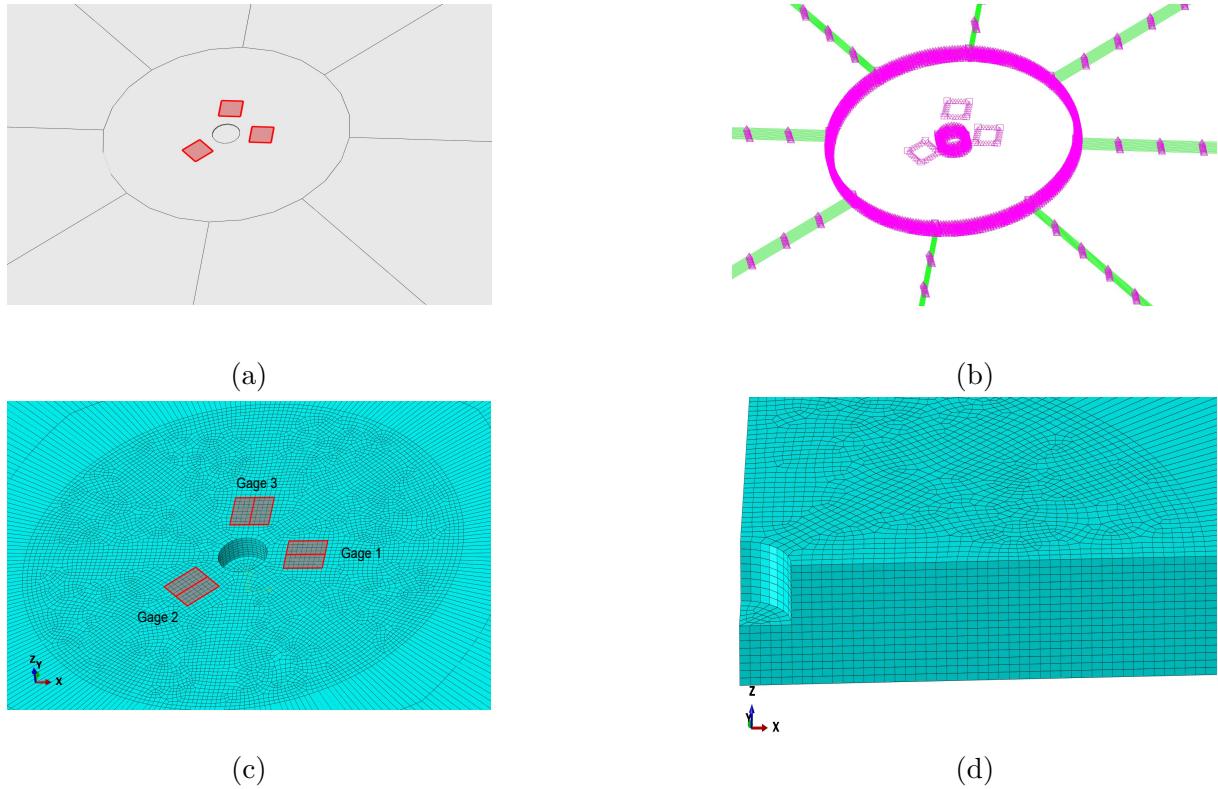


Figure 2.22 – Mesh strategy: (a) Partitions used for the mesh, (b) distribution of nodes on the edges (seed edge), (c) Mesh refinement area and gage positions, (d) Mesh in the thickness

- Boundary conditions and load cases:

The external boundaries of the model are fixed in the x and y directions. It is important to note that there is no symmetry boundary conditions, the cutaway views, presented here, are only used to facilitate understanding. Here, the approach is incremental, so equation 2.35 (recalled below) is used to calculate the calibration coefficients.

$$\frac{1}{\sqrt{E_x E_y}} \begin{bmatrix} c_{ij11} & c_{ij12} & c_{ij13} \\ c_{ij21} & c_{ij22} & c_{ij23} \\ c_{ij31} & c_{ij32} & c_{ij33} \end{bmatrix} \begin{Bmatrix} \sigma_x^j \\ \sigma_{xy}^j \\ \sigma_y^j \end{Bmatrix} = \begin{Bmatrix} \epsilon_1^i \\ \epsilon_2^i \\ \epsilon_3^i \end{Bmatrix}$$

When an increment "i" is numerically drilled (removal of elements), the 3 load cases, described in subsection 2.4.1 - b, are successively applied to the different increments j,  $0 \leq j \leq i$ . For example, to calculate the matrix  $[c_{31gs}]$  (Fig. 2.23b), the loads

2.4. CALCULATION OF CALIBRATION COEFFICIENTS USING FINITE ELEMENT SIMULATIONS

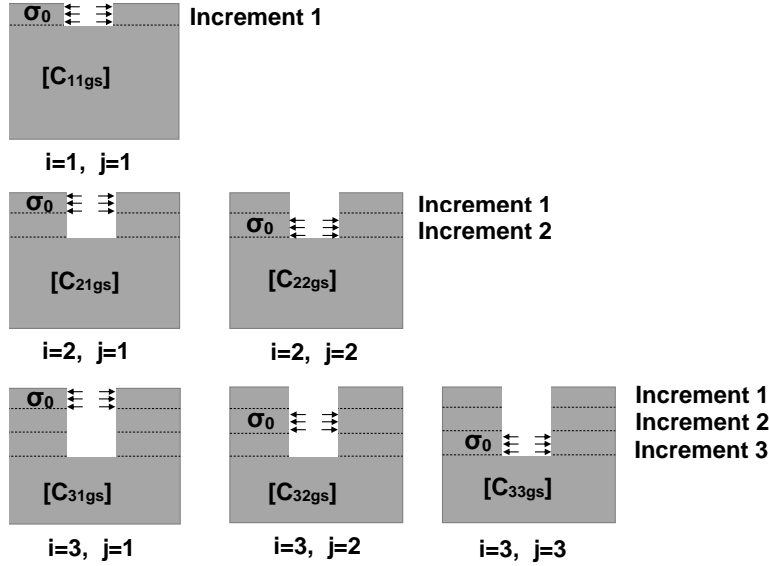
$E_1(MPa)$	$E_2(MPa)$	$E_3(MPa)$	$G_{12}(MPa)$	$G_{13}(MPa)$	$G_{23}(MPa)$	$\nu_{12}$	$\nu_{13}$	$\nu_{23}$
229003.0	12000.0	12000.0	5140.0	5140.0	6589.2	0.32	0.32	0.56

Table 2.4 – Material properties used for the application [117]

must be applied to the first increment (j=1) when i=3, see Fig. 2.24. If gage 1 is oriented in on-axis direction of the first layer then  $c_{ij12}$  and  $c_{ij32}$  are always equal to zero.

$$\begin{pmatrix} \varepsilon_1^1 \\ \varepsilon_2^1 \\ \varepsilon_3^1 \\ \varepsilon_1^2 \\ \varepsilon_2^2 \\ \varepsilon_3^2 \\ \varepsilon_1^3 \\ \varepsilon_2^3 \\ \varepsilon_3^3 \end{pmatrix} = \begin{bmatrix} [C_{1111} & C_{1112} & C_{1113}] & [0 & 0 & 0] & [0 & 0 & 0] \\ [C_{1121} & C_{1122} & C_{1123}] & [0 & 0 & 0] & [0 & 0 & 0] \\ [C_{1131} & C_{1132} & C_{1133}] & [0 & 0 & 0] & [0 & 0 & 0] \\ [C_{2111} & C_{2112} & C_{2113}] & [C_{2211} & C_{2212} & C_{2213}] & [0 & 0 & 0] \\ [C_{2121} & C_{2122} & C_{2123}] & [C_{2221} & C_{2222} & C_{2223}] & [0 & 0 & 0] \\ [C_{2131} & C_{2132} & C_{2133}] & [C_{2231} & C_{2232} & C_{2233}] & [0 & 0 & 0] \\ [C_{3111} & C_{3112} & C_{3113}] & [C_{3211} & C_{3212} & C_{3213}] & [C_{3311} & C_{3312} & C_{3313}] \\ [C_{3121} & C_{3122} & C_{3123}] & [C_{3221} & C_{3222} & C_{3223}] & [C_{3321} & C_{3322} & C_{3323}] \\ [C_{3131} & C_{3132} & C_{3133}] & [C_{3231} & C_{3232} & C_{3233}] & [C_{3331} & C_{3332} & C_{3333}] \end{bmatrix} \begin{pmatrix} \sigma_x^1 \\ \sigma_{xy}^1 \\ \sigma_y^1 \\ \sigma_x^2 \\ \sigma_{xy}^2 \\ \sigma_y^2 \\ \sigma_x^3 \\ \sigma_{xy}^3 \\ \sigma_y^3 \end{pmatrix}$$

(a)



(b)

Figure 2.23 – (a) Expansion of the relation between residual stresses and relaxation strains for three increments, (b) Load cases to calculate the different matrices of calibration coefficients  $[C_{31gs}]$  ( $\sigma_0$  is the magnitude of the load cases)

- Obtained results:

The considered material is a  $[0_2/90_2]_s$  carbon/epoxy composite laminates of dimensions 150x150 mm. Each layer has a thickness of 0.2 mm, 2 increments per ply are simulated. The radius of the hole is 1 mm and the material properties are given in Table 2.4.

For the first increment, one obtains:

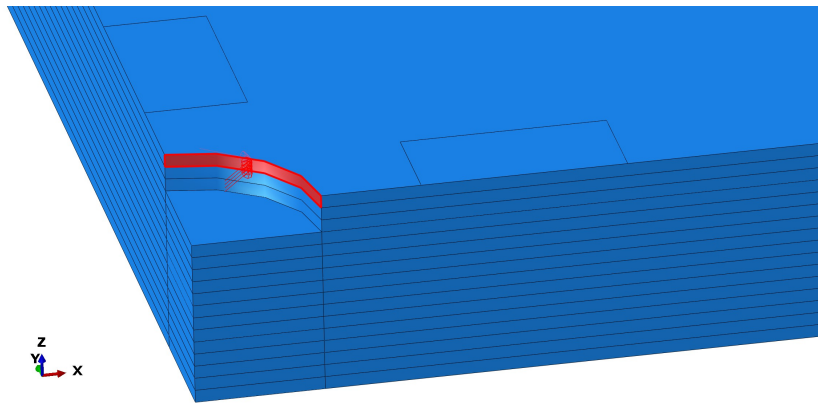


Figure 2.24 – Load case to be applied to calculate coefficients  $c_{31gs}$  (Cutaway view of the model)

$$[c_{11gs}] = \begin{bmatrix} -0.0291 & 0 & 0.0008 \\ -0.0106 & -0.0713 & -0.0268 \\ -0.0014 & 0 & -0.0545 \end{bmatrix} \quad (2.57)$$

## 2.5 Development of a configurable numerical model

### 2.5.1 About Python scripts in Abaqus

The object-oriented programming language Python is incorporated into the commercial finite element software Abaqus. When a user creates a model or executes a task through the graphical user interface (GUI) of the software, the corresponding Python commands are created and sent to the Abaqus/CAE kernel. The kernel can be considered as the brain of Abaqus and the GUI is the interface between the user and the kernel. However, it is possible to directly communicate with the kernel using a Python script or by programming in the command line interface (a zone dedicated to programming in Abaqus) as presented in Fig. 2.25.

The scripting can be used to automate repetitive tasks, to perform parametric studies, to extract specific data in an output database, to quickly modify and regenerate complex model databases. In Abaqus scripting, a command that creates an object is called a constructor and always starts with an uppercase character. In the example below, the constructor is "Model", it creates a new object (a new model in this case) named "composite". "mdb" is a model database in which the new model "composite" is stored. This new model is assigned to the variable "var".

Example: `var = mdb.Model(name='composite').`

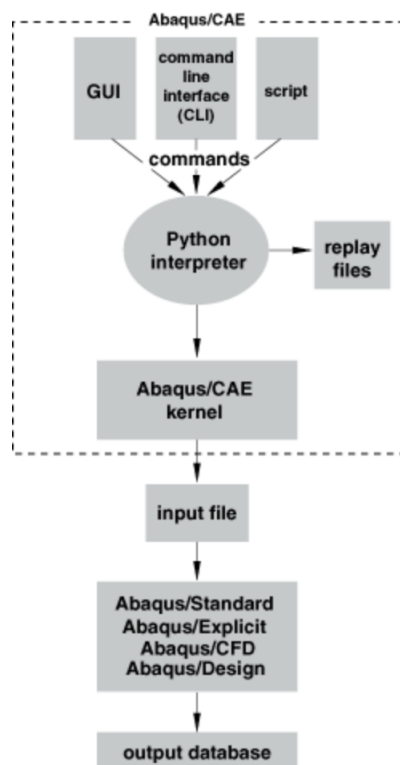


Figure 2.25 – Interaction between the different types of commands and the kernel [118]

To facilitate understanding, a simple script (which creates a parallelepiped) is detailed in Table 2.5 and the generated model is shown in Fig. 2.26.

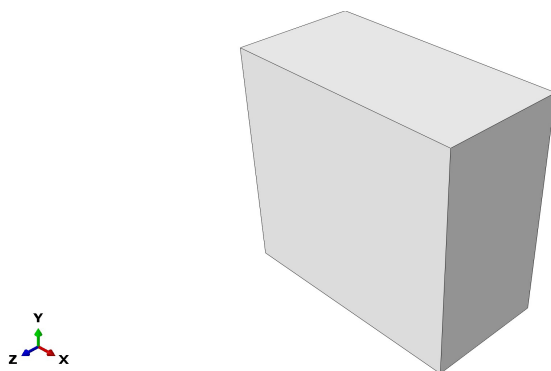


Figure 2.26 – Example of a simple model generated by a script

## 2.5.2 Configurable numerical model using Python scripts

Researchers generally use scripts to automate post-processing and computation of calibrations coefficients. In this work, the choice was made to automate modelling and simulation steps also (Fig. 2.27). An advantage of this choice, is the capability to quickly and easily modify the modeling parameters such as the stratification strategy or the geometry of

Beginning of the script:

(loading required libraries and modules)

```

- *- coding: mbc - *-
from part import *
from material import *
from section import *
from assembly import *
from step import *
from interaction import *
from load import *
from mesh import *
from optimization import *
from job import *
from sketch import *
from visualization import *
from connectorBehavior import *
    
```

(creation of the sketch: a rectangle)

```

mdb.models['Example'].ConstrainedSketch(name='profile', sheetSize=200.0)
mdb.models['Example'].sketches['profile'].rectangle(point1=(-20.0, 20.0), point2=(20.0, -20.0))
mdb.models['Example'].Part(dimensionality=THREE_D, name='Part-1', type=DEFORMABLE_BODY)
    
```

(extrusion of the sketch)

```

mdb.models['Example'].parts['Part-1'].BaseSolidExtrude(depth=20.0, sketch=mdb.models['Example'].sketches['profile'])
del mdb.models['Example'].sketches['profile']
    
```

End of the script.

Table 2.5 – Example of a simple script: modelling of a parallepiped

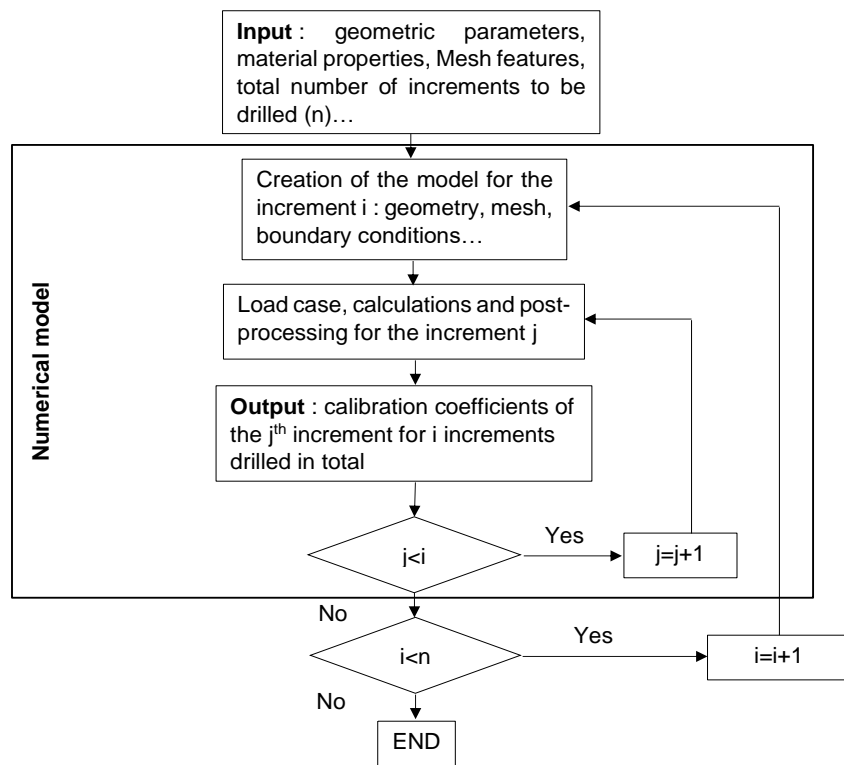


Figure 2.27 – The different steps of the configurable numerical model for custom calculation of calibration coefficients

the gages used for example. In a standard model, changing a parameter may make some of its related parameters obsolete, causing additional work to update these parameters. An another advantage is the possibility of performing parametric studies. This aspect is detailed in the next chapter.

One of the main tasks of this thesis was to develop a configurable model capable of simulating the IHDM, post-processing the results and calculating the calibration coefficients autonomously. The developed script is composed of 3 parts. Part 1 is the input section, part 2 corresponds to the modelling and simulation steps and part 3 is the post-processing. In part 1, the user sets the input parameters such as the dimensions of the model, the number of plies, the fiber directions, the number of increments per ply, the total number of increments to be drilled ( $n$ ), the mechanical properties of the material, the size of the elements for the mesh... Once the input data is entered and the script executed in Abaqus, its operation can be explained step by step as follows (this corresponds to part 2 of the script):

- Step 1: the model is created with all its geometric and mechanical characteristics according to the input data (as described in subsection 2.4.2 - b).

- Step 2: the first increment ( $i=1, j=1$ ) is drilled, boundary conditions and the first load case (presented in subsection 2.4.1 - b) are applied.

- Step 3: the model is meshed according to the element sizes given in the input data. To always have a coherent mesh, the element sizes and the refinement area are defined according to the dimensions of the model. For example, if larger gages are used, the refinement area increases so that the gages are always in a richly meshed area.

- Step 4: the simulation is performed and the results database file (ODB file) is stored in a defined directory.

- Step 5: the first load is disabled and the second load case is applied. The simulation is performed and the results are stored. This is repeated for the third load case.

- Step 6: The second increment ( $i=2$ ) is drilled. The previous steps are performed for  $j=1$  and then  $j=2$ . In other words, the three load cases are applied successively to the increments 1 and 2 when the depth of the hole corresponds to 2 increments.

- Step 7: the third increment ( $i=3$ ) is drilled. The previous steps are performed for  $j=1$ ,  $j=2$  and  $j=3$ . This is repeated in a loop until the total number of increments to be drilled is reached ( $i=n$ ).

Once all the simulations have been carried out, the post-processing of the results is carried out in part 3 of the script. The script opens the appropriate ODB file (results database) in Abaqus from the storage directory. The relaxation strains are extracted in the area corresponding to the strain gages. The calibration coefficients are calculated for all the increments ( $i,j$ ), with  $1 \leq i \leq n$  and  $1 \leq j \leq i$ , using the appropriate equation. The calibration coefficients are then stored in text or csv files. The configurable numerical model used in this work is presented in Fig.2.27.

### 2.5.3 Analysis of the influence of the mesh on the calibration coefficients

The size of the mesh elements and/or their type may have a significant influence on the value of the calibration coefficients. In order to determine precisely these coefficients, a mesh convergence study is carried out. For this, 4 mesh sizes, from very coarse to very fine, are simulated and the values of the calibration coefficients as well as the calculation time and the number of generated elements are compared. The aim is to find the best compromise between the size of the mesh elements and the calculation time. In addition, simulations with linear and quadratic elements are performed in order to see the influence of the shape function of the mesh elements on the calibration coefficients.

As it can be seen in Table 2.6, the calibration coefficients are very sensitive to the mesh elements size. However, from the fine mesh (401517 elements) the value of the calibration coefficients seem to reach an asymptote. The very fine mesh requires about 3 times more calculation time than the fine mesh without a great change in the calibration coefficients values. The dimensions of the model have not a great influence on the calibration coefficients as shown in Table 2.7. Thus, time and resource can be saved by considering as smaller numerical sample, as long as the adequate boundary conditions are applied and the assumption of a hole infinitely far from the edges is respected. Compared to a simulation with linear elements, a simulation with quadratic elements gives about the same calibration coefficients (Table 2.8). However, it requires about 25 times more calculation time. As conclusion to this study, the best compromise between calculation time and calibration coefficients accuracy is a 50x50 mm model with a fine mesh (element size in the area of the gage = 0.2) and linear elements.

An intrinsic limitation of the IHDM is related to the fact that the values of the calibration coefficients decrease with the increase of the hole depth. Indeed, the gages are



## 2.5. DEVELOPMENT OF A CONFIGURABLE NUMERICAL MODEL

	Very coarse mesh 150x150 mm (element size=1)	Coarse mesh 150x150 mm (element size=0.5)	Fine mesh 150x150 mm (element size=0.2)	Very fine mesh 50x50 mm (element size=0.1)
$c_{1111}$	-0.0214	-0.0291	-0.0291	-0.0296
$c_{1121}$	0.0024	-0.0091	-0.0106	-0.0108
$c_{1131}$	-0.0017	-0.0023	-0.0014	-0.0014
$c_{1122}$	0.0058	-0.0887	-0.0714	-0.0730
$c_{1113}$	0.0015	0.0009	-0.0008	-0.0008
$c_{1123}$	0.0488	-0.0423	-0.0269	-0.0267
$c_{1133}$	0.0799	-0.0788	-0.0545	-0.0568
Number of elements	114548	124438	401517	861901
Average calculation time (s)	131	154	840	2545

Table 2.6 – Influence of the size of the mesh elements in the area of the gage on the value of the first increment calibration coefficients. The average calculation time is the average of the calculation time of the 3 simulations corresponding to the 3 load cases. The considered material is the composite laminate presented in section 2.4.2 - b

	Fine mesh (size=0.2) 150x150 mm	Fine mesh (size=0.2) 50x50 mm
$c_{1111}$	-0.0291	-0.0294
$c_{1121}$	-0.0106	-0.0107
$c_{1131}$	-0.0014	-0.0014
$c_{1122}$	-0.0714	-0.0725
$c_{1113}$	-0.0008	-0.0008
$c_{1123}$	-0.0269	-0.0271
$c_{1133}$	-0.0545	-0.0549
Number of elements	401517	246957
Average calculation time (s)	840	360

Table 2.7 – Influence of the model size (length and width) on the value of the first increment calibration coefficients.

less sensitive to the load cases when the hole is deep (principle of Saint-Venant). The consequence is a numerical instability when inverting the matrix of calibration coefficients ( $i=j$ ) for the calculation of residual stresses. For isotropic materials, regularization methods such as Tikhonov regularisation method can be used to improve the stability of the calculations [119]. It is also possible to progressively increase the depth of the increment with the depth of the hole so that the calibration coefficients matrices keep comparable sizes [120]. Some authors recommended limiting the calculation steps [121, 120] and the depth of the hole [120].

	Fine mesh with linear elements 50x50 mm	Fine mesh with quadratic elements 50x50 mm
$c_{1111}$	-0.0294	-0.0297
$c_{1121}$	-0.0107	-0.0107
$c_{1131}$	-0.0014	-0.0014
$c_{1122}$	-0.0725	-0.0717
$c_{1113}$	-0.0008	-0.0013
$c_{1123}$	-0.0271	-0.0258
$c_{1133}$	-0.0549	-0.0549
Number of elements	246957	246957
Average calculation time (s)	360	8860

Table 2.8 – Influence of the shape function of the mesh elements on the value of the first increment calibration coefficients

## 2.6 Conclusion

In this work, the incremental hole drilling is used to determine residual stresses in parts. This chapter details the equations used in the HDM (for thin parts) and the IHDM (for thick parts) to determine residual stresses. These equations depend on the behavior of the materials and require to be calibrated using calibration coefficients. The number of required calibration coefficients depend on the type of material: 2 calibration coefficients are needed for thin isotropic materials, " $2*i$ " (" $i$ " is the number of drilled increments) coefficients per increment are needed for thick isotropic materials, 9 coefficients are needed for thin orthotropic materials and " $9*i$ " coefficients per increment are needed for composite laminates. For a fixed hole diameter and gages dimensions, the calibration coefficients are constant, however, they must be recomputed if one of these parameters changes.

The calibration coefficients are calculated using finite element simulations. They are then compared with good agreement to the results of the literature. A Python script is developed to automate the creation of the model, the simulation of the IHDM, the extraction of the relaxation strains and the calculation of the calibration coefficients. The capability of the script to generate configurable models allowed us to perform a parametric study and to assess the influence of experimental errors on calibration coefficients as detailed in the next chapter.



# Chapter 3

## Numerical study of the influence of experimental errors on calibration coefficients and development of the experimental procedure

### Sommaire

---

<b>3.1</b>	<b>Introduction</b>	<b>80</b>
<b>3.2</b>	<b>Study of the influence of experimental errors on calibration coefficients</b>	<b>80</b>
3.2.1	Errors on increment depth	82
3.2.2	Angular deviation of the gages from their theoretical position	85
3.2.3	Hole eccentricity errors	87
<b>3.3</b>	<b>Numerical correction of the calibration coefficients</b>	<b>89</b>
3.3.1	Presentation of the numerical correction method	89
3.3.2	Numerical validation of the correction method	93
<b>3.4</b>	<b>Development of the experimental device</b>	<b>94</b>
3.4.1	General description of the experimental device	94
3.4.2	Bonding protocol for gages	95
3.4.3	Perpendicularity of the milling cutter with respect to the surface of the sample	97
3.4.4	Optical centering of the milling cutter	98
3.4.5	Detection of the drilling reference	100
<b>3.5</b>	<b>Conclusion</b>	<b>101</b>

---

### 3.1 Introduction

The Incremental Hole Drilling Method (IHDM) is very effective in measuring the residual stress gradient in composite laminates. However, its reliability depends on the accuracy with which the calibration coefficients are determined. The samples' features and the real experimental conditions must be taken into account in the finite element simulation. Any mismatch can lead to inadequate calibration coefficients, thus introducing errors on residual stresses. Several calibration coefficients correction models exist for isotropic materials. One can cite the works of Ajovalasit [122] who proposed an analytical correction of the eccentricity of the hole for thin isotropic materials. More recently, Beghini et al. [123, 124] introduced the influence functions to analytically correct the eccentricity for blind hole in thick isotropic materials. It is important to note that there is a lack of information on this subject concerning composite laminates.

In this chapter, the influence of three major experimental errors on the calibration coefficients is numerically investigated for composite laminates through a parametric study. The results highlight the sensitivity of the coefficients to these errors and give an order of magnitude of the precision required on the experimental device to have reliable measurements. A novel numerical correction method based on the developed configurable model (Fig. 2.27) is then introduced. This numerical correction method is adapted for thick composite laminates for which the analytical approach is too complex. The method is formulated to correct any errors that can be experimentally measured and numerically modelled. The experimental protocol (method and device), developed to measure the relaxation strains, is presented.

### 3.2 Study of the influence of experimental errors on calibration coefficients

The IHDM must be performed with great care to have reliable results. The experimental errors can be divided into 2 categories, according to their sources. Category 1 concerns strain measurement errors which may occur due to additional thermal strains, instrument calibration errors, additional residual stresses caused by hole drilling [115]. These errors affect the right side of equation 2.35 (recalled below).

$$\frac{1}{\sqrt{E_x E_y}} \begin{bmatrix} c_{ij11} & c_{ij12} & c_{ij13} \\ c_{ij21} & c_{ij22} & c_{ij23} \\ c_{ij31} & c_{ij32} & c_{ij33} \end{bmatrix} \begin{Bmatrix} \sigma_x^j \\ \sigma_{xy}^j \\ \sigma_y^j \end{Bmatrix} = \begin{Bmatrix} \epsilon_1^i \\ \epsilon_2^i \\ \epsilon_3^i \end{Bmatrix}$$

They are independent of the initial state of residual stresses within the material and their effect is additive. The category 1 errors are difficult to assess and to correct. Cat-

egory 2 (category 2-5 type errors of reference [115]) concerns errors in the experimental parameters such as errors on increment depth, misalignment of the gages with respect to the fibers, hole eccentricity errors, hole diameter measurement errors... The effects of these errors are proportional to the initial state of residual stresses. For example, if a material without residual stresses is considered, whatever the errors on the increment depth no additional residual stresses will be measured. The category 2 errors affect the left side of equation 2.35 and they can be measured and corrected. The overall errors on the measured residual stresses are the sum of the category 1 and category 2 errors. This chapter focuses on the study of category 2 errors.

The residual stresses errors caused by category 2 errors are due to the mismatches between the numerical simulation and the experimental procedure of the IHDM. In general, there are three scenarios. These scenarios apply to all category 2 errors, but, for the sake of understanding, they are detailed below using the example of errors on increment depth (Fig. 3.1a).

- Scenario 1:

The residual stresses are determined using the calibration coefficients calculated for the desired experimental parameters ( $d_{model}$ , Fig. 3.1a) and the relaxation strains measured for the desired experimental parameters ( $d_{model}$ ). There is no mismatch between the experimentation and the numerical simulation  $\Rightarrow$  ideal experimental device.

- Scenario 2:

The residual stresses are determined using the calibration coefficients calculated for the desired experimental parameters ( $d_{model}$ ) and the relaxation strains measured for the real experimental parameters ( $d_{exp}$ ). There is a mismatch between the experimentation and the numerical simulation  $\Rightarrow$  standard error.

- Scenario 3:

The calibration coefficients are corrected by taking into account the experimental errors in the simulation. The residual stresses are determined using the corrected calibration coefficients ( $d_{exp}$ ) and the relaxation strains measured for the real experimental parameters ( $d_{exp}$ ). There is no more mismatch between the experimentation and the simulation  $\Rightarrow$  numerical correction of the calibration coefficients.

In practice, Scenario 2 is always carried out. Scenario 3 corresponds to one of the main

### 3.2. STUDY OF THE INFLUENCE OF EXPERIMENTAL ERRORS ON CALIBRATION COEFFICIENTS

aims of this chapter: the numerical correction of the calibration coefficients. Scenario 3 is detailed in section 3.3.

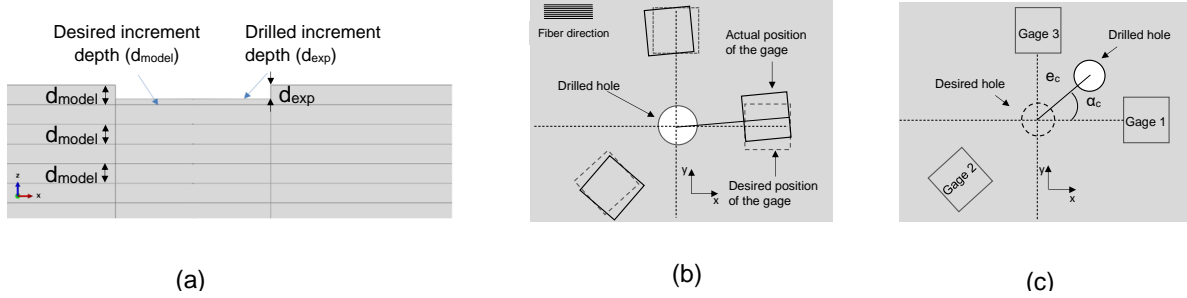


Figure 3.1 – Studied errors: (a) Illustration of error on increment depth, (b) Angular deviation of the gages from their theoretical position, (c) Radial ( $e_c$ ) and angular ( $\alpha_c$ ) eccentricity of the hole

#### 3.2.1 Errors on increment depth

Inaccuracies in the depth of increments are generally caused by the positioning uncertainties of the motor driving the spindle advance and by geometric defects of the experimental device. Due to these inaccuracies, the drilled increment depth  $d_{exp}$  is different from the desired increment depth  $d_{model}$  (Fig. 3.1a). This is one of the main sources of error when measuring residual stresses.

$$d_{exp} = d_{model} \pm \delta d_{model} \quad (3.1)$$

Where  $\delta d_{model}$  is the error on increment depth.

All calibration coefficients  $c_{ijgs}$  are calculated for the desired increment depth  $d_{model}$ . To determine the correct residual stresses, relaxation strains must be experimentally measured for the exact same increment depth. However, the experimentally measured strains correspond to the drilled increment depths ( $d_{exp}$ ). This leads to errors in the calculation of residual stresses.

From equation 2.35, one can write (by inverting the matrix of the calibration coefficients):

$$\sigma_x^j = (k_1^{ij} \epsilon_1^i + k_2^{ij} \epsilon_3^i) \sqrt{E_x E_y} \quad (3.2)$$

$$\sigma_y^j = (k_3^{ij} \epsilon_1^i + k_4^{ij} \epsilon_3^i) \sqrt{E_x E_y} \quad (3.3)$$

$$\sigma_{xy}^j = (k_5^{ij} \epsilon_1^i + k_6^{ij} \epsilon_2^i + k_7^{ij} \epsilon_3^i) \sqrt{E_x E_y} \quad (3.4)$$

The expressions of all the coefficients  $k_p^{ij}$ ,  $1 \leq p \leq 16$ , are given in Appendix A. For example,  $k_1^{ij} = c_{ij33} / (c_{ij11}c_{ij33} - c_{ij13}c_{ij31})$  and  $k_2^{ij} = -c_{ij13} / (c_{ij11}c_{ij33} - c_{ij13}c_{ij31})$ .

Considering category 2 errors, the non-correction of the calibration coefficients leads to errors on the residual stresses. These errors are determined by using the notion of exact total differential of multi-variable functions (equations 3.5, 3.6 and 3.7):

$$d\sigma_x^j = \delta\sigma_x^j = \sum_{g=1}^3 \sum_{s=1}^3 \frac{\partial\sigma_x^j}{\partial c_{ijgs}} \Delta c_{ijgs} \Rightarrow \delta\sigma_x^j = (K_1^{ij} \epsilon_1^i + K_2^{ij} \epsilon_3^i) \sqrt{E_x E_y} \quad (3.5)$$

$$d\sigma_y^j = \delta\sigma_y^j = \sum_{g=1}^3 \sum_{s=1}^3 \frac{\partial\sigma_y^j}{\partial c_{ijgs}} \Delta c_{ijgs} \Rightarrow \delta\sigma_y^j = (K_3^{ij} \epsilon_1^i + K_4^{ij} \epsilon_3^i) \sqrt{E_x E_y} \quad (3.6)$$

$$d\sigma_{xy}^j = \delta\sigma_{xy}^j = \sum_{g=1}^3 \sum_{s=1}^3 \frac{\partial\sigma_{xy}^j}{\partial c_{ijgs}} \Delta c_{ijgs} \Rightarrow \delta\sigma_{xy}^j = (K_5^{ij} \epsilon_1^i + K_6^{ij} \epsilon_3^i) \sqrt{E_x E_y} \quad (3.7)$$

Where  $\delta\sigma_x^j$ ,  $\delta\sigma_y^j$  and  $\delta\sigma_{xy}^j$  are the errors on residual stresses.  $\Delta c_{ijgs}$  is the variation of the calibration coefficients for a given category 2 error. The expressions of the coefficients  $K_p^{ij}$ ,  $1 \leq p \leq 15$ , are given in Appendix A.

Depth perturbations  $\delta d_{model}$  are introduced in the numerical model in order to study the variations of the coefficients  $c_{ijgs}$ . The results are presented in the form of a table which gives the value of the calibration coefficients for the different errors on increment depth (Table 3.1) and in the form of 2 graphs, one giving the variation of the calibration coefficients in percentage (Fig. 3.2a) and the other giving the variation of the coefficients  $K_p^{ij}$ ,  $1 \leq p \leq 6$ , of Eq.3.5-3.7 (Fig. 3.2b).

Table 3.1 – variation of the calibration coefficients  $c_{11gs}$  for different errors on increment depth  $\delta d_{model}$  (increment depth  $d_{model} = 100\mu m$ ).

$\delta d_{model}/d_{model}$	$c_{1111}$	$c_{1121}$	$c_{1131}$	$c_{1122}$	$c_{1113}$	$c_{1123}$	$c_{1133}$
0	-0.0291	-0.0106	-0.0014	-0.0713	0.0008	-0.0268	-0.0545
-10%	-0.0265	-0.0095	-0.0013	-0.0641	0.0006	-0.0236	-0.0508
+10%	-0.0326	-0.0120	-0.0015	-0.0793	0.0011	-0.0287	-0.0614
+25%	-0.0385	-0.0147	-0.0016	-0.0925	0.0014	-0.0340	-0.0693
+50	-0.0485	-0.0181	-0.0017	-0.1107	0.0019	-0.0400	-0.0854

For the different depth perturbations  $\delta d_{model}$ , the variation of the coefficients as a function of the depth is increasing. This variation is quasi-linear for all the coefficients. The coefficients are proportional to the relaxation strains. As seen in subsection 2.3.2 - b of chapter 2, the relaxation strains depend on the hole depth since they are the sum of all infinitesimal strains from the surface to the bottom of the hole. Thus, if  $d_{exp}$  is greater than  $d_{model}$ , the strains are overestimated and if  $d_{exp}$  is less than  $d_{model}$ , they are underestimated. The influence on residual stresses is more directly reflected by the variation of coefficients  $K_p^{ij}$ ,  $1 \leq p \leq 6$  (Eq.3.5-3.7).  $K_1^{11}$  and  $K_4^{11}$  which appear respectively in the



### 3.2. STUDY OF THE INFLUENCE OF EXPERIMENTAL ERRORS ON CALIBRATION COEFFICIENTS

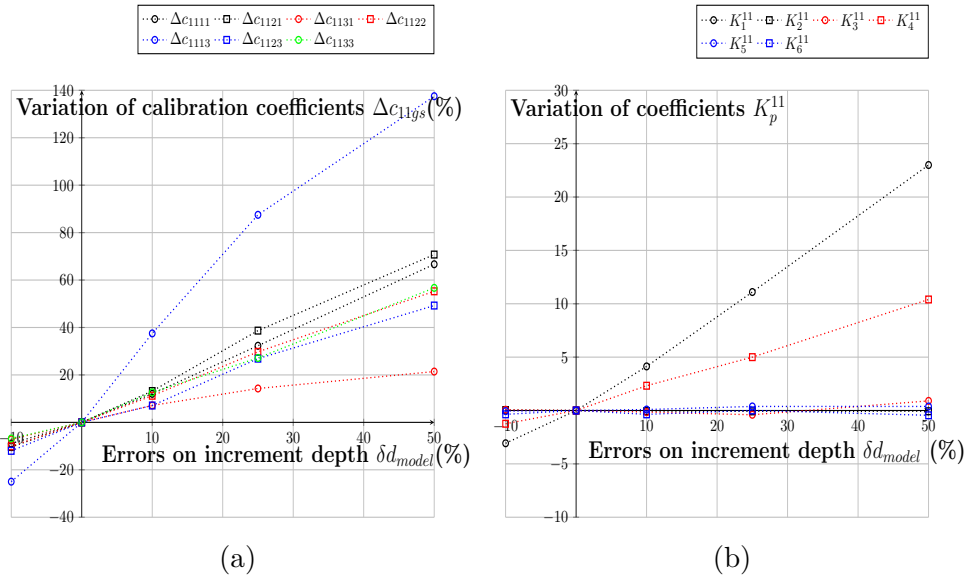


Figure 3.2 – Variation of the calibration coefficients  $c_{11gs}$  (a) and the coefficients  $K_p^{11}$  (b) for different errors on increment depth  $\delta d_{model}$  ranging from  $-10\%$  to  $50\%$  of the desired increment depth  $d_{model}$

expression of  $\delta\sigma_x^1$  and  $\delta\sigma_y^1$  (errors on the residual stresses of the first increment) are the most sensitive to errors on increments depth.

As a reminder, the considered material in this numerical study is a  $[0_2/90_2]_s$  carbon/epoxy composite laminates (see application in section 2.4.2 - b). The same study, as previously, is done at the  $0/90$  interface which is between the fourth and fifth increment. The variations of the coefficients  $c_{44gs}$  are presented in Fig. 3.3a and those of coefficients  $K_p^{44}$ ,  $1 \leq p \leq 6$  are presented in Fig 3.3b. It can be seen that there are coefficients whose variations present a change of slope at the interface and those whose variations are linear. The coefficients  $c_{4411}$ ,  $c_{4421}$  and  $c_{4431}$ , which are calculated from the first load case (longitudinal uni-axial tensile stress, see subsection 2.4.1 - b of chapter 2), vary linearly. This is due to the fact that one goes from a  $0$ -degree oriented layer with a higher longitudinal Young's modulus to a  $90$ -degree oriented layer with a lower longitudinal Young's modulus, there is therefore no sudden variation in relaxation deformations at the beginning of the transition. In the contrary, for coefficients  $c_{4413}$ ,  $c_{4423}$  and  $c_{4433}$ , which are calculated from load case 2 (transverse uni-axial tensile stress, as soon as the layer oriented at  $90$  degrees is drilled, there is a non-linear change of the Young's modulus in the transverse direction. Similarly, there is a non-linear increase in the shear modulus at the  $0/90$  interface, this is the reason why the variation of the coefficient  $c_{4422}$  presents a change of slope.

For composite laminates, it is difficult to model precisely the location of the different ply-ply interfaces because of the uncertainties on the layers' thickness. Generally, the mean thickness of the layers are considered in finite element simulations, however this can

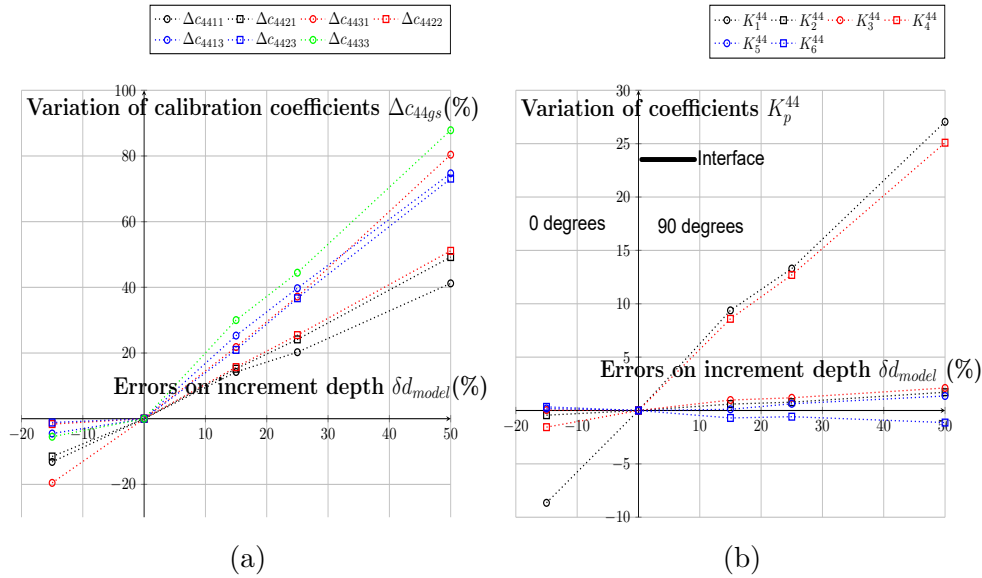


Figure 3.3 – Variation of the calibration coefficients  $c_{44gs}$  (a) and the coefficients  $K_p^{44}$  (b) for different errors on increment depth  $\delta d_{model}$  ranging from  $-15\%$  to  $50\%$  of the desired increment depth  $d_{model}$  at the 0/90 interface

cause mismatches between the simulation and the experimentation of the hole drilling process and cause deviations on the calibration coefficients similar to those presented on Fig. 3.3a and 3.3b. For example, due to the uncertainties on the layers' thickness, one can go from a layer to the next in the experimentation without reaching the interface in the simulation or vice versa. To avoid such errors, the real thickness of each layer must be considered in the numerical simulation, unfortunately, such information can only be accessed precisely by cutting and observing the sample at the hole location.

### 3.2.2 Angular deviation of the gages from their theoretical position

In equation 2.35, coefficients  $c_{ij12}$  and  $c_{ij32}$  are always equal to zero if the gage 1 is oriented in on-axis direction of the first layer.

$$\frac{1}{\sqrt{E_x E_y}} \begin{bmatrix} c_{ij11} & 0 & c_{ij13} \\ c_{ij21} & c_{ij22} & c_{ij23} \\ c_{ij31} & 0 & c_{ij33} \end{bmatrix} \begin{Bmatrix} \sigma_x^j \\ \sigma_{xy}^j \\ \sigma_y^j \end{Bmatrix} = \begin{Bmatrix} \epsilon_1^i \\ \epsilon_2^i \\ \epsilon_3^i \end{Bmatrix}$$

But, if there is an angular offset when gluing the gages (Fig. 3.1b), the calibration coefficients vary.  $c_{ij12}$  and  $c_{ij32}$  are no longer equal to zero. Not taking these variations into account in the calculations leads to errors on residual stresses determination. Different angular deviations, in the counter-clockwise direction, are introduced in the numerical model to study variations of calibration coefficients (Table 3.2).

### 3.2. STUDY OF THE INFLUENCE OF EXPERIMENTAL ERRORS ON CALIBRATION COEFFICIENTS

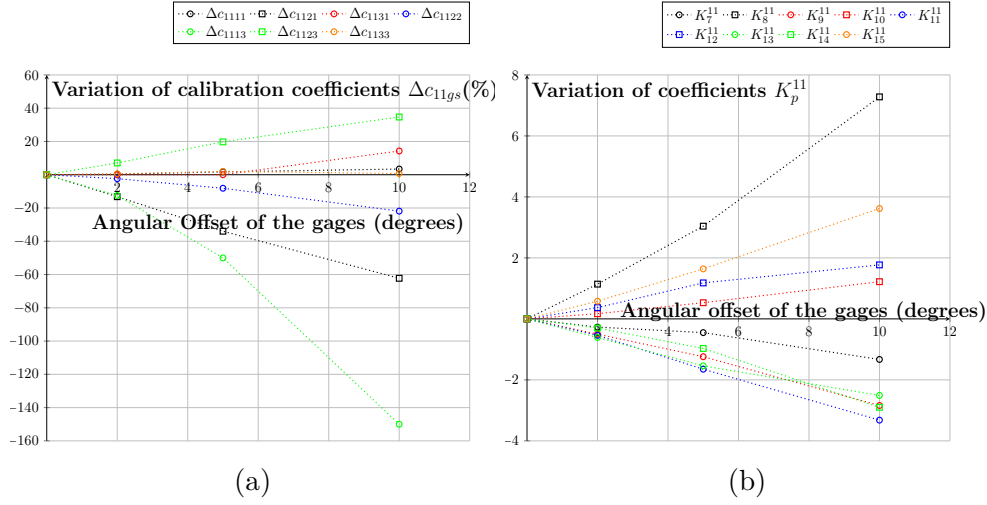


Figure 3.4 – Variation of coefficients  $c_{11gs}$  (a) and  $K_p^{11}$  (b) for different angular deviations in the counter-clockwise direction

To take into account coefficients  $c_{ij12}$  and  $c_{ij32}$ , equations 3.2, 3.3 and 3.4 become:

$$\sigma_x^j = (k_8^{ij} \epsilon_1^i + k_9^{ij} \epsilon_2^i + k_{10}^{ij} \epsilon_3^i) \sqrt{E_x E_y} \quad (3.8)$$

$$\sigma_y^j = (k_{11}^{ij} \epsilon_1^i + k_{12}^{ij} \epsilon_2^i + k_{13}^{ij} \epsilon_3^i) \sqrt{E_x E_y} \quad (3.9)$$

$$\sigma_{xy}^j = (k_{14}^{ij} \epsilon_1^i + k_{15}^{ij} \epsilon_2^i + k_{16}^{ij} \epsilon_3^i) \sqrt{E_x E_y} \quad (3.10)$$

And equations 3.5, 3.6 and 3.7 become:

$$\delta \sigma_x^j = (K_7^{ij} \epsilon_1^i + K_8^{ij} \epsilon_2^i + K_9^{ij} \epsilon_3^i) \sqrt{E_x E_y} \quad (3.11)$$

$$\delta \sigma_y^j = (K_{10}^{ij} \epsilon_1^i + K_{11}^{ij} \epsilon_2^i + K_{12}^{ij} \epsilon_3^i) \sqrt{E_x E_y} \quad (3.12)$$

$$\delta \sigma_{xy}^j = (K_{13}^{ij} \epsilon_1^i + K_{14}^{ij} \epsilon_2^i + K_{15}^{ij} \epsilon_3^i) \sqrt{E_x E_y} \quad (3.13)$$

Table 3.2 – variation of the calibration coefficients  $c_{11gs}$  for different angular deviations in the counter-clockwise direction

Angular deviation	$c_{1111}$	$c_{1121}$	$c_{1131}$	$c_{1112}$	$c_{1122}$	$c_{1132}$	$c_{1113}$	$c_{1123}$	$c_{1133}$
0 degrees	-0.0291	-0.0106	-0.0014	0.0000	-0.0713	0.0000	0.0008	-0.0268	-0.0545
2 degrees	-0.0292	-0.0092	-0.0014	-0.0024	-0.0696	0.0020	0.0007	-0.0287	-0.0548
5 degrees	-0.0296	-0.0070	-0.0014	-0.0064	-0.0655	0.0061	0.0004	-0.0321	-0.0556
10 degrees	-0.0301	-0.0040	-0.0016	-0.0153	-0.0557	0.0122	-0.0004	-0.0361	-0.0549

The analysis of the radial strain field shows that, for an angular shift of 0-10 degrees, the absolute values of  $\epsilon_1^i$  (gage 1) increase, those of  $\epsilon_2^i$  (gage 2) decrease and those of  $\epsilon_3^i$  (gage 3) are almost constant for load case 1, 2 and 3 respectively. Consequently, the absolute values of the coefficient  $c_{1111}$  increase, those of the coefficient  $c_{1122}$  decrease and

those of  $c_{1133}$  vary very lightly (Table 3.2). However, this variation is not monotonous and is reversed with larger angles since the distribution of the radial strain around the hole is globally sinusoidal.  $c_{1113}$  is small in terms of value, but is the most sensitive to angular deviations (Fig. 3.4a). The variation of coefficients  $c_{1121}$ ,  $c_{1122}$ ,  $c_{1123}$ , depends on the angular deviation direction.

The influence of the angular deviations on residual stresses calculation can be observed by the variation of coefficients  $K_p^{ij}$ ,  $7 \leq p \leq 15$  (Fig. 3.4b) of equations 3.11, 3.12 and 3.13.  $K_8^{11}$  is particularly sensitive to this error. The angular deviation of the gages is a frequent error because of the difficulty to locally orient the gage 1 of the rosette in the direction of the fibers. However, as shown in this section, an accurate calculation of residual stress uncertainties needs a rigorous control of the angular offset of the gages.

### 3.2.3 Hole eccentricity errors

Centering the spindle, in relation to the hole, is a delicate operation that must be performed with great care. Any eccentricity  $e_c$ ,  $\alpha_c$  (Fig. 3.1c) of the hole leads to errors in the values of the calibration coefficients. The study of hole eccentricity errors on calibration coefficients is decoupled into a study of the influence of radial eccentricity (Table 3.3) and a study of the influence of angular eccentricity (Table 3.4). The variations of coefficients  $K_p^{11}$  are presented in Fig. 3.5b and 3.5d.

**Influence of radial eccentricity:**  $\alpha_c = 0$  and  $e_c$  varies along x-axis

Table 3.3 – variation of the calibration coefficients  $c_{11gs}$  for different radial eccentricities

$e_c/r_m$	$c_{1111}$	$c_{1121}$	$c_{1131}$	$c_{1122}$	$c_{1113}$	$c_{1123}$	$c_{1133}$
0	-0.0291	-0.0106	-0.0014	-0.0713	0.0008	-0.0268	-0.0545
-2%	-0.0268	-0.0138	-0.0015	-0.0782	-0.0003	-0.0258	-0.0546
-5%	-0.0232	-0.0190	-0.0018	-0.0891	-0.0021	-0.0247	-0.0565
-10%	-0.0175	-0.0283	-0.0026	-0.1059	-0.0054	-0.0225	-0.0526
2%	-0.0315	-0.0074	-0.0015	-0.0643	0.0019	-0.0274	-0.0559
5%	-0.0356	-0.0032	-0.0018	-0.0529	0.0034	-0.0277	-0.0542
10%	-0.0424	0.0031	-0.0025	-0.0359	0.0061	-0.0303	-0.0519

The calibration coefficients vary linearly with radial eccentricity (Fig. 3.5a). The absolute values of coefficients  $c_{1111}$  and  $c_{1113}$  (which are calculated from the strain of gage 1) increase with positive values of  $e_c$  and decrease with negative values of  $e_c$ . This is explained by the fact that the closer the hole is to the gage 1, the greater the strains measured by this gage whether the load is in the longitudinal or transverse (Poisson effect) direction. The strain measured from gage 3 is similar for positive and negative values of  $e_c$ , thus, the variations of the coefficients calculated from this gage, i.e.  $c_{1131}$  and  $c_{1133}$ , are symmetrical

### 3.2. STUDY OF THE INFLUENCE OF EXPERIMENTAL ERRORS ON CALIBRATION COEFFICIENTS

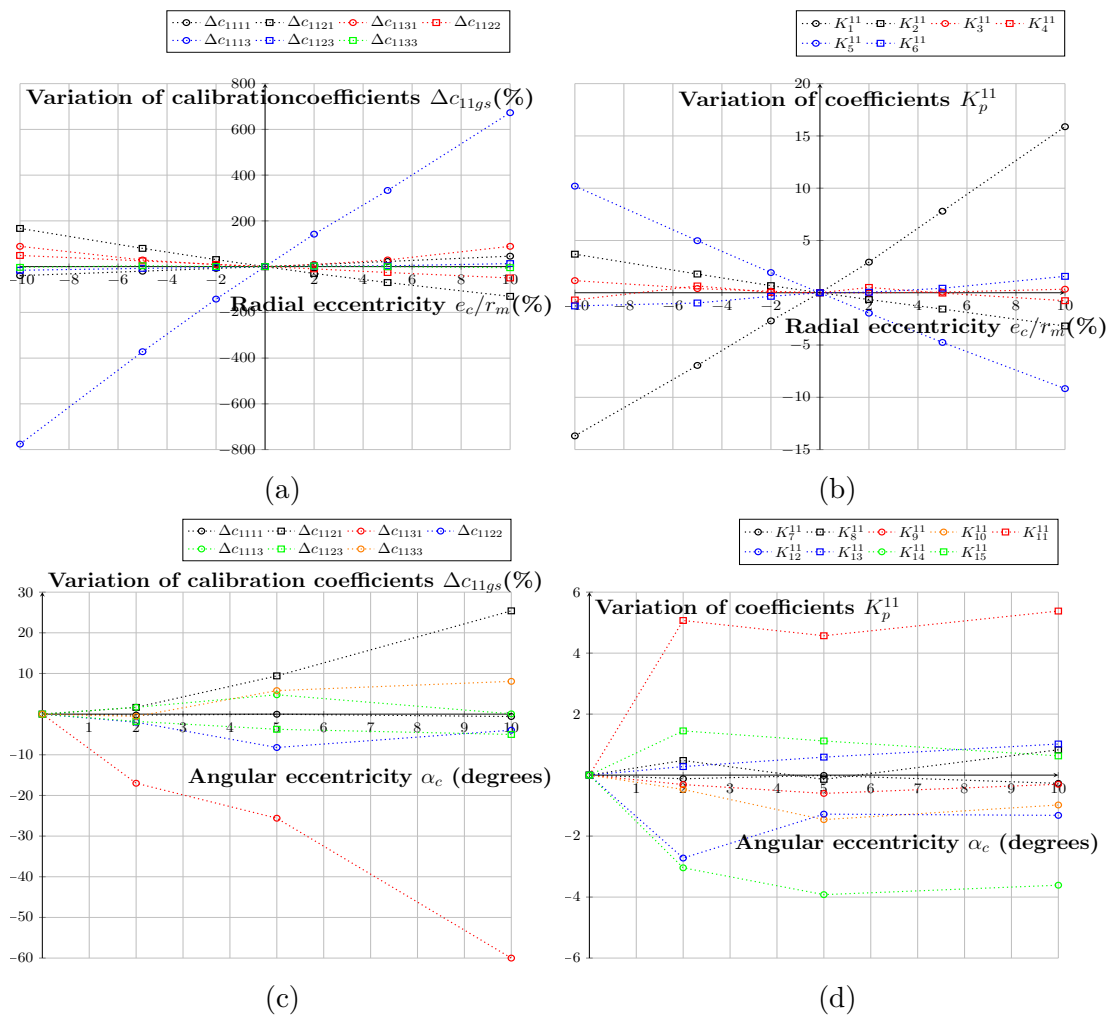


Figure 3.5 – Radial eccentricities: variation of coefficients  $c_{11gs}$  (a) and  $K_p^{11}$  (b), Angular eccentricities: variation of coefficients  $c_{11gs}$  (c) and  $K_p^{11}$  (d)

with respect to the y axis.

The variation of coefficients  $K_p^{11}$ ,  $1 \leq p \leq 6$ , depends on the chosen radial direction. Here, only the results along the x-axis are presented. The coefficients  $K_1^{11}$  and  $K_5^{11}$  in the expression of  $\delta\sigma_x^1$  and  $\delta\sigma_{xy}^1$  are the most sensitive to the radial eccentricity along x-axis (Fig. 3.5b).

**Influence of angular eccentricity:**  $e_c/r_m = 5\%$  and  $\alpha_c$  varies in the counter-clockwise direction

Table 3.4 – variation of the calibration coefficients  $c_{11gs}$  for different angular eccentricities

$\alpha_c$	$c_{1111}$	$c_{1121}$	$c_{1131}$	$c_{1112}$	$c_{1122}$	$c_{1132}$	$c_{1113}$	$c_{1123}$	$c_{1133}$
0 degrees	-0.0356	-0.0032	-0.0018	0.0000	-0.0529	0.0000	0.0034	-0.0277	-0.0542
2 degrees	-0.0355	-0.0032	-0.0015	0.0000	-0.0519	-0.0146	0.0035	-0.0272	-0.0539
5 degrees	-0.0356	-0.0035	-0.0013	0.0011	-0.0486	-0.0131	0.0036	-0.0267	-0.0574
10 degrees	-0.0354	-0.0040	-0.0007	-0.0006	-0.0508	-0.0155	0.0034	-0.0263	-0.0586

The radial eccentricity is fixed to 5% of  $r_m$  (i.e. 0.12 mm here) and the angular eccentricity is varied from 0 to 10 degrees in the counter-clockwise direction. The coefficient  $c_{1131}$  is the most sensitive to the angular eccentricities (Fig. 3.5c). In fact, the larger the angular eccentricity, the closer the hole is to the gage 3 and the greater the Poisson effect for load case 1. Coefficients  $K_{11}^{11}$ ,  $K_{14}^{11}$  and  $K_{12}^{11}$  have a relatively large deviation between  $\alpha_c = 0$  degrees and  $\alpha_c = 2$  degrees. However, between  $\alpha_c = 2$  degrees and  $\alpha_c = 10$  degrees, the coefficients  $K_p^{11}$  vary little (Fig. 3.5d). It is important to note the appearance of two non-null coefficients in the matrix  $[c_{11gs}]$ . If  $\alpha_c \neq 0$ ,  $c_{1112} \neq 0$  and  $c_{1132} \neq 0$ , except for small angles ( $\alpha_c \leq 2$  degrees) for which  $c_{1112} \simeq 0$  (Table 3.4).

As the errors studied previously, hole eccentricity errors can be minimized but not be avoided. Given the deviations generated on the coefficients  $K_p^{11}$ , one cannot calculate the residual stresses accurately without taking into account the experimental errors. A precise measurement of these errors makes it possible to calculate the uncertainties on the residual stresses or even to correct their effects.

### 3.3 Numerical correction of the calibration coefficients

#### 3.3.1 Presentation of the numerical correction method

The experimental errors can be minimized by optimizing the used experimental device and protocol but they cannot be avoided (Scenario 2 of section 3.2). One solution is to propose a method to correct the effect of these errors on the results. Some researchers have shown that residual stresses can be reliably calculated from relaxation strains mea-

sured with category 2 errors [122, 111, 112, 115]. For this, the calibration coefficients must be adequately corrected. For thin isotropic materials, for which residual stresses are considered uniform in thickness, Ajovalasit [122] proposed the theory of eccentric-hole method. This theory consists in correcting the calibration coefficients by introducing the eccentricity of the hole in the equations. Finite element simulations was used by Blödorn et al. [112] to correct the effect of hole bottom chamfer and by Barsanti et al. [111] to correct eccentricity of the hole but they limited their work to isotropic materials.

In this work, a numerical approach is proposed which consists in taking into account experimental errors in the numerical model to correct the calibration coefficients (Fig. 3.6). This allow to remove the mismatches between the numerical simulation and the experimental process (Scenario 3 of section 3.2). The correction method requires a numerical model that has the flexibility to take into account different category 2 errors, hence the interest of developing a configurable model (presented in section 2.5.2 of chapter 2). However, this numerical-experimental coupling requires an accurate experimental measurement of the considered error.

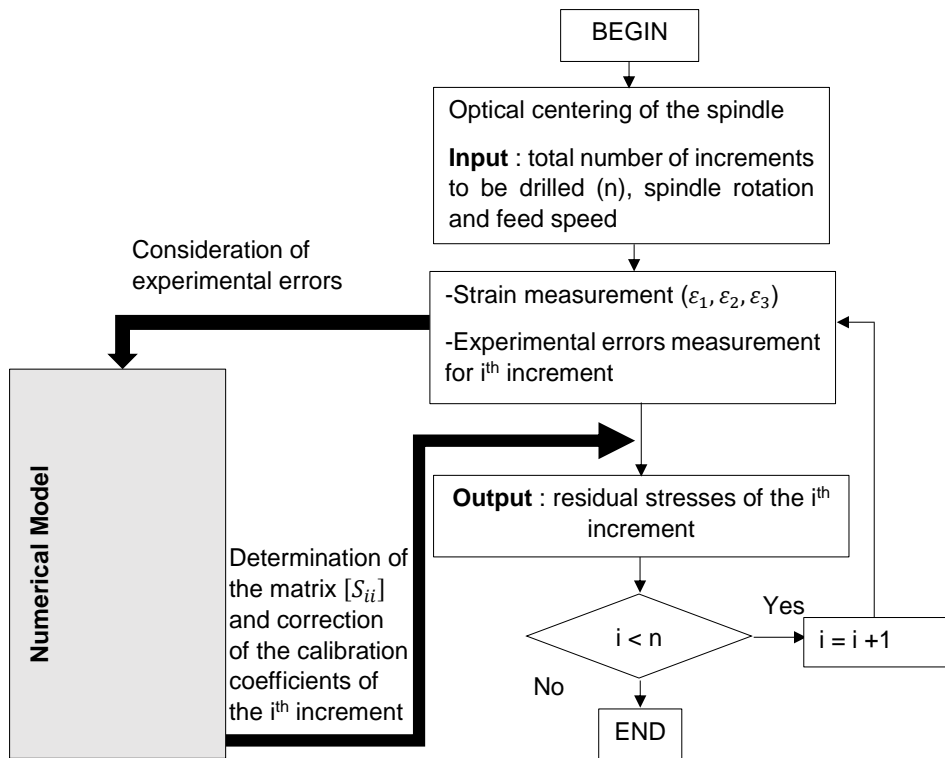


Figure 3.6 – Numerical correction of the calibration coefficients by a configurable experimental-numerical coupling

Consider a reference test for which the parameters have been optimized to minimize errors (Eq. 3.14), a test with at least one category 2 error introduced (Eq. 3.15) and the

corrected residual stresses (Eq. 3.16).

$$\{\sigma_s^i\}_{ref} = [C_{iigs}]_{ref}^{-1} \{\epsilon_g^i\}_{ref}^{increment\ i} \quad (3.14)$$

$$\{\sigma_s^i\}_{error} = [C_{iigs}]_{ref}^{-1} \{\epsilon_g^i\}_{error}^{increment\ i} \quad (3.15)$$

$$\{\sigma_s^i\}_{corr} = [C_{iigs}]_{corr}^{-1} \{\epsilon_g^i\}_{error}^{increment\ i} \quad (3.16)$$

$$1 \leq s \leq 3, 1 \leq g \leq 3$$

Where  $\{\sigma_s^i\}_{ref}$ ,  $\{\sigma_s^i\}_{error}$  and  $\{\sigma_s^i\}_{corr}$  are respectively the reference residual stresses, the residual stresses calculated with the error and the corrected residual stresses of increment  $i$ .

$[C_{iigs}]_{ref}^{-1}$  and  $[C_{iigs}]_{corr}^{-1}$  are respectively the inverse of the matrix of the initial and corrected calibration coefficients of increment  $ij$  ( $j=i$ ).

$\{\epsilon_g^i\}_{ref}^{increment\ i}$  and  $\{\epsilon_g^i\}_{error}^{increment\ i}$  are respectively the reference relaxation strains and the relaxation strain measured with the error for increments  $i$  exclusively. The relaxation strains exclusively due to increment  $i$  are the subtraction of the total strains measured at the surface ( $\{\epsilon_g^i\}$ ) and the strains due to the previous increments:  $\{\epsilon_g^i\}_{error}^{increment\ i} = \{\epsilon_g^i\} - \sum_{j=1}^{i-1} [C_{ijgs}] \{\sigma_s^j\}$ .

The correction must be made in such a way as to obtain ideally  $\{\sigma_s^i\}_{corr} = \{\sigma_s^i\}_{ref}$ .

$$\{\sigma_s^i\}_{corr} = \{\sigma_s^i\}_{ref} \Rightarrow [C_{iigs}]_{corr}^{-1} \{\epsilon_g^i\}_{error}^{increment\ i} = [C_{iigs}]_{ref}^{-1} \{\epsilon_g^i\}_{ref}^{increment\ i} \quad (3.17)$$

The expansion of Eq. 3.17, for a considered increment, gives a system of three equations which are satisfied by considering a term by term equality for each equation. Thus, the inverse of the matrix of the corrected calibration coefficients is given by Eq. 3.18.

$$[C_{iigs}]_{corr}^{-1} = [C_{iigs}]_{ref}^{-1} [S_{ii}] \quad (3.18)$$



Where  $[S_{ii}]$  is the correction matrix:

$$[S_{ii}] = \begin{bmatrix} \frac{(\epsilon_1^i)_{ref}^{increment\ i}}{(\epsilon_1^i)_{error}^{increment\ i}} & 0 & 0 \\ 0 & \frac{(\epsilon_2^i)_{ref}^{increment\ i}}{(\epsilon_2^i)_{error}^{increment\ i}} & 0 \\ 0 & 0 & \frac{(\epsilon_3^i)_{ref}^{increment\ i}}{(\epsilon_3^i)_{error}^{increment\ i}} \end{bmatrix} \quad (3.19)$$

Experimentally, only the relaxation strains for the real parameters  $\{\epsilon_g^i\}_{error}^{increment\ i}$  are known (Scenario 2 of section 3.2). Therefore, the correction is based on a numerical estimation of the matrix  $[S_{ii}]$ .

For the first increment, the corrected calibration coefficients can be written from Eq. 3.18:

$$C_{11gs(corr)} = C_{11gs(ref)} \frac{\epsilon_g^1(error)}{\epsilon_g^1(ref)} \quad (3.20)$$

The reference calibration coefficients are given by:

$$C_{11gs(ref)} = \frac{\epsilon_g^1(ref)}{\sigma_0} \quad (3.21)$$

Where  $\sigma_0$  is the magnitude of the load cases.

Then, Eq. 3.20 becomes:

$$C_{11gs(corr)} = \frac{\epsilon_g^1(error)}{\sigma_0} \quad (3.22)$$

By comparing Eq. 3.22 to Eq. 4.4-4.6 of chapter 2, one understands that, for the first increment, the numerical correction simply consists in recalculating the calibration coefficient with the conventional method (Eq. 4.4-4.6) by taking in to account the errors

of interest in the simulation.

### 3.3.2 Numerical validation of the correction method

In this application, the IHDM is numerically simulated with a hole eccentricity of 10% of  $r_m$  (i.e. 0.257 mm). The obtained numerical residual stresses are corrected using the method described in this section and compared to the reference residual stresses (simulation without eccentricity). The results are presented in Table 3.5. The same stress profile is applied to the 2 simulations as initial state of residual stresses (input). The same material and gages geometry as the application of section 2.4.2 - b) are used.

Table 3.5 – Numerical validation of the proposed correction method: comparison between the reference residual stresses, the corrected residual stresses and residual stresses with an eccentric hole obtained by numerical simulations of the incremental hole drilling for the considered initial residual stress profile.

Residual stresses	Reference (MPa)	Eccentric hole, 10% of $r_m$ (MPa)	Corrected (MPa)
$\sigma_x^1$	-5.79	-7.93	-5.79
$\sigma_{xy}^1$	0.35	1.23	0.35
$\sigma_y^1$	-3.28	-3.06	-3.28
$\sigma_x^2$	-223.50	-276.71	-223.50
$\sigma_{xy}^2$	14.11	52.96	14.11
$\sigma_y^2$	-38.76	-34.90	-38.76
$\sigma_x^3$	-1372.29	-1478.10	-1372.29
$\sigma_{xy}^3$	62.68	258.19	62.68
$\sigma_y^3$	-227.58	-220.03	-227.58
$\sigma_x^4$	28.66	181.57	28.66
$\sigma_{xy}^4$	15.07	-40.18	15.07
$\sigma_y^4$	-72.10	-62.45	-72.10
$\sigma_x^5$	-300.24	-239.31	-300.24
$\sigma_{xy}^5$	-19.91	7.17	-19.91
$\sigma_y^5$	-359.27	-353.64	-359.27
$\sigma_x^6$	533.35	639.62	533.35
$\sigma_{xy}^6$	-115.81	-232.50	-115.81
$\sigma_y^6$	-739.31	-693.20	-739.31

The results presented in Table 3.5 show that residual stresses calculated numerically

with a hole eccentricity of 10% of  $r_m$  can be corrected by determining the appropriate  $[S_{ii}]$  matrix. All the data used to calculate the results presented in Table 3.5 are given in Appendix B. Results with other category 2 errors, other initial stress profiles and the  $[S_{ii}]$  matrices used are also given in Appendix B. As expected, the corrected values are equal to the reference values. This is explained by the fact that the reference values and those with errors are known which allows to calculate the exact  $[S_{ii}]$  matrices. Experimentally, the reference values are not known, the correction is therefore based on a numerical estimation of the real  $[S_{ii}]$  matrices. Here, the results only validate the mathematical approach of the proposed method. Qualitative and quantitative experimental testing data are needed to experimentally validate the method.

## 3.4 Development of the experimental device

In this section, the experimental device and protocol, developed to measure the relaxation strains, are described in detail. This is a key step of the thesis project since the consistency between the measured relaxation strains and the calibration coefficients directly depends on the accuracy of the experimental device. The more accurate the device, the smaller the mismatch between the experimentation and the simulation (scenario 2 of section 3.2). As presented in the previous section, a numerical correction of the experimental errors is possible. However, this numerical correction requires a precise measurement of the experimental errors. The aim, here, is to minimize errors such as errors on increment depth, angular deviation of the gages and eccentricity of the hole, by optimizing the experimental protocol. The experimental optimizations proposed for this purpose are presented here.

### 3.4.1 General description of the experimental device

The experimental device used to measure the relaxation strains is presented in Fig. 3.7. The structure of the machine is composed by aluminium profiles. Those profiles are reinforced by steel brackets to rigidify the structure and avoid instabilities during drilling. A milling spindle with a rotation speed of 2000 to 20000 rpm is used to drill the hole. The rotation speed of the spindle is regulated by a control box. A camera is used to center the milling cutter with respect to the strain gage rosette (as presented below, in subsection 3.4.4). The camera and the spindle are mounted on the same holder (camera and spindle holder in Fig. 3.7). The distance between their axes is calibrated and known. The holder is fixed on a linear stage with a minimum incremental motion of  $0.2 \mu m$  and a repeatability of  $1 \mu m$ . This makes it possible to control very precisely the vertical advance of the spindle, and thus, to minimize errors on increments depths. The linear

stage is mounted on a vertical axis, the displacement of which is ensured by a belt and a handwheel. Once this axis is set, the vertical displacements are made exclusively using the linear stage. The sample holder is fixed on 2 linear stages which control its movement in the horizontal plane. The acquisition of the gages is done using a quarter-bridge strain gage module.

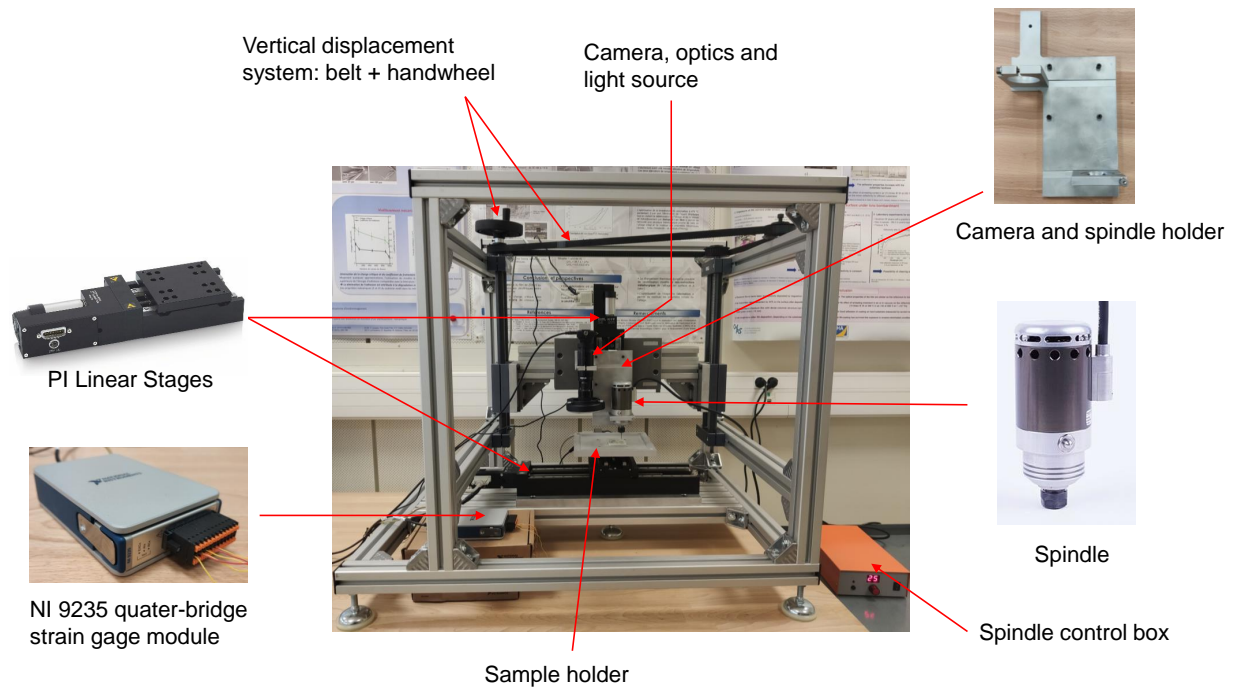


Figure 3.7 – General presentation of the experimental device used to measure the relaxation strains

### 3.4.2 Bonding protocol for gages

To avoid errors on residual stresses, the grids of gage 1 must be oriented in the principal direction of the composite (the fibers, here). The accuracy of manual bonding is limited due to the difficulty of seeing the fiber and accurately orienting the rosette. This is the reason why the angular deviation of the gage from their theoretical position is one of the most frequent errors when performing the IHDM. In this work, a device composed of a translation column and a camera is used to precisely bond the rosettes on the samples. The bonding device is presented in Fig. 3.8.

The camera is mounted on the column and can move vertically. The composite sample is placed on a support that can rotate. The strain gage rosette is fixed on a rigid and transparent plastic with double-sided tape and placed just under the camera. The column goes down until the camera focuses on the grids of gage 1 and the fibers (Fig 3.9). A raking light is used to expose the fibers. Image processing can be used to estimate the angle between the fibers and gage 1 grid. The sample is rotated until a satisfactory alignment

### 3.4. DEVELOPMENT OF THE EXPERIMENTAL DEVICE

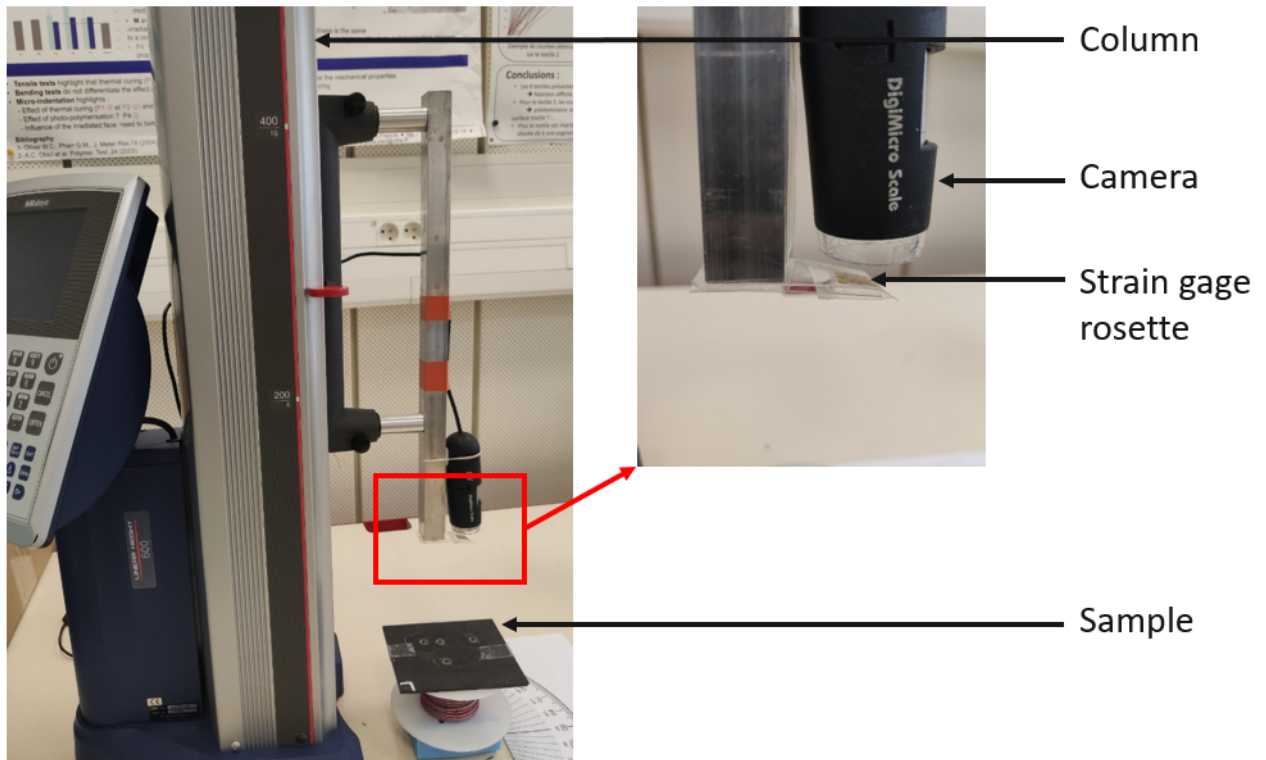


Figure 3.8 – Bonding protocol for gages: presentation of the device used to minimize angular offset between gage 1 and the fibers

is obtained then the rosette is bonded. The strain gage adhesive used to bond the rosette is a cyanoacrylate manufactured by VPG (M-Bond 200 [125]).

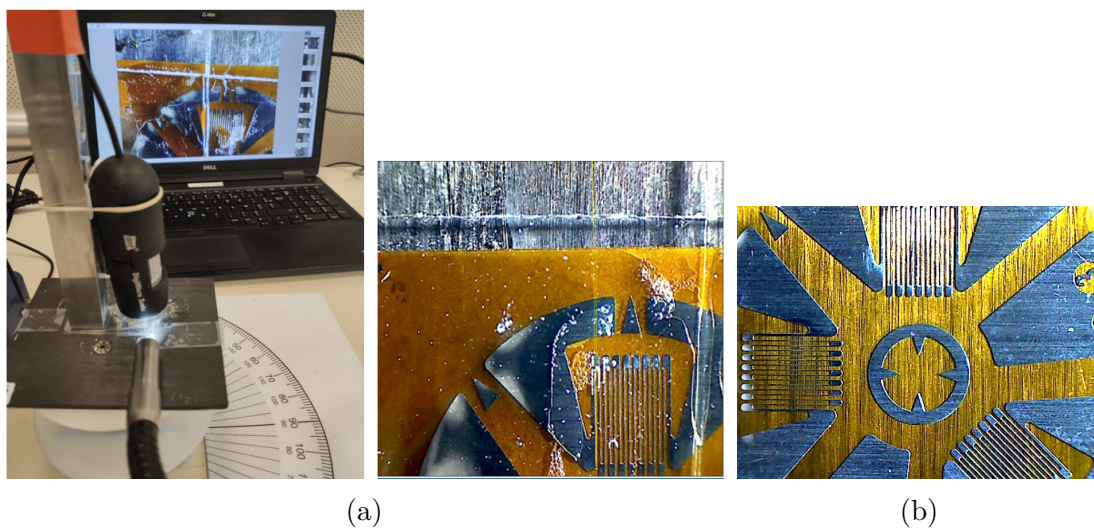


Figure 3.9 – (a) Alignment of composite fibers and grids of gage 1 of the rosette, (b) Verification of the quality of the orientation after bonding

### 3.4.3 Perpendicularity of the milling cutter with respect to the surface of the sample

The perpendicularity of the milling cutter with respect to the surface of the sample (Fig. 3.10) is an important parameter when performing the hole drilling method. This perpendicularity must not only be respected but the displacement of the z-axis must also be perpendicular to the composite plane. Ideally, the reference surface would be that of the composite, however, the surface condition varies from sample to sample. This would involve adjusting the perpendicularity for each sample which would be time consuming and not sustainable in the long term.

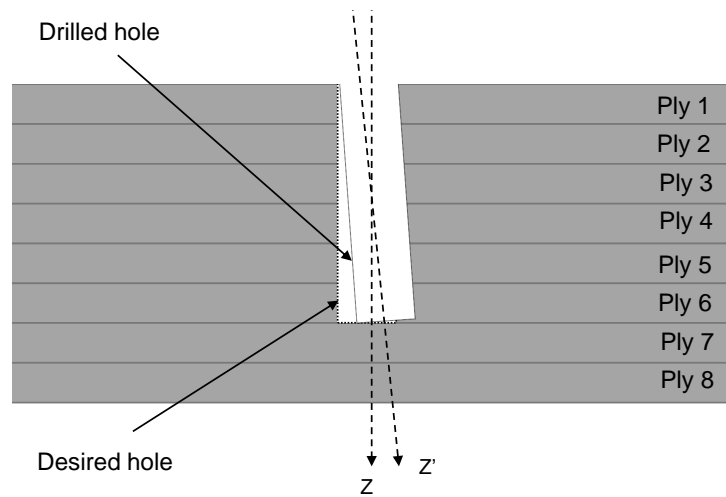


Figure 3.10 – Schematic representation of the perpendicularity error of the milling cutter with respect to the surface of the sample

To overcome this problem, the surface of the sample holder is considered as the reference surface. A dial indicator is used to adjust the perpendicularity. The planing principle is shown in Fig. 3.11a. A point is taken on the reference surface, along x-axis, the dial indicator is placed on this point and a 180 degrees rotation is made. If the variation ( $\Delta e$ ) given by the indicator is too large (greater than  $10 \mu m$ ), the z-axis is adjusted (using properly placed pressure screws and shims) until a satisfactory result is obtained. The process is repeated for a point taken on the y-axis. To control the perpendicularity of the z-axis translation with respect to the plane of the composite, a machinist square is used (Fig. 3.11b). The square is placed on the sample holder and put in contact with the dial indicator, the z-axis is translated and adjusted until a satisfactory result is obtained.

In this work, the z-axis was adjusted so as to obtain the following perpendicularity measurements:

- For the milling cutter with respect to the surface of the sample holder, one obtained:  $0.0047 \pm 0.0009^\circ$  in the xz plane (corresponding to a  $\Delta e = 10 \mu m$  for a 180 degree

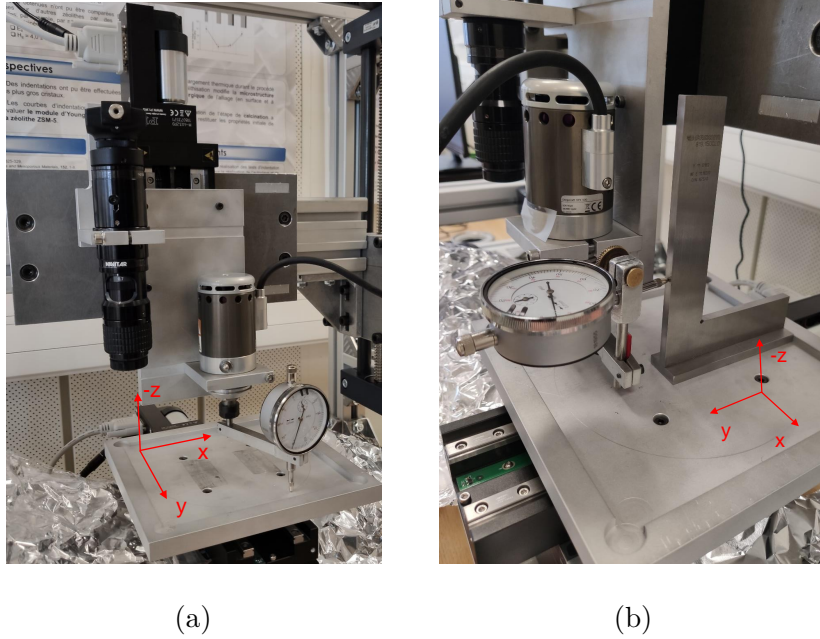


Figure 3.11 – Adjustment of the perpendicularity: (a) perpendicularity of the milling cutter with respect to the surface of the sample holder, (b) perpendicularity of the z-axis translation with respect to the plane of the composite (yz plane).

rotation of the dial indicator from a point on the x-axis) and  $0.0023 \pm 0.0009^\circ$  in the yz plane ( $\Delta e = 5\mu m$  for a rotation from a point taken along y-axis).

- For the perpendicularity of the z-axis translation with respect to the plane of the composite, one obtained:  $0.0047 \pm 0.0009^\circ$  in the xz plane ( $\Delta e = 10\mu m$ ) and  $0.0023 \pm 0.0009^\circ$  in the yz plane ( $\Delta e = 5\mu m$ ).

#### 3.4.4 Optical centering of the milling cutter

The centering of the milling cutter with respect to the strain gage rosette is performed using a camera (Fig. 3.12).

A picture of the rosette is taken (Fig. 3.13a), the coordinates of its center is determined by image processing using OpenCV combined to Python. First, the image is thresholded, the contour of the central pattern is drawn (Fig. 3.13b) and the coordinates of the contour center are extracted. The coordinates of the image center are known, so the distance between the detected center of the rosette and that of the image (which corresponds to the axis of the camera) can be determined to pixel accuracy ( $\pm 2\mu m$ ). The corresponding translations dx and dy (Fig. 3.13c) are written in a macro file by the OpenCV-Python program. This macro is executed by the software controlling the motion of the linear stages to center the camera with respect to the gages. The distance between the axis of the camera and the axis of the milling cutter is known and calibrated. Thus, a simple translation allows to place the axis of the milling cutter in the center of the rosette. The



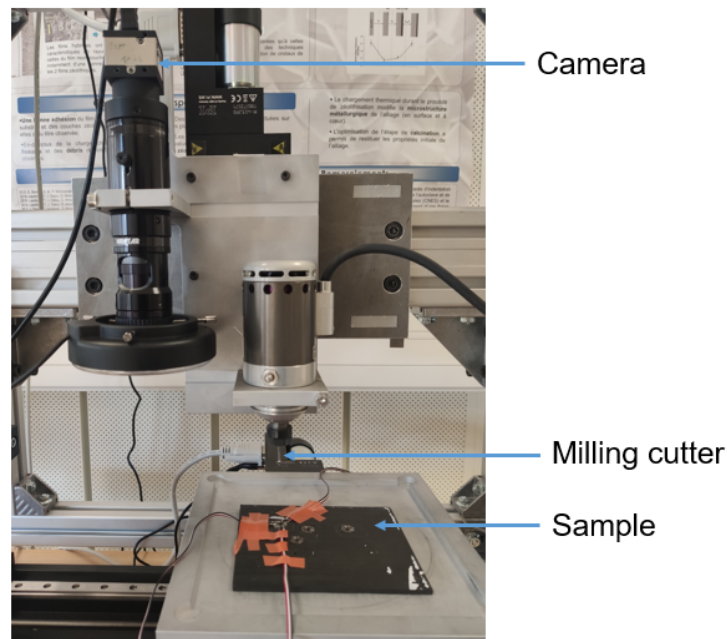


Figure 3.12 – Centering of the milling cutter with respect to the strain gage rosette using a camera

overall accuracy of centering depends on the accuracy of contour detection.

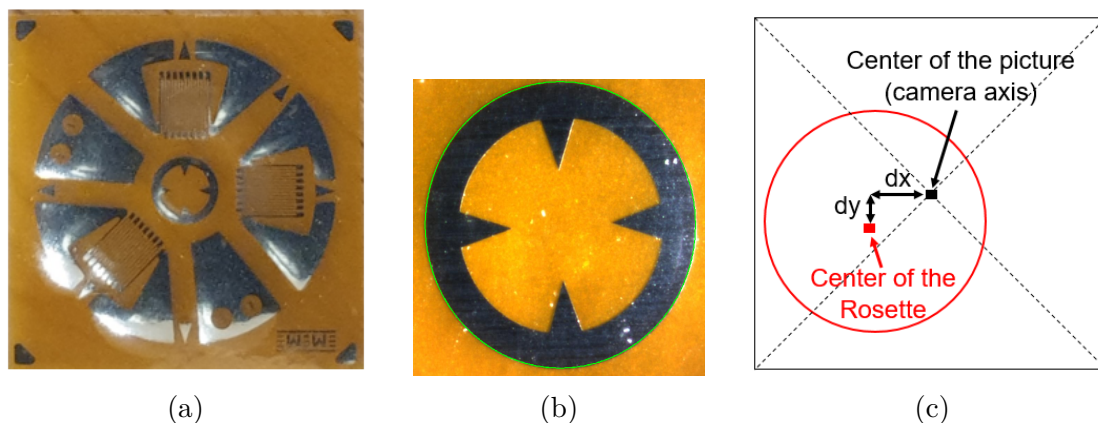


Figure 3.13 – Image processing of the strain gage rosette to determine its center: (a) picture of the strain gage rosette, (b) central pattern contour detection and center coordinates extraction, (c) schematic representation of the  $dx$  and  $dy$  translations needed to center the camera with respect to the rosette

As it can be seen in Fig. 3.14 and 3.15, the quality of the threshold and the contour detection depend on the light intensity which depends on the uniformity of the light source and the surface condition. To have a good threshold, it is necessary to have uniform light and no scratches in the central area of the rosette. However, the surface condition may be affected randomly by the bonding and welding steps. To overcome this problem, 2 contour plot techniques are used: the fitting method and the circumscribed circle method. If the contour of the central pattern of the rosette cannot be fully detected due to non-



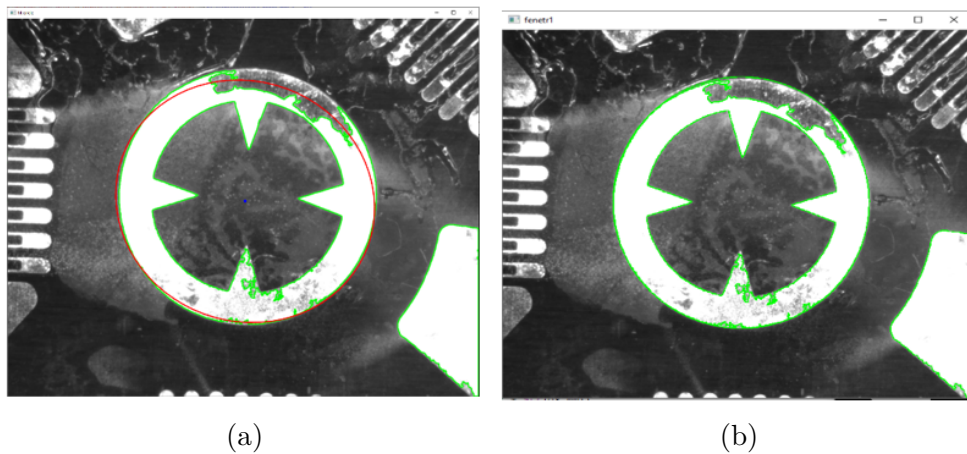


Figure 3.14 – Determination of the center of the rosette in case of incomplete detection of the contour of the central pattern of the rosette: (a) fitting method and (b) circumscribed circle method

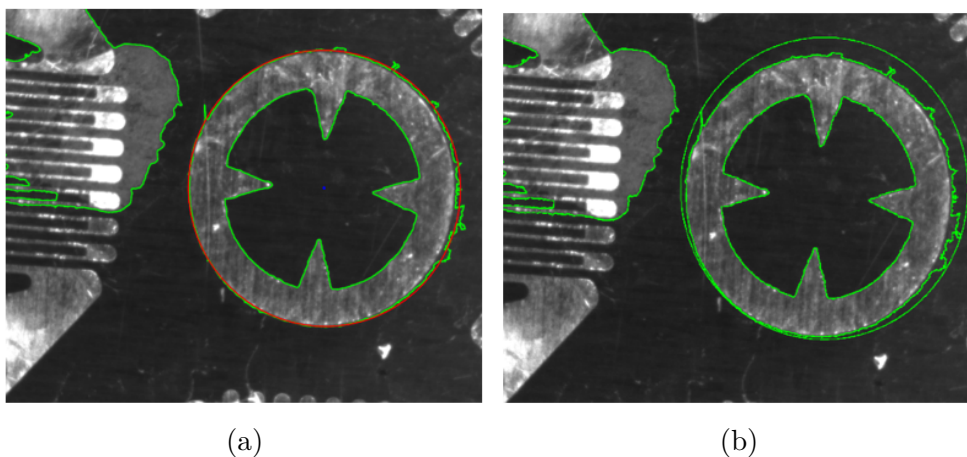


Figure 3.15 – Determination of the center of the rosette if the contour of the central pattern of the rosette is not detected clean: (a) fitting method and (b) circumscribed circle method

uniform light intensity, the circumscribed circle method is more suitable for determining the center of the rosette (Fig. 3.14). If the contour of the central pattern of the rosette is fully detected but not clean (Fig. 3.15) the fitting method is more suitable for determining the center of the rosette.

### 3.4.5 Detection of the drilling reference

The drilling reference, along the z-axis (vertical direction), must be correctly defined before the start of the acquisition. This reference,  $z=0$ , corresponds to the contact between the milling cutter and the surface of the composite. If the reference is incorrectly determined, the depth of the first increment will be inaccurate and this will create an offset between the drilled increments and the desired increments. Thus, this experimental error

has a similar effect on residual stresses as errors on increment depth.

A simple technique to determine the drilling reference would have been to use an electric circuit with the contact between the end mill and sample as circuit closure point. As soon as an electrical signal is detected the contact is established. This technique can be adapted to composite laminates using a metal standard. However, the contact with the standard, which generally has very good mechanical properties, can be harmful to the drilling edge. Therefore, a technique based on calibrated papers is used in this work. The principle is similar, a paper with a known and calibrated thickness is placed on the surface of the composite. The end mill approaches the composite surface with very small increment motion as long as the calibrated paper can slide over the surface of the composite. As soon as the paper is stuck, the contact coordinates correspond to the current coordinates plus the thickness of the calibrated paper (following the z-axis). The smaller the increment motion, the more accurate the surface detection. At this stage of the experimental procedure, the rosette being already glued to the sample, the contact detection is done in an area very close to the rosette.

### 3.5 Conclusion

In this chapter, the influence of three main experimental errors on the accuracy of the IHDM, for a  $[0_2/90_2]_s$  carbon/epoxy composite laminates, is numerically investigated. These errors are the errors on increment depth, the angular deviation of the gages from their theoretical position and the eccentricity of the hole with respect to the strain-gage rosette. A precise determination of the calibration coefficients is crucial to ensure the reliability of the residual stresses. A detailed analysis of the sensitivity of the calibration coefficients to the studied errors is presented. This chapter introduces a novel approach based on a configurable numerical-experimental coupling to correct the calibration coefficients for composite laminates.

The analysis of the sensitivity of the calibration coefficients showed that they are very sensitive to experimental errors, particularly radial eccentricity of the hole. A radial eccentricity equal to 10% of the mean radius of the gages (i.e. 0.257 mm for EA-06-062RE-120 strain gages) along the x-axis causes 130% error on the coefficient  $c_{1121}$  and up to 673% error on  $c_{1113}$ . The matrix diagonal coefficients,  $c_{11gg}, g = s$ , are more sensitive to errors on increment depth. The angular deviation of the gages from their theoretical position is one of the most frequent error. However, the coefficients  $K_p^{11}, 7 \leq p \leq 15$  which are in the expression of residual stress errors ( $\delta\sigma_s^i$ ) are less sensitive to this error.

### 3.5. CONCLUSION

---

The calibration coefficients can be corrected by calculating the matrix  $[S_{ii}]$  which is given by the ratios of the reference relaxation strains (optimized experimental parameters) and the relaxation strains measured with errors. However, in practice, if a correction is needed, then only the relaxation strains measured with errors are available. Thus, the matrix  $[S_{ii}]$  must be approximated by numerical simulations. For this, precise measurements of the experimental errors is required. The proposed correction method (its mathematical approach) is numerically validated by numerical simulations of the IHDM. However, further work is needed to validate the method experimentally with qualitative testing data.

The development of the experimental device required to measure relaxation strains is detailed. The optimization protocols established to minimize the experimental errors are presented. By contributing to improve the accuracy of the calibration coefficients calculation and the relaxation strains measurement, the work carried out in this chapter contributes to determine residual stresses more reliably in composite laminates. This will permit to estimate more precisely the mechanical properties of such materials and therefore, to better adapt their functionalities.

# Chapter 4

## Tests campaign: results and discussion

### Sommaire

---

<b>4.1</b>	<b>Introduction</b>	<b>105</b>
<b>4.2</b>	<b>Materials manufacturing and experimental methods</b>	<b>105</b>
4.2.1	Manufacturing process	105
4.2.2	Sample preparation	107
4.2.3	Experimental methods	107
<b>4.3</b>	<b>Analysis of the raw acquisition data of relaxation strains</b>	<b>110</b>
4.3.1	Presentation of the raw acquisition data	110
4.3.2	Thermal and mechanical contributions of drilling on raw acquisition data	111
<b>4.4</b>	<b>Thermal effects of the drilling on the local chemical and mechanical properties of the raw resin</b>	<b>119</b>
4.4.1	Differential Scanning Calorimetry (DSC) tests	119
4.4.1 - a	Principle of the DSC	119
4.4.1 - b	Sample preparation and experimental parameters	119
4.4.1 - c	Results and discussion	120
4.4.2	Dynamique Mechanical Analysis (DMA) tests	122
4.4.2 - a	Principle of the DMA	122
4.4.2 - b	Sample preparation and experimental parameters	122
4.4.2 - c	Results and discussion	123
<b>4.5</b>	<b>Determination of the residual stress profile</b>	<b>125</b>
4.5.1	Measurement of relaxation strains	125

---

4.5.2	Calculation of residual stresses . . . . .	126
<b>4.6</b>	<b>Discussion and Conclusion . . . . .</b>	<b>129</b>

---

## 4.1 Introduction

The experimental measurement of the relaxation strains by the Incremental Hole Drilling Method (IHDM) is a relatively complex task. This measurement involves material removal and local heating induced by the drilling. The first objective of this chapter is to investigate the effects of the drilling steps on the strain measurements and the consequences of the induced mechanisms on the local properties of the composites. The second objective is to determine, analyse and compare the residual stresses of the manufactured samples.

First, the material used and a complete description of the experimental approach are presented. Then, the raw acquisition data of the relaxation strains are analysed and explained in detail. Infrared (IR) camera was used to measure the thermal fields induced by the drilling in order to understand their contributions to the recorded strains. Modulated Differential Scanning Calorimetry (DSC) and Dynamic Mechanical Analysis (DMA) were performed to study the effects of the drilling on the local chemical and mechanical properties of the composites. In the last section of this chapter, the residual stresses of samples manufactured under different curing conditions are analysed and compared.

## 4.2 Materials manufacturing and experimental methods

### 4.2.1 Manufacturing process

The material studied in this work is a unidirectional carbon/epoxy composite. It is fabricated and provided by the G. MAGYAR group. The samples are composite plates composed of 12 layers with a thickness of approximately 0.33 mm each, i.e. a total thickness of 4 mm approximately. T700SC-24000-50C carbon fibers are used with Araldite 1564 epoxy resin. Aradur 3474 hardner is used as curing agent. The fiber content of the composites is 70% by mass and 60% by volume. The material was mechanically characterized by tensile tests (according to the standard NF EN ISO 527-5 of October 2009 [126]) in a previous work. The longitudinal ( $E_x$ ) and transverse ( $E_y$ ) Young's moduli are equal to 143 GPa and 7 GPa respectively.

The composite plates were fabricated by filament winding process according to the international standard ISO 1268-5 [127]. The process is similar to the filament winding used to make cylindrical parts except that the mould used is specially designed to fabricate plates. The fiber spools are mounted on a reel equipped with a fiber tension regulation system. The carbon fiber pass through a guide and then through the impregnation system.

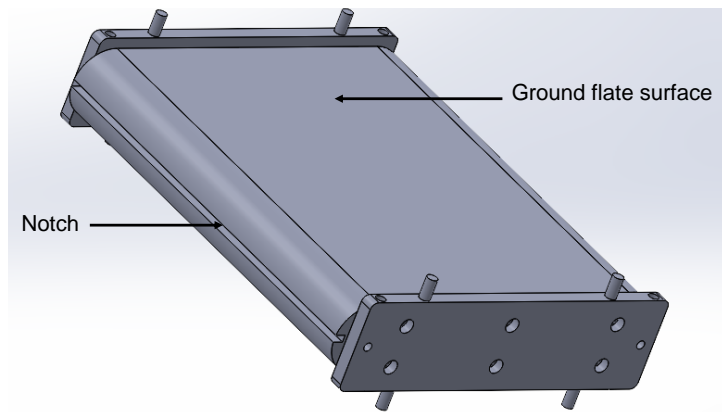


Figure 4.1 – 3D model of the mould used to manufacture composite plates by filament winding method

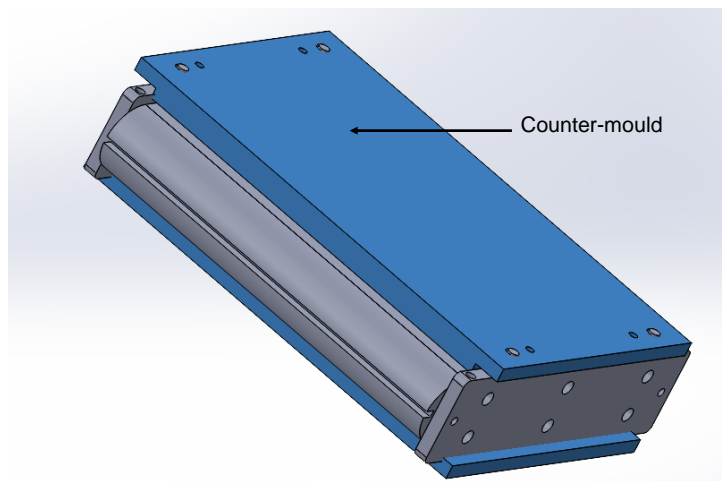


Figure 4.2 – 3D model of the counter-moulds used to fix the thickness of the composite and to ensure the sealing of the mould during curing

The resin-impregnated carbon fibers are then wound onto the mould in successive layers. The tension of the fibers is regulated to 20 N to have a uniform winding. The used mould is presented in Fig. 4.1 and Fig. 4.2. It is composed of two ground flat surfaces on which winding is carried out. The mould is rotated by a winding machine, on the spindle of which the mould is fixed. The mould has notches that allow to cut the plates after manufacture. The filament winding allows to obtain 2 identical plates. A counter-mould (Fig. 4.2) is used to precisely fix the thickness of the composite and to ensure the sealing of the mould during curing thanks to elastomeric seals.

The curing is carried out in a furnace. Three different curing cycles was used (table 4.1) to manufacture the three plates of this study.

Table 4.1 – Curing cycles used to manufacture the composite plates

Plates	curing cycle	cooling
Plate 1	1 hour curing at 80°C then 4 hours at 120°C in a furnace (recommended by the manufacturer)	cooling in the furnace
Plate 2	10 hours curing at 70°C in a furnace	cooling in the furnace
Plate 3	10 hours curing at 70°C in a furnace	ambient air cooling

## 4.2.2 Sample preparation

The in-plane dimensions of the manufactured plates are 300x300 mm. To avoid any influence due to the thickness variation, the samples are cut in such a way as to minimize the thickness variation in the same sample. For this purpose, the thicknesses of the plates are determined by scanning (Fig. 4.3) and the samples are extracted in areas where the gradient of the thickness is low (Fig. C.1a and C.1b). A GOM scanner working with the fringe projection principle is used. The scan head (ATOS core 5M) is equipped with 2 cameras of 5 million pixels each and a fringe projector. (for more details, the reader can refer to reference [128]).

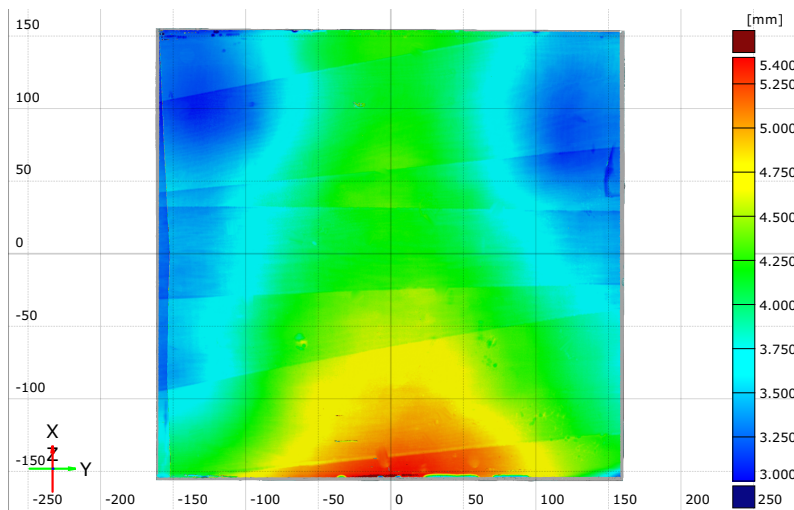


Figure 4.3 – Thickness of plate 3 determined by scanning

## 4.2.3 Experimental methods

The aim, here, is not to present the principle of the IHDM (presented in Chapter 2) but to describe the different steps of the experimental procedure used to measure the relaxation strains. These steps are presented as follow:

- Step 1: an EA-06-062RE-120 strain-gage rosette is bound on the surface of the sample following the method described in subsection 3.4.2 of chapter 3 in order to



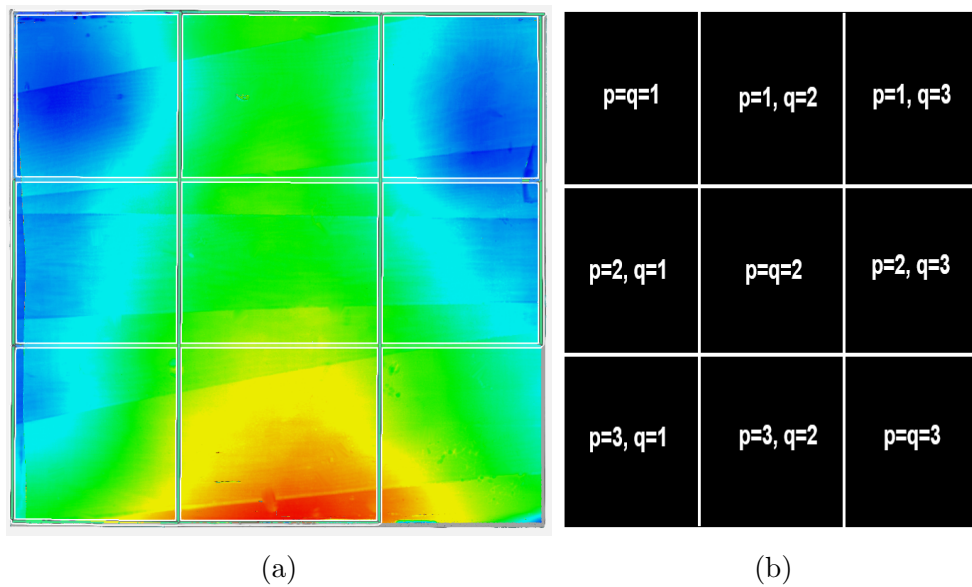


Figure 4.4 – (a) Cut of samples from plate 3 in the areas where the thickness gradient is low, (b) Sample identification method as a matrix. For example, sample 1-3 is the sample for which  $p=1$  and  $q=3$

minimize angular shift of gage 1 with respect to the fibers.

- Step 2: by micro-welding the gages are linked to a quarter-bridge acquisition circuit through a strain gage module.
- Step 3: The sample is fixed on the sample holder and the milling cutter is centered with respect to the strain gage rosette according to the method described in subsection 3.4.4 of chapter 3.
- Step 4: The contact between the milling cutter and the surface of the composite (drilling reference) is detected according to the method described in subsection 3.4.5 of chapter 3.
- Step 5: The drilling parameters are set (total number of increments, depth of increments, spindle rotation and feed speed...). The trajectories of the spindle are programmed and the acquisition is run.

Sicot et al. [30] showed that the optimal rotation and feed speeds for carbon/epoxy composites are 5000 rpm and 0.01 mm/s respectively. In this work, several rotation speeds

were tested. The damage induced on the surface (observed using a high-resolution camera) is considered as quality criteria. It was found, as in reference [30], that 5000 rpm gives the best hole quality. The results are presented in Appendix C.

A complete description of the drilling scheme (the trajectories of the spindle for a complete increment) is important to understand the raw data of the acquisition. The start position of the milling cutter is 1 increment above the drilling reference. The scheme of the first increment is simple: the milling cutter approaches with the considered feed speed (0.01 mm/s), the increment is drilled, the milling cutter gets back to the start position with a speed of 5 mm/s and a 90 seconds relaxation time is considered to allow residual stresses redistribution, thermal effect stabilization and material relaxation (Ghasemi et al. considered 60 seconds of relaxation time in their work [129]). From the second increment, the drilling cycles can be described as follow:

- Rapid approach of the milling cutter: from the start position, the milling cutter descends with a speed of 1 mm/s until it reaches 85% of the current depth of the hole (depth obtained after the previous increment).
- Slow approach of the milling cutter and drilling of the increment: from 85% of the current depth, the feed speed of the milling cutter is slowed down to 0.01 mm/s.
- Drilling step: the increment is drilled with a feed speed of 0.01 mm/s.
- Rapid withdrawal: after the drilling, the milling cutter gets back to the start position with a speed of 5 mm/s.
- Relaxation: a relaxation time of 90 seconds is observed.

The aim of such a programming of the trajectory of the milling cutter is to limit the total duration of the acquisition while maintaining the same drilling conditions for each increment. As presented in Appendix D, the output speed has no influence on the acquisition data. Therefore, it is better to consider a high output speed (5 mm/s here) to limit the duration of the acquisition.

### 4.3. ANALYSIS OF THE RAW ACQUISITION DATA OF RELAXATION STRAINS

Now that the experimental protocol is described, it is important to understand the curves obtained for a typical IHDM result. For this, the relaxation strain acquisition curves are presented and analyzed.

## 4.3 Analysis of the raw acquisition data of relaxation strains

### 4.3.1 Presentation of the raw acquisition data

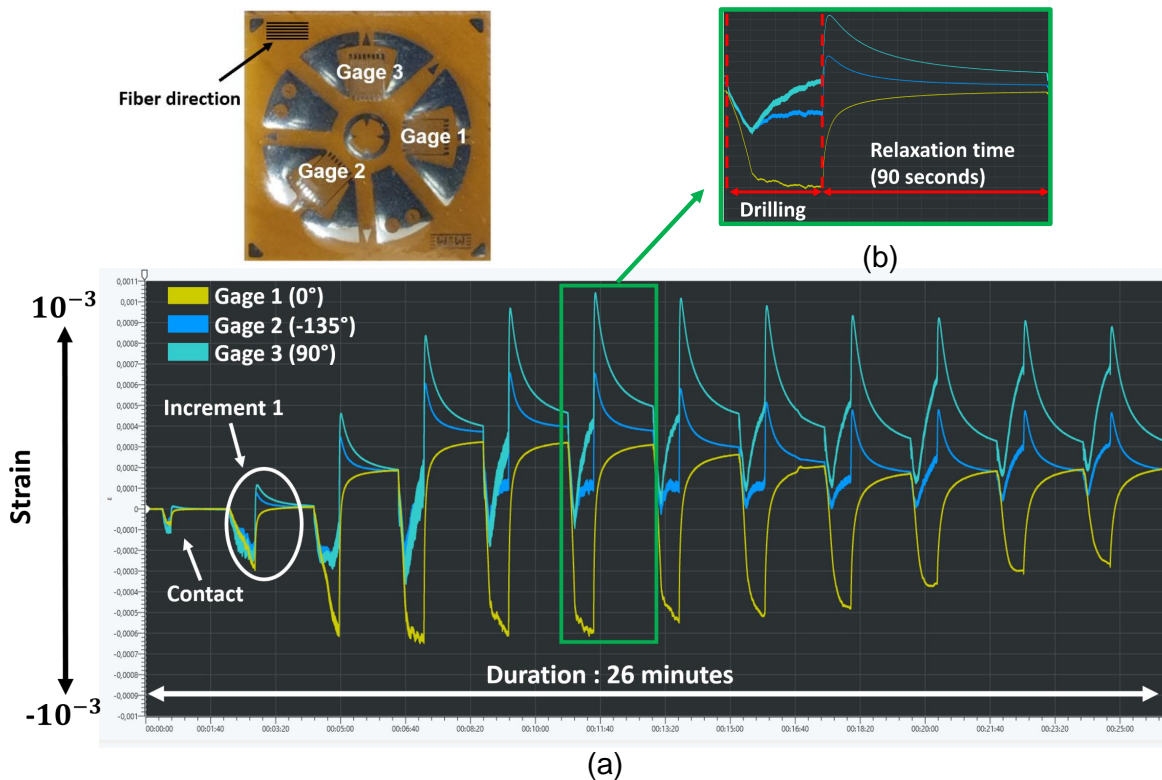


Figure 4.5 – (a) Raw acquisition data obtained for sample 1-3 of plate 3, (b) detail for one increment cycle

Fig. 4.5 presents the raw acquisition data obtained for sample 1-3 of plate 3 (Fig. C.1). These data correspond to the strains measured by the gages of the rosette during the incremental hole drilling process. Gage 1 is oriented in the fiber direction (0 degrees), gage 2 at -135 degrees with respect to the fibers and gage 3 in the direction perpendicular to the fibers (90 degrees). The experimental parameters and conditions are given in table 4.2.

The contact between the material surface and the milling cutter is established after the execution of the first increment in the drilling program. This can be observed on the acquisition data ("contact" in Fig. 4.5a) and is supposed to correspond to the drilling

Table 4.2 – Experimental parameters and conditions of the incremental hole drilling test

Increment depth	Rotation speed	feed speed	Ambient temperature	Ambient humidity
0.33 mm (one increment per pli)	5000 rpm	0.01 mm/s	$22 \pm 2 \text{ }^\circ\text{C}$	$46 \pm 2 \%$

of the rosette and the glue. Each increment cycle is composed of a drilling step and a relaxation step (Fig. 4.5b). The withdrawal of the milling cutter (end of the drilling step) is followed by an abrupt change of slope of curves. The data considered in the IHDM are the strains at the end of the relaxation time. However, during the drilling step, one records strains due to the material removal, to the local heating induced by drilling and to residual stresses. In the next section, an investigation is carried out on the thermal and mechanical effects of the drilling.

### 4.3.2 Thermal and mechanical contributions of drilling on raw acquisition data

Thermal tests are carried out to observe the behaviour of the 3 gages without any mechanical strain induced by material removal. These thermal tests aim to understand the overall thermal behaviour of the gages. Sample 2-3 is considered (see the cut of samples in Fig. C.1b). A heat flow generated by a heat blower is applied to the sample at the rosette location during 210 seconds until the temperature at the gages location reaches  $60^\circ\text{C}$  approximately (temperature measured by IR camera). The result is presented in Fig. 4.6.

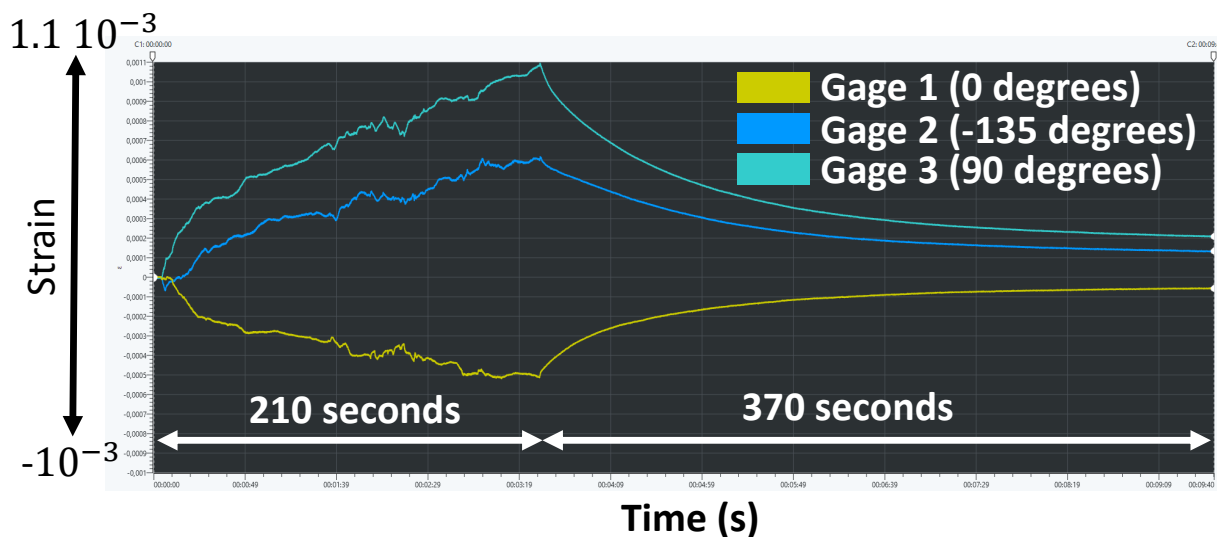


Figure 4.6 – Thermal strains recorded for the composite (sample 2-3) after applying a heat flow at the rosette location

One can clearly see that the strains recorded by gage 1 are negative and those recorded

### 4.3. ANALYSIS OF THE RAW ACQUISITION DATA OF RELAXATION STRAINS

by gage 2 and 3 are positive. In fact, gage 1 is contracted due to the negative thermal expansion coefficient of the carbon fibers in the longitudinal direction. Gage 3 expands due to the positive thermal expansion coefficient of the resin. Gage 2 undergoes both the thermal behaviour of the fibers and the resin. Therefore, the curve recorded by gage 2 is between the curve recorded by gage 1 and gage 3.

To validate the fibers influence, an additional test is performed to decouple the thermal behaviour of the carbon fibers and the epoxy resin. For that, a sample of raw resin is fabricated in the same conditions than the considered composite (plate 3). The same test as above is performed. The heat flow generated by the heat blower is applied to the sample at the rosette location during 120 seconds until the temperature at the gages location reaches  $60^{\circ}C$  approximately. The result is presented in Fig. 4.7.

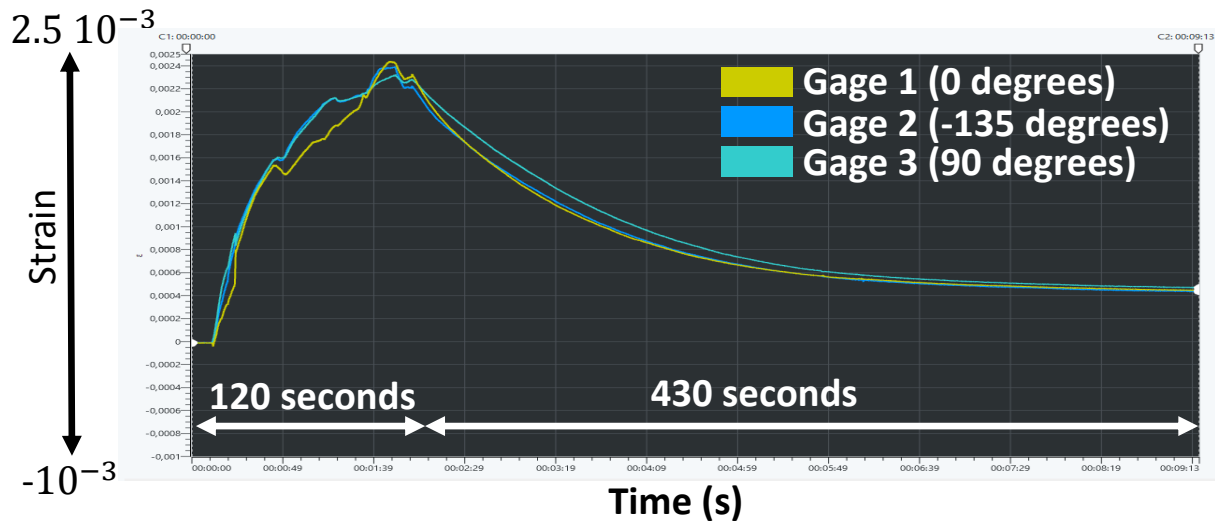


Figure 4.7 – Thermal strains recorded for the resin (plate 3) after applying a heat flow at the rosette location

In the absence of fibers, the strains recorded by the three gages are positive. The responses of the gages are almost simultaneous and the magnitude of these strains are almost equivalent because the thermal behavior of the raw resin is isotropic.

For the IHDM tests, IR camera (ThermaCam SC3000 designed by FLIR) is used to characterize the thermal field during and after the drilling. This allowed to understand the shapes of the acquisition curves, to check that the temperatures at the location of the gages are within the range of use of the strain gage adhesive (short term temperature range  $-185^{\circ}$  to  $95^{\circ}C$  [125]) and to verify the adequacy of the chosen relaxation time. The thermal tests were performed in an ambient temperature of  $22 \pm 2^{\circ}C$  degrees, without convective flux and isolated from any light source. Fig 4.8 shows the thermal field evolution during a complete cycle of increment (Fig. 4.8e) drilling for sample 1-3 of plate 3.

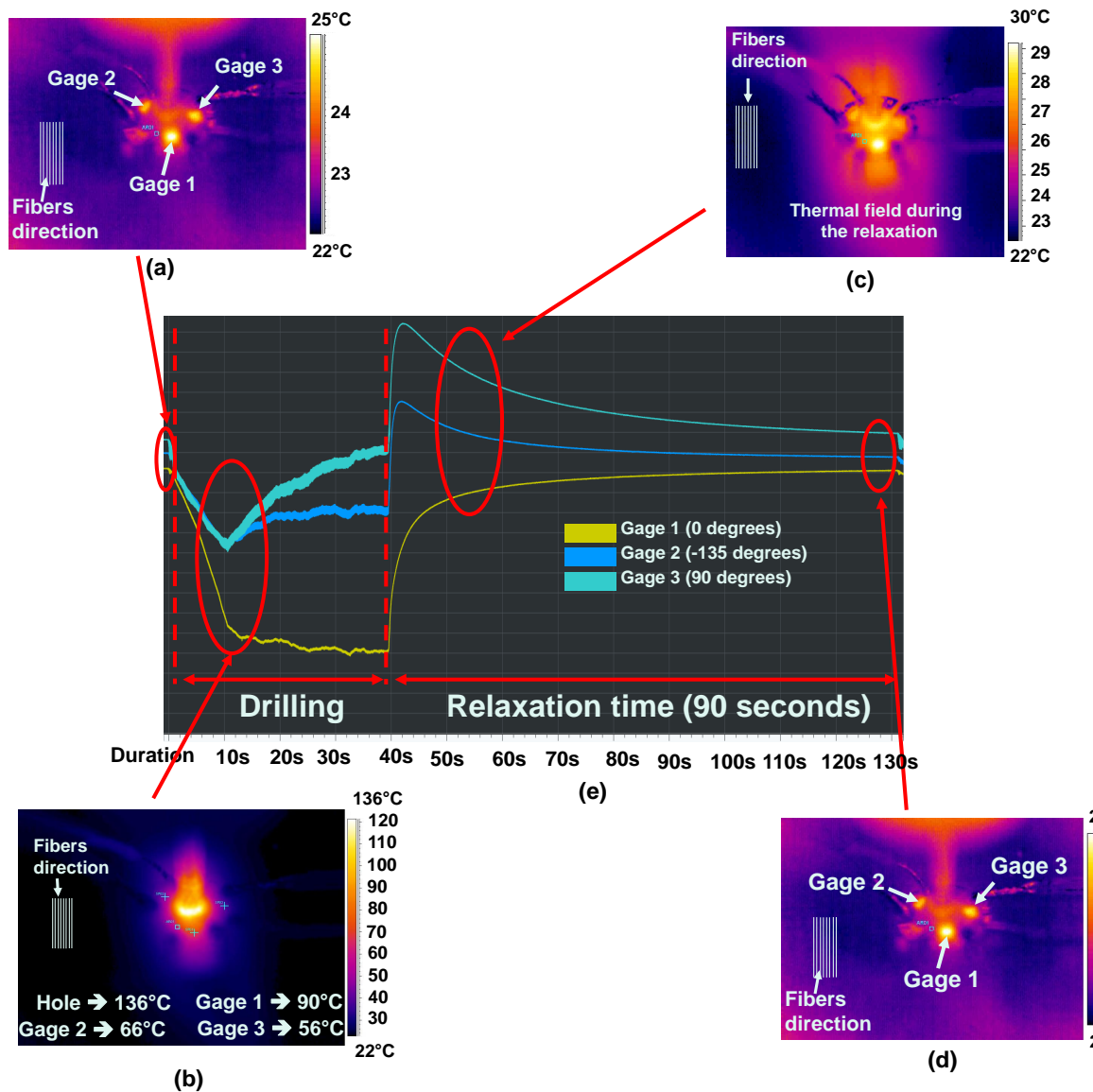


Figure 4.8 – Variation of the thermal field (measured using an IR camera) during an increment cycle: thermal field (a) at the end of the previous increment, (b) during the drilling step, (c) during the relaxation and (d) at the end of the relaxation time

The results obtained show that during the drilling, temperatures reach  $56 \pm 2^\circ\text{C}$  at gage 3 location,  $66 \pm 2^\circ\text{C}$  at gage 2 location,  $90 \pm 2^\circ\text{C}$  at gage 1 location and up to  $136 \pm 2^\circ\text{C}$  in the hole (Fig. 4.8b). Fig 4.8a corresponds to the thermal field at the end of the relaxation time of the previous increment, just before the current increment. Fig 4.8b corresponds to the maximal temperature reached during the drilling of the increment. Fig 4.8c shows the temperature during the relaxation time, after the withdrawal of the milling cutter. This thermal field is elliptical due to the thermal conductivity of the fibers. Fig 4.8d corresponds to the thermal field at the end of the current relaxation time.

For the three gages, the variations of the temperature during the IHDM were measured

and plotted as function of time for two points: one point at the gage location and the other between the hole and the gage (intermediate point, see Fig. 4.9). The points are manually selected on the recorded frames using ThermaCAM Researcher Professional 2.8 SR-2 software. This limited the repeatability from a selection to another.

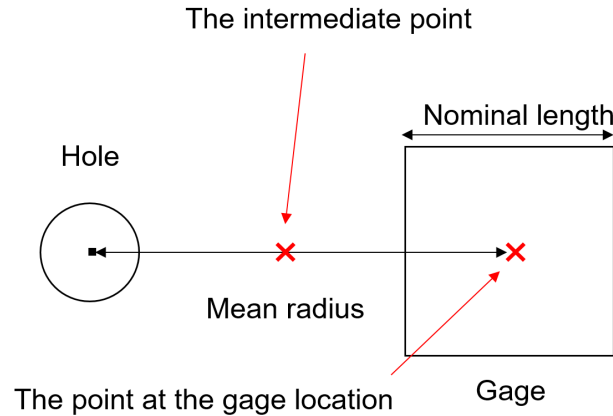
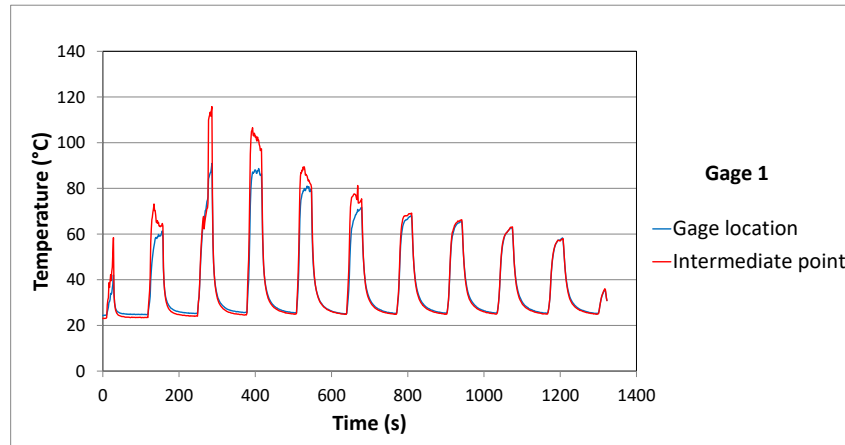


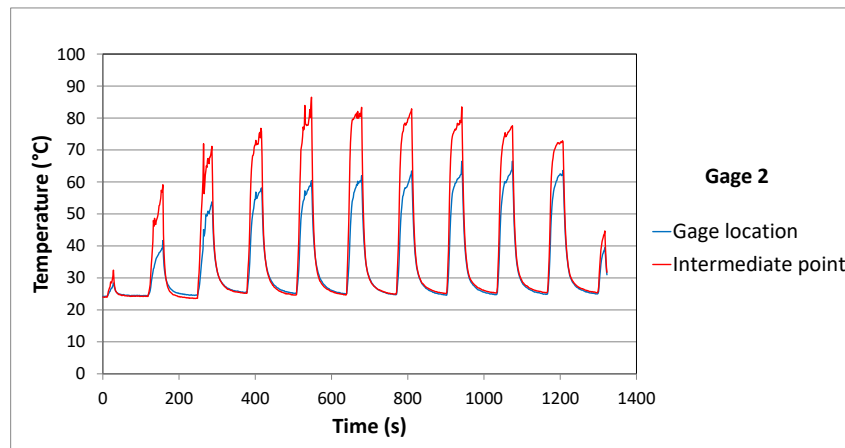
Figure 4.9 – Locations of the selected points to plot the variation of the temperature throughout the IHDM

The results are given in Fig. 4.10a, 4.10b and 4.10c. As expected, the temperatures at the intermediate point are higher than those of the point at the gage location. The closer the measuring point is to the contact area (hole location), the higher the temperature. One can observe that for a given increment, the difference of temperature between the gage location and the location of the intermediate point depends on the considered gage. The analyse of this difference from a gage to another is complicated because of the difficulty in selecting the points with good repeatability. However, it is relevant to analyse the variation of this difference (the difference of temperature between the gage location and the location of the intermediate point) as function of time for a given gage. The difference is important for the first increments and decreases with depth. For the last increments the temperature at the hole and the gage location are close. This is due to the fact that for the last increments, the drilling area, where the highest temperature is generated, is far from the surface. Thus, temperature tends to become uniform on the surface. This also explains why the temperatures measured for the last increments are lower. Consequently, the shapes of the raw acquisition data of the relaxation strains are expected to be different for the first and the last increments.

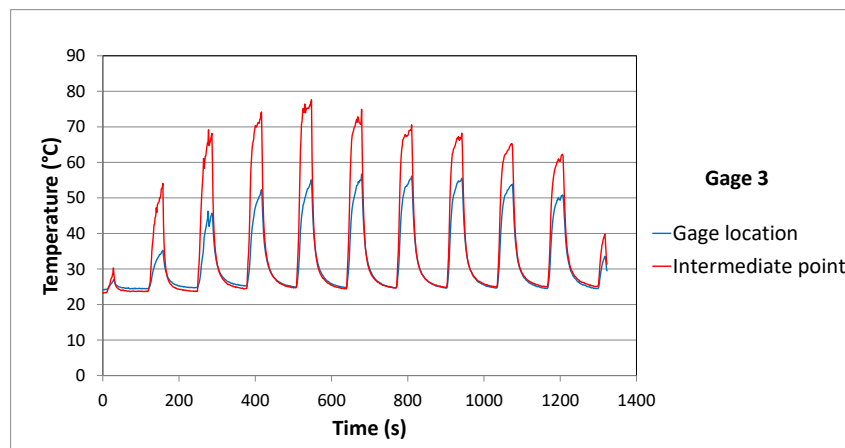
Each increment cycle is composed of a drilling step and a relaxation step. During the drilling, mechanical and thermal strains occur at the same time. Note that the mechanical strains are composed of the strains induced by the milling cutter and the ones induced by the residual stresses. Strains are competing for the gage 2 (oriented at -135 degrees with respect to the fibers) and the gage 3 (oriented in the direction perpendicular to the fibers) and additive for the gage 1 (oriented in the fibers direction). In fact, as explained above,



(a)



(b)



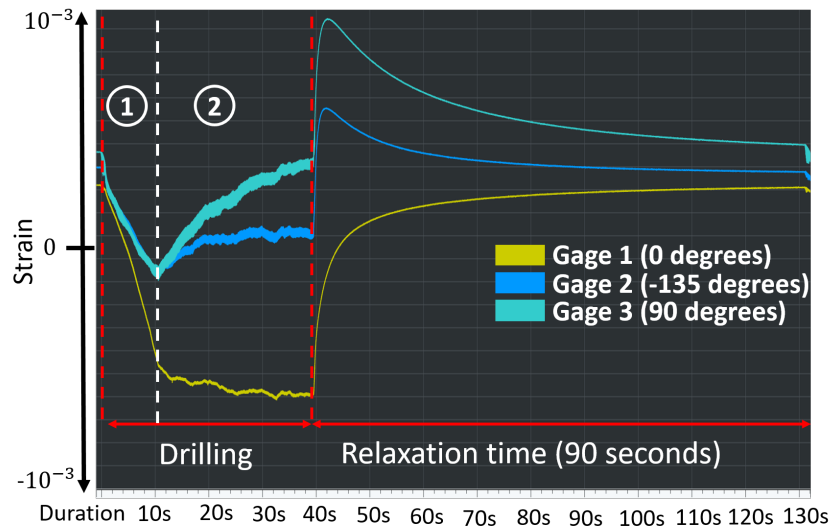
(c)

Figure 4.10 – Variation of the temperature throughout the IHDM at the gage and the intermediate point locations: (a) for gage1, (b) for gage 2 and (c) for gage 3

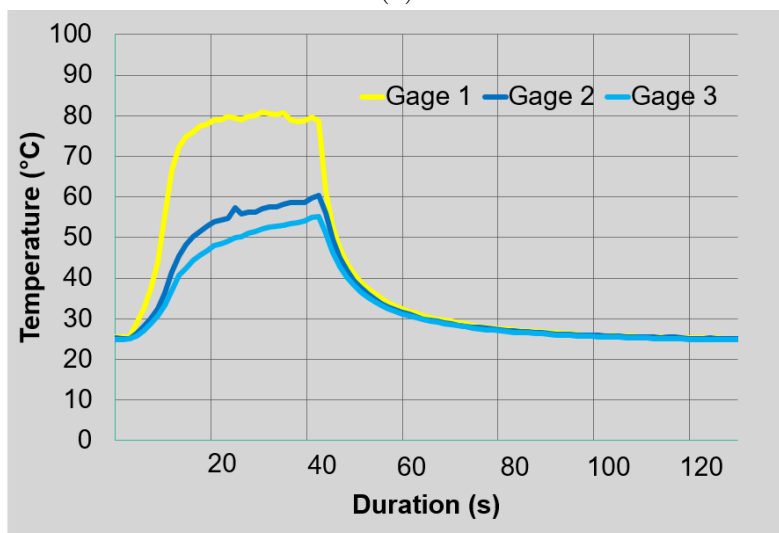
the heat causes negative strains in the fibers direction and positive strains in the resin direction. In the other hand, material removal causes negative strains for all gages. To better understand, the drilling step is divided into 2 steps (Fig. 4.11a). The corresponding



variations of temperatures are presented in Fig. 4.11b.



(a)



(b)

Figure 4.11 – (a) Different steps of an increment cycle, (b) Variation of the temperatures during the increment cycle

In the first step, the strains recorded by all the gages are negative (the gages are contracted). The mechanical compressive strains induced by the milling cutter are the most influential. In the second step, the temperature reaches values high enough for thermal strains to prevail over mechanical strains for gage 2 and 3. This is shown by the change in the direction of the curves for these gages. Curves become increasing as the gages 2 and 3 expand. The increase in the gage 2 curve is less important because it records part of the contraction in the direction of the fibers. For gage 1, the strains keep decreasing, during the drilling step, since the thermal and mechanical strains are both compressive. This is the reason why the peaks recorded by the gage 1 are the deepest for all the increments.

Once the increment is drilled, the milling cutter is withdrawn and the relaxation step takes place. In this step, the thermal strains induced by the material removal relax as the temperature decreases. The curve recorded by the gage 1 varies until reaching an asymptote at the end of relaxation. For the gage 2 and 3, as soon as the drilling is stopped, there are jumps of the curves. Only the thermal strains and those due to residual stresses remain. The jump in the curves is explained by the difference in sign between the thermal strains and the strains induced by the removal of material (which become zero). The asymptotes of the curves correspond to the relaxation strain considered in the calculation of the residual stresses. The difference between the relaxation strains from one increment to the next is due to the residual stresses.

In Fig. 4.12, one can observe that the drilling step and the relaxation step are not identical for all the increments.

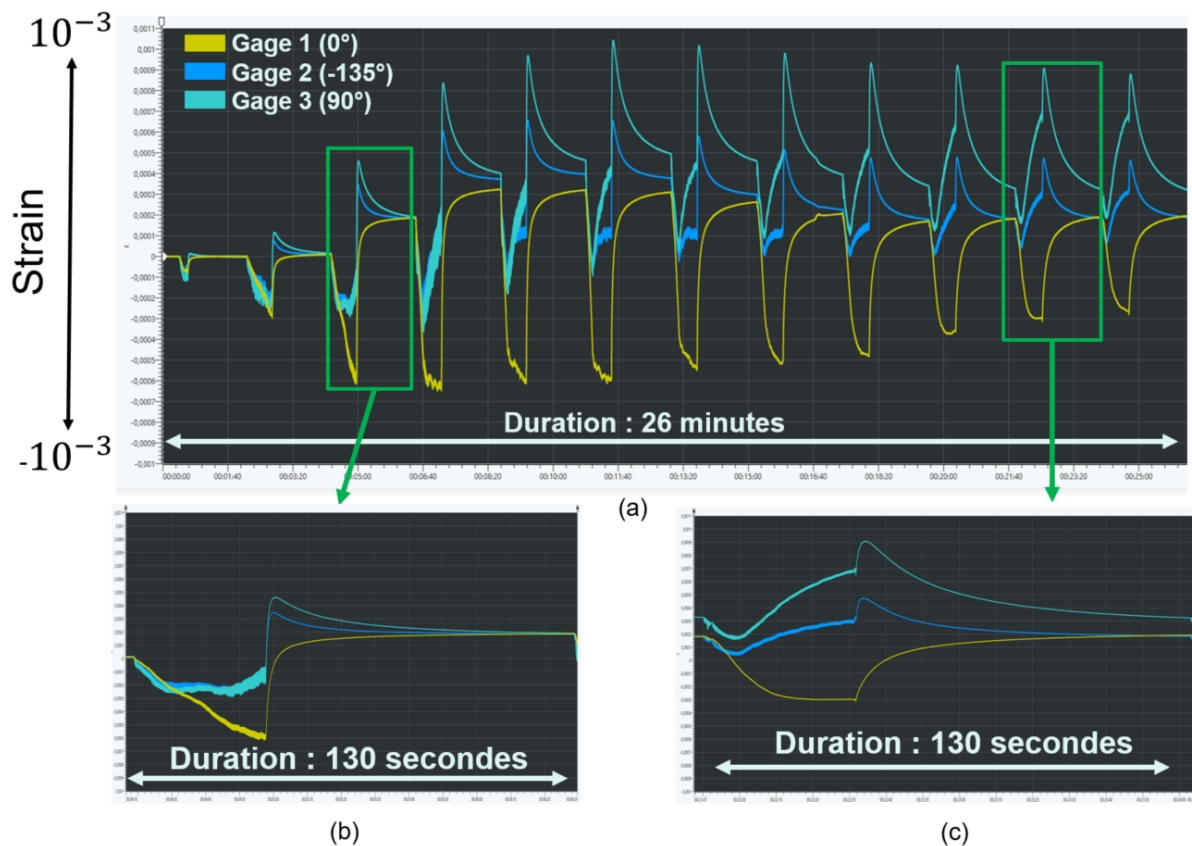


Figure 4.12 – Differences between the first and last increments: (a) Whole test data, example among the (b) first and (b) last increments

4 assumptions are proposed to explain these differences:

- For the first increments, the curves reach their asymptotes at the end of the relaxation time while they do not reach their asymptotes for the last increments for the same relaxation time (Fig. 4.12a). In fact, the deeper the hole, the slower the

cooling. This is shown in Fig. 4.12c: the relaxation time is not long enough to allow a total stabilization of the temperature for the last increments. For the first increments, the cooling is faster because convection is more important. Thus, the relaxation time should be adaptive (longer for the last increments) and not constant to allow cooling of the composite for all increments.

- For gage 2 and 3, the direction of variation of the curves in the second step of the drilling (Fig. 4.11a) is positive and increasingly accentuated (tending to be vertical, Fig. 4.12b and 4.12c). Since the drilling-induced mechanical strains (negative) and the thermal strains (positive) are competing for these gages, if the direction of variation of the curves is positive, it means that the thermal strains are greater than the mechanical strains. The fact that the deeper the hole the steeper the direction of variation of the curves means that the thermal strains are increasingly superior to drilling-induced mechanical strains with depth. Indeed, when the hole is deep, the gages are less sensitive to the mechanical strains and the cooling is slower. Thus, the effect of the thermal strains are increasingly greater than the effect of the mechanical strain.
- For gage 1, the peaks of strains (maximum recorded by gage 1 during the drilling step) are low for the first and last increments compared to the intermediate increments. This variations are directly linked to temperature peaks (Fig. 4.10) which have a similar variation. The temperature increases up to a certain depth from which it decreases.
- For the last increments, the relaxation strains (strains recorded at the end of the relaxation time) are almost the same. In fact, the relaxation strains stabilize and become constant (Fig. 4.12a). This is due to the fact that the gages are less and less sensitive to deep stress (Saint Venant principle).

The results obtained from the thermal tests show that the influence of the heat is important in the drilling step of the IHDM. One can wonder about the reversible and non-reversible effects of such high temperatures on the local resin properties.

## 4.4 Thermal effects of the drilling on the local chemical and mechanical properties of the raw resin

### 4.4.1 Differential Scanning Calorimetry (DSC) tests

#### 4.4.1 - a Principle of the DSC

The DSC is a thermal analysis technique used to determine the thermal transitions of polymers. It can be used to determine quantities such as the glass transition temperature, the melting temperature or the enthalpy of the reaction. The DSC consists of heating the sample placed in a metal pan and a reference (that can be an empty pan) and measure the heat flow necessary to maintain the sample at nearly the same temperature than the reference during the experiment. The amount of heat flow depends on whether the reaction is exothermic or endothermic. The obtained result is the total heat flow as function of the temperature. The total heat flow is composed of reversible heat flow (corresponding to phenomena such as glass transition, melting) and non-reversible heat flow (corresponding to phenomena such as cross-linking, decomposition). Conventional DSC allow to obtain only the total heat flow. Modulated DSC test is required to dissociate the reversible and the non-reversible heat flow. In modulated DSC, a particular heating profile is used. The heating ramps are not linear (as for conventional DSC) but sinusoidal. Thus, the temperature increases or decreases by oscillating around an average value that corresponds to the conventional DSC temperature.

#### 4.4.1 - b Sample preparation and experimental parameters

To obtain precise results, the tests are carried out on raw resin plates manufactured in the same conditions than the composite plates. The processing conditions are recalled below.

- Plate 1: 1 hour curing at 80°C then 4 hours at 120°C in a furnace. The plate is cooled in the furnace.
- Plate 2: 10 hours curing at 70°C in a furnace. The plate is cooled in the furnace
- Plate 3: 10 hours curing at 70°C in a furnace. The plate is cooled in ambient air ( $22 \pm 2^\circ\text{C}$ )

For each plate, modulated DSC are carried out on cold-extracted sample and sample extracted by drilling. The Discovery DSC 25 instrument designed by TA instruments is used with Trios software version 5.1.0.46403. The aim is to compare the results of these samples to assess the influence of the drilling on the glass transition temperature and the cross-linking of the resin. The cold-extracted sample is obtained using a manual deburrer.

On the other hand, IHDM tests are performed on the resin plate, and the removed material is considered as the sample extracted by drilling. Only a few milligrams of material is required. The experimental parameters of the modulated DSC are summarized in table 4.3.

Table 4.3 – Experimental parameters for Modulated DSC

Ramp	Maximal temperature	Modulate Temperature
$3^{\circ}C/min$	$250^{\circ}C$	$1^{\circ}C$ for 60 seconds

#### 4.4.1 - c Results and discussion

The Results obtained for the cold-extracted raw resin of plate 1, 2 and 3 are presented in Fig. 4.13a, 4.13c and 4.13e respectively. The Fig. 4.13b, 4.13d and 4.13f correspond to the results of the raw resin extracted by drilling on plate 1, 2 and 3 respectively.

By comparing the results of plate 1, 2 and 3 whether for the cold-extracted resin (Fig. 4.13a, 4.13c and 4.13e) or for the resin extracted by drilling (Fig. 4.13b, 4.13d and 4.13f), one observe that the enthalpy obtained for plate 3 is greater than that of plate 2 which is greater than that of plate 1. This means that plate 1 has the highest degree of cure and plate 3 the lowest. This is consistent with the cure cycles of the plates. In fact, plate 1 undergoes the highest temperature during curing (1 hour at  $80^{\circ}C$  then 4 hours at  $120^{\circ}C$ ). Plate 2 and 3 are cured at the same temperature, during the same duration (10 hours at  $70^{\circ}C$ ). However, plate 2 is cooled in the furnace, which allowed it to have a higher degree of cure than plate 3 which is cooled in ambient air. For the same reasons, one can observe that the glass transition temperature of plate 1 ( $101^{\circ}C$  for the cold-extracted sample and  $116^{\circ}C$  for the sample extracted by drilling) is higher than that of plate 2 ( $85^{\circ}C$  for the cold-extracted sample and  $97^{\circ}C$  for the sample extracted by drilling) which is higher than that of plate 3 ( $79^{\circ}C$  for the cold-extracted sample and  $86^{\circ}C$  for the sample extracted by drilling).

For all the plates, the enthalpy of the reaction is greater for the cold-extracted resin compared to that extracted by drilling. In addition, the glass transition temperature is higher for the resin extracted by drilling. From these observations, one can conclude that the drilling causes a progression of the cure reaction and an increase in the glass transition temperature of the resin at the hole location. These modifications of the local resin properties are believed to influence the local residual stresses. However, further investigations are needed to assess how influent these property modifications are regarding the local residual stresses.

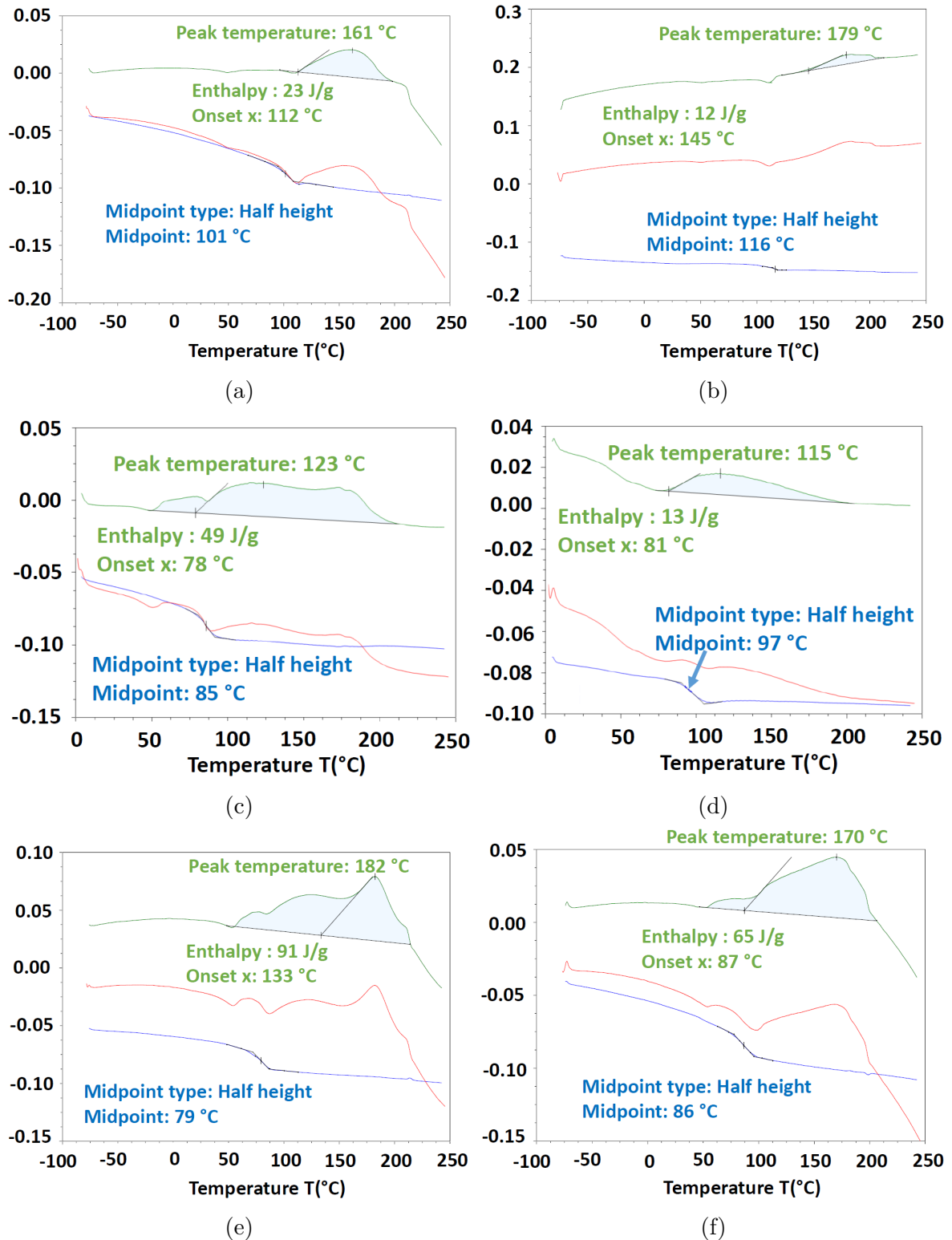


Figure 4.13 – Modulates DSC tests results: cold extracted samples for (a) plate 1, (c) plate 2 and (e) plate 3. Samples extracted by drilling for (b) plate 1, (b) plate 2 and (f) plate 3. "Enthalpy" corresponds to the enthalpy of the reaction and "Midpoint" to the glass transition temperature.

To better understand the effect of the drilling on the local mechanical properties of the material, Dynamique Mechanical Analysis tests are carried out.

## 4.4.2 Dynamique Mechanical Analysis (DMA) tests

### 4.4.2 - a Principle of the DMA

DMA is a thermal analysis test that is used to characterize the viscoelastic properties of materials such as composites. The sample is placed in an environmental chamber which allows to control the temperature. Mechanical tests such as tensile, flexure or shear can be carried out in a wide temperature range (from  $-20$  to  $250^{\circ}\text{C}$  for exemple). These tests are dynamic, so the stress or displacement applied to the sample is sinusoidal. The results depend on the frequency considered for the test. DMA allows to determine quantities such as the storage modulus, the loss modulus and the damping (tangent of the phase angle) as a function of the temperature. The storage modulus corresponds to the reversible energy stored (elastic) during the test. The loss modulus corresponds to the dissipated energy (viscous). The damping (also called loss factor) is obtained by dividing the loss modulus by the storage modulus.

### 4.4.2 - b Sample preparation and experimental parameters

Dual cantilever DMA are performed on samples cut from plate 1, 2 and 3. DMA Q800 V21.1 Build 51 instrument is used. The dimensions of each sample are: length  $\approx 60$  mm, width  $\approx 12$  mm and thickness  $\approx 3.96$  (Fig. 4.14). A diamond saw with lubrication and water cooling is used to cut the samples. The experimental parameters of the tests are given in table 4.4.

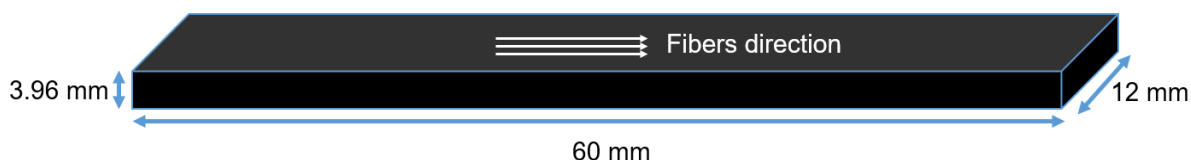


Figure 4.14 – DMA sample dimensions

Table 4.4 – Experimental parameters and conditions for DMA

Temperature range	Ramp	Oscillation amplitude	frequency
$-20^{\circ}\text{C}$ to $250^{\circ}\text{C}$	$3^{\circ}\text{C}/\text{min}$	$20\mu\text{m}$	1 Hz

#### 4.4.2 - c Results and discussion

For the plate 1, 2 and 3 (Fig. 4.15a, 4.15b and 4.15c) the standard results consist of three curves which give the evolution of the storage modulus, the loss modulus and the damping ( $\tan \delta$ , ratio of the two previous moduli) as a function of the temperature.

The first quantity characterises the elastic property of the material (in this case the flexural modulus), the next two characterise the viscous properties. During the transition from the glassy state of the material to the rubbery state, a characteristic temperature is determined for each curve. For the storage modulus this temperature corresponds to the beginning of the drop in elastic properties and is usually compared to the glass transition temperature given by the DSC test. For the loss modulus the temperature indicates the beginning of mobility of the macro molecular chains of the polymer. The temperature calculated for the damping corresponds to the maximum viscous properties of the material.

These results confirm the DSC results: due to the curing cycle, the plate 1 has a higher degree of cure than plate 2 and 3. For the storage modulus the associated characteristic temperatures are 111 °C, 96 °C and 92 °C for plate 1, 2 and 3 respectively. For these temperature values the storage modulus has lost about 50% of its initial value. The temperatures associated with the onset of mobility of the epoxy matrix chains (loss modulus) and the maximum  $\tan \delta$  are 115 °C/122 °C, 100 °C/105 °C and 96 °C/102 °C respectively for plate 1, 2 and 3. The maximum values of  $\tan \delta$  are respectively 0.64, 0.76 and 0.81 for plate 1, 2 and 3 (average over 2 samples). The viscous effects are therefore more important for the plate 3, reflecting a lower degree of cure.

The DSC and DMA tests show the significant influence of temperature on the elastic and viscous properties of the epoxy matrix and this for temperature values corresponding to those obtained during drilling (from 56 to 90°C at the location of the gages and up to 136°C at the hole location). One can legitimately wonder about the influence of the temperature-dependent viscoelastic properties of the epoxy on the determination of residual stresses in the composite. Remember that the relaxation strains (used to calculate the residual stresses) are measured after a relaxation time when the composite cools down. However, it is believed that mechanisms induced by the drilling, such as cross-linking (DSC results) or macro-molecular rearrangement of the resin, have an influence on the storage modulus obtained after the relaxation time. The equilibrium reached after each drilling is different not only because of the residual stresses but also because of the effects of the drilling on the local mechanical properties. One can therefore wonder about the accuracy of the calibration coefficients since the effects of these drilling-induced mechanisms are not taken into account in the finite element simulations used to calculate them (constant mechanical properties are considered). The influence of these complex mechanisms on the measured residual stresses is difficult to assess.



4.4. THERMAL EFFECTS OF THE DRILLING ON THE LOCAL CHEMICAL AND MECHANICAL PROPERTIES OF THE RAW RESIN

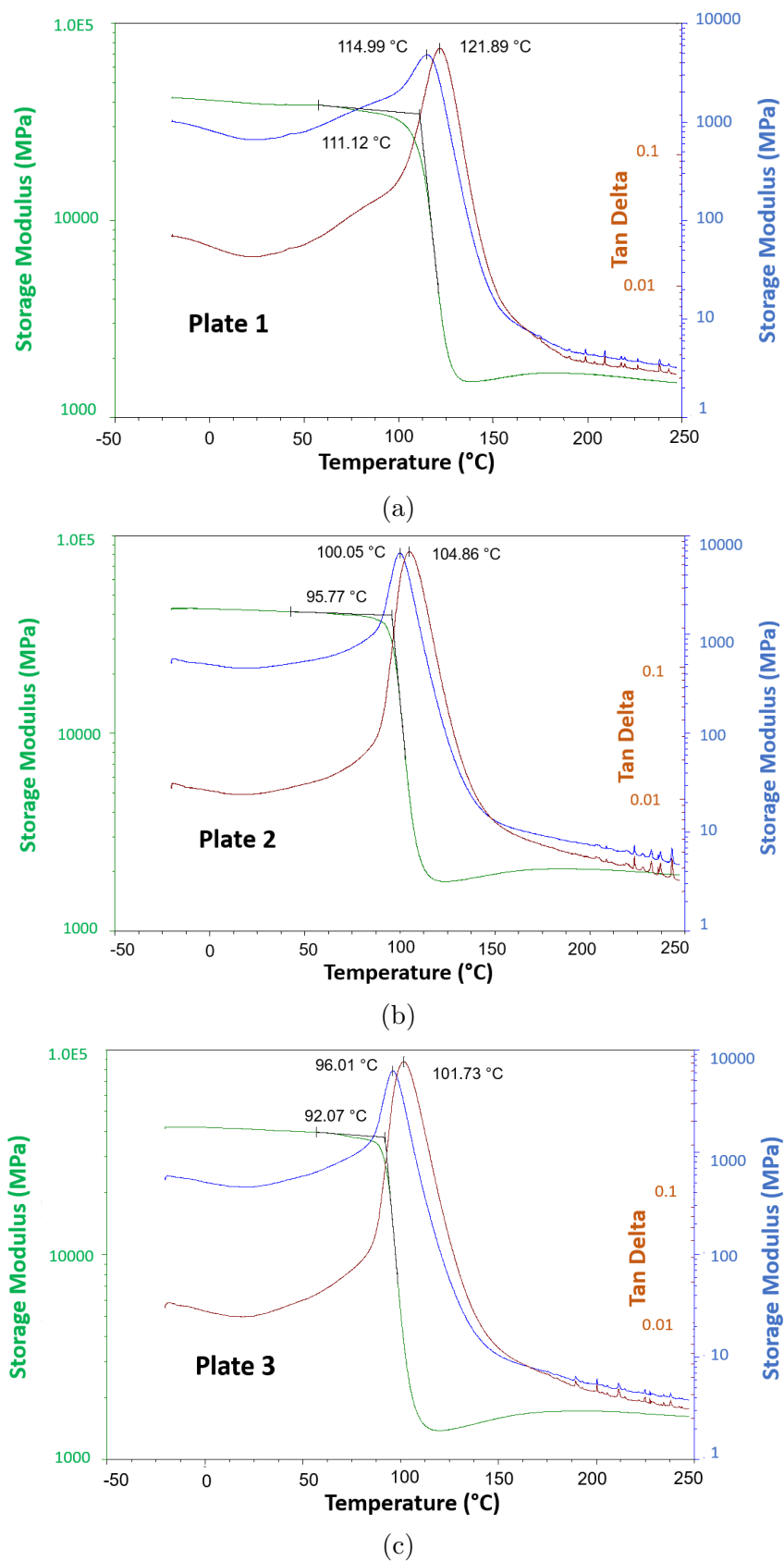


Figure 4.15 – DMA results for (a) plate 1, (b) plate 2 and (c) plate 3

## 4.5 Determination of the residual stress profile

### 4.5.1 Measurement of relaxation strains

Relaxation strains are measured at the end of the relaxation time (Fig. 4.16). The aim is to allow strains to stabilize after a local redistribution of residual stresses. To determine the strain of a given gage, the data acquired during the 4 last seconds of the relaxation time are averaged.

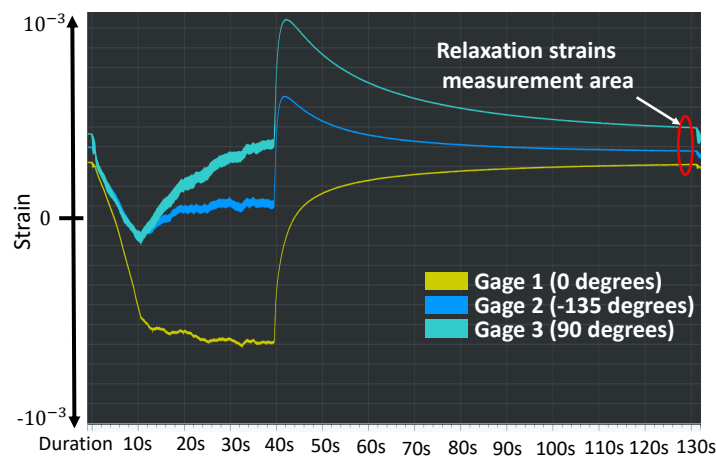
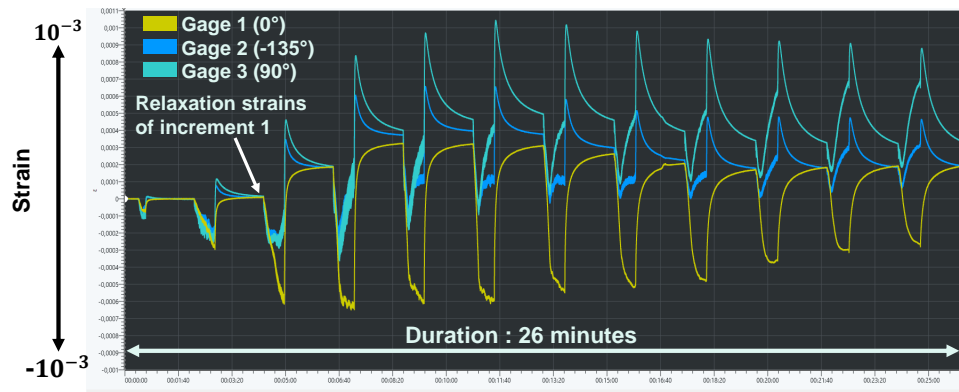


Figure 4.16 – Measuring area for relaxation strains

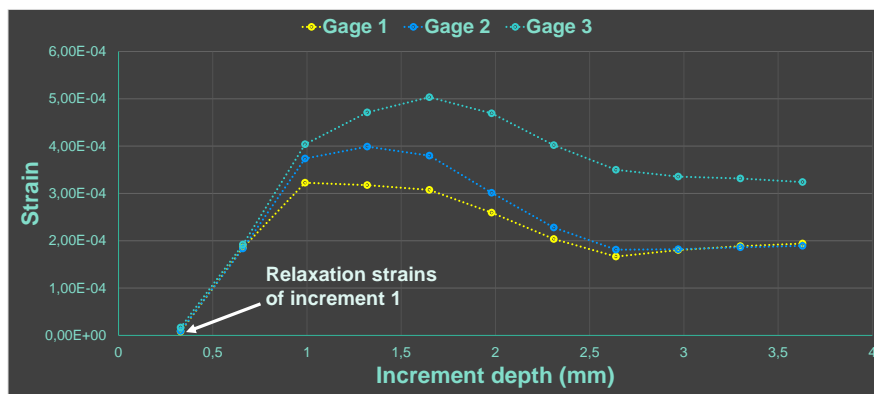
Fig. 4.17a shows a typical raw acquisition data of the IHDM (sample 2-3 of plate 3) and Fig. 4.17b corresponds to the post-processed relaxation strain curves.

In this work, 1 increment per ply is considered for the IHDM. Thus, the depth of an increment corresponds to 0.33 mm approximately. In fact, small increment depths are interesting near the interfaces of the layers with different orientations (in cross-ply laminates for example). Since the material studied here is a unidirectional composite, there is no need for a refined increment depth. In addition, as explained in the next section (4.5.2), a small increment depth can lead to instability in the calculation of residual stresses.

The relaxation strains obtained for plate 1, 2 and 3 are presented in Fig.4.18. Means and dispersions are determined from 3 tests. The strains of all gages are positive which means that residual stresses tend to reduce the diameter of the drilled hole. As expected, the strains in the fiber direction (Gage 1, Fig.4.18a) are smaller than those in the matrix direction (Gage 3, Fig.4.18c). The strains recorded by gage 2 is between the two. The results show a larger dispersion in the fiber direction. The composite samples were manufactured under semi-industrial conditions by filament winding using a flat mould. Thus,



(a)



(b)

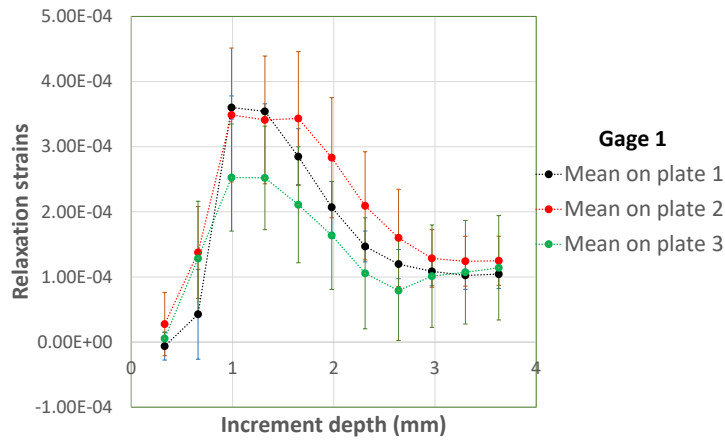
Figure 4.17 – Typical relaxation strains measurement curves: (a) raw acquisition data, (b) strains at the end of the relaxation time (strains used to calculate the residual stresses)

it is believed that the dispersions in the direction of the fibers are due to local variations in fiber alignment and content. The results also show that the strains tend towards an asymptote from a certain depth. This is due to a loss of sensitivity of the gages when the hole reaches a certain depth (Principle of Saint Venant).

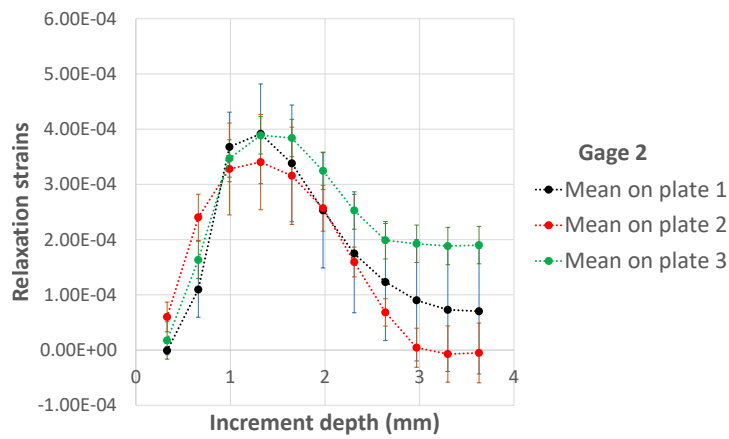
### 4.5.2 Calculation of residual stresses

The relaxation strains presented in the previous section and the calibration coefficients presented in section 2.4.2 - b of Chapter 2 (and available in appendix E) are used to calculate the residual stresses in the plates. The results are presented in Fig. 4.19.

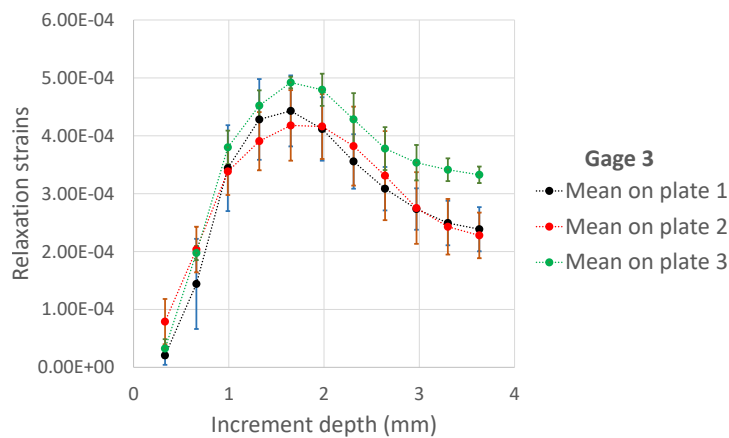
Here, the calculation of the residual stresses is limited to a hole depth of 0.8 mm because the results become unstable above this depth. This is caused by the fact that the predominant calibration coefficients in the residual stresses calculation (those of the diagonal) are lower and lower with depth. From a certain depth (0.99 mm here, which corresponds to the third increment), the inverse of these calibration coefficients becomes large enough to generate instability in the calculation. This is one of the reasons why



(a)



(b)

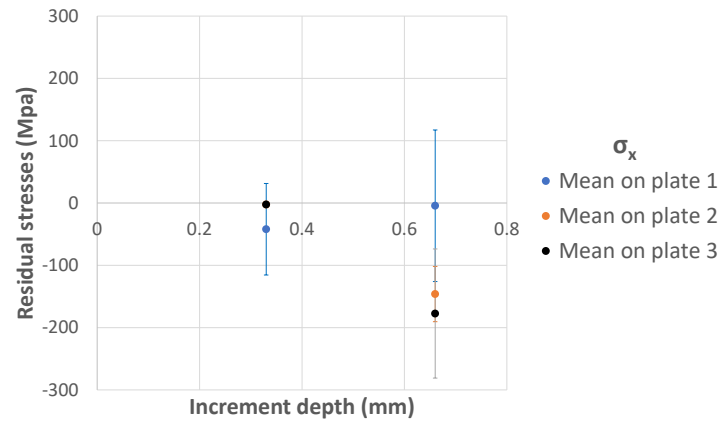


(c)

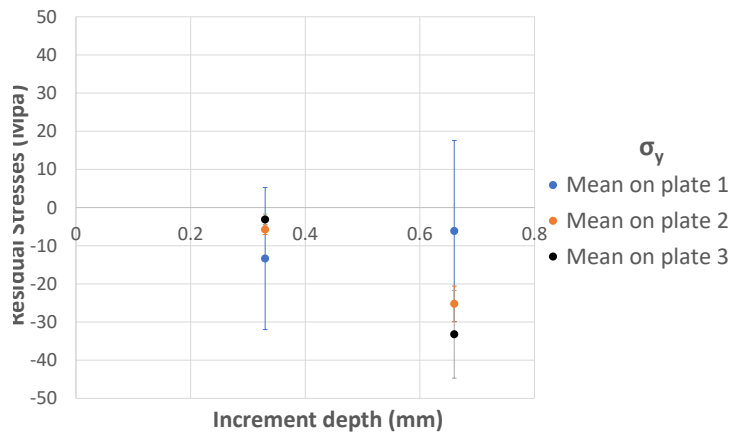
Figure 4.18 – Relaxation strains measured for the three plates (means and dispersions are determined from 3 tests): results obtained for (a) gage 1, (b) gage 2 and (c) gage 3

the IHDM is not valid for deep measurement. The onset of the instability depend on the material properties and on the increment depth chosen. As shown by Zuccarello [121], small increment depth leads to larger instability on residual stress calculation. In fact,

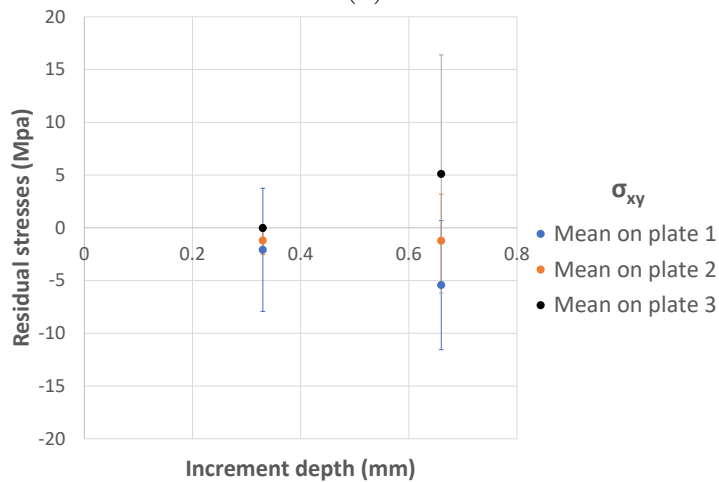
#### 4.5. DETERMINATION OF THE RESIDUAL STRESS PROFILE



(a)



(b)



(c)

Figure 4.19 – Residual stresses determined for the three plates: (a)  $\sigma_x$  ( $\sigma_x$  of plate 2 is hidden by that of plate 3 at the first increment), (b)  $\sigma_y$  and (c)  $\sigma_{xy}$ .

the equations used to calculate the residual stresses are cumulative (the residual stresses of a given increment is calculated using the residual stresses of the previous increments). Thus, the lower the increment depth, the more calculation steps there will be, the more

errors will accumulate and the more unstable the calculation will be.

One can observe that the residual stresses  $\sigma_x$  (in the fiber direction, Fig.4.19a) and  $\sigma_y$  (in the transverse direction, Fig.4.19b) are lower for plate 1 (manufactured according to the manufacturer's recommended cycle). Those of plate 3 are slightly higher than those of plate 2. As expected for unidirectional composite laminates, the residual stresses  $\sigma_{xy}$  is very low for the 3 plates. The results show that, for all the plates, the residual stresses in the direction of the fibers ( $\sigma_x$ ) are higher than those in the transverse direction ( $\sigma_y$ ). The results obtained for plate 1 may seem difficult to analyze since it undergoes the highest temperatures. However, this plate experience a second dwell temperature higher than its first glass transition temperature, which can allow the residual stresses to relax while maintaining a high degree of cure. The difference between the results of plate 2 and 3 can be explained by the fact that plate 3 is cooled in ambient air. This rapid cooling generates higher residual stresses.

## 4.6 Discussion and Conclusion

The analysis of the raw acquisition data of the relaxation strains showed two distinct areas for all the increments: one corresponding to drilling step and the other to the relaxation step. During the drilling steps, thermal and mechanical strains (due to the material removal and residual stresses) occur at the same time. IR camera measurements showed that temperature reaches up to  $136 \pm 2^\circ C$  at the hole location during the drilling. The mechanical strains due to the material removal and the thermal once are all negative for gage 1 which is oriented in the fiber direction (this is due to the negative longitudinal thermal expansion coefficient of carbon fibers) whereas they are of opposite sign for gage 2 (oriented at -135 degrees with respect to the fibers) and gage 3 (perpendicular to the fibers). This difference of sign explains the jumps recorded for gage 2 and 3 at the onset of the relaxation step. The comparison between the temperature evolution and the strains of the first and last increments showed that the considered relaxation time (90 seconds) is suitable for the first increments but not long enough to allow stabilisation of the strains for the last increments. Modulated Differential Scanning Calorimetry (DSC) and Dynamique Mechanical Analysis (DMA) tests showed that the drilling causes an evolution of the cross-linking, an increase of the glass transition temperature and a drop of the storage modulus. These drilling-induced mechanisms are believed to affect the local residual stresses. However, further investigations are needed to fully understand their effects.

The residual stresses were determined for three composite plates manufactured in differ-

ent curing conditions. The results showed a low level of residual stresses for plate 1 which underwent two dwell temperatures during curing cycle. The residual stresses are believed to relax during the second cure. Higher residual stresses were obtained for plate 3. This can be explained by the rapid cooling of plate 3, which generates higher residual stresses.

Due to the intrinsic limitations of the Incremental Hole Drilling Method, the calculation of the residual stresses are limited to a hole depth of 0.8 mm. In fact, from the third increment (0.99 mm), the predominant calibration coefficients in the residual stresses calculation become low enough to induce instability in the results. The limitations of the IHDM can be summerized in 3 points:

- Experimental limitations: there is a loss of sensitivity of the gages with depth.
- Numerical limitations: the values of the predominant calibration coefficients in the calculation of residual stresses (coefficients of the diagonal) decrease rapidly with depth.
- Limitations in the formulation of the method: the approach is cumulative and causes instability for low increment depth.

Among the solutions proposed to overcome these problems of instability, the most used are the regularization of Tikhonov [130] and the gradual increase of the depth of increments to keep the same order of magnitude for the calibration coefficients [120]. These two solutions constitute interesting axes of reflection to improve the results obtained.

# General Conclusion & Perspectives

## General Conclusion

The study of residual stresses in fiber reinforced composite laminates remains a complicated scientific subject on the one hand because of the complexity of the mechanisms generating them and on the other hand because of the difficulty specific to their modeling and their measurement. Due to the current environmental and ecological issues, this problematic is taking more and more importance. The principal objective of the present work was to develop numerical and experimental tools adapted to the measurement of residual stresses, induced by several multi-physical mechanism during manufacturing process, by the Incremental Hole Drilling Method (IHDM). The final goal was to determine the residual stress profile in laminates manufactured under different curing cycles and investigate on the effects of the IHDM itself on the local properties of the composites.

The problem of residual stresses has given and still gives rise to a lot of research in the literature. These research, presented in the first chapter (no-exhaustive presentation), allowed to understand the origins and the importance of residual stresses in thermoset and thermoplastic composite laminates. Due to their possible detrimental effects on material properties, which can be very important, residual stresses are important data to consider in the dimensioning of composite parts. Many methods for measuring residual stresses exist. Although these methods all have limitations, some allow a good approximation of residual stresses and among them, this work focuses on the IHDM well adapted to fiber reinforced composite.

The second chapter presented the theoretical and numerical approach of this method. To facilitate understanding, the method was first presented for thin materials for which the approach was not incremental. A through-the-thickness hole was drilled and the residual stresses was calculated. For thick materials, an incremental hole and the IHDM were required. Thus, the approach is incremental and the equations are discrete and cumulative. This means that the residual stresses of a given increment is calculated from the residual stresses of the previous increments. Rigour is required as errors can accumulate and become significant. The calculation of the calibration coefficients using finite element



simulations are explained. For each increment "i",  $\sum_{k=1}^{k=i} (k * 3)$  simulations are needed to determine all the required coefficients (for example: 18 simulations are need for 3 increments). To automate these simulations and to allow parametric studies, a configurable numerical model is developed and presented in detail.

In the chapter 3, parametric studies were performed using the developed configurable model in order to evaluate the sensitivity of the calibration coefficients to experimental errors. Three experimental errors were considered: errors on increment depth, angular deviation of the gages from their theoretical positions and eccentricity of the hole. The results showed a particular sensitivity of coefficients to errors on increment depth and eccentricity of the hole. For example, a radial eccentricity corresponding to 10% of the mean radius of the strain gage rosette causes a variation of 130% and up to 673% on certain calibration coefficients. The errors on residual stresses are caused by errors in the measurement of the relaxation strains, errors in the calculation of the calibration coefficients or a combination of both. Thus, it is possible to counterbalance experimental errors on relaxation strains by calculating adequately the calibration coefficients. A correction method based on this principle is introduced and explained in this chapter. This method defined a matrix [Sii] that is used to numerically correct the calibration coefficients depending on the experimental errors on the relaxation strains. However, accurate measurement of the errors is required. The achieved parametric study allowed to identify to most critical steps of the experiment protocol. The development of the experimental device and the optimizations proposed to minimize errors are also presented.

In the chapter 4, the residual stresses of unidirectional carbon/epoxy composite laminates fabricated by filament winding were estimated using the Incremental Hole Drilling Method and the corresponding device developed. Investigations were carried out on the thermal and mechanical contributions of the drilling on the raw acquisition data of the relaxation strains. The drilling induces positive thermal strains for gage 2 and 3 oriented at  $-135^\circ$  and  $90^\circ$  relative to the fibers respectively. However, thermal strains are negative for gage 1 (oriented in the fiber direction) because of the negative thermal expansion coefficient of carbon fibers in the longitudinal direction. In addition, the mechanical strains due to material removal is negative for all gages. The combination of these thermal and mechanical strains that occur at the same time allowed to understand and discuss the shapes of the raw acquisition data. The residual stresses of the unidirectional carbon/epoxy composite laminates were determined for three plates manufactured in different curing conditions. The results showed a low level of residual stresses for plate 1 which underwent two dwell temperatures during curing cycle. The residual stresses are believed to relax during the second cure. Higher residual stresses were obtained for plate 3. This

can be explained by the rapid cooling of this plate, which generates higher residual stresses.

This thesis leads to an important question: "how correct is what has been done today?". Indeed, the calculation of residual stresses uses the value of deformations at the end of the relaxation of the material. All the thermomechanical and chemical effects induced during and just after the drilling are not taken into account.

## Perspectives

This work is a work of investigation which has certainly allowed a better understanding of the IHDM applied to composites, but has also led to openings of reflection and questions. Thus, several perspectives are envisaged and listed below from a numerical and experimental point of view.

- An experimental validation of the proposed numerical correction method could be considered. For this, the  $[S_{ii}]$  matrix should be numerically approached and used to correct calibration coefficients in order to counterbalance the errors on relaxation strains.
- An investigation on the stability of the calculation of residual stresses with varying increment depth would be necessary to estimate this quantity and its influence. A great number of tests with different increment depth (one increment per ply, two increments per ply,...) would be required. To reduce the cost of experiments, it may be relevant to establish a measurement of the relaxation strains by image correlation.
- The stabilization of the calculation of the residual stresses using Tikhonov regularization would be a prospect. The progressive increase of the increment depth could also be used in order to maintain the same order of magnitude for the calibration coefficients and avoid instability. A greater hole diameter could be employed to allow the determination of deeper residual stresses.
- Other tests should quickly be implemented:
  - to try to minimize the heat generated during the drilling step using for example an inverted cone end mills. This would allow a better differentiation between thermal and mechanical phenomena
  - to have more accurate results specially for the last increments, tests with adaptive relaxation times should be carried out
  - to study the influence of the variation of local properties on the state of residual stresses

- A powerful prospect would be the calculation of the residual stress profile in photocomposites (i.e. composites obtained by photopolymerization of the resin) in collaboration with the LPIM, (Laboratoire de Photochimie et d'Ingenierie Macromoleculaires) of UHA. An important step would be the study of the manufacturing parameters and more particularly the photopolymerization parameters on the residual stresses. The numerical model could then be enriched and optimization loops could be written and combined with artificial intelligence to optimize manufacturing parameters in order to obtain a desired state of residual stress according to the use conditions of the composite.

# Résumé en Français

## Introduction générale

Les progrès technologiques et l'urgence écologique ont suscité un intérêt particulier pour la recherche avancée sur les matériaux. Cela concerne la recherche sur de nouveaux matériaux et l'optimisation des matériaux existants afin d'améliorer leurs performances d'utilisation et de réduire leur empreinte carbone et celle des systèmes dans lesquels ils sont utilisés. En réponse à l'urgence écologique, plusieurs pays mettent en place des stratégies qui comprennent l'utilisation massive de l'électromobilité, des carburants de remplacement (biogaz, biocarburants, hydrogène, etc.), le contrôle de la croissance de la demande de transport, l'amélioration des performances des véhicules (réduction de la consommation de carburant par km). Pour ce dernier, une solution est la réduction de la masse totale des véhicules. Depuis plusieurs décennies, de nombreuses recherches ont été menées dans ce sens, pour développer de nouveaux matériaux capables de répondre à ce besoin. Les composites, qui sont des matériaux ayant de bonnes propriétés spécifiques, connaissent donc un fort développement et sont de plus en plus utilisés pour alléger la structure des modes de transport émettant du CO<sub>2</sub>. Ceci est particulièrement efficace dans le cas des véhicules lourds tels que les avions et les camions-citernes pour lesquels le gain de poids est considérable.

A cet égard, les composites stratifiés à renforts fibreux sont de bons candidats. Cependant, en raison de leur nature hétérogène et de leur processus de fabrication comprenant des réactions chimiques complexes et des contraintes thermomécaniques, ils sont soumis à des contraintes internes résiduelles importantes, avec des conséquences souvent préjudiciables à leur géométrie et/ou à leur performance dans leurs conditions d'utilisation. Par conséquent, les contraintes résiduelles sont des données importantes à prendre en compte lors du dimensionnement des pièces composites et de la prévision de leur comportement.

De nombreux travaux existent dans la littérature sur plusieurs techniques visant à minimiser les contraintes résiduelles dans les composites thermodurcissables et thermostoplastiques principalement. Cependant, ces techniques ont très souvent des effets néfastes

sur les propriétés mécaniques des composites. Un autre problème important est la mesure des contraintes résiduelles, dont les techniques conduisent à de nombreuses questions sur la valeur à donner aux résultats (mesures locales, mesures elles-mêmes induisant des contraintes , ...). C'est pourquoi la mesure des contraintes résiduelles dans les composites et la validité des résultats constituent le principal objectif de cette étude. Parmi les techniques existantes, ce travail se concentre sur la méthode du trou incrémental.

Ce travail s'inscrit dans un programme de recherche plus vaste mené au laboratoire dont le sujet principal est la fabrication et le comportement des composites. Dans ce thème, un projet appelé "Light Tank" (projet ademe UHA/Magyar) vise à fabriquer des camions-citernes avec des réservoirs composites pour le transport de liquides dangereux. Un de leurs problèmes est la mesure et le contrôle des contraintes résiduelles afin de pouvoir établir à plus long terme une corrélation entre les paramètres de fabrication des différents types de composites et les contraintes résiduelles induites. Ainsi, le premier objectif de ce travail est de résumer les mécanismes multi-physiques et les interactions matrice/fibre qui conduisent à la formation de contraintes résiduelles dans les composites. Le deuxième objectif est de développer des outils expérimentaux et numériques adaptés à la mesure des contraintes résiduelles par la méthode du trou incrémental. Le troisième objectif est de développer une expertise dans la mesure des contraintes résiduelles par la méthode du trou incrémental et de fournir des réponses sur certains aspects qui ne sont pas ou très peu étudiés dans la littérature tels qu'une explication détaillée des données d'acquisition brutes ou l'influence du perçage sur les propriétés chimiques locales de la résine.

Dans le premier chapitre, le problème des contraintes résiduelles est présenté. Les origines des contraintes résiduelles, leur influence sur les propriétés des composites stratifiés , les techniques de minimisation les plus courantes sont présentées. Les méthodes de prédiction et de mesure des contraintes résiduelles sont également décrites dans ce chapitre.

Dans le deuxième chapitre, le trou incrémental est présenté. La formulation théorique de la méthode est présentée non seulement pour les composites stratifiés , mais aussi pour les matériaux orthotropes minces afin de permettre une compréhension globale de la méthode. Une partie importante de ce chapitre est le calcul des coefficients de calibration à l'aide de simulations par éléments finis. Une bonne compréhension de ces calculs numériques est nécessaire pour comprendre la détermination du gradient de contrainte résiduelle à travers l'épaisseur du matériau. Le modèle numérique configurable codé en Python et basé sur Abaqus qui est utilisé pour simuler la méthode du trou incrémental

est décrit.

Dans le troisième chapitre, l'aspect configurable du modèle est utilisé pour effectuer une étude paramétrique et évaluer numériquement la sensibilité de la méthode du trou incrémental aux erreurs expérimentales. Cela a permis de proposer une méthode de correction pour les coefficients de calibration et d'identifier les tâches critiques dans le protocole expérimental. Le dispositif expérimental développé pour mesurer les déformations de relaxation et les solutions proposées pour minimiser les erreurs expérimentales sont présentés.

Dans le quatrième chapitre, le matériau étudié est présenté. Une courbe d'acquisition brute typique de déformation de relaxation est présentée et expliquée. L'accent est mis sur l'effet du perçage sur les propriétés locales de la résine. Pour cela, des mesures thermiques sont effectuées pour caractériser le champ thermique pendant et après le perçage et des tests de calorimétrie à balayage différentiel (DSC) sont effectuées pour caractériser les propriétés locales de la résine. Les contraintes résiduelles d'échantillons fabriqués dans différentes conditions de cuisson sont présentées et comparées. Ensuite, une conclusion résumera les principaux résultats et les questions soulevées. Elles feront l'objet des perspectives à donner à ce travail.

## **Chapitre 1 : généralité sur les contraintes résiduelles (CR)**

### **C1.1 Introduction**

Ce premier chapitre vise à introduire le problème des contraintes résiduelles (CR) en général. La formation de contrainte résiduelle pendant la fabrication des composites à renforts fibreux est présentée afin de permettre une compréhension globale de ce travail. Comprendre l'influence de ces CR (induites par le procédé de fabrication) sur les composites stratifiés thermoplastiques et thermodurcissables est nécessaire pour appréhender les enjeux d'une telle étude. Pour de nombreuses applications, les CR doivent être optimisées afin d'améliorer les propriétés et la durée de vie des composites fabriqués. À cette fin, les techniques les plus fréquentes utilisées pour réduire les CR sont présentées. Les modèles de prédiction et les méthodes de mesure des CR les plus couramment utilisés sont également abordés.

## C1.2 Origines des contraintes résiduelles

La formation des CR dans les composites à renforts fibreux est principalement due aux phénomènes chimiques et thermiques qui se produisent lors de leur fabrication. D'un point de vue chimique, la matrice subit, pendant le cycle de cuisson, un retrait volumique causé par la réticulation (cas des résines thermodurcissables). Ce retrait volumique provoque une compression des fibres et engendre des CR dont les valeurs dépendent de la nature de la résine et de paramètres tels que la densité de réticulation [4], la température maximale du cycle de cuisson [9].

D'un point de vue thermique, les CR se forment principalement pendant la phase de refroidissement du cycle de cuisson. Elles sont dues à la différence entre les coefficients de dilation thermique de la matrice et des fibres [10]. A l'échelle des constituants, cette différence provoque une non-uniformité entre les déformations thermiques de la fibre et de la matrice. Cela entraîne des CR dans la fibre, la matrice et à l'interface fibre/matrice. A l'échelle du pli, l'influence de l'orientation des fibres sur les déformations thermiques du pli joue un rôle clé. En effet, deux plis successifs, ayant des orientations de fibres différentes, se déforment de manière non-uniformes, provoquant des CR dans les plis et à leur interface. A l'échelle du composite, les CR sont dues au gradient de température à travers l'épaisseur. En effet, le gradient de température génère un gradient de déformation qui à son tour génère un gradient de contrainte résiduelle.

## C1.3 Influence des contraintes résiduelles sur les propriétés des matériaux et techniques de minimisation

Les contraintes résiduelles (CR) ont une influence considérable sur les propriétés de la matrice. Des CR de compression provoquent une augmentation de la température ultime de transition vitreuse de la matrice alors que des CR de tension et de cisaillement provoquent sa diminution [17]. D'Amore et al [17] ont montré que les CR causent une modification des propriétés de vieillissement de la matrice. Les CR à l'interface fibre/matrice (rappelons que la matrice comprime les fibres) renforce l'interface dans le sens radial. Cependant, elles peuvent causer un délaminage de la fibre si la liaison fibre-matrice est faible [21]. Les CR peuvent causer des microfissures de la matrice qui peuvent se propager et provoquer des délaminages voire la rupture du composite. Ces microfissures ont des conséquences sur les propriétés des composites [15] : diminution des modules élastiques et de la rigidité des composites en particulier pour une stratification quasi-isotrope, diminution du module de flexion, réduction du module de cisaillement, diminution des propriétés mécaniques transversales et du coefficient de Poisson, chute de la résistance à la rupture interlaminaire modes I et II, diminution de la résistance à la fatigue, augmentation de la déformation

pendant le chargement par fluage, absorption accrue de l'humidité (les fissures agissent comme des voies de diffusion), réduction de la résistance chimique (les fissures servent d'entrée aux liquides corrosifs), diminution de la conductivité électrique transversale des stratifiés renforcés de fibres de carbone. Les CR ont également des conséquences sur la géométrie des composites. Elles peuvent, par exemple, provoquer une courbure des pièces ou un flambement des fibres [15].

Il existe plusieurs techniques pour minimiser le niveau des CR dans les composites à renforts fibreux. Les plus connues sont : la modification du cycle de cuisson [45] pour réduire les CR, le recuit [10, 52, 53] et l'absorption d'humidité par la matrice (vieillessement hygrothermique) [54] pour relaxer les CR, l'insertion de particules moléculaires dans la résine [59] pour limiter le retrait de la matrice et réduire les CR. Cependant, des techniques telles que l'absorption d'humidité et l'insertion de particules sont généralement suivies d'une chute des propriétés mécaniques des composites.

## **C1.4 Méthodes de mesure et de prédiction des contraintes résiduelles**

La prédiction des CR nécessite la prise en compte de l'évolution des phénomènes chimiques et thermo-mécaniques pendant le cycle de cuisson du composite. Ainsi, il est possible de modéliser l'évolution des CR en fonction de celle des propriétés mécaniques et des déformations pendant le cycle de cuisson. L'évolution des propriétés mécaniques elle-même dépend de celle du degré de cuisson de la résine. L'évolution du degré de cuisson est définie par des relations phénoménologiques comme celle proposée par Adams [65]. A l'échelle micro-mécanique les méthodes de prédiction des CR les plus récentes sont basées sur des simulations par éléments finis. Yuan et al. [2] ont développé un modèle numérique multi-échelle et multi-physique pour prédire l'évolution des CR micro-mécaniques.

Il existe de nombreuses méthodes pour mesurer les CR. Ces méthodes peuvent être classées en 3 catégories : les méthodes non-destructives, les méthodes destructives et les méthodes utilisant l'insertion d'un capteur de déformation dans le composite. Comme méthodes non-destructives, l'on peut citer la méthode de la courbure [69, 70, 71], l'interferométrie [75, 76], la spectroscopie Raman [78], l'utilisation de la conductivité électrique des fibres de carbone [73], la photo-élasticité [73, 81]. Parmi les méthodes destructives, les plus connues, il y a la méthode par enlèvement de plis [82], le trou incrémental [85, 86], la méthode de la compliance [90]. Concernant la dernière catégorie de méthode, le capteur de déformation peut être une jauge de déformation [91], une fibre optique [73, 94] ou des particules métalliques [98] pour rendre possible une mesure par diffraction de rayons X.



## **C1.5 Conclusion**

Dans les matériaux hétérogènes et anisotropes tels que les composites stratifiés à renforts fibreux, les CR sont inévitables. Ces contraintes sont principalement dues aux mécanismes chimiques, mécaniques et thermiques complexes qui se produisent pendant le processus de fabrication. Des CR existent également dans les pièces obtenues par impression 3D et même dans certaines structures biologiques. Ils peuvent modifier les propriétés mécaniques, chimiques et électriques des composites stratifiés et diminuer la qualité globale des pièces. De nombreuses techniques existent pour minimiser ou plutôt optimiser l'état de contrainte résiduelle. Cependant, très souvent, les moyens utilisés pour réduire les CR ont un effet préjudiciable sur certaines propriétés mécaniques du composite ou nécessitent des ressources supplémentaires. Des formulations thermo-viscoélastiques complexes sont de plus en plus mises en œuvre dans des modèles éléments finis pour prédire les CR aux échelles microscopiques et macroscopiques. Grâce à l'amélioration continue des outils numériques et à l'expérience croissante des chercheurs, les modèles de prédiction sont de plus en plus précis. Les modèles les plus récents utilisent des boucles d'optimisation numérique pour trouver les meilleurs paramètres du cycle de cuisson. De nombreuses méthodes expérimentales ont été développées pour évaluer l'état de contrainte résiduelle dans les composites stratifiés. Les méthodes les plus couramment utilisées sont présentées dans ce chapitre. Dans le reste de ce travail, la détermination expérimentale des CR sera effectuée à l'aide de la méthode du trou incrémental. Cette méthode est utilisée, entre autres, en raison de sa bonne capacité à déterminer les gradients de CR à travers l'épaisseur, même dans des éprouvettes symétriques et équilibrées. Les formulations de la méthode du trou incrémental sont présentées dans le chapitre suivant.

## **Chapitre 2 : Formulation de la méthode du trou incrémental**

### **C2.1 Introduction**

La méthode du trou (MT) est l'une des méthodes les plus utilisées pour mesurer les contraintes résiduelles (CR) en raison de sa fiabilité, de sa précision et de la disponibilité de procédures d'essai standardisées [101]. La MT est une méthode semi-destructive qui consiste à percer un trou à travers l'épaisseur du matériau et à mesurer les déformations de relaxation autour du trou. Ces déformations sont ensuite converties en CR à l'aide de coefficients appelés coefficients de calibration. Les coefficients de calibration sont calculés à l'aide de simulations par éléments finis. La MT est donc une combinaison entre une partie expérimentale qui consiste à mesurer les déformations de relaxation (voir chapitre

4) et une partie numérique qui consiste à déterminer les coefficients de calibration (voir la section C2.3 de ce chapitre). Pour les structures épaisses, le trou est percé par incréments successifs (méthode du trou incrémental : MTI) à travers l'épaisseur du matériau afin de permettre la détermination du gradient des CR. Le but de ce chapitre est d'expliquer les formulations théoriques de la MT et de la MTI et de présenter les calculs numériques des coefficients de calibration. L'une des tâches importantes de ce projet de thèse est de développer un modèle configurable basé sur des scripts pour automatiser le calcul des coefficients de calibration et permettre des études paramétriques. Ce modèle configurable est présenté dans la dernière section de ce chapitre.

## C2.2 Formulation théorique de la méthode du trou incrémental

Pour les matériaux orthotropes :

Schajer et Yang [108] ont proposé une relation permettant de relier les déformations de relaxation aux CR. Cette relation (équation 4.1) fait intervenir une matrice de 9 coefficients de calibration.

$$\frac{1}{\sqrt{E_x E_y}} \begin{bmatrix} c_{11} & c_{12} & c_{13} \\ c_{21} & c_{22} & c_{23} \\ c_{31} & c_{32} & c_{33} \end{bmatrix} \begin{Bmatrix} \sigma_x \\ \sigma_{xy} \\ \sigma_y \end{Bmatrix} = \begin{Bmatrix} \epsilon_1 \\ \epsilon_2 \\ \epsilon_3 \end{Bmatrix} \quad (4.1)$$

Où:  $c_{ij}$  sont les coefficients de calibration.  $E_x$  et  $E_y$  sont les modules de Young suivant les directions principales du matériau.  $\epsilon_1$ ,  $\epsilon_2$  et  $\epsilon_3$  sont les déformations de relaxation.  $\sigma_x$ ,  $\sigma_y$  et  $\sigma_{xy}$  et les CR.

Pour les matériaux composites :

Les composites stratifiés sont composés de plusieurs couches qui sont individuellement considérées comme des matériaux orthotropes. Ainsi, le cas des matériaux orthotropes épais peut être assimilé à un cas particulier de composites stratifiés (composites stratifiés unidirectionnels). De ce fait, l'équation qui décrit la relations entre les déformations de relaxations et les CR (équation 4.2) est la forme incrémentale de l'équation 4.1.

$$\epsilon_g^i = \sum_{s=1}^3 \sum_{j=1}^i \sigma_s^j C_{ijgs} \quad (4.2)$$

$C_{ijgs}$  est la matrice des coefficients de calibration liés à l'incrément "j" lorsque le nombre total d'incrément percés est "i". Physiquement, elle correspond à la déformation

mesurée par jauge "g" lorsque des charges unitaires sont appliquées à l'incrément "j" pour une profondeur totale correspondant à "i" incréments.

L'équation 4.2 peut être écrite sous forme matricielle :

$$\frac{1}{\sqrt{E_x E_y}} \begin{bmatrix} c_{ij11} & c_{ij12} & c_{ij13} \\ c_{ij21} & c_{ij22} & c_{ij23} \\ c_{ij31} & c_{ij32} & c_{ij33} \end{bmatrix} \begin{Bmatrix} \sigma_x^j \\ \sigma_{xy}^j \\ \sigma_y^j \end{Bmatrix} = \begin{Bmatrix} \epsilon_1^i \\ \epsilon_2^i \\ \epsilon_3^i \end{Bmatrix} \quad (4.3)$$

Il est important de noter que, dans la MTI, les CR de tous les incréments "j" ( $1 \leq j \leq i$ ) contribuent à la déformation totale mesurée.

### C2.3 Calcul des coefficients de calibration par simulations par éléments finis

Pour les matériaux orthotropes :

Les différentes étapes des simulations par éléments finis permettant de calculer les coefficients de calibration sont expliquées ci-dessous :

- Modélisation et maillage : Une modélisation 2D en contraintes planes est utilisée. Un comportement mécanique orthotrope est défini et attribué au matériau. Les jauges de déformation (EA-06-062RE-120) sont modélisées à l'aide de partitions et définies comme zones d'extraction des déformations. Des éléments quadratiques 2D formulés en contraintes planes en intégration réduite (CPS8R) sont utilisés pour mailler le modèle.
- Conditions aux limites et cas de charges : Le trou est supposé infiniment loin des bords du matériau. Pour tenir compte de cela, les 4 bords du modèle sont fixés dans la direction x et y (le plan xy correspond au plan du composite).

Les coefficients de calibration sont calculés à partir d'Eq. 4.1 en utilisant 3 cas de charge différents. Si la jauge 1 est orientée dans le sens de l'axe du matériau, alors les coefficients  $c_{12}$  et  $c_{32}$  sont toujours égaux à zéro [108].

**Cas de charge 1** : traction longitudinale uni-axiale pour déterminer  $c_{11}$ ,  $c_{21}$  et  $c_{31}$  (figure 4.20a)

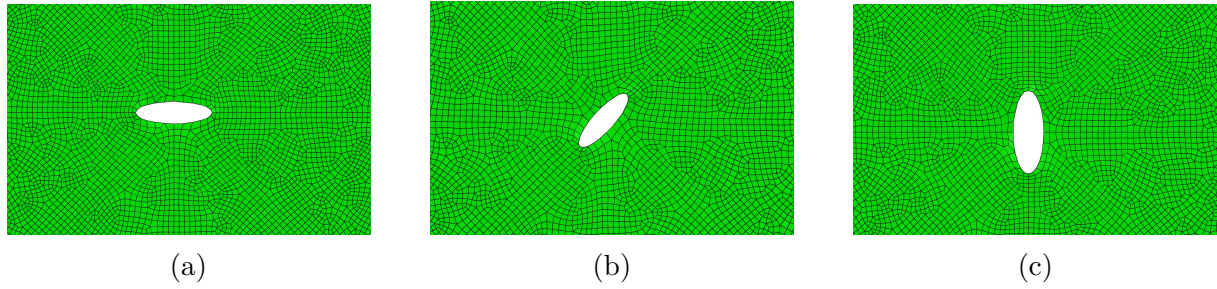


Figure 4.20 – Déformée associée au cas de charge : (a)  $\sigma_x$ , (b)  $\sigma_{xy}$  and (c)  $\sigma_y$

$$\frac{1}{\sqrt{E_x E_y}} \begin{bmatrix} c_{11} & c_{12} & c_{13} \\ c_{21} & c_{22} & c_{23} \\ c_{31} & c_{32} & c_{33} \end{bmatrix} \begin{Bmatrix} \sigma_x \\ 0 \\ 0 \end{Bmatrix} = \begin{Bmatrix} \epsilon_1 \\ \epsilon_2 \\ \epsilon_3 \end{Bmatrix} \quad (4.4)$$

$$c_{11} = \sqrt{E_x E_y} \frac{\epsilon_1}{\sigma_x} \quad c_{21} = \sqrt{E_x E_y} \frac{\epsilon_2}{\sigma_x} \quad \text{and} \quad c_{31} = \sqrt{E_x E_y} \frac{\epsilon_3}{\sigma_x}$$

**Cas de charge 2** : cisaillement pour déterminer  $c_{12}$ ,  $c_{22}$  et  $c_{32}$  (figure 4.20b) :

$$\frac{1}{\sqrt{E_x E_y}} \begin{bmatrix} c_{11} & c_{12} & c_{13} \\ c_{21} & c_{22} & c_{23} \\ c_{31} & c_{32} & c_{33} \end{bmatrix} \begin{Bmatrix} 0 \\ \sigma_{xy} \\ 0 \end{Bmatrix} = \begin{Bmatrix} \epsilon_1 \\ \epsilon_2 \\ \epsilon_3 \end{Bmatrix} \quad (4.5)$$

**Cas de charge 3** : traction uni-axiale transversale pour déterminer  $c_{13}$ ,  $c_{23}$  et  $c_{33}$  (figure 4.20c) :

$$\frac{1}{\sqrt{E_x E_y}} \begin{bmatrix} c_{11} & c_{12} & c_{13} \\ c_{21} & c_{22} & c_{23} \\ c_{31} & c_{32} & c_{33} \end{bmatrix} \begin{Bmatrix} 0 \\ 0 \\ \sigma_y \end{Bmatrix} = \begin{Bmatrix} \epsilon_1 \\ \epsilon_2 \\ \epsilon_3 \end{Bmatrix} \quad (4.6)$$

La simulation est effectuée et les déformations de relaxation (voir exemple de la déformation radiale dans la direction x pour la charge 1 sur figure 4.21) sont extraites sur les points Gauss des éléments des jauges.

Pour les matériaux composites :

- Modélisation et maillage : Le composite est modélisé comme un solide 3D déformable. Comme pour le cas orthotrope, des jauges de déformation de type EA-06-062RE-120 sont considérés. Le modèle est divisé en partitions de façon à ce

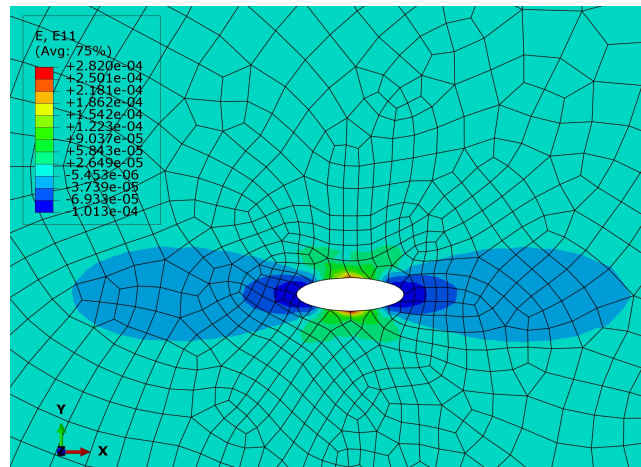


Figure 4.21 – Champ de déformation (E11) correspondant à une traction longitudinale uni-axiale de  $\sigma_x = 20\text{MPa}$

que chaque partition corresponde à un incrément (figure 4.22). Si  $x$  incréments par couche sont percés alors une couche correspond à  $x$  partitions. Dans l'exemple de la figure 4.22, une couche correspond à 2 partitions. Chaque couche du composite est considérée comme un matériau orthotrope. L'orientation adéquate du matériau est ensuite attribuée à chaque couche en fonction de la stratification souhaitée. La jauge 1 est orientée à 0 degré, la jauge 2 à -135 degrés et la jauge 3 à 90 degrés par rapport à la direction principale de la première couche.

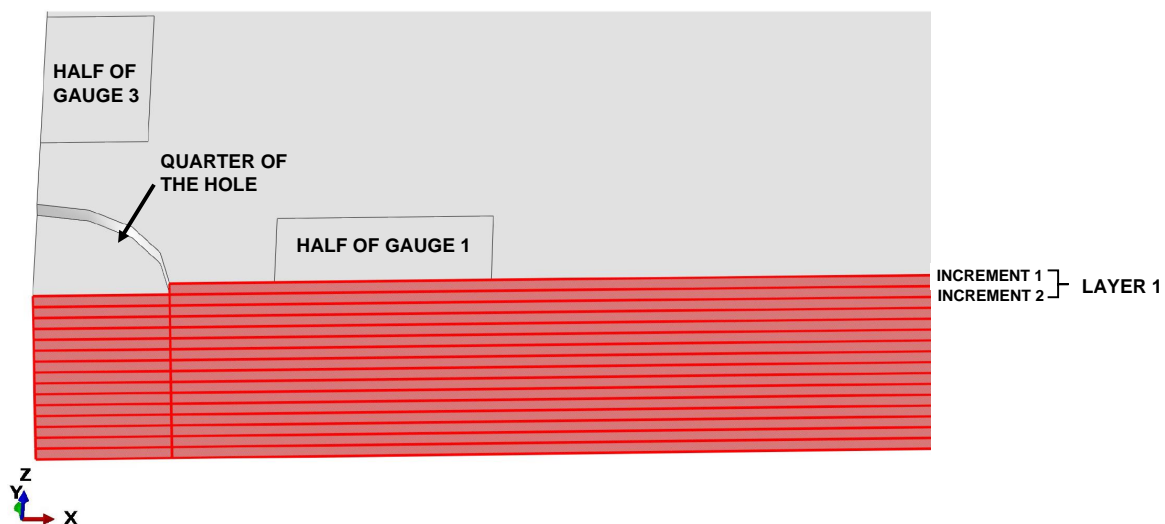


Figure 4.22 – Vue en coupe du modèle 3D du composite (quart du modèle)

Le maillage est une étape clé de la simulation. Plus le maillage est bon, plus les résultats sont précis. Le modèle est maillé avec des éléments isoparamétriques hexaédriques linéaires (8 nœuds) 3D en intégration réduite (C3D8R). Le maillage est con-

figuré de manière à garantir sa qualité quels que soient les paramètres géométriques. Pour avoir le maillage le plus uniforme, le modèle est divisé le long de ses diagonales et de ses deux axes de symétrie (figure 4.23a et 4.23b). La taille des éléments dépend des paramètres géométriques du modèle. De plus, une partition circulaire autour du trou délimite une zone d'intérêt où le maillage est affiné (figure 4.23c). Suivant l'épaisseur, la taille des éléments est définie par le choix du nombre d'éléments par incrément (figure 4.23d).

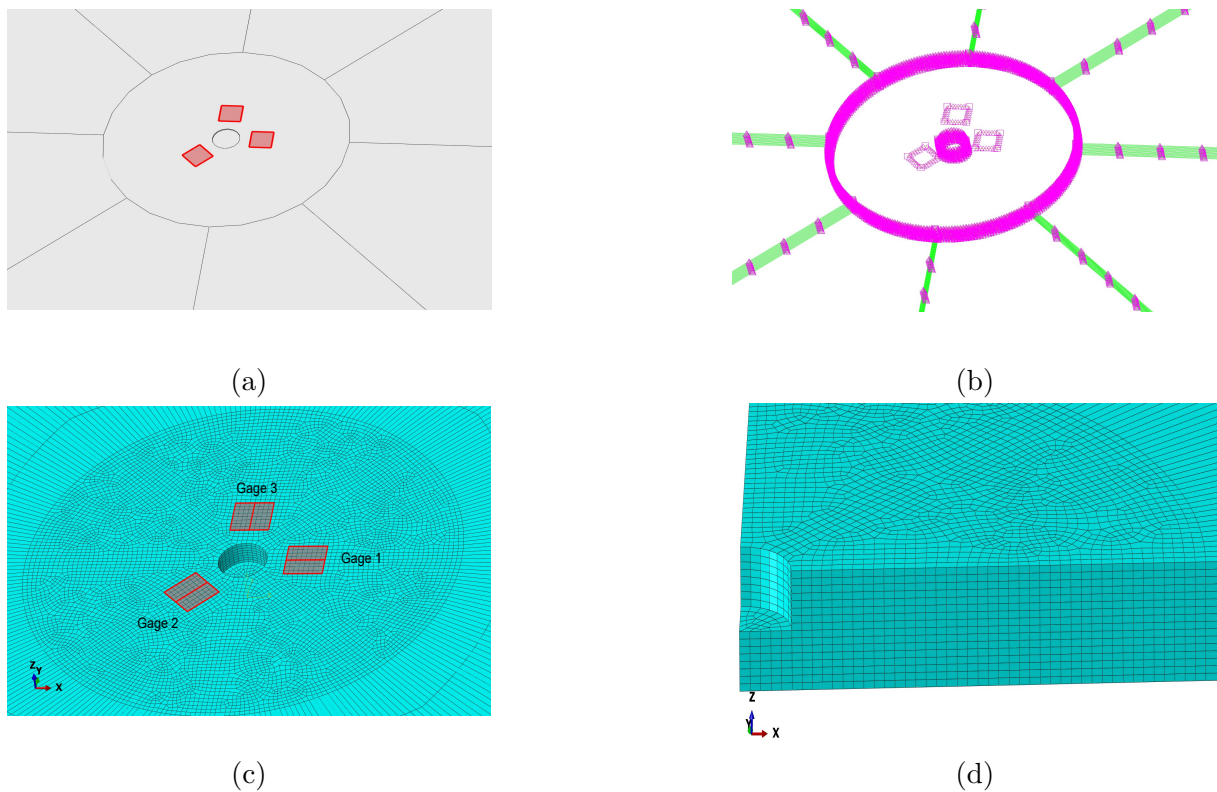


Figure 4.23 – Stratégie de maillage: (a) Partitions utilisées pour le maillage, (b) Distribution des noeuds sur les arêtes (seed edge), (c) Zone d'affinage du maillage et positions des jauges, (d) Maillage suivant l'épaisseur

- Conditions aux limites et cas de charges : Le trou est supposé infiniment loin des bords du matériau. Pour tenir compte de cela, les 4 bords du modèle sont fixés dans la direction x et y.

Les limites externes du modèle sont fixées dans les directions x et y. Ici, l'approche est incrémentale, Lorsqu'un incrément "i" est numériquement percé (enlèvement d'éléments), les 3 cas de charge, décrits pour les matériaux orthotropes, sont successivement appliqués aux différents incréments j,  $0 \leq j \leq i$ . Par exemple, pour calculer la matrice  $[c_{31gs}]$ , les charges doivent être appliquées au premier incrément (j=1) lorsque i=3.

## C2.4 Développement d'un modèle numérique paramétrable

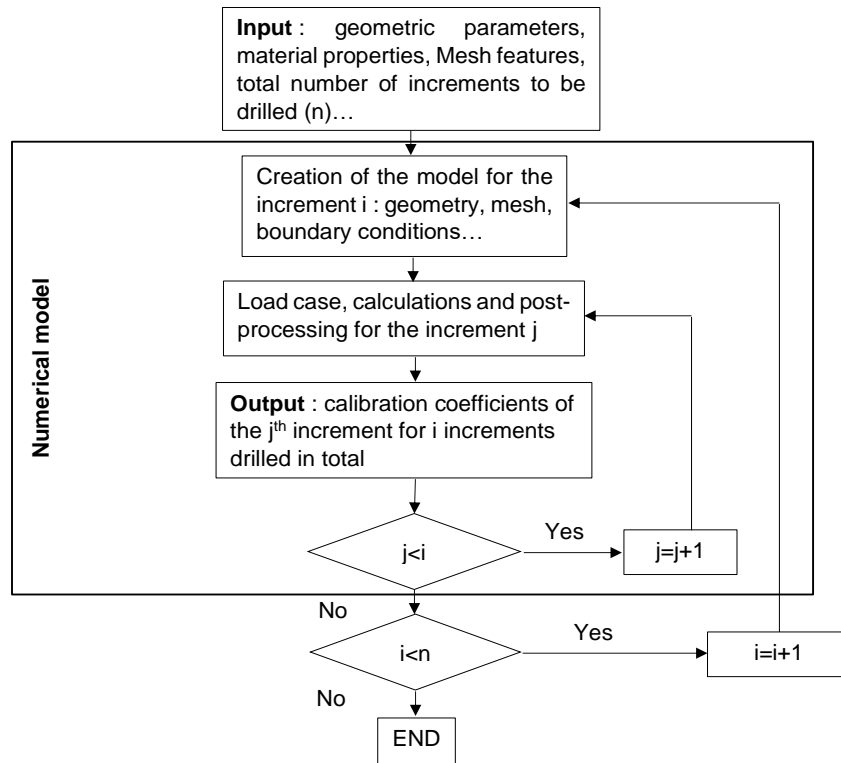


Figure 4.24 – Les différentes étapes du modèle numérique configurable pour un calcul personnalisé des coefficients de calibration

Les chercheurs utilisent généralement des scripts pour automatiser le post-traitement et le calcul des coefficients de calibration. Dans ce travail, le choix a été fait d'automatiser les étapes de modélisation et de simulation (figure 4.24) également. Un avantage de ce choix, est la possibilité de modifier rapidement et facilement les paramètres de modélisation tels que la stratégie de stratification ou la géométrie des jauges utilisés par exemple. Dans un modèle standard, la modification d'un paramètre peut rendre certains de ses paramètres connexes obsolètes, ce qui entraîne un travail supplémentaire pour mettre à jour ces paramètres. Un autre avantage est la possibilité de réaliser des études paramétriques. Cet aspect est abordé dans le chapitre suivant.

Une des tâches principales de cette thèse est de développer un modèle configurable capable de simuler la MTI, de post-traiter les résultats et de calculer les coefficients de calibration de manière autonome. Le script développé est composé de 3 parties. La partie 1 est la section d'entrée, la partie 2 correspond aux étapes de modélisation et de simulation et la partie 3 est le post-traitement. Dans la partie 1, l'utilisateur définit les paramètres d'entrée tels que les dimensions du composite, le nombre de couches, le sens de la fibre, le nombre d'incrément par couche, le nombre total d'incrément à percer (n), les propriétés mécaniques du matériau, la taille des éléments pour le maillage... Une fois les données

saisies et le script exécuté dans Abaqus, son fonctionnement peut être expliqué étape par étape comme suit (cela correspond à la partie 2 du script) :

- Etape 1 : le modèle est créé avec toutes ses caractéristiques géométriques et mécaniques selon les données d'entrée.

- Etape 2 : le premier incrément ( $i=1, j=1$ ) est percé, les conditions limites et le premier cas de charge sont appliqués.

- Etape 3 : le modèle est maillé selon les tailles d'éléments indiquées dans les données d'entrée. Pour toujours avoir un maillage cohérent, les tailles des éléments et la zone de raffinement sont définies en fonction des dimensions du modèle. Par exemple, si de plus grands jauges sont utilisés, la zone de raffinage augmente de diamètre de sorte que les jauges sont toujours dans une zone finement maillée.

- Etape 4 : la simulation est effectuée et le fichier résultats (fichier base de données de type ODB) est stocké dans un répertoire défini.

- Étape 5 : la première charge est désactivée et le deuxième cas de charge est appliqué. La simulation est effectuée et les résultats sont stockés. Ceci est répété pour le troisième cas de charge.

- Etape 6 : Le deuxième incrément ( $i=2$ ) est percé. Les étapes précédentes sont réalisées pour  $j=1$  puis  $j=2$ . En d'autres termes, les trois cas de charge sont appliqués successivement aux incréments 1 et 2 lorsque la profondeur du trou correspond à 2 incréments.

- Etape 7 : le troisième incrément ( $i=3$ ) est percé. Les étapes précédentes sont réalisées pour  $j=1, j=2$  et  $j=3$ .

Ceci est répété dans une boucle jusqu'à ce que le nombre total d'incréments à percer soit atteint ( $i=n$ ).

Une fois que toutes les simulations sont effectuées, le post-traitement des résultats est effectué dans la partie 3 du script. Le script ouvre le fichier ODB approprié (base de données de résultats) dans Abaqus à partir du répertoire de stockage. Les déformations de relaxation sont extraites dans la zone correspondant aux jauges de déformation. Les coefficients de calibration sont calculés pour tous les incréments ( $i,j$ ), avec  $1 \leq i \leq n$  et  $1 \leq j \leq i$ , en utilisant l'équation appropriée. Les coefficients de calibration sont ensuite stockés dans des fichiers texte ou csv. Le modèle numérique configurable utilisé dans ce travail est présenté en figure 4.24.

## C2.5 Conclusion

Dans ce travail, le trou incrémental est utilisé pour déterminer les CR dans les pièces. Ce chapitre présente les équations utilisées dans la MT (pour les pièces minces) et la MTI



(pour les pièces épaisses) pour déterminer les CR. Ces équations dépendent du comportement des matériaux et doivent être étalonnées à l'aide de coefficients de calibration. Le nombre de coefficients de calibration requis dépend du type de matériau : 9 coefficients sont nécessaires pour les matériaux orthotropes fins et "9\*i" coefficients par incrément pour les composites stratifiés. Pour un diamètre de trou et des dimensions de jauges fixes, les coefficients de calibration sont constants, mais ils doivent être recalculés si l'un de ces paramètres change.

Les coefficients de calibration sont calculés à l'aide de simulations par éléments finis. Un script Python est développé pour automatiser la création du modèle, la simulation de la MTI, l'extraction des déformations de relaxation et le calcul des coefficients de calibration. La capacité du script à générer des modèles configurables nous a permis d'effectuer une étude paramétrique et d'évaluer l'influence des erreurs expérimentales sur les coefficients de calibration.

## **Chapitre 3 : Etude numérique de l'influence des erreurs expérimentales sur les coefficients de calibration et développement du protocole expérimental**

### **C3.1 Introduction**

La méthode du trou incrémental (MTI) est très efficace pour mesurer le gradient de contrainte résiduelle dans les composites stratifiés. Toutefois, sa fiabilité dépend de la précision avec laquelle les coefficients de calibration sont déterminés. Les caractéristiques des échantillons et les conditions expérimentales réelles doivent être prises en compte dans la simulation par éléments finis. Toute discordance peut conduire à des coefficients de calibration inadéquats, introduisant ainsi des erreurs dans le calcul des contraintes résiduelles (CR). Il existe plusieurs modèles de correction des coefficients de calibration pour les matériaux isotropes. On peut citer les travaux d'Ajvalasit [122] qui ont proposé une correction analytique de l'excentricité du trou pour les matériaux isotropes fins. Plus récemment, Beghini et al. [123, 124] ont introduit les fonctions d'influence pour corriger analytiquement l'excentricité du trou (cas d'un perçage borgne) dans les matériaux isotropes épais. Il est important de noter qu'il y a un manque d'information à ce sujet concernant les composites stratifiés. Dans ce chapitre, une étude paramétrique est réalisée pour étudier numériquement l'influence de trois erreurs expérimentales majeures sur les coefficients de calibration pour les composites stratifiés. Les résultats mettent en évidence la sensibilité des coefficients à ces erreurs et donnent un ordre de grandeur de la précision requise sur le dispositif expérimental pour avoir des mesures fiables. Une

nouvelle méthode de correction numérique basée sur le modèle configurable développé (figure 4.24) est ensuite introduite. Cette méthode de correction numérique est adaptée aux composites stratifiés épais pour lesquels l'approche analytique est trop complexe. La méthode est formulée pour corriger toute erreur qui peut être expérimentalement mesurée et numériquement modélisée. Le protocole expérimental (méthode et dispositif), développé pour mesurer les déformations de relaxation, est présenté.

### C3.2 Etude de l'influence des erreurs expérimentales sur les coefficients de calibration

L'aspect configurable du modèle numérique a permis d'étudier l'influence de certaines erreurs expérimentales sur les coefficients de calibration. Le principe de cette étude a consisté à prendre en compte une erreur expérimentale donnée dans la simulation et à analyser la variation des coefficients de calibration. Une telle approche n'est, cependant, valable que pour les erreurs expérimentales qui sont mesurables et modélisables. Dans cette étude, 3 erreurs sont considérées : les erreurs sur la profondeur des incréments, la déviation angulaire des jauges de leurs positions théoriques et le décentrement du trou par rapport au centre de la rosette. Les résultats des simulations (variation des coefficients de calibration en %) pour une certaine plage de chaque type d'erreur sont présentés en figures 4.25, 4.26, 4.27.

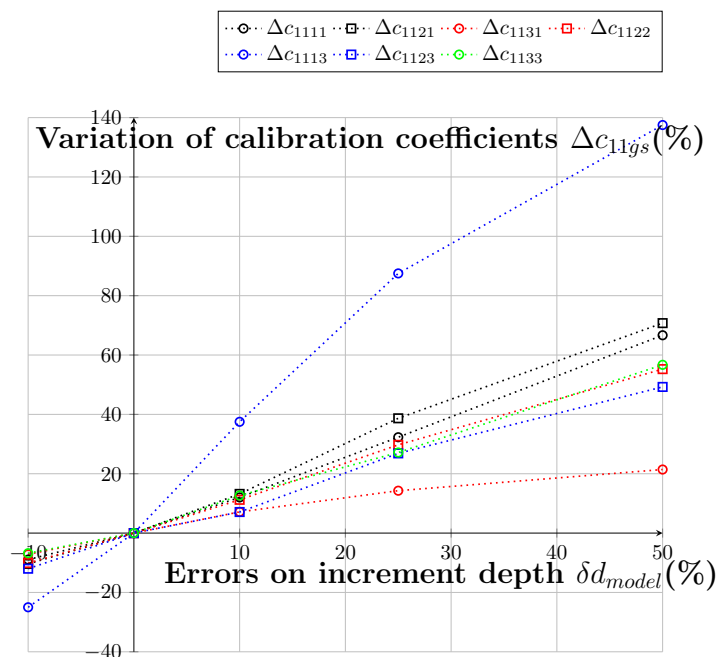


Figure 4.25 – Variation des coefficients de calibration  $c_{11gs}$  pour différentes erreurs sur la profondeur des incréments  $\delta d_{model}$  allant de  $-10\%$  à  $50\%$  de la profondeur d'incrément souhaitée  $d_{model}$

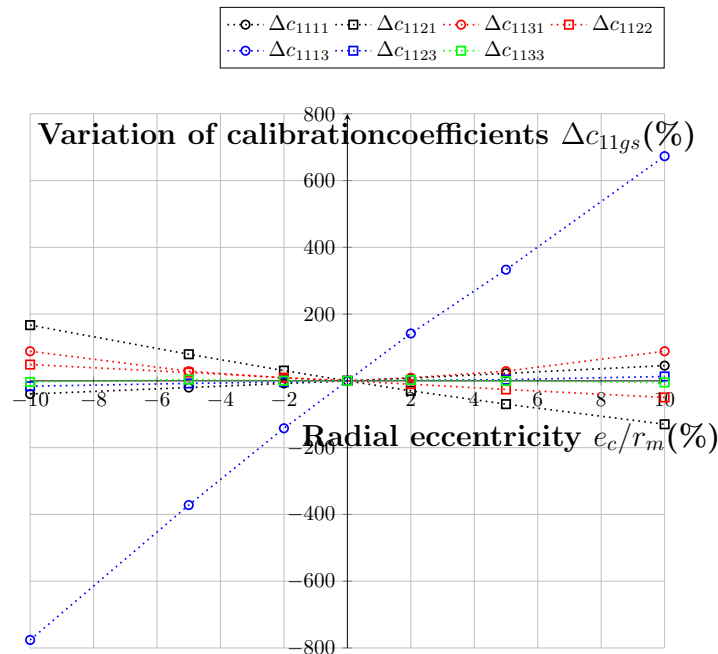


Figure 4.26 – Variation des coefficients de calibration  $c_{11gs}$  pour différentes excentricité du trou dans le sens radial suivant l'axe de la jauge 1

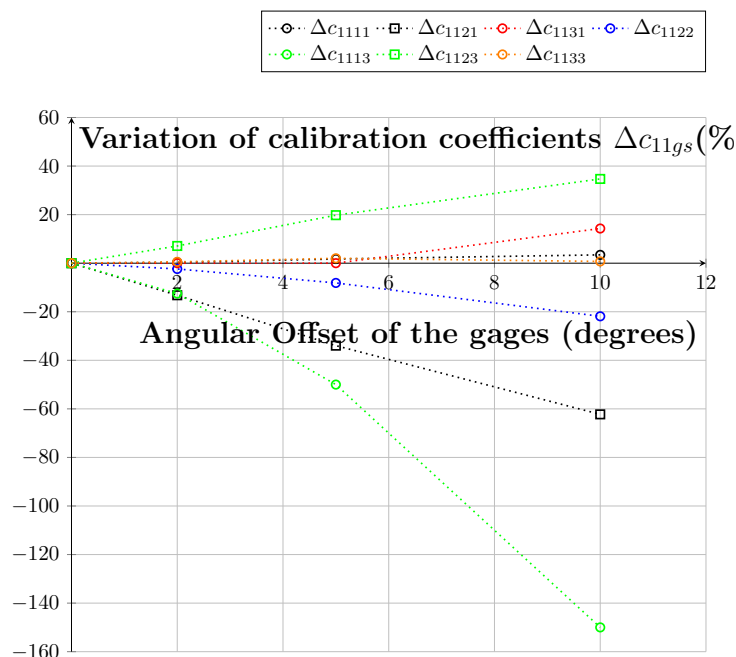


Figure 4.27 – Variation des coefficients de calibration  $c_{11gs}$  pour différentes déviations angulaires dans le sens anti-horaire

L'analyse des résultats montre une grande sensibilité des coefficients aux erreurs expérimentales. Par exemple, une excentricité radiale égale à 10% du rayon moyen des jauges (c.-à-d. 0,257 mm pour une rosette de type EA-06-062RE-120) le long de l'axe des abscisses provoque une erreur de 130% sur le coefficient  $c_{1121}$  et jusqu'à 673% d'erreur sur  $c_{1113}$ . L'on peut également remarquer que parmi les 3 trois erreurs, les coefficients sont

moins sensibles aux déviations angulaire des jauges. De manière générale, les résultats montrent que la méthode du trou incrémental nécessite une grande rigueur expérimentale. Ainsi, pour avoir des résultats fiables, il est nécessaire d'optimiser le dispositif expérimental et/ou de mettre en place une méthode de correction efficace.

### C3.3 Correction numérique des coefficients de calibration

Les erreurs expérimentales peuvent être minimisées en optimisant le dispositif expérimental et le protocole utilisés, mais elles ne peuvent pas être évitées. Une solution consiste à proposer une méthode pour corriger l'effet de ces erreurs sur les résultats. Les CR étant calculées à partir des coefficients de calibration et des déformations de relaxations, l'on peut compenser les erreurs expérimentales de mesure de déformation en ajustant les coefficients de calibration. Ainsi, il est possible de calculer une matrice de coefficients réajustée ou corrigée en définissant une matrice de correction [Sii] (equation 4.7).

$$[C_{iigs}]_{corr}^{-1} = [C_{iigs}]_{ref}^{-1} [S_{ii}] \quad (4.7)$$

La matrice de correction [Sii] est une matrice diagonale calculée en divisant les déformations de références (obtenues par optimisation des paramètres expérimentaux) par les déformations avec erreurs (obtenues en introduisant une erreur connue et maîtrisée dans le test). En pratique, dans un test classique, avec au moins une erreur, seules les déformations erronnées sont disponibles, ainsi, la matrice [Sii] doit être approximée numériquement (travail toujours en cours).

$$[S_{ii}] = \begin{bmatrix} \frac{(\epsilon_1^i)_{ref}^{increment\ i}}{(\epsilon_1^i)_{erreur}^{increment\ i}} & 0 & 0 \\ 0 & \frac{(\epsilon_2^i)_{ref}^{increment\ i}}{(\epsilon_2^i)_{erreur}^{increment\ i}} & 0 \\ 0 & 0 & \frac{(\epsilon_3^i)_{ref}^{increment\ i}}{(\epsilon_3^i)_{erreur}^{increment\ i}} \end{bmatrix} \quad (4.8)$$

### C3.4 Développement du dispositif expérimental

Le dispositif expérimental utilisé pour mesurer les déformations de relaxation est présenté à la figure 4.28. La structure de la machine est composée de profilés en aluminium. Ces profilés sont renforcés par des équerres de fixation en acier pour rigidifier la structure et éviter toute instabilité pendant le perçage. Une broche à fraisage avec une vitesse

de rotation allant de 2000 à 20000 rpm est utilisée pour percer le trou. La vitesse de rotation de la broche est réglée par un boîtier de commande. Une caméra est utilisée pour centrer la fraiseur par rapport à la rosette de jauges de déformation. La caméra et la broche sont montées sur le même support (caméra et porte-broche dans figure 4.28). La distance entre l'axe de la caméra et celui de la broche est étalonnée et connue. Le support est fixé sur une platine linéaire avec un pas minimum de  $0,2 \mu m$  et une répétabilité de  $1 \mu m$ . Ceci permet de contrôler très précisément l'avance verticale de la broche, et donc de minimiser les erreurs sur les profondeurs d'incrément. La platine linéaire est montée sur un axe vertical dont le déplacement est assuré par une courroie et un volant. Une fois cet axe défini, les déplacements verticaux sont effectués exclusivement en utilisant la platine linéaire. Le porte-échantillon est fixé sur 2 platines linéaires qui contrôlent son mouvement dans le plan horizontal. L'acquisition des jauges est effectuée à l'aide d'un module en quart de pont. Un dispositif annexe a été développé pour permettre une orientation précise des grilles des jauges par rapport aux fibres lors du collage.

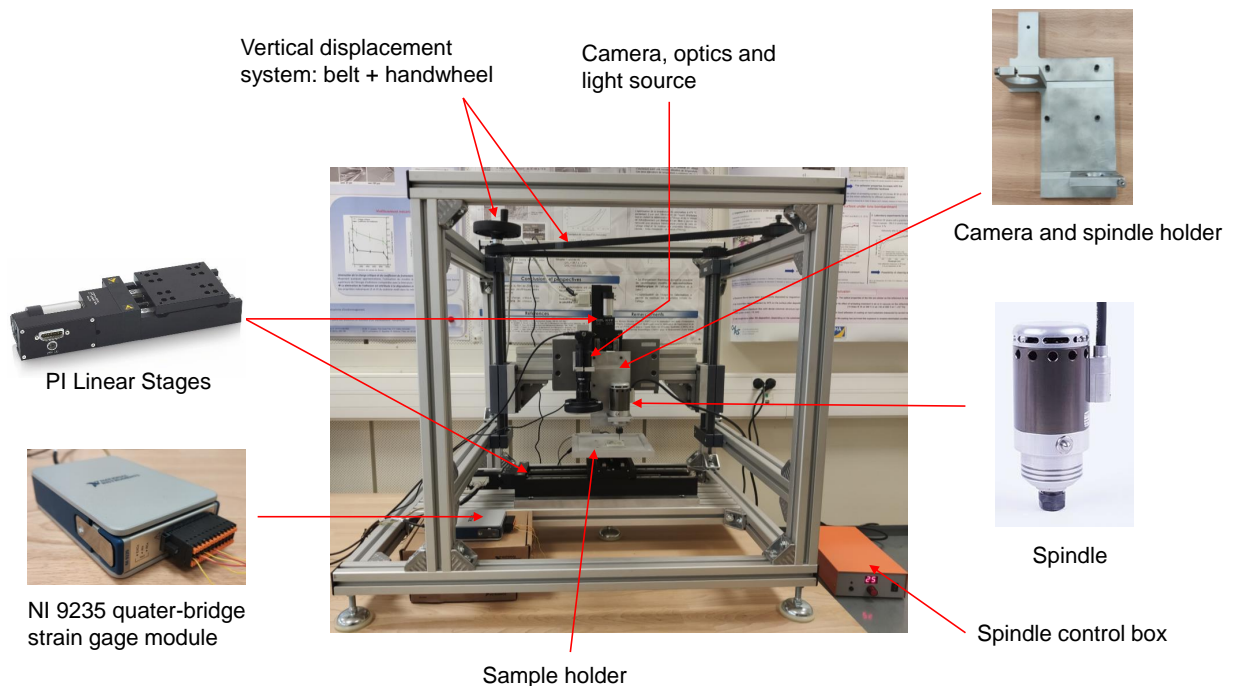


Figure 4.28 – Présentation générale du dispositif expérimental utilisé pour mesurer les déformations de relaxation

### C3.5 Conclusion

Dans ce chapitre, l'influence de trois erreurs expérimentales sur la précision de la MTI, pour un  $[0_2/90_2]_s$  carbone/époxy composites stratifiés, est étudiée numériquement. Il s'agit des erreurs de profondeur sur les incréments, la déviation angulaire des jauges par rapport à leur position théorique et l'excentricité du trou par rapport à la rosette. Une

détermination précise des coefficients de calibration est essentielle pour assurer la fiabilité des CR. Une analyse de la sensibilité des coefficients de calibration aux erreurs étudiées est présentée. Ce chapitre introduit une nouvelle approche basée sur un couplage numérique-expérimental configurable pour corriger les coefficients de calibration des composites stratifiés. Ces coefficients peuvent être corrigés en calculant la matrice  $[S_{ii}]$  qui est obtenue par le rapport des déformations de relaxation de référence (paramètres expérimentaux optimisés) et des déformations de relaxation mesurées avec une erreur identifiée. Toutefois, dans la pratique, si une correction est nécessaire, seules les déformations de relaxation mesurées avec l'erreur sont disponibles. Ainsi, la matrice  $[S_{ii}]$  doit être déterminée par des simulations numériques.

Le développement du dispositif expérimental nécessaire pour mesurer les déformations de relaxation est présenté. En contribuant à améliorer la précision du calcul des coefficients de calibration et de la mesure des déformations de relaxation, les travaux réalisés dans ce chapitre contribuent à déterminer les CR de manière plus fiable dans les composites stratifiés. Cela permettra d'estimer plus précisément les propriétés mécaniques de ces matériaux et donc de mieux adapter leurs fonctionnalités.

## Chapitre 4 Campagne de tests : résultats et discussions

### C4.1 Introduction

La mesure expérimentale des déformations de relaxation par la méthode du trou incrémental (MTI) est une tâche relativement complexe. Cette mesure implique un enlèvement de matière par perçage et par conséquent un échauffement local. Le premier objectif de ce chapitre est d'étudier les effets du perçage sur les mesures de déformation, ainsi que leurs conséquences sur les propriétés locales des composites. Le deuxième objectif consiste à déterminer, analyser et comparer les contraintes résiduelles (CR) des différents échantillons.

Tout d'abord, le dispositif expérimental utilisé et une description complète de l'approche expérimentale sont présentés. Ensuite, les données d'acquisition brutes des déformations de relaxation sont analysées et expliquées en détail. Une caméra infrarouge a été utilisée pour mesurer les champs thermiques induits par le perçage afin de comprendre leurs contributions aux déformations enregistrées. Des tests de calorimétrie différentielle à balayage modulé (DSC) ont été réalisés pour étudier les effets du perçage sur les propriétés chimiques locales des composites. Dans la dernière section de ce chapitre, les CR d'échantillons fabriqués suivant différents cycles de cuisson sont analysées et comparées.

## C4.2 Matériaux

Le matériau étudié est un composite carbone/époxy unidirectionnel. Il est fabriqué et fourni par le groupe G. MAGYAR. Les échantillons sont des plaques de composites stratifiés composées de 12 couches d'une épaisseur d'environ 0,33 mm chacune, soit une épaisseur totale d'environ 4 mm. Les fibres de carbone T700SC-24000-50C sont utilisées avec la résine époxy Araldite 1564. L'Aradur 3474 est utilisé comme agent de durcissement. La teneur en fibres des composites est de 70% en masse et de 60% en volume. Le matériau a été caractérisé mécaniquement par des essais de traction (selon la norme NF EN ISO 527-5 d'octobre 2009 [126]) dans un travail précédent. Le module de Young longitudinal ( $E_x$ ) et transversal ( $E_y$ ) sont égaux à 143 GPa et 7 GPa respectivement. Les plaques composites ont été fabriquées par enroulement filamentaire selon la norme internationale ISO 1268-5 [127]. Trois cycles de cuisson différents (tableau 4.5) ont été utilisés pour fabriquer les trois plaques de cette étude.

Table 4.5 – Cycles de cuisson utilisés pour fabriquer les plaques de composite

Plaques	cycle de cuisson	refroidissement
Plaque 1	1h de cuisson à 80°C puis 4h à 120°C à l'étuve (cycle de cuisson recommandé par le fabricant)	refroidissement à l'étuve
Plaque 2	10h de cuisson à 70°C à l'étuve	refroidissement à l'étuve
Plaque 3	10h de cuisson à 70°C à l'étuve	refroidissement à l'air ambiant

## C4.3 Analyse des données d'acquisition brutes des déformations de relaxation

La figure 4.29 présente les données d'acquisition brutes correspondant aux déformations mesurées par les jauges de la rosette pendant la MTI. La jauge 1 est orientée dans la direction des fibres (0 degrés), la jauge 2 à -135 degrés par rapport aux fibres et la jauge 3 dans la direction perpendiculaire aux fibres (90 degrés). Les paramètres et conditions expérimentaux sont donnés dans le tableau 4.6.

TABLE 4.6 – Conditions et paramètres expérimentaux du test de trou incrémental

Profondeur d'incrément	Vitesse de rotation	Vitesse d'avance	Temperature ambiant	Humidité
0,33 mm (un incrément par pli)	5000 rpm	0,01 mm/s	22 ± 2 °C	46 ± 2 %

Le contact entre la surface du matériau et la fraise est établi après l'exécution du premier incrément dans le programme de perçage. Ceci peut être observé sur les données d'acquisition ("contact" dans figure 4.29a) et est supposé correspondre au perçage de la rosette et de la colle. Chaque cycle d'incrément est composé d'une étape de perçage et

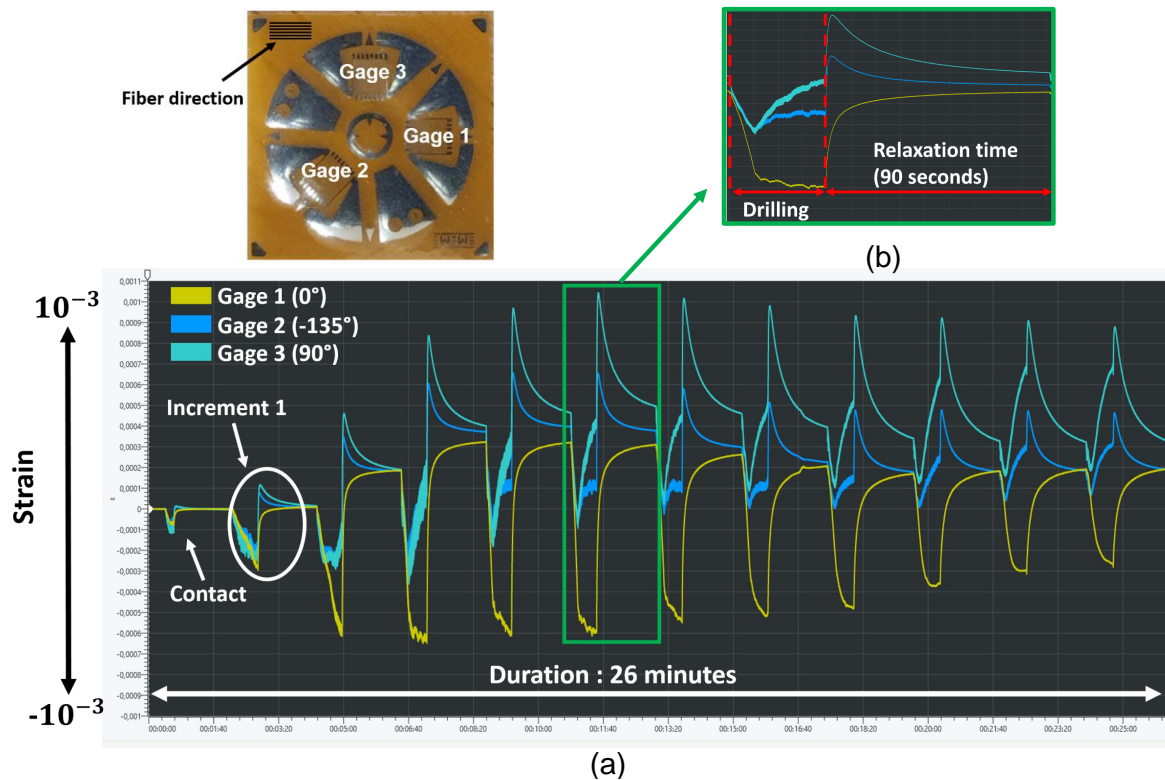


Figure 4.29 – (a) Données brutes d’acquisition obtenues pour la plaque 3, (b) détails pour un cycle d’incrément

d’une étape de relaxation (figure 4.29b). Les déformations prises en compte pour le calcul des CR sont celles à la fin du temps de relaxation.

Des mesures de champs thermiques réalisés pendant et après perçage (à l’aide d’une caméra thermique ThermoCam SC3000 fabriquée par FLIR), ont montré des fluctuations importantes de la température (figure 4.30). Ainsi, les déformations enregistrées correspondent à des déformations thermiques dues à l’échauffement local et à des déformations mécaniques dues à l’enlèvement de matière et aux CR. Au début de l’incrément, la température est ambiante (4.30a) et les déformations prépondérantes sont celles dues à l’enlèvement de matière. De ce fait, les courbes d’acquisitions sont toutes négatives (4.30e), car l’enlèvement de matière entraîne une compression des 3 jauges. A une certaine profondeur, les températures deviennent assez importantes pour que les déformations thermiques prennent le dessus sur les déformations mécaniques. Les courbes de la jauge 2 (bleue) et 3 (cyan) changent de sens de variation car les déformations thermiques (positives) et les déformations mécaniques dues à l’enlèvement de matière sont de signes opposés. Par contre ces déformations sont de même signe pour la jauge 1 (jaune) ce qui explique les déformations négatives importantes enregistrées par cette jauge. En effet, le coefficient de dilatation thermique des fibres de carbone est négatif dans les sens longitudinal, ainsi, lorsque la température augmente, ces fibres se contracte longitudinalement. Pendant la phase de relaxation, les températures diminuent jusqu’à atteindre la tempéra-



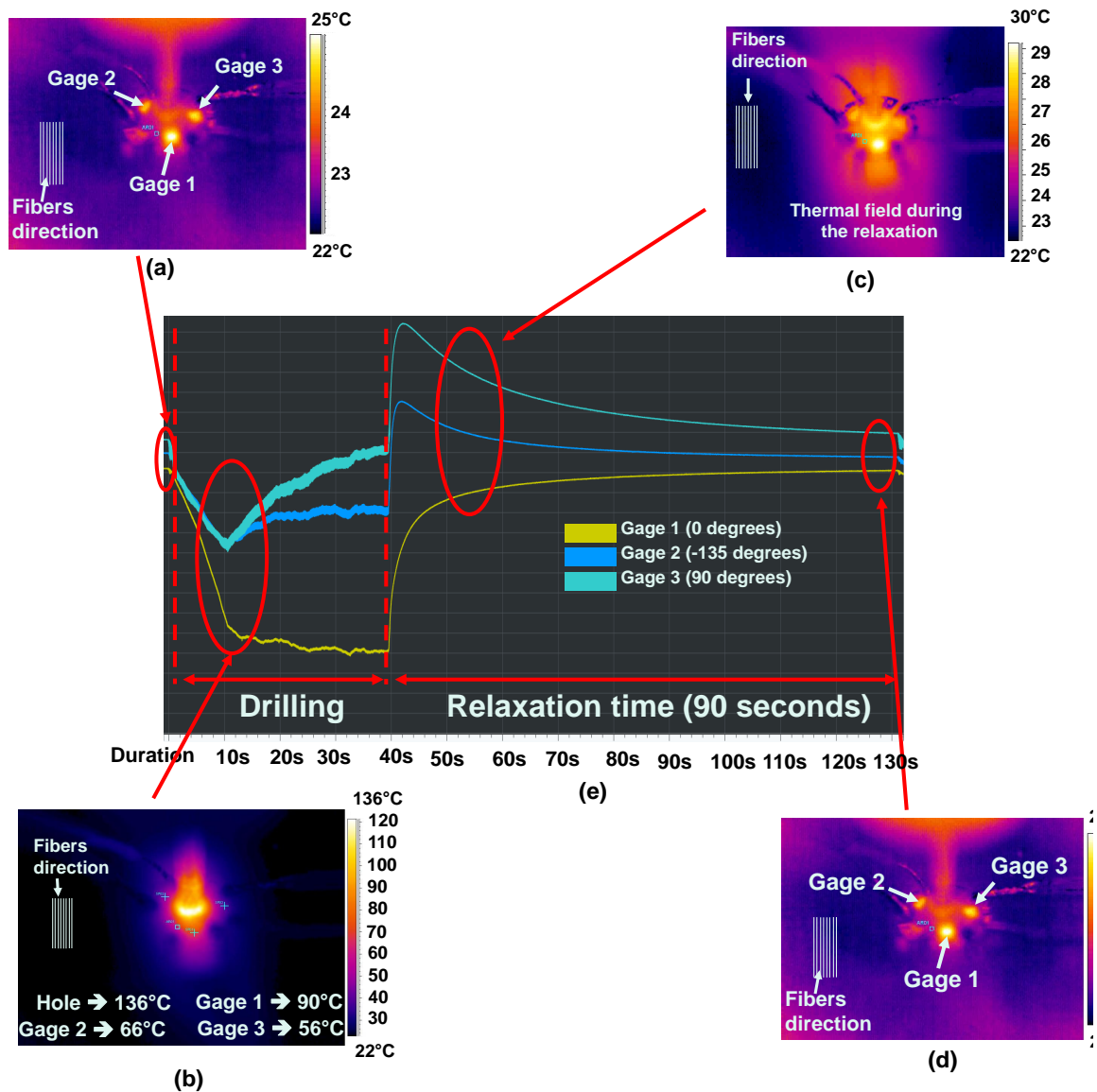


Figure 4.30 – Variation du champ thermique (mesuré en utilisant une caméra thermique) pour un incrément : champ thermique (a) à la fin du précédent incrément , (b) pendant le perçage, (c) pendant la relaxation et (d) à la fin du temps de relaxation

ture ambiante et les déformations évoluent vers leurs asymptôtes respectives. Ces analyses des données d'acquisition brutes du trou incrémental ont permis d'expliquer les allures des courbes et de mettre en évidence la contribution de l'échauffement local dans les résultats obtenus.

#### C4.4 Effects thermiques du perçage sur les propriétés locales de la résine

Après avoir montré la contribution de la température sur les résultats, un travail d'investigation a consisté à évaluer l'influence des effets thermiques du perçage sur les propriétés locales

de la résine. Pour cela, des tests de calorimétrie différentielle à balayage (DSC) ont été réalisés sur des échantillons de résines (pour des raisons de précision) fabriqués dans les mêmes conditions que les échantillons de composites. Les conditions de fabrication sont rappelées ci-dessous :

- Plaque 1 : 1h de cuisson à 80 °C, puis 4h à 120 °C dans un four. La plaque est refroidie dans le four.
- Plaque 2 : 10h de cuisson à 70°C dans un four. La plaque est refroidie dans le four.
- Plaque 3 : 10h de cuisson à 70°C dans un four. La plaque est refroidie à température ambiante ( $22 \pm 2^{\circ}C$ )

Pour chaque plaque, un test de DSC modulé est réalisé sur un échantillon extrait à froid et un échantillon extrait par perçage. L'instrument Discovery DSC 25 conçu par les instruments TA est utilisé avec la version 5.1.0.46403 du logiciel Trios. Le but est de comparer les résultats de ces échantillons pour évaluer l'influence du perçage sur la température de transition vitreuse et sur la réticulation de la résine. L'échantillon extrait à froid est obtenu à l'aide d'un ébavurateur manuel. Des tests MTI sont effectués sur la plaque de résine, et le matériau retiré est considéré comme l'échantillon extrait par perçage. Seulement quelques milligrammes de matière sont nécessaires. Les paramètres expérimentaux des tests DSC modulé sont résumés dans le tableau 4.7

Table 4.7 – Paramètres expérimentaux des tests de DSC modulé

Rampe	Temperature maximale	Temperature modulée
$3^{\circ}C/min$	$250^{\circ}C$	$1^{\circ}C$ pour 60 secondes

Les résultats obtenus pour la résine brute extraite à froid des plaques 1, 2 et 3 sont présentés dans la figure 4.31a, 4.31c et 4.31e respectivement. La figure 4.31b, 4.31d et 4.31f correspondent aux résultats de la résine brute extraite par perçage sur les plaques 1, 2 et 3 respectivement.

Pour toutes les plaques, l'enthalpie de la réaction est plus grande pour la résine extraite à froid. De plus, la température de transition vitreuse est plus élevée pour la résine extraite par perçage. Ces observations permettent de conclure que le perçage entraîne une progression de la réaction de polymérisation et une augmentation de la température de transition vitreuse de la résine à l'emplacement du trou. L'état de CR locales est donc influencé par ces modifications des propriétés de la résine. Cependant, d'autres études sont nécessaires pour évaluer dans quelle mesure ces modifications des propriétés influent sur les CR locales.

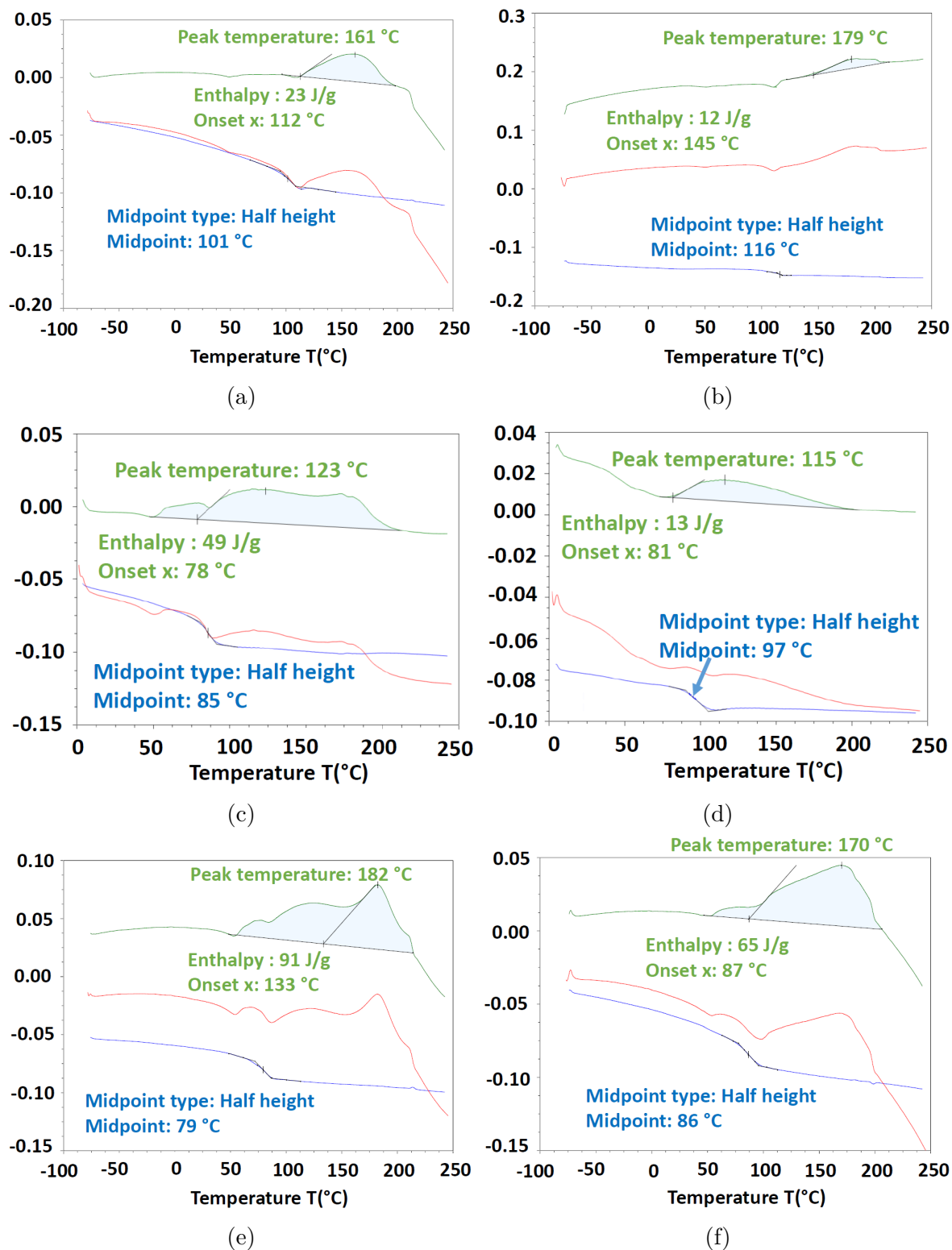


Figure 4.31 – Résultats des tests de DSC modulés : échantillons extraits à froid (a) de la plaque 1, (c) de la plaque 2 et (e) de la plaque 3. Echantillons extraits par perçage (b) de la plaque 1, (b) de la plaque 2 et (f) de la plaque 3. "Enthalpy" correspond à l'enthalpie de la réaction et "Midpoint" à la température de transition vitreuse.

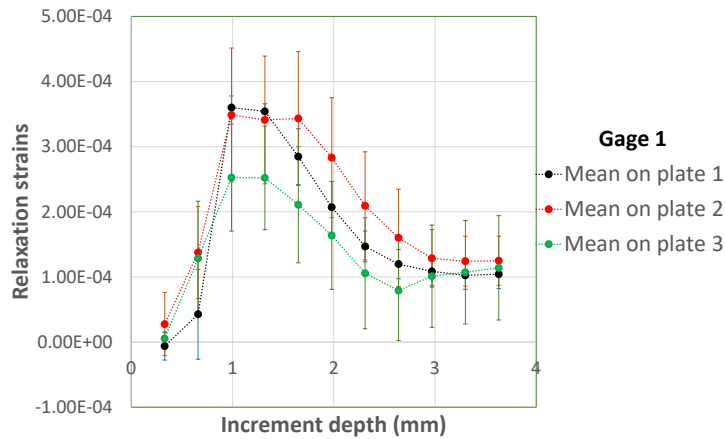
## C4.5 Détermination du profil de contraintes résiduelles

Dans un premier temps, les déformations de relaxations sont calculées pour les plaques 1, 2 et 3. Rappelons que les déformations considérées sont celles en fin de relaxation. Le but étant de laisser aux CR locales le temps de se redistribuer. Les résultats obtenus pour les plaques 1, 2 et 3 sont présentés dans la figure 4.32.

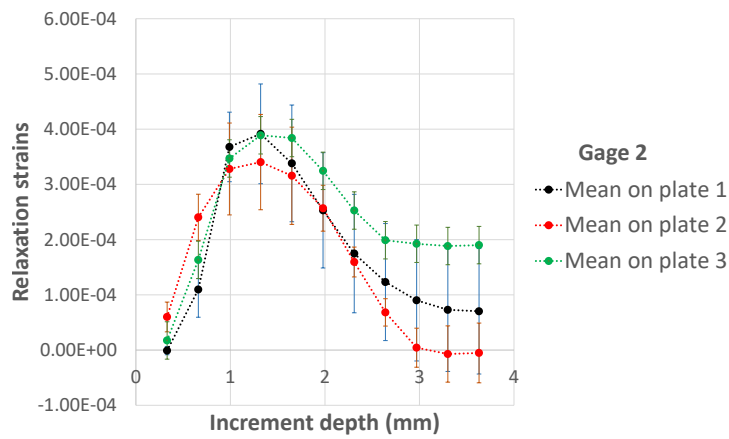
Les moyennes et les dispersions sont déterminées à partir de 3 essais. Les déformations de toutes les jauges sont positives, ce qui signifie que les CR ont tendance à réduire le diamètre du trou percé. Comme on pouvait s'y attendre, les contraintes dans la direction de la fibre (jauge 1, figure 4.32a) sont plus petites que celles dans la direction de la matrice (jauge 3, figure 4.32c). Les déformations enregistrées par la jauge 2 sont entre les deux. Les résultats montrent une plus grande dispersion dans la direction de la fibre. Les échantillons composites ont été fabriqués dans des conditions semi-industrielles à l'aide d'un moule plat. Ainsi, il est probable que les dispersions dans la direction des fibres soient dues à des variations locales d'alignement et de taux de fibres. Les résultats montrent également que les déformations tendent vers une asymptote à partir d'une certaine profondeur. Ceci est dû à une perte de sensibilité des jauges lorsque le trou atteint une certaine profondeur (Principe de Saint-Venant).

A partir des déformations mesurées et des coefficients de calibration calculés, il est possible de déterminer les CR. Ici, la détermination des CR est limitée à une profondeur de trou de 0,8 mm car les résultats deviennent instables au delà de cette profondeur. Cela est dû au fait que les valeurs des coefficients de calibration prédominants dans le calcul des CR (ceux de la diagonale) sont de plus en plus petites avec la profondeur. A partir d'une certaine profondeur (0,99 mm ici, ce qui correspond au troisième incrément), les inverses de ces coefficients de calibration deviennent trop grands et génèrent des instabilités dans le calcul. C'est l'une des raisons pour lesquelles la MTI n'est pas valable pour des mesures profondes. Le début de l'instabilité dépend des propriétés du matériau et de la profondeur d'incrément choisie. Comme l'a montré Zuccarello [121], une faible profondeur d'incrément entraîne une plus grande instabilité du calcul des CR. En fait, les équations utilisées pour calculer les CR sont cumulatives (les CR d'un incrément donné sont calculées en utilisant les CR des incréments précédents). Ainsi, plus la profondeur de l'incrément est faible, plus il y aura d'étapes de calcul, plus les erreurs s'accumuleront et plus le calcul sera instable.

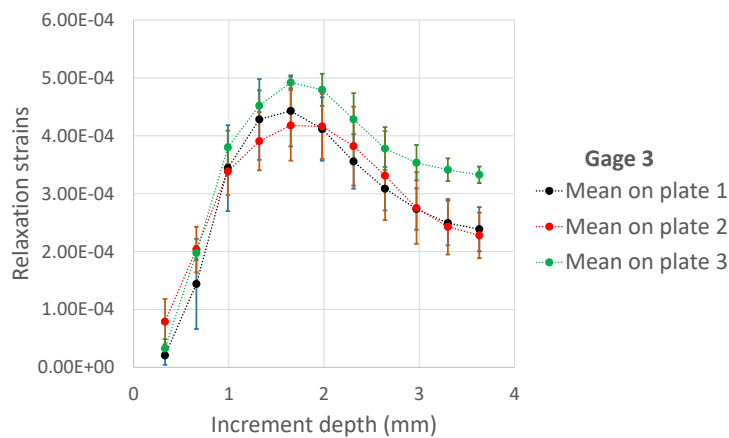
On peut observer que les CR  $\sigma_x$  (dans le sens de la fibre, figure 4.33a) et  $\sigma_y$  (dans le sens transversal, figure 4.33b) sont plus faibles pour la plaque 1 (fabriquée selon le cycle recommandé par le fabricant). Celles de la plaque 3 sont légèrement plus élevées que



(a)



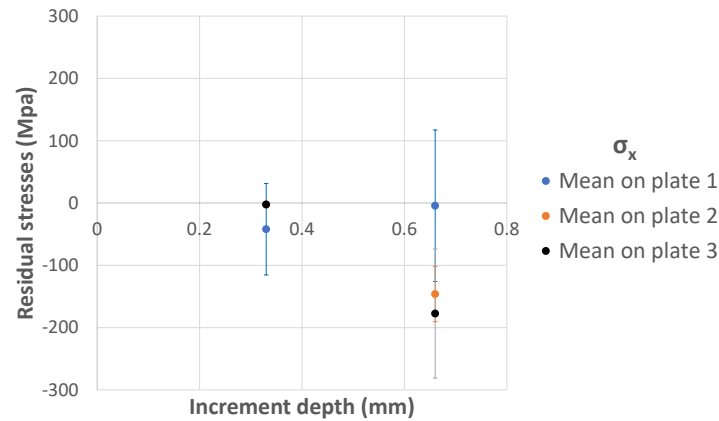
(b)



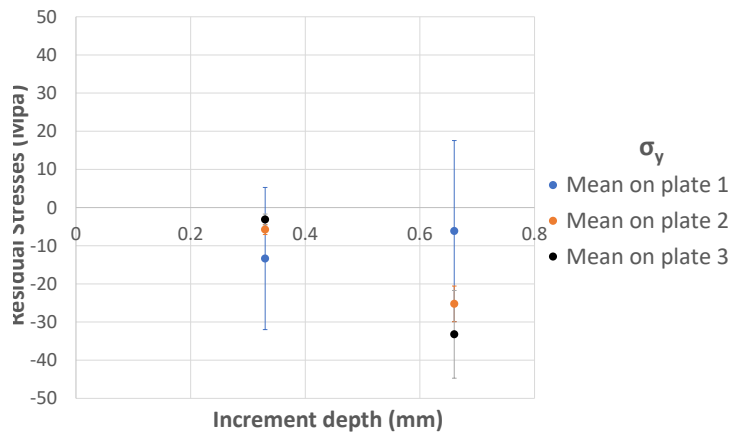
(c)

Figure 4.32 – Relaxation strains measured for the three plates (means and dispersions are determined from 3 tests): results obtained for (a) jauge 1, (b) jauge 2 and (c) jauge 3

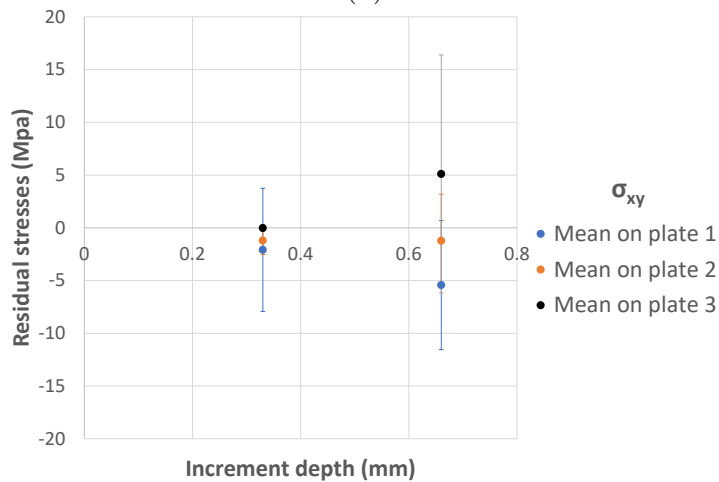
celles de la plaque 2. Comme on pouvait s’y attendre pour les composites stratifiés uni-directionnels, les CR  $\sigma_{xy}$  sont très faibles pour les 3 plaques. Les résultats montrent que, pour toutes les plaques, les CR dans le sens des fibres ( $\sigma_x$ ) sont supérieures à celles dans



(a)



(b)



(c)

Figure 4.33 – CR déterminées pour les 3 plaques : (a)  $\sigma_x$  ( $\sigma_x$  de la plaque 2 est caché par celui de la plaque 3 au 1er incrément), (b)  $\sigma_y$  and (c)  $\sigma_{xy}$ .

le sens transversal ( $\sigma_y$ ). Les résultats obtenus pour la plaque 1 peuvent sembler difficiles à analyser puisqu'elle subit les températures les plus élevées pendant la cuisson. Cependant, le cycle de cuisson de cette plaque est constitué d'un deuxième palier isotherme dont la

température est supérieure à sa température de transition vitreuse, ce qui pourrait permettre aux CR de se relaxer tout en maintenant un degré élevé de polymérisation. La différence entre les résultats des plaques 2 et 3 s'explique par le fait que la plaque 3 est refroidie à l'air ambiant. Ce refroidissement rapide génère des CR plus élevées.

## C.6 Discussion et Conclusion

L'analyse des données d'acquisition brutes des déformations de relaxation a montré deux zones distinctes pour tous les incréments : l'une correspondant à l'étape de perçage et l'autre à l'étape de relaxation. Pendant les étapes de perçage, des tensions thermiques et mécaniques (dues à l'enlèvement de matière et aux CR) se produisent simultanément. Les mesures de la caméra infrarouge ont montré que la température peut atteindre  $136\pm 2^\circ\text{C}$  à l'emplacement du trou pendant le perçage. Les contraintes mécaniques dues à l'enlèvement du matériau et les contraintes thermiques sont toutes négatives pour la jauge 1 qui est orientée dans la direction de la fibre (ceci est dû au coefficient de dilatation thermique longitudinal négatif des fibres de carbone) alors qu'elles sont du signes opposés pour la jauge 2 (orientée à  $-135$  degrés par rapport aux fibres) et à la jauge 3 (perpendiculaire aux fibres). Cette différence de signe explique les sauts enregistrés sur les courbes des jauges 2 et 3 au début de l'étape de relaxation. Les tests de calorimétrie différentielle à balayage modulé (DSC) ont montré que le perçage provoque une évolution de la polymérisation et une augmentation de la température de transition vitreuse. Ces mécanismes induits par le perçage auraient une influence sur les CR locales. Toutefois, d'autres études sont nécessaires pour mieux comprendre leurs effets.

Les CR ont été déterminées pour trois plaques composites fabriquées dans différentes conditions de cuisson. Les résultats ont montré un faible niveau de CR pour la plaque 1 qui a subi deux paliers isothermes pendant le cycle de cuisson. Les CR sont supposées s'être relaxées pendant le deuxième palier. Des CR plus élevées ont été obtenues pour la plaque 3. Cela peut s'expliquer par le refroidissement rapide de la plaque 3, qui génère des CR plus élevées.

En raison des limites intrinsèques de la méthode du trou incrémental, le calcul des CR est limité à une profondeur de trou de 0,8 mm. En fait, à partir du troisième incrément (0,99 mm), les coefficients de calibration prédominants dans le calcul des CR deviennent très faibles et induisent des instabilités dans les résultats. Les limites de la MTI peuvent être résumées en 3 points :

- Limites expérimentales : perte de sensibilité des jauges avec profondeur.
- Limites numériques : les valeurs des coefficients de calibration prédominants dans le calcul des CR (coefficients de la diagonale) diminuent rapidement avec la profondeur.

- Limites dans la formulation de la méthode : l'approche est cumulative et entraîne une instabilité pour une faible profondeur d'incrément.

Parmi les solutions proposées pour surmonter ces problèmes d'instabilité, les plus utilisées sont la régularisation de Tikhonov [130] et l'augmentation progressive de la profondeur des incréments pour garder le même ordre de grandeur pour les coefficients de calibration [120]. Ces deux solutions constituent des axes de réflexion intéressants pour améliorer les résultats obtenus.

## Conclusion générale

### Conclusion générale

L'étude des contraintes résiduelles (CR) dans les composites stratifiés à renforts fibreux reste un sujet scientifique complexe d'une part en raison de la complexité des mécanismes qui les génèrent et d'autre part en raison de la difficulté spécifique à leur modélisation et à leur mesure. En raison des enjeux environnementaux et écologiques actuels, cette problématique prend de plus en plus d'importance. Le but principal de ces travaux est de mettre au point des outils numériques et expérimentaux adaptés à la mesure des CR par la méthode du trou incrémental (MTI). Le but final est de déterminer le profil de contrainte résiduelle dans les stratifiés fabriqués dans différents cycles de cuisson et d'étudier les effets de la MTI elle-même sur les propriétés locales des composites.

Le problème des CR a donné et donne encore lieu à beaucoup de recherches dans la littérature. Ces recherches, présentées dans le premier chapitre (présentation non exhaustive), ont permis de comprendre les origines et l'importance des CR dans les stratifiés thermoplastiques et thermodurcissables. En raison de leurs effets néfastes sur les propriétés des matériaux, les CR sont des données importantes à prendre en compte dans le dimensionnement des pièces composites. Il existe de nombreuses méthodes de mesure des CR. Bien que ces méthodes aient toutes des limites, certaines permettent une bonne approximation des CR et parmi elles, ce travail se concentre sur la MTI qui est bien adaptée aux composites à renforts fibreux.

Le deuxième chapitre a présenté l'approche théorique et numérique de cette méthode. Pour faciliter la compréhension, la méthode a d'abord été présentée pour les matériaux orthotropes minces pour lesquels l'approche n'est pas incrémentale. Un trou traversant l'épaisseur suffit à déterminer les CR. Pour les matériaux épais, un trou incrémental est nécessaire. Ainsi, l'approche est incrémentale et les équations sont discrètes et cumula-



tives. Cela signifie que les CR d'un incrément donné sont calculées à partir des CR des incréments précédents. Il faut faire preuve de rigueur, car les erreurs peuvent s'accumuler et devenir importantes. Le calcul des coefficients de calibration à partir de simulations par éléments finis est expliqué dans ce chapitre. Pour chaque incrément "i",  $\sum_{k=1}^{k=i} (k * 3)$  simulations sont nécessaires pour déterminer tous les coefficients requis (par exemple : 18 simulations sont nécessaires pour 3 incréments). Pour automatiser ces simulations et permettre des études paramétriques, un modèle numérique configurable est développé et présenté.

Dans le chapitre 3, des études paramétriques ont été réalisées à l'aide du modèle configurable développé afin d'évaluer la sensibilité des coefficients de calibration aux erreurs expérimentales. Trois erreurs expérimentales ont été considérées : erreurs sur la profondeur d'incrément, déviations angulaires des jauges par rapport à leurs positions théoriques et excentricité du trou. Les résultats ont montré une sensibilité particulière des coefficients aux erreurs sur la profondeur d'incrément et l'excentricité du trou. Par exemple, une excentricité radiale correspondant à 10% du rayon moyen de la rosette de jauge de déformation provoque une variation de 130% et jusqu'à 673% sur certains coefficients de calibration. Les erreurs sur les CR sont causées par des erreurs dans la mesure des déformations de relaxation, des erreurs dans le calcul des coefficients de calibration ou une combinaison des deux. Il est donc possible de contrebalancer les erreurs expérimentales sur les déformations de relaxation en ajustant correctement les coefficients de calibration. Une méthode de correction basée sur ce principe est présentée et expliquée dans ce chapitre. Cette méthode définit une matrice [Sii] qui est utilisée pour corriger numériquement les coefficients de calibration en fonction des erreurs expérimentales sur les déformations de relaxation. Ainsi, une mesure précise des erreurs est nécessaire. L'étude paramétrique réalisée a permis d'identifier les étapes les plus critiques du protocole expérimental. Le développement du dispositif expérimental est également présenté.

Dans le chapitre 4, les CR de stratifiés unidirectionnels carbone/époxy fabriqués par enroulement filamentaire ont été estimées à l'aide de la méthode du trou incrémental. Des recherches ont été effectuées sur les contributions thermiques et mécaniques du perçage sur les données d'acquisition brutes des déformations de relaxation. Le perçage induit des contraintes thermiques positives pour les jauges 2 et 3 orientées respectivement à  $-135^\circ$  et  $90^\circ$  par rapport aux fibres. Cependant, les contraintes thermiques sont négatives pour la jauge 1 (orientée dans la direction de la fibre) en raison du coefficient de dilatation thermique négatif des fibres de carbone dans la direction longitudinale. De plus, les contraintes mécaniques dues à l'enlèvement de matière sont négatives pour toutes les jauges. La combinaison de ces contraintes thermiques et mécaniques qui se produisent en

même temps a permis de comprendre et de discuter les formes des courbes des données d'acquisition brutes.

Les CR ont été déterminées pour trois plaques fabriquées dans différentes conditions de cuisson. Les résultats ont montré un faible niveau de CR pour la plaque 1 qui a subi deux paliers isothermes pendant le cycle de cuisson. Les CR sont supposées se relaxer pendant le deuxième palier. Des CR plus élevées ont été obtenues pour la plaque 3. Cela peut s'expliquer par le refroidissement rapide de cette plaque, qui génère des CR plus élevées.

Cette thèse conduit à une question importante : "Dans quelle mesure ce qui a été fait aujourd'hui est-il correct?". En effet, le calcul des CR utilise la valeur des déformations en fin de relaxation du matériau. Tous les effets thermomécaniques et chimiques induits pendant et juste après le perçage ne sont pas pris en compte.

## Perspectives

Ce travail est un travail d'investigation qui a certainement permis une meilleure compréhension de la MTI appliquée aux composites, mais a également conduit à des ouvertures de réflexion et de questions. Ainsi, plusieurs perspectives sont envisagées et présentées ci-dessous d'un point de vue numérique et expérimental.

- Une validation expérimentale de la méthode de correction numérique proposée est envisagée. Pour cela, la matrice  $[S_{ii}]$  doit être approximée numériquement et utilisée pour corriger les coefficients de calibration.
- Une enquête sur l'influence du nombre d'incrémentes par pli sur le calcul des contraintes résiduelles. Un grand nombre d'essais avec des profondeurs d'incrémentes différentes (un incrément par pli, deux incements par pli,...) seraient nécessaires. Pour réduire le coût des expériences, il peut être pertinent d'établir une mesure des déformations de relaxation par corrélation d'image.
- La stabilisation du calcul des contraintes résiduelles par la régularisation de Tikhonov est une perspective. L'augmentation progressive de la profondeur de l'incrément pourrait également être utilisée pour maintenir le même ordre de grandeur pour les coefficients de calibration et éviter les instabilités de calcul. On pourrait utiliser un plus grand diamètre de trou pour déterminer des contraintes résiduelles plus profondes.
- Des tests complémentaires devraient rapidement être réalisés :

- Des tests de minimisation de la chaleur générée lors du perçage en utilisant par exemple une fraise à extrémité conique inversée. Cela permettrait un meilleur découplage entre les phénomènes thermiques et mécaniques
  - Des tests avec des temps de relaxation adaptatifs pour avoir des résultats plus précis particulièrement pour les derniers incréments
  - Une étude de l'influence de la variation des propriétés locales sur l'état des contraintes résiduelles
- Le calcul du profil de contraintes résiduelles dans les photocomposites (c.-à-d. les composites obtenus par photopolymérisation de la résine) en collaboration avec le LPIM (Laboratoire de Photochimie et d'Ingénierie Macromoléculaires) de l'UHA serait une perspective intéressante. Une étape importante serait l'étude de l'influence des paramètres de fabrication et plus particulièrement des paramètres de photopolymérisation sur les contraintes résiduelles. Le modèle numérique pourrait alors être enrichi et des boucles d'optimisation pourraient être écrites et combinées avec une intelligence artificielle pour optimiser les paramètres de fabrication afin d'obtenir un état souhaité de contrainte résiduelle selon les conditions d'utilisation du composite.

# References

- [1] Dongna Li, Xudong Li, and Jianfeng Dai. Process Modelling of Curing Process-Induced Internal Stress and Deformation of Composite Laminate Structure with Elastic and Viscoelastic Models. *Applied Composite Materials*, 25(3):527–544, June 2018.
- [2] Zhenyi Yuan, Yongjun Wang, Guigeng Yang, Aofei Tang, Zhenchao Yang, Shujuan Li, Yan Li, and Danlong Song. Evolution of curing residual stresses in composite using multi-scale method. *Composites Part B: Engineering*, 155:49–61, December 2018.
- [3] Mohammad Mohseni, Navid Zobeiry, and Göran Fernlund. Process-induced matrix defects: Post-gelation. *Composites Part A: Applied Science and Manufacturing*, 137:106007, October 2020.
- [4] Jakob Lange, Staffan Toll, Jan-Anders E. Månson, and Anders Hult. Residual stress build-up in thermoset films cured below their ultimate glass transition temperature. *Polymer*, 38(4):809–815, February 1997.
- [5] Nuri Ersoy, Tomasz Garstka, Kevin Potter, Michael R. Wisnom, David Porter, and Graeme Stringer. Modelling of the spring-in phenomenon in curved parts made of a thermosetting composite. *Composites Part A: Applied Science and Manufacturing*, 41(3):410–418, March 2010.
- [6] Nuri Ersoy, Tomasz Garstka, Kevin Potter, Michael R. Wisnom, David Porter, Martin Clegg, and Graeme Stringer. Development of the properties of a carbon fibre reinforced thermosetting composite through cure. *Composites Part A: Applied Science and Manufacturing*, 41(3):401–409, March 2010.
- [7] Jakob Lange, Staffan Toll, Jan-Anders E. Månson, and Anders Hult. Residual stress build-up in thermoset films cured above their ultimate glass transition temperature. *Polymer*, 36(16):3135–3141, January 1995.

- [8] Travis A. Bogetti and John W. Gillespie. Process-Induced Stress and Deformation in Thick-Section Thermoset Composite Laminates. *Journal of Composite Materials*, 26(5):626–660, March 1992.
- [9] S.R. White and H.T. Hahn. Process Modeling of Composite Materials: Residual Stress Development during Cure. Part II. Experimental Validation. *Journal of Composite Materials*, 26(16):2423–2453, January 1992. Publisher: SAGE Publications Ltd STM.
- [10] Patricia P. Parlevliet, Harald E. N. Bersee, and Adriaan Beukers. Residual stresses in thermoplastic composites—A study of the literature—Part I: Formation of residual stresses. *Composites Part A: Applied Science and Manufacturing*, 37(11):1847–1857, November 2006.
- [11] J. A. Barnes, I. J. Simms, G. J. Farrow, D. Jackson, G. Wostenholm, and B. Yates. Thermal expansion characteristics of PEEK composites. *Journal of Materials Science*, 26(8):2259–2271, April 1991.
- [12] R. J. Young, R. J. Day, M. Zakikhani, and I. M. Robinson. Fibre deformation and residual thermal stresses in carbon fibre reinforced PEEK. *Composites Science and Technology*, 34(3):243–258, January 1989.
- [13] Y. Youssef and J. Denault. Thermoformed glass fiber reinforced polypropylene: Microstructure, mechanical properties and residual stresses. *Polymer Composites*, 19(3):301–309, 1998. [\\_eprint: https://onlinelibrary.wiley.com/doi/pdf/10.1002/pc.10103](https://onlinelibrary.wiley.com/doi/pdf/10.1002/pc.10103).
- [14] G. Schwarz, F. Krahn, and G. Hartwig. Thermal expansion of carbon fibre composites with thermoplastic matrices. *Cryogenics*, 31(4):244–247, April 1991.
- [15] Patricia P. Parlevliet, Harald E. N. Bersee, and Adriaan Beukers. Residual stresses in thermoplastic composites – a study of the literature. Part III: Effects of thermal residual stresses. *Composites Part A: Applied Science and Manufacturing*, 38(6):1581–1596, June 2007.
- [16] Mitsukazu Ochi, Kiichi Yamashita, and Masaki Shimbo. The mechanism for occurrence of internal stress during curing epoxide resins. *Journal of Applied Polymer Science*, 43(11):2013–2019, 1991. [\\_eprint: https://onlinelibrary.wiley.com/doi/pdf/10.1002/app.1991.070431108](https://onlinelibrary.wiley.com/doi/pdf/10.1002/app.1991.070431108).
- [17] A. D’Amore, G. Caprino, L. Nicolais, and G. Marino. Long-term behaviour of PEI and PEI-based composites subjected to physical aging. *Composites Science and Technology*, 59(13):1993–2003, October 1999.

## REFERENCES

---

- [18] J. Middleton, J. Hoffman, B. Burks, P. Predecki, and M. Kumosa. Aging of a polymer core composite conductor: Mechanical properties and residual stresses. *Composites Part A: Applied Science and Manufacturing*, 69:159–167, February 2015.
- [19] G. D. Sims and W. R. Broughton. Glass fiber reinforced plastics - properties. pages 151–197. Elsevier, July 2000.
- [20] Yonghui Zhou, Mizi Fan, and Lihui Chen. Interface and bonding mechanisms of plant fibre composites: An overview. *Composites Part B: Engineering*, 101:31–45, September 2016.
- [21] A Sjögren, R Joffe, L Berglund, and E Mäder. Effects of fibre coating (size) on properties of glass fibre/vinyl ester composites. *Composites Part A: Applied Science and Manufacturing*, 30(8):1009–1015, August 1999.
- [22] T. Q Li, M. Q Zhang, K Zhang, and H. M Zeng. Long-range effects of carbon fiber on crystallization of semicrystalline thermoplastics. *Polymer*, 41(1):161–168, January 2000.
- [23] A. Abedian and W. Szyszkowski. Influence of the free surface on the thermal stresses in unidirectional composites. *Composites Part A: Applied Science and Manufacturing*, 28(6):573–579, January 1997.
- [24] C. Filiou and C. Galiotis. In situ monitoring of the fibre strain distribution in carbon-fibre thermoplastic composites1. Application of a tensile stress field. *Composites Science and Technology*, 59(14):2149–2161, November 1999.
- [25] John F. Timmerman, Brian S. Hayes, and James C. Seferis. Cure temperature effects on cryogenic microcracking of polymeric composite materials. *Polymer Composites*, 24(1):132–139, 2003. [\\_eprint: https://onlinelibrary.wiley.com/doi/pdf/10.1002/pc.10013](https://onlinelibrary.wiley.com/doi/pdf/10.1002/pc.10013).
- [26] John A. Nairn and Paul Zoller. Matrix solidification and the resulting residual thermal stresses in composites. *Journal of Materials Science*, 20(1):355–367, January 1985.
- [27] J. A. Nairn and S. Hu. Matrix Microcracking. *Departement of Material Science and Engineering, University of Utah, Salt Lake City, Utah 84112*, pages 187–243, 1994.
- [28] D. M. Grogan, S. B. Leen, C. O. A. Semprimoschnig, and C. M. Ó Brádaigh. Damage characterisation of cryogenically cycled carbon fibre/PEEK laminates. *Composites Part A: Applied Science and Manufacturing*, 66:237–250, November 2014.

- [29] Byeong-Sam Kim, Nicolas Bernet, Paul Sunderland, and Jan-Anders Manson. Numerical Analysis of the Dimensional Stability of Thermoplastic Composites Using a Thermoviscoelastic Approach. *Journal of Composite Materials*, 36(20):2389–2403, October 2002. Publisher: SAGE Publications Ltd STM.
- [30] O. Sicot, X. L. Gong, A. Cherouat, and J. Lu. Determination of Residual Stress in Composite Laminates Using the Incremental Hole-drilling Method. *Journal of Composite Materials*, 37(9):831–844, May 2003.
- [31] Victor Giurgiutiu. Chapter 9 - Impact and Acoustic Emission Monitoring for Aerospace Composites SHM. In Victor Giurgiutiu, editor, *Structural Health Monitoring of Aerospace Composites*, pages 317–394. Academic Press, Oxford, January 2016.
- [32] M. S. Bhalerao. On process-induced fiber waviness in composites: Theory and experiments - ProQuest, 1996.
- [33] Danielle Kugler and Tess J. Moon. Identification of the Most Significant Processing Parameters on the Development of Fiber Waviness in Thin Laminates. *Journal of Composite Materials*, 36(12):1451–1479, June 2002. Publisher: SAGE Publications Ltd STM.
- [34] Michael R. Wisnom and J. W. Atkinson. Fibre Waviness Generation and Measurement and Its Effect on Compressive Strength. *Journal of Reinforced Plastics and Composites*, 19(2):96–110, January 2000. Publisher: SAGE Publications Ltd STM.
- [35] Paul Sunderland, Wonjae Yu, and Jan-Anders Månson. A thermoviscoelastic analysis of process-induced internal stresses in thermoplastic matrix composites. *Polymer Composites*, 22(5):579–592, 2001. \_eprint: <https://onlinelibrary.wiley.com/doi/pdf/10.1002/pc.10561>.
- [36] Michael W Hyer. Some observations on the cured shape of thin unsymmetric laminates. *Journal of Composite Materials*, 15(2):175–194, 1981.
- [37] N. Zahlan and J. M. O’Neill. Design and fabrication of composite components; the spring-forward phenomenon. *Composites*, 20(1):77–81, January 1989.
- [38] W. J. Cantwell, P. Davies, and H. H. Kausch. The effect of cooling rate on deformation and fracture in IM6/PEEK composites. *Composite Structures*, 14(2):151–171, January 1990.
- [39] Subhash C. Khatri and Michael J. Koczak. Thick-section AS4-graphite/E-glass/PPS hybrid composites: Part I. Tensile behavior. *Composites Science and Technology*, 56(2):181–192, January 1996.

- [40] J. F. Guillén and W. J. Cantwell. The Influence of Cooling Rate on the Fracture Properties of a Thermoplastic-Based Fibre-Metal Laminate. *Journal of Reinforced Plastics and Composites*, 21(8):749–772, May 2002. Publisher: SAGE Publications Ltd STM.
- [41] H. M. Jensen. Residual stress effects on the compressive strength of uni-directional fibre composites. *Acta Materialia*, 50(11):2895–2904, June 2002.
- [42] Nawras H. Mostafa. Stress relaxation effect on fatigue life of biaxial prestressed woven E-glass/polyester composites. *Mechanics of Time-Dependent Materials*, 23(4):497–507, November 2019.
- [43] John A. Nairn. Transverse Fracture in Unidirectional Graphite/Polysulfone Composites. *Journal of Composite Materials*, 21(9):798–808, September 1987. Publisher: SAGE Publications Ltd STM.
- [44] J.W. Gillespie and T.J. Chapman. The Influence of Residual Stresses on Mode I Interlaminar Fracture of Thermoplastic Composites. *Journal of Thermoplastic Composite Materials*, 6(2):160–174, April 1993. Publisher: SAGE Publications Ltd STM.
- [45] S.R. White and H.T. Hahn. Cure Cycle Optimization for the Reduction of Processing-Induced Residual Stresses in Composite Materials. *Journal of Composite Materials*, 27(14):1352–1378, December 1993. Publisher: SAGE Publications Ltd STM.
- [46] Jong Woon Kim, Ji Hyung Lee, Hyoung Geun Kim, Hak Sung Kim, and Dai Gil Lee. Reduction of residual stresses in thick-walled composite cylinders by smart cure cycle with cooling and reheating. *Composite Structures*, 75(1):261–266, September 2006.
- [47] PH Shah, VA Halls, JQ Zheng, and RC Batra. Optimal cure cycle parameters for minimizing residual stresses in fiber-reinforced polymer composite laminates. *Journal of Composite Materials*, 52(6):773–792, March 2018. Publisher: SAGE Publications Ltd STM.
- [48] Edu Ruiz and F. Trochu. Multi-criteria thermal optimization in liquid composite molding to reduce processing stresses and cycle time. *Composites Part A: Applied Science and Manufacturing*, 37(6):913–924, June 2006.
- [49] Xuerui Li, Xu Han, Shuyong Duan, and Gui-Rong Liu. A Two-Stage Genetic Algorithm for Molding Parameters Optimization for Minimized Residual Stresses in Composite Laminates During Curing. *Applied Composite Materials*, May 2021.



- [50] Alex J. Hsieh, C. Richard Desper, and Nathaniel S. Schneider. Transient crystallization of an aromatic polyetherimide: effect of annealing. *Polymer*, 33(2):306–313, January 1992.
- [51] Gilbert Lebrun and Johanne Denault. Effect of annealing on the thermal expansion and residual stresses of bidirectional thermoplastic composite laminates. *Composites Part A: Applied Science and Manufacturing*, 41(1):101–107, January 2010.
- [52] J A Barnes. THE FORMATION OF RESIDUAL STRESSES IN LAMINATED THERMOPLASTIC COMPOSITES. page 16, 1994.
- [53] D. D. L. Chung. Continuous carbon fiber polymer-matrix composites and their joints, studied by electrical measurements. *Polymer Composites*, 22(2):250–270, 2001. \_eprint: <https://onlinelibrary.wiley.com/doi/pdf/10.1002/pc.10536>.
- [54] B. D. Harper and Y. Weitsman. On the effects of environmental conditioning on residual stresses in composite laminates. *International Journal of Solids and Structures*, 21(8):907–926, January 1985.
- [55] Frank W. Crossman, R. E. Mauri, and W. J. Warren. Hygrothermal Damage Mechanisms in Graphite-Epoxy Composites. Technical report, LOCKHEED MISSILES AND SPACE CO INC PALO ALTO CA PALO ALTO RESEARCH LAB, December 1979. Section: Technical Reports.
- [56] Charles E. Browning. The mechanisms of elevated temperature property losses in high performance structural epoxy resin matrix materials after exposures to high humidity environments. *Polymer Engineering & Science*, 18(1):16–24, 1978. \_eprint: <https://onlinelibrary.wiley.com/doi/pdf/10.1002/pen.760180104>.
- [57] M. Gentz, D. Armentrout, P. Rupnowski, L. Kumosa, E. Shin, J. K. Sutter, and M. Kumosa. In-plane shear testing of medium and high modulus woven graphite fiber reinforced/polyimide composites. *Composites Science and Technology*, 64(2):203–220, February 2004.
- [58] Xiaohui Zhang. *Manufacturing of hemp/PP composites and study of its residual stress and aging behavior*. thesis, Troyes, May 2016.
- [59] L. S. Penn, R. C. T. Chou, A. S. D. Wang, and W. K. Binienda. The Effect of Matrix Shrinkage on Damage Accumulation in Composites:. *Journal of Composite Materials*, August 1988.
- [60] A. J. Fletcher and J. L. Oakeshott. Thermal residual microstress generation during the processing of unidirectional carbon fibre/epoxy resin composites: random fibre arrays. *Composites*, 25(8):806–813, September 1994.

- [61] T. J. Vaughan and C. T. McCarthy. A combined experimental–numerical approach for generating statistically equivalent fibre distributions for high strength laminated composite materials. *Composites Science and Technology*, 70(2):291–297, February 2010.
- [62] B. HARPER and Y. WEITSMAN. Residual thermal stresses in an unsymmetrical cross-ply graphite/epoxy laminate. In *22nd Structures, Structural Dynamics and Materials Conference*. American Institute of Aeronautics and Astronautics. \_eprint: <https://arc.aiaa.org/doi/pdf/10.2514/6.1981-580>.
- [63] H.T. Hahn and N.J. Pagano. Curing Stresses in Composite Laminates. *Journal of Composite Materials*, 9(1):91–106, January 1975. Publisher: SAGE Publications Ltd STM.
- [64] O. Hayden Griffin. Three-Dimensional Curing Stresses in Symmetric Cross-Ply Laminates with Temperature-Dependent Properties. *Journal of Composite Materials*, 17(5):449–463, September 1983. Publisher: SAGE Publications Ltd STM.
- [65] David C Adams. Cure behavior of unsaturated polyester resin composites. In *Technical Report CCM-88-16*. Center for Composite Materials, University of Delaware Newark, DE, 1988.
- [66] Alfred C. Loos and George S. Springer. Curing of Graphite/Epoxy Composites. Technical report, MICHIGAN UNIV ANN ARBOR DEPT OF MECHANICAL ENGINEERING AND APPLIED MECHANICS, March 1983. Section: Technical Reports.
- [67] Scott R. White and Yeong K. Kim. Process-Induced Residual Stress Analysis of as4/3501-6 Composite Material. *Mechanics of Composite Materials and Structures*, 5(2):153–186, April 1998. Publisher: Taylor & Francis \_eprint: <https://www.tandfonline.com/doi/pdf/10.1080/10759419808945897>.
- [68] Yeong K. Kim and Scott R. White. Viscoelastic Analysis of Processing-Induced Residual Stresses in Thick Composite Laminates. *Mechanics of Composite Materials and Structures*, 4(4):361–387, October 1997. Publisher: Taylor & Francis \_eprint: <https://www.tandfonline.com/doi/pdf/10.1080/10759419708945889>.
- [69] S.R. White and H.T. Hahn. Process Modeling of Composite Materials: Residual Stress Development during Cure. Part I. Model Formulation. *Journal of Composite Materials*, 26(16):2402–2422, January 1992.
- [70] KS Kim and HT Hahn. Residual stress development during processing of graphite/epoxy composites. *Composites Science and Technology*, 36(2):121–132, 1989.

## REFERENCES

---

- [71] Yasir Nawab, Frédéric Jaquemin, Pascal Casari, Nicolas Boyard, and Vincent Sobotka. Evolution of chemical and thermal curvatures in thermoset-laminated composite plates during the fabrication process. *Journal of Composite Materials*, 47(3):327–339, February 2013.
- [72] G. S. Schajer. Hole-Drilling Residual Stress Measurements at 75: Origins, Advances, Opportunities. *Experimental Mechanics*, 50(2):245–253, February 2010.
- [73] Patricia P. Parlevliet, Harald E. N. Bersee, and Adriaan Beukers. Residual stresses in thermoplastic composites—A study of the literature—Part II: Experimental techniques. *Composites Part A: Applied Science and Manufacturing*, 38(3):651–665, March 2007.
- [74] M. J. Pechersky. Determination of Residual Stresses by Thermal Relaxation and Speckle Correlation Interferometry. *Strain*, 38(4):141–149, 2002. [\\_eprint: https://onlinelibrary.wiley.com/doi/pdf/10.1111/j.1475-1305.2002.00030.x](https://onlinelibrary.wiley.com/doi/pdf/10.1111/j.1475-1305.2002.00030.x).
- [75] Wei Xing, Di Ouyang, Ning Li, and Lin Liu. Estimation of Residual Stress in Selective Laser Melting of a Zr-Based Amorphous Alloy. *Materials*, 11(8):1480, August 2018. Number: 8 Publisher: Multidisciplinary Digital Publishing Institute.
- [76] Gianni Nicoletto. Moiré interferometry determination of residual stresses in the presence of gradients. *Experimental Mechanics*, 31(3):252–256, September 1991.
- [77] D Karalekas and A Aggelopoulos. Study of shrinkage strains in a stereolithography cured acrylic photopolymer resin. *Journal of Materials Processing Technology*, 136(1):146–150, May 2003.
- [78] B. P. Arjyal, C. Galiotis, S. L. Ogin, and R. D. Whattingham. Monitoring local strains in cracked cross-ply composites using an embedded aramid fibre strain sensor. *Journal of Materials Science*, 33(11):2745–2750, June 1998.
- [79] Anders S. Nielsen and Ryszard Pyrz. THE EFFECT OF COOLING RATE ON THERMAL RESIDUAL STRAINS IN CARBON/POLYPROPYLENE MICROCOMPOSITES. *Science and Engineering of Composite Materials*, 7(1-2):1–22, June 1998. Publisher: De Gruyter.
- [80] Hans Mueller. The Theory of Photoelasticity \*. *Journal of the American Ceramic Society*, 21(1):27–33, 1938. [\\_eprint: https://onlinelibrary.wiley.com/doi/pdf/10.1111/j.1151-2916.1938.tb15726.x](https://onlinelibrary.wiley.com/doi/pdf/10.1111/j.1151-2916.1938.tb15726.x).
- [81] Achyut Adhikari, Thomas Bourgade, and Anand Asundi. Residual stress measurement for injection molded components. *Theoretical and Applied Mechanics Letters*, 6(4):152–156, July 2016.

- [82] M. Eijpe and P. Powell. Residual stress evaluation in composites using a modified layer removal method. 1997.
- [83] Jan-Anders E. Manson and James C. Seferis. Process Simulated Laminate (PSL) : A Methodology to Internal Stress Characterization in Advanced Composite Materials. *Journal of Composite Materials*, 26(3):405–431, March 1992. Publisher: SAGE Publications Ltd STM.
- [84] G. Jeronimidis and A.T. Parkyn. Residual Stresses in Carbon Fibre-Thermoplastic Matrix Laminates. *Journal of Composite Materials*, 22(5):401–415, May 1988. Publisher: SAGE Publications Ltd STM.
- [85] S. Akbari, F. Taheri-Behrooz, and M. M. Shokrieh. Characterization of residual stresses in a thin-walled filament wound carbon/epoxy ring using incremental hole drilling method. *Composites Science and Technology*, 94:8–15, April 2014.
- [86] A. R. Ghasemi and M. M. Mohammadi. Residual stress measurement of fiber metal laminates using incremental hole-drilling technique in consideration of the integral method. *International Journal of Mechanical Sciences*, 114:246–256, August 2016.
- [87] N. J. Rendler and I. Vigness. Hole-drilling strain-gage method of measuring residual stresses. *Experimental Mechanics*, 6(12):577–586, December 1966.
- [88] J. Lu, A. Niku-Lari, and J.-F. Flavenot. Récents développements de la mesure des contraintes résiduelles par perçage incrémental. *Matériaux & Techniques*, 73(12):709–718, 1985.
- [89] G. S. Schajer. Application of Finite Element Calculations to Residual Stress Measurements. *Journal of Engineering Materials and Technology*, 103(2):157–163, April 1981.
- [90] Nuri Ersoy and Oktem Vardar. Measurement of residual stresses in layered composites by compliance method. *Journal of Composite Materials*, 34(7):575–598, 2000.
- [91] M. Kanerva, P. Antunes, E. Sarlin, O. Orell, J. Jokinen, M. Wallin, T. Brander, and J. Vuorinen. Direct measurement of residual strains in CFRP-tungsten hybrids using embedded strain gauges. *Materials & Design*, 127:352–363, August 2017.
- [92] Fujian Tang, ZhaoChao Li, Yan Tang, Yizheng Chen, and Hong-Nan Li. Simultaneous measurement of shrinkage and coefficient of thermal expansion of mortar based on EFPI sensors with nanometer resolution. *Measurement*, 152:107376, February 2020.

## REFERENCES

---

- [93] J. S. Leng and A. Asundi. Real-time cure monitoring of smart composite materials using extrinsic Fabry-Perot interferometer and fiber Bragg grating sensors. *Smart Materials and Structures*, 11(2):249–255, April 2002. Publisher: IOP Publishing.
- [94] Tiange Wu, Guowei Liu, Shenggui Fu, and Fei Xing. Recent Progress of Fiber-Optic Sensors for the Structural Health Monitoring of Civil Infrastructure. *Sensors*, 20(16):4517, January 2020. Number: 16 Publisher: Multidisciplinary Digital Publishing Institute.
- [95] S. A. Martinez, S. Sathish, M. P. Blodgett, and M. J. Shepard. Residual stress distribution on surface-treated Ti-6Al-4V by X-ray diffraction. *Experimental Mechanics*, 43(2):141–147, June 2003.
- [96] I. C. Noyan, T. C. Huang, and B. R. York. Residual stress/strain analysis in thin films by X-ray diffraction. *Critical Reviews in Solid State and Materials Sciences*, 20(2):125–177, January 1995. Publisher: Taylor & Francis \_eprint: <https://doi.org/10.1080/10408439508243733>.
- [97] J Pina, A Dias, and J. L Lebrun. Study by X-ray diffraction and mechanical analysis of the residual stress generation during thermal spraying. *Materials Science and Engineering: A*, 347(1):21–31, April 2003.
- [98] Paul Predecki and Charles S Barrett. Stress measurement in graphite/epoxy composites by x-ray diffraction from fillers. *Journal of composite materials*, 13(1):61–71, 1979.
- [99] R. Meske and E. Schnack. A Micromechanical Model for X-Ray Stress Analysis of Fiber Reinforced Composites. *Journal of Composite Materials*, 35(11):972–998, June 2001.
- [100] C. Balasingh and Vandana Singh. Measurement of residual stresses in CFRP laminates by X-ray diffraction method. *Bulletin of Materials Science*, 20(3):325–332, June 1997.
- [101] ASTM. Astm e837-01e1, standard test method for determining residual stresses by the hole-drilling strain-gage method, astm international, west conshohocken, pa, 2001, [www.astm.org](http://www.astm.org). 2001.
- [102] Josef Mathar. Determination of inherent stresses by measuring deformations of drilled holes. 1933.
- [103] W. Soete and R. Vancrombrugge. An industrial method for the determination of residual stresses. *Proc. SESA*, 8(1):17–28, 1950.

## REFERENCES

---

- [104] Charles W. Bert and Gary L. Thompson. A Method for Measuring Planar Residual Stresses in Rectangularly Orthotropic Materials. *Journal of Composite Materials*, 2(2):244–253, April 1968.
- [105] M. Bijak-Zochowski. A semidestructive method of measuring residual stresses. In (*Verein Deutscher Ingenieure, Internationale Konferenz ueber experimentelle Spannungsanalyse, 6 th, Munich, West Germany, Sept. 18-22, 1978.*) *VDI-Berichte*,, pages 469–476, 1978.
- [106] A. Niku-Lari, J. Lu, and J. F. Flavenot. Measurement of residual-stress distribution by the incremental hole-drilling method. *Journal of Mechanical Working Technology*, 11(2):167–188, May 1985.
- [107] M. T. Flaman and B. H. Manning. Determination of residual-stress variation with depth by the hole-drilling method. *Experimental Mechanics*, 25(3):205–207, September 1985.
- [108] G. S. Schajer and L. Yang. Residual-stress measurement in orthotropic materials using the hole-drilling method. *Experimental Mechanics*, 34(4):324–333, December 1994.
- [109] Jong-Ning Aoh and Chung-Sheng Wei. On the Improvement of Calibration Coefficients for Hole-Drilling Integral Method: Part I—Analysis of Calibration Coefficients Obtained by a 3-D FEM Model. *Journal of Engineering Materials and Technology*, 124(2):250–258, April 2002.
- [110] Mahmood M. Shokrieh and Ahmad R. Ghasemi K. Simulation of Central Hole Drilling Process for Measurement of Residual Stresses in Isotropic, Orthotropic, and Laminated Composite Plates. *Journal of Composite Materials*, 41(4):435–452, February 2007.
- [111] Michele Barsanti, Marco Beghini, Leonardo Bertini, Bernardo D Monelli, and Ciro Santus. First-order correction to counter the effect of eccentricity on the hole-drilling integral method with strain-gage rosettes , First-order correction to counter the effect of eccentricity on the hole-drilling integral method with strain-gage rosettes. *The Journal of Strain Analysis for Engineering Design*, 51(6):431–443, August 2016. Publisher: IMECHE.
- [112] Rodrigo Blödorn, Lucas Bonomo, Matias Viotti, Rolf Schroeter, and Albertazzi Jr. Calibration Coefficients Determination Through Fem Simulations for the Hole-Drilling Method Considering the Real Hole Geometry. *Experimental Techniques*, 41, September 2016.

## REFERENCES

---

- [113] G. S. Schajer. Compact Calibration Data for Hole-Drilling Residual Stress Measurements in Finite-Thickness Specimens. *Experimental Mechanics*, February 2020.
- [114] Tech Note TN-503 Micro-Measurements. Measurement of Residual Stresses by the Hole-Drilling\* Strain Gage Method, 2007.
- [115] GS Schajer and E Altus. Stress calculation error analysis for incremental hole-drilling residual stress measurements. *Journal of Engineering Materials and Technology*, 1996.
- [116] GS Schajer. Measurement of non-uniform residual stresses using the hole-drilling method. part i—stress calculation procedures. *Journal of Engineering Materials and Technology*, 1988.
- [117] Paulius Ragauskas and Rimantas Belevičius. Identification of material properties of composite materials. *Aviation*, 13(4):109–115, December 2009. Number: 4.
- [118] Dassault Systèmes Simulia. Abaqus Scripting User’s Guide (6.13).
- [119] Gary S. Schajer. Hole-Drilling Residual Stress Profiling With Automated Smoothing. *Journal of Engineering Materials and Technology*, 129(3):440–445, March 2007.
- [120] G. S. Schajer. Measurement of Non-Uniform Residual Stresses Using the Hole-Drilling Method. Part II—Practical Application of the Integral Method. *Journal of Engineering Materials and Technology*, 110(4):344–349, October 1988.
- [121] B. Zuccarello. Optimal calculation steps for the evaluation of residual stress by the incremental hole-drilling method. *Experimental Mechanics*, 39(2):117–124, June 1999.
- [122] A Ajovalasit. Measurement of residual stresses by the hole-drilling method: influence of hole eccentricity. *The journal of strain analysis for engineering design*, 14(4):171–178, 1979.
- [123] M. Beghini, L. Bertini, and L. F. Mori. Evaluating Non-Uniform Residual Stress by the Hole-Drilling Method With Concentric and Eccentric Holes. Part II: Application of the Influence Functions to the Inverse Problem. *Strain*, 46(4):337–346, 2010. \_eprint: <https://onlinelibrary.wiley.com/doi/pdf/10.1111/j.1475-1305.2009.00684.x>.
- [124] M. Beghini, L. Bertini, and L. F. Mori. Evaluating Non-Uniform Residual Stress by the Hole-Drilling Method with Concentric and Eccentric Holes. Part I. Definition and Validation of the Influence Functions. *Strain*, 46(4):324–336, 2010. \_eprint: <https://onlinelibrary.wiley.com/doi/pdf/10.1111/j.1475-1305.2009.00683.x>.

## REFERENCES

---

- [125] VPG | Performance through Precision: <http://www.vishaypg.com/docs/50001/sgaccess.pdf>.
- [126] NF EN ISO 527-5.
- [127] Standard - Fibre-reinforced plastics - Methods of producing test plates - Part 5: Filament winding ISO 1268-5.
- [128] ATOS 5: Industrial metrology | high-speed, high-precision.
- [129] A. R. Ghasemi, F. Taheri-Behrooz, and M. M. Shokrieh. 4 - Measuring residual stresses in composite materials using the simulated hole-drilling method. In Mahmood M. Shokrieh, editor, *Residual Stresses in Composite Materials*, pages 76–120. Woodhead Publishing, January 2014.
- [130] T. C. Smit, J. P. Nobre, R. G. Reid, T. Wu, T. Niendorf, D. Marais, and A. M. Venter. Assessment and Validation of Incremental Hole-Drilling Calculation Methods for Residual Stress Determination in Fiber-Metal Laminates. *Experimental Mechanics*, April 2022.



## *REFERENCES*

---

# Appendix A

## Expressions of coefficients $k_p^{ij}$ and $K_p^{ij}$

$$D_1 = (c_{ij11}c_{ij33} - c_{ij13}c_{ij31})$$

$$D_2 = (c_{ij11}c_{ij22}c_{ij33} - c_{ij13}c_{ij22}c_{ij31})$$

$$D_3 = (-c_{ij13}c_{ij22}c_{ij31} + c_{ij12}c_{ij23}c_{ij31} + c_{ij13}c_{ij21}c_{ij32} - c_{ij11}c_{ij23}c_{ij32} - c_{ij12}c_{ij21}c_{ij33} + c_{ij11}c_{ij22}c_{ij33})$$

### Coefficients $k_p$

$$k_1^{ij} = c_{ij33}/D_1$$

$$k_2^{ij} = -c_{ij13}/D_1$$

$$k_3^{ij} = -c_{ij31}/D_1$$

$$k_4^{ij} = c_{ij11}/D_1$$

$$k_5^{ij} = (c_{ij23}c_{ij31} - c_{ij21}c_{ij33})/D_2$$

$$k_6^{ij} = (c_{ij11}c_{ij33} - c_{ij13}c_{ij31})/D_2$$

$$k_7^{ij} = (c_{ij21}c_{ij13} - c_{ij11}c_{ij23})/D_2$$

$$k_8^{ij} = (c_{ij22}c_{ij33} - c_{ij23}c_{ij32})/D_3$$

---


$$k_9^{ij} = (c_{ij13}c_{ij32} - c_{ij12}c_{ij33})/D_3$$

$$k_{10}^{ij} = (c_{ij12}c_{ij23} - c_{ij13}c_{ij22})/D_3$$

$$k_{11}^{ij} = (c_{ij21}c_{ij32} - c_{ij22}c_{ij31})/D_3$$

$$k_{12}^{ij} = (c_{ij12}c_{ij31} - c_{ij11}c_{ij32})/D_3$$

$$k_{13}^{ij} = (c_{ij11}c_{ij22} - c_{ij12}c_{ij21})/D_3$$

$$k_{14}^{ij} = (c_{ij23}c_{ij31} - c_{ij21}c_{ij33})/D_3$$

$$k_{15}^{ij} = (c_{ij11}c_{ij33} - c_{ij13}c_{ij31})/D_3$$

$$k_{16}^{ij} = (c_{ij21}c_{ij13} - c_{ij11}c_{ij23})/D_3$$

## Coefficients $K_p$

$dc_{ijkl}$  : variation of coefficients  $c_{ijkl}$

$$K_1^{ij} = (-c_{ij13}c_{ij31}dc_{ij33} + c_{ij31}c_{ij33}dc_{ij13} - c_{ij33}^2dc_{ij11} + c_{ij13}c_{ij33}dc_{ij31})/D_1^2$$

$$K_2^{ij} = (c_{ij11}c_{ij13}dc_{ij33} - c_{ij11}c_{ij33}dc_{ij13} + c_{ij13}c_{ij33}dc_{ij11} - c_{ij13}^2dc_{ij31})/D_1^2$$

$$K_3^{ij} = (-c_{ij11}c_{ij33}dc_{ij31} + c_{ij31}c_{ij33}dc_{ij11} + c_{ij11}c_{ij31}dc_{ij33} - c_{ij31}^2dc_{ij13})/D_1^2$$

$$K_4^{ij} = (c_{ij11}c_{ij13}dc_{ij31} - c_{ij13}c_{ij31}dc_{ij11} - c_{ij11}^2dc_{ij33} + c_{ij11}c_{ij31}dc_{ij13})/D_1^2$$

$$K_5^{ij} = (D_2c_{ij31}dc_{ij23} + (c_{ij23}c_{ij11}c_{ij22}c_{ij33} - c_{ij13}c_{ij22}c_{ij21}c_{ij33})dc_{ij31} - D_2c_{ij33}dc_{ij21} + (c_{ij21}c_{ij13}c_{ij22}c_{ij31} - c_{ij11}c_{ij22}c_{ij23}c_{ij31})dc_{ij33} + (c_{ij22}c_{ij33}^2c_{ij21} - c_{ij22}c_{ij33}c_{ij23}c_{ij31})dc_{ij11} + (c_{ij22}c_{ij31}^2c_{ij23} - c_{ij22}c_{ij31}c_{ij21}c_{ij33})dc_{ij13})/D_2^2$$

$$K_6^{ij} = (-D_2c_{ij11}dc_{ij23} + (c_{ij13}^2c_{ij22}c_{ij21} - c_{ij13}c_{ij22}c_{ij11}c_{ij23})dc_{ij31} + D_2c_{ij13}dc_{ij21} + (c_{ij11}^2c_{ij22}c_{ij23} - c_{ij11}c_{ij22}c_{ij21}c_{ij13})dc_{ij33} + (c_{ij23}c_{ij13}c_{ij22}c_{ij31} - c_{ij22}c_{ij33}c_{ij21}c_{ij13})dc_{ij11} + (c_{ij21}c_{ij11}c_{ij22}c_{ij33} - c_{ij22}c_{ij31}c_{ij11}c_{ij23})dc_{ij13})/D_2^2$$

$$\begin{aligned}
 K_7^{ij} = & -(c_{ij23}^2 c_{ij32}^2 dc_{ij11} - 2c_{ij22} c_{ij23} c_{ij32} c_{ij33} dc_{ij11} + c_{ij22}^2 c_{ij33}^2 dc_{ij11} - c_{ij23}^2 c_{ij31} c_{ij32} dc_{ij12} + \\
 & c_{ij22} c_{ij23} c_{ij31} c_{ij33} dc_{ij12} + c_{ij21} c_{ij23} c_{ij32} c_{ij33} dc_{ij12} - c_{ij21} c_{ij22} c_{ij33}^2 dc_{ij12} + c_{ij22} c_{ij23} c_{ij31} c_{ij32} dc_{ij13} - \\
 & c_{ij21} c_{ij23} c_{ij32}^2 dc_{ij13} - c_{ij22}^2 c_{ij31} c_{ij33} dc_{ij13} + c_{ij21} c_{ij22} c_{ij32} c_{ij33} dc_{ij13} - c_{ij13} c_{ij23} c_{ij32}^2 dc_{ij21} + c_{ij13} c_{ij22} \\
 & c_{ij32} c_{ij33} dc_{ij21} + c_{ij12} c_{ij23} c_{ij32} c_{ij33} dc_{ij21} - c_{ij12} c_{ij22} c_{ij33}^2 dc_{ij21} + c_{ij13} c_{ij23} c_{ij31} c_{ij32} dc_{ij22} - c_{ij12} c_{ij23} \\
 & c_{ij31} c_{ij33} dc_{ij22} - c_{ij13} c_{ij21} c_{ij32} c_{ij33} dc_{ij22} + c_{ij12} c_{ij21} c_{ij33}^2 dc_{ij22} - c_{ij13} c_{ij22} c_{ij31} c_{ij32} dc_{ij23} + c_{ij13} c_{ij21} \\
 & c_{ij32}^2 dc_{ij23} + c_{ij12} c_{ij22} c_{ij31} c_{ij33} dc_{ij23} - c_{ij12} c_{ij21} c_{ij32} c_{ij33} dc_{ij23} + c_{ij13} c_{ij22} c_{ij23} c_{ij32} dc_{ij31} - c_{ij12} c_{ij23}^2 \\
 & c_{ij32} dc_{ij31} - c_{ij13} c_{ij22}^2 c_{ij33} dc_{ij31} + c_{ij12} c_{ij22} c_{ij23} c_{ij33} dc_{ij31} - c_{ij13} c_{ij22} c_{ij23} c_{ij31} dc_{ij32} + c_{ij12} c_{ij23}^2 c_{ij31} \\
 & dc_{ij32} + c_{ij13} c_{ij21} c_{ij22} c_{ij33} dc_{ij32} - c_{ij12} c_{ij21} c_{ij23} c_{ij33} dc_{ij32} + c_{ij13} c_{ij22}^2 c_{ij31} dc_{ij33} - c_{ij12} c_{ij22} c_{ij23} c_{ij31} dc_{ij33} - \\
 & c_{ij13} c_{ij21} c_{ij22} c_{ij32} dc_{ij33} + c_{ij12} c_{ij21} c_{ij23} c_{ij32} dc_{ij33}) / D_3^2
 \end{aligned}$$

$$\begin{aligned}
 K_8^{ij} = & -(-c_{ij13} c_{ij23} c_{ij32}^2 dc_{ij11} + c_{ij13} c_{ij22} c_{ij32} c_{ij33} dc_{ij11} + c_{ij12} c_{ij23} c_{ij32} c_{ij33} dc_{ij11} - c_{ij12} c_{ij22} c_{ij33}^2 dc_{ij11} + \\
 & c_{ij13} c_{ij23} c_{ij31} c_{ij32} dc_{ij12} - c_{ij13} c_{ij22} c_{ij31} c_{ij33} dc_{ij12} - c_{ij11} c_{ij23} c_{ij32} c_{ij33} dc_{ij12} + c_{ij11} c_{ij22} c_{ij33}^2 dc_{ij12} - \\
 & c_{ij12} c_{ij23} c_{ij31} c_{ij32} dc_{ij13} + c_{ij11} c_{ij23} c_{ij32}^2 dc_{ij13} + c_{ij12} c_{ij22} c_{ij31} c_{ij33} dc_{ij13} - c_{ij11} c_{ij22} c_{ij32} c_{ij33} dc_{ij13} + \\
 & c_{ij13}^2 c_{ij32}^2 dc_{ij21} - 2c_{ij12} c_{ij13} c_{ij32} c_{ij33} dc_{ij21} + c_{ij12}^2 c_{ij33}^2 dc_{ij21} - c_{ij13}^2 c_{ij31} c_{ij32} dc_{ij22} + c_{ij12} c_{ij13} c_{ij31} c_{ij33} dc_{ij22} + \\
 & c_{ij11} c_{ij13} c_{ij32} c_{ij33} dc_{ij22} - c_{ij11} c_{ij12} c_{ij33}^2 dc_{ij22} + c_{ij12} c_{ij13} c_{ij31} c_{ij32} dc_{ij23} - c_{ij11} c_{ij13} c_{ij32}^2 dc_{ij23} - \\
 & c_{ij12}^2 c_{ij31} c_{ij33} dc_{ij23} + c_{ij11} c_{ij12} c_{ij32} c_{ij33} dc_{ij23} - c_{ij13}^2 c_{ij22} c_{ij32} dc_{ij31} + c_{ij12} c_{ij13} c_{ij23} c_{ij32} dc_{ij31} + \\
 & c_{ij12} c_{ij13} c_{ij22} c_{ij33} dc_{ij31} - c_{ij12}^2 c_{ij23} c_{ij33} dc_{ij31} + c_{ij13}^2 c_{ij22} c_{ij31} dc_{ij32} - c_{ij12} c_{ij13} c_{ij23} c_{ij31} dc_{ij32} - \\
 & c_{ij11} c_{ij13} c_{ij22} c_{ij33} dc_{ij32} + c_{ij11} c_{ij12} c_{ij23} c_{ij33} dc_{ij32} - c_{ij12} c_{ij13} c_{ij22} c_{ij31} dc_{ij33} + c_{ij12}^2 c_{ij23} c_{ij31} dc_{ij33} + \\
 & c_{ij11} c_{ij13} c_{ij22} c_{ij32} dc_{ij33} - c_{ij11} c_{ij12} c_{ij23} c_{ij32} dc_{ij33}) / D_3^2
 \end{aligned}$$

$$\begin{aligned}
 K_9^{ij} = & -(c_{ij13} c_{ij22} c_{ij23} c_{ij32} dc_{ij11} - c_{ij12} c_{ij23}^2 c_{ij32} dc_{ij11} - c_{ij13} c_{ij22}^2 c_{ij33} dc_{ij11} + c_{ij12} c_{ij22} c_{ij23} c_{ij33} dc_{ij11} - \\
 & c_{ij13} c_{ij21} c_{ij23} c_{ij32} dc_{ij12} + c_{ij11} c_{ij23}^2 c_{ij32} dc_{ij12} + c_{ij13} c_{ij21} c_{ij22} c_{ij33} dc_{ij12} - c_{ij11} c_{ij22} c_{ij23} c_{ij33} dc_{ij12} + \\
 & c_{ij12} c_{ij21} c_{ij23} c_{ij32} dc_{ij13} - c_{ij11} c_{ij22} c_{ij23} c_{ij32} dc_{ij13} - c_{ij12} c_{ij21} c_{ij22} c_{ij33} dc_{ij13} + c_{ij11} c_{ij22}^2 c_{ij33} dc_{ij13} - \\
 & c_{ij13}^2 c_{ij22} c_{ij32} dc_{ij21} + c_{ij12} c_{ij13} c_{ij23} c_{ij32} dc_{ij21} + c_{ij12} c_{ij13} c_{ij22} c_{ij33} dc_{ij21} - c_{ij12}^2 c_{ij23} c_{ij33} dc_{ij21} + \\
 & c_{ij13}^2 c_{ij21} c_{ij32} dc_{ij22} - c_{ij11} c_{ij13} c_{ij23} c_{ij32} dc_{ij22} - c_{ij12} c_{ij13} c_{ij21} c_{ij33} dc_{ij22} + c_{ij11} c_{ij12} c_{ij23} c_{ij33} dc_{ij22} - \\
 & c_{ij12} c_{ij13} c_{ij21} c_{ij32} dc_{ij23} + c_{ij11} c_{ij13} c_{ij22} c_{ij32} dc_{ij23} + c_{ij12}^2 c_{ij21} c_{ij33} dc_{ij23} - c_{ij11} c_{ij12} c_{ij22} c_{ij33} dc_{ij23} + \\
 & c_{ij13}^2 c_{ij22}^2 dc_{ij31} - 2c_{ij12} c_{ij13} c_{ij22} c_{ij23} dc_{ij31} + c_{ij12}^2 c_{ij23}^2 dc_{ij31} - c_{ij13}^2 c_{ij21} c_{ij22} dc_{ij32} + c_{ij12} c_{ij13} c_{ij21} c_{ij23} dc_{ij32} + \\
 & c_{ij11} c_{ij13} c_{ij22} c_{ij23} dc_{ij32} - c_{ij11} c_{ij12} c_{ij23}^2 dc_{ij32} + c_{ij12} c_{ij13} c_{ij21} c_{ij22} dc_{ij33} - c_{ij11} c_{ij13} c_{ij22}^2 dc_{ij33} - \\
 & c_{ij12}^2 c_{ij21} c_{ij23} dc_{ij33} + c_{ij11} c_{ij12} c_{ij22} c_{ij23} dc_{ij33}) / D_3^2
 \end{aligned}$$

$$\begin{aligned}
 K_{10}^{ij} = & -(c_{ij22} c_{ij23} c_{ij31} c_{ij32} dc_{ij11} - c_{ij21} c_{ij23} c_{ij32}^2 dc_{ij11} - c_{ij22}^2 c_{ij31} c_{ij33} dc_{ij11} + c_{ij21} c_{ij22} c_{ij32} c_{ij33} dc_{ij11} - \\
 & c_{ij22} c_{ij23} c_{ij31}^2 dc_{ij12} + c_{ij21} c_{ij23} c_{ij31} c_{ij32} dc_{ij12} + c_{ij21} c_{ij22} c_{ij31} c_{ij33} dc_{ij12} - c_{ij21}^2 c_{ij32} c_{ij33} dc_{ij12} + \\
 & c_{ij22}^2 c_{ij31}^2 dc_{ij13} - 2c_{ij21} c_{ij22} c_{ij31} c_{ij32} dc_{ij13} + c_{ij21}^2 c_{ij32}^2 dc_{ij13} - c_{ij12} c_{ij23} c_{ij31} c_{ij32} dc_{ij21} + c_{ij11} c_{ij23} c_{ij32}^2 dc_{ij21} + \\
 & c_{ij12} c_{ij22} c_{ij31} c_{ij33} dc_{ij21} - c_{ij11} c_{ij22} c_{ij32} c_{ij33} dc_{ij21} + c_{ij12} c_{ij23} c_{ij31}^2 dc_{ij22} - c_{ij11} c_{ij23} c_{ij31} c_{ij32} dc_{ij22} - \\
 & c_{ij12} c_{ij21} c_{ij31} c_{ij33} dc_{ij22} + c_{ij11} c_{ij21} c_{ij32} c_{ij33} dc_{ij22} - c_{ij12} c_{ij22} c_{ij31}^2 dc_{ij23} + c_{ij12} c_{ij21} c_{ij31} c_{ij32} dc_{ij23} + \\
 & c_{ij11} c_{ij22} c_{ij31} c_{ij32} dc_{ij23} - c_{ij11} c_{ij21} c_{ij32}^2 dc_{ij23} + c_{ij12} c_{ij21} c_{ij23} c_{ij32} dc_{ij31} - c_{ij11} c_{ij22} c_{ij23} c_{ij32} dc_{ij31} - \\
 & c_{ij12} c_{ij21} c_{ij22} c_{ij33} dc_{ij31} + c_{ij11} c_{ij22}^2 c_{ij33} dc_{ij31} - c_{ij12} c_{ij21} c_{ij23} c_{ij31} dc_{ij32} + c_{ij11} c_{ij22} c_{ij23} c_{ij31} dc_{ij32} + \\
 & c_{ij12} c_{ij21} c_{ij33} dc_{ij32} - c_{ij11} c_{ij21} c_{ij22} c_{ij33} dc_{ij32} + c_{ij12} c_{ij21} c_{ij22} c_{ij31} dc_{ij33} - c_{ij11} c_{ij22}^2 c_{ij31} dc_{ij33} -
 \end{aligned}$$



$$\begin{aligned}
& c_{ij13}^2 c_{ij31}^2 dc_{ij22} - 2c_{ij11} c_{ij13} c_{ij31} c_{ij33} dc_{ij22} + c_{ij11}^2 c_{ij33}^2 dc_{ij22} - c_{ij12} c_{ij13} c_{ij31}^2 dc_{ij23} + c_{ij11} c_{ij13} c_{ij31} c_{ij32} dc_{ij23} + \\
& c_{ij11} c_{ij12} c_{ij31} c_{ij33} dc_{ij23} - c_{ij11}^2 c_{ij32} c_{ij33} dc_{ij23} + c_{ij13}^2 c_{ij21} c_{ij32} dc_{ij31} - c_{ij11} c_{ij13} c_{ij23} c_{ij32} dc_{ij31} - \\
& c_{ij12} c_{ij13} c_{ij21} c_{ij33} dc_{ij31} + c_{ij11} c_{ij12} c_{ij23} c_{ij33} dc_{ij31} - c_{ij13}^2 c_{ij21} c_{ij31} dc_{ij32} + c_{ij11} c_{ij13} c_{ij23} c_{ij31} dc_{ij32} + \\
& c_{ij11} c_{ij13} c_{ij21} c_{ij33} dc_{ij32} - c_{ij11}^2 c_{ij23} c_{ij33} dc_{ij32} + c_{ij12} c_{ij13} c_{ij21} c_{ij31} dc_{ij33} - c_{ij11} c_{ij12} c_{ij23} c_{ij31} dc_{ij33} - \\
& c_{ij11} c_{ij13} c_{ij21} c_{ij32} dc_{ij33} + c_{ij11}^2 c_{ij23} c_{ij32} dc_{ij33} ) / D_3^2
\end{aligned}$$

$$\begin{aligned}
K_{15}^{ij} = & -(-c_{ij13} c_{ij22} c_{ij23} c_{ij31} dc_{ij11} + c_{ij12} c_{ij23}^2 c_{ij31} dc_{ij11} + c_{ij13} c_{ij21} c_{ij22} c_{ij33} dc_{ij11} - c_{ij12} c_{ij21} c_{ij23} c_{ij33} \\
& dc_{ij11} + c_{ij13} c_{ij21} c_{ij23} c_{ij31} dc_{ij12} - c_{ij11} c_{ij23}^2 c_{ij31} dc_{ij12} - c_{ij13} c_{ij21}^2 c_{ij33} dc_{ij12} + c_{ij11} c_{ij21} c_{ij23} c_{ij33} dc_{ij12} - \\
& c_{ij12} c_{ij21} c_{ij23} c_{ij31} dc_{ij13} + c_{ij11} c_{ij22} c_{ij23} c_{ij31} dc_{ij13} + c_{ij12} c_{ij21}^2 c_{ij33} dc_{ij13} - c_{ij11} c_{ij21} c_{ij22} c_{ij33} dc_{ij13} + \\
& c_{ij13}^2 c_{ij22} c_{ij31} dc_{ij21} - c_{ij12} c_{ij13} c_{ij23} c_{ij31} dc_{ij21} - c_{ij11} c_{ij13} c_{ij22} c_{ij33} dc_{ij21} + c_{ij11} c_{ij12} c_{ij23} c_{ij33} dc_{ij21} - \\
& c_{ij13}^2 c_{ij21} c_{ij31} dc_{ij22} + c_{ij11} c_{ij13} c_{ij23} c_{ij31} dc_{ij22} + c_{ij11} c_{ij13} c_{ij21} c_{ij33} dc_{ij22} - c_{ij11}^2 c_{ij23} c_{ij33} dc_{ij22} + \\
& c_{ij12} c_{ij13} c_{ij21} c_{ij31} dc_{ij23} - c_{ij11} c_{ij13} c_{ij22} c_{ij31} dc_{ij23} - c_{ij11} c_{ij12} c_{ij21} c_{ij33} dc_{ij23} + c_{ij11}^2 c_{ij22} c_{ij33} dc_{ij23} - \\
& c_{ij13}^2 c_{ij21} c_{ij22} dc_{ij31} + c_{ij12} c_{ij13} c_{ij21} c_{ij23} dc_{ij31} + c_{ij11} c_{ij13} c_{ij22} c_{ij23} dc_{ij31} - c_{ij11} c_{ij12} c_{ij23}^2 dc_{ij31} + \\
& c_{ij13}^2 c_{ij21}^2 dc_{ij32} - 2c_{ij11} c_{ij13} c_{ij21} c_{ij23} dc_{ij32} + c_{ij11}^2 c_{ij23}^2 dc_{ij32} - c_{ij12} c_{ij13} c_{ij21}^2 dc_{ij33} + c_{ij11} c_{ij13} c_{ij21} c_{ij22} dc_{ij33} + \\
& c_{ij11} c_{ij12} c_{ij21} c_{ij23} dc_{ij33} - c_{ij11}^2 c_{ij22} c_{ij23} dc_{ij33} ) / D_3^2
\end{aligned}$$



## Appendix B

Numerical relaxation strains ( $\epsilon_k^i$ ), calibration coefficients ( $c_{ijgs}$ ) and  $[S_{ii}]$  matrices used for the numerical validation of the correction method (presented in section 3.3 of chapter 3)



Table B.1 – Numerical relaxation strains and  $[S_{ii}]$  matrices used for the numerical validation of the correction method (section 3.3 of chapter 3)

Numerical relaxation strains ( $\epsilon_k^i$ )	Reference	Eccentric hole, 10% of $r_m$	$[S_{ii}]$
$\epsilon_1^1$	3.17e-06	4.36e-06	$[S_{11}] = \begin{bmatrix} 0.72 & 0 & 0 \\ 0 & 1.58 & 0 \\ 0 & 0 & 1.05 \end{bmatrix}$
$\epsilon_2^1$	2.38e-06	1.50e-06	
$\epsilon_3^1$	3.57e-06	3.41e-06	
$\epsilon_1^2$	116.52e-06	145.39e-06	$[S_{22}] = \begin{bmatrix} 0.80 & 0 & 0 \\ 0 & 11.51 & 0 \\ 0 & 0 & 1.10 \end{bmatrix}$
$\epsilon_2^2$	51.41e-06	6.50e-06	
$\epsilon_3^2$	45.03e-06	41.08e-06	
$\epsilon_1^3$	605.58e-06	679.27e-06	$[S_{33}] = \begin{bmatrix} 0.92 & 0 & 0 \\ 0 & 5.11 & 0 \\ 0 & 0 & 1.05 \end{bmatrix}$
$\epsilon_2^3$	348.37e-06	79.08e-06	
$\epsilon_3^3$	240.60e-06	226.49e-06	
$\epsilon_1^4$	795.35e-06	846.04e-06	$[S_{44}] = \begin{bmatrix} 0.19 & 0 & 0 \\ 0 & -0.11 & 0 \\ 0 & 0 & 1.00 \end{bmatrix}$
$\epsilon_2^4$	499.11e-06	235.88e-06	
$\epsilon_3^4$	309.63e-06	290.74e-06	
$\epsilon_1^5$	870.33e-06	907.26e-06	$[S_{55}] = \begin{bmatrix} 1.30 & 0 & 0 \\ 0 & 1.29 & 0 \\ 0 & 0 & 0.99 \end{bmatrix}$
$\epsilon_2^5$	723.12e-06	403.90e-06	
$\epsilon_3^5$	640.37e-06	614.60e-06	
$\epsilon_1^6$	775.55e-06	791.47e-06	$[S_{66}] = \begin{bmatrix} 0.86 & 0 & 0 \\ 0 & 0.68 & 0 \\ 0 & 0 & 1.02 \end{bmatrix}$
$\epsilon_2^6$	933.12e-06	665.85e-06	
$\epsilon_3^6$	1106.52e-06	1069.2e-06	

ANNEXE B

Table B.2 – Calibration coefficients ( $c_{ijkl}$ ) used for the numerical validation of the correction method (Table 6 of the paper).

$c_{ijkl}$	j=1	j=2	j=3	j=4	j=5	j=6
i=1	$\begin{bmatrix} -0.0291 & 0 & 0.0008 \\ -0.0106 & -0.0713 & -0.0268 \\ -0.0014 & 0 & -0.0545 \end{bmatrix}$					
i=2	$\begin{bmatrix} -0.0459 & 0 & 0.0006 \\ -0.0160 & -0.0810 & -0.0306 \\ -0.0017 & 0 & -0.0693 \end{bmatrix}$	$\begin{bmatrix} -0.0264 & 0 & 0.0017 \\ -0.0113 & -0.0723 & -0.0263 \\ -0.0002 & 0 & -0.0535 \end{bmatrix}$				
i=3	$\begin{bmatrix} -0.0532 & 0 & 0.0005 \\ -0.0198 & -0.0884 & -0.0348 \\ -0.0015 & 0 & -0.0799 \end{bmatrix}$	$\begin{bmatrix} -0.0350 & 0 & 0.0020 \\ -0.0158 & -0.0816 & -0.0313 \\ 0.0002 & 0 & -0.0665 \end{bmatrix}$	$\begin{bmatrix} -0.0175 & 0 & 0.0020 \\ -0.0100 & -0.0641 & -0.0204 \\ 0.0008 & 0 & -0.0483 \end{bmatrix}$			
i=4	$\begin{bmatrix} -0.0583 & 0 & 0.0007 \\ -0.0235 & -0.0931 & -0.037 \\ -0.0010 & 0 & -0.0864 \end{bmatrix}$	$\begin{bmatrix} -0.0404 & 0 & 0.0023 \\ -0.0197 & -0.0868 & -0.0335 \\ 0.0009 & 0 & -0.0733 \end{bmatrix}$	$\begin{bmatrix} -0.0244 & 0 & 0.0024 \\ -0.0150 & -0.0714 & -0.0235 \\ 0.0018 & 0 & -0.0577 \end{bmatrix}$	$\begin{bmatrix} -0.0146 & 0 & 0.0016 \\ -0.0114 & -0.0569 & -0.0147 \\ 0.0023 & 0 & -0.0370 \end{bmatrix}$		
i=5	$\begin{bmatrix} -0.0590 & 0 & 0.0009 \\ -0.0241 & -0.0968 & -0.0428 \\ -0.0008 & 0 & -0.1025 \end{bmatrix}$	$\begin{bmatrix} -0.0411 & 0 & 0.0027 \\ -0.0202 & -0.0907 & -0.0395 \\ 0.0013 & 0 & -0.0902 \end{bmatrix}$	$\begin{bmatrix} -0.0251 & 0 & 0.0029 \\ -0.0156 & -0.0759 & -0.0300 \\ 0.0024 & 0 & -0.0760 \end{bmatrix}$	$\begin{bmatrix} -0.0157 & 0 & 0.00023 \\ -0.0123 & -0.0632 & -0.0223 \\ 0.0030 & 0 & -0.0588 \end{bmatrix}$	$\begin{bmatrix} -0.0114 & 0 & 0.0014 \\ -0.0102 & -0.0504 & -0.0137 \\ 0.0036 & 0 & -0.0357 \end{bmatrix}$	
i=6	$\begin{bmatrix} -0.0595 & 0 & 0.0010 \\ -0.0246 & -0.0989 & -0.0461 \\ -0.007 & 0 & -0.1106 \end{bmatrix}$	$\begin{bmatrix} -0.0416 & 0 & 0.0029 \\ -0.0207 & -0.0928 & -0.0427 \\ 0.0016 & 0 & -0.09832 \end{bmatrix}$	$\begin{bmatrix} -0.0256 & 0 & 0.0032 \\ -0.0160 & -0.0782 & -0.0332 \\ 0.0028 & 0 & -0.0841 \end{bmatrix}$	$\begin{bmatrix} -0.0164 & 0 & 0.0027 \\ -0.0129 & -0.0661 & -0.0257 \\ 0.0036 & 0 & -0.0673 \end{bmatrix}$	$\begin{bmatrix} -0.0132 & 0 & 0.0018 \\ -0.0117 & -0.0559 & -0.0178 \\ 0.0048 & 0 & -0.0461 \end{bmatrix}$	$\begin{bmatrix} -0.0096 & 0 & 0.0011 \\ -0.0094 & -0.0422 & -0.0102 \\ 0.0050 & 0 & -0.0218 \end{bmatrix}$

Table B.3 – Comparison between the reference residual stresses, the corrected residual stresses and residual stresses with an angular deviation of the gages obtained by numerical simulations of the incremental hole drilling for the initial residual stress profile 1 (stress profile used in Table 6 of the paper).

Residual stresses	Reference (MPa)	Angular deviation of the gages, 10 degrees (MPa)	Corrected (MPa)	$[S_{ii}]$
$\sigma_x^1$	-5.79	-4.76	-5.79	$[S_{11}] = \begin{bmatrix} 1.22 & 0 & 0 \\ 0 & 0.98 & 0 \\ 0 & 0 & 1.14 \end{bmatrix}$
$\sigma_{xy}^1$	0.35	-0.02	0.35	
$\sigma_y^1$	-3.28	-2.89	-3.28	
$\sigma_x^2$	-223.50	-171.00	-223.50	$[S_{22}] = \begin{bmatrix} 1.31 & 0 & 0 \\ 0 & 1.99 & 0 \\ 0 & 0 & 0.87 \end{bmatrix}$
$\sigma_{xy}^2$	14.11	25.50	14.11	
$\sigma_y^2$	-38.76	-44.93	-38.76	
$\sigma_x^3$	-1372.29	-1013.75	-1372.29	$[S_{33}] = \begin{bmatrix} 1.36 & 0 & 0 \\ 0 & 1.93 & 0 \\ 0 & 0 & 1.01 \end{bmatrix}$
$\sigma_{xy}^3$	62.68	111.93	62.68	
$\sigma_y^3$	-227.58	-217.72	-227.58	
$\sigma_x^4$	28.66	37.75	28.66	$[S_{44}] = \begin{bmatrix} 0.81 & 0 & 0 \\ 0 & 0.07 & 0 \\ 0 & 0 & 1.07 \end{bmatrix}$
$\sigma_{xy}^4$	15.07	38.32	15.07	
$\sigma_y^4$	-72.10	-66.55	-72.10	
$\sigma_x^5$	-300.24	-231.22	-300.24	$[S_{55}] = \begin{bmatrix} 1.32 & 0 & 0 \\ 0 & 0.78 & 0 \\ 0 & 0 & 1.18 \end{bmatrix}$
$\sigma_{xy}^5$	-19.91	-100.02	-19.91	
$\sigma_y^5$	-359.27	-300.41	-359.27	
$\sigma_x^6$	533.35	315.77	533.35	$[S_{66}] = \begin{bmatrix} 1.61 & 0 & 0 \\ 0 & 0.41 & 0 \\ 0 & 0 & 1.31 \end{bmatrix}$
$\sigma_{xy}^6$	-115.81	-356.19	-115.81	
$\sigma_y^6$	-739.31	-585.92	-739.31	

Table B.4 – Comparison between the reference residual stresses, the corrected residual stresses and residual stresses with an eccentric hole obtained by numerical simulations of the incremental hole drilling for the initial residual stress profile 2.

Residual stresses	Reference (MPa)	Eccentric hole, 10% of $r_m$ (MPa)	Corrected (MPa)	$[S_{ii}]$
$\sigma_x^1$	-22.53	-29.97	-20.57	$[S_{11}] = \begin{bmatrix} 0.74 & 0 & 0 \\ 0 & 1.36 & 0 \\ 0 & 0 & 1.03 \end{bmatrix}$
$\sigma_{xy}^1$	2.67	6.31	2.67	
$\sigma_y^1$	-27.43	-26.39	-27.43	
$\sigma_x^2$	56.45	77.56	56.45	$[S_{22}] = \begin{bmatrix} 0.74 & 0 & 0 \\ 0 & 0.70 & 0 \\ 0 & 0 & 1.05 \end{bmatrix}$
$\sigma_{xy}^2$	0.77	-10.70	0.77	
$\sigma_y^2$	-71.12	-67.41	-71.12	
$\sigma_x^3$	34.05	38.69	34.05	$[S_{33}] = \begin{bmatrix} 0.92 & 0 & 0 \\ 0 & 0.83 & 0 \\ 0 & 0 & 1.07 \end{bmatrix}$
$\sigma_{xy}^3$	0.66	-7.68	0.66	
$\sigma_y^3$	-102.41	-94.80	-102.41	
$\sigma_x^4$	11.03	4.98	11.21	$[S_{44}] = \begin{bmatrix} 1.79 & 0 & 0 \\ 0 & 0.64 & 0 \\ 0 & 0 & 1.09 \end{bmatrix}$
$\sigma_{xy}^4$	-1.63	-4.84	-1.63	
$\sigma_y^4$	-28.93	-26.73	-28.93	
$\sigma_x^5$	-12.54	-20.01	-12.54	$[S_{55}] = \begin{bmatrix} 0.88 & 0 & 0 \\ 0 & 0.92 & 0 \\ 0 & 0 & 1.07 \end{bmatrix}$
$\sigma_{xy}^5$	-2.01	9.07	-2.01	
$\sigma_y^5$	241.00	223.53	241.00	
$\sigma_x^6$	-8.72	-7.97	-8.72	$[S_{66}] = \begin{bmatrix} 1.08 & 0 & 0 \\ 0 & 0.69 & 0 \\ 0 & 0 & 1.07 \end{bmatrix}$
$\sigma_{xy}^6$	-3.48	0.13	-3.48	
$\sigma_y^6$	49.53	46.05	49.53	

Table B.5 – Comparison between the reference residual stresses, the corrected residual stresses and residual stresses with an eccentric hole obtained by numerical simulations of the incremental hole drilling for the initial residual stress profile 3.

Residual stresses	Reference (MPa)	Eccentric hole, 10% of $r_m$ (MPa)	Corrected (MPa)	$[S_{ii}]$
$\sigma_x^1$	-16.06	-25.55	-16.06	$[S_{11}] = \begin{bmatrix} 0.64 & 0 & 0 \\ 0 & 0.63 & 0 \\ 0 & 0 & 1.08 \end{bmatrix}$
$\sigma_{xy}^1$	-1.65	3.72	-1.65	
$\sigma_y^1$	26.17	24.41	26.17	
$\sigma_x^2$	-11.03	-11.73	-11.03	$[S_{22}] = \begin{bmatrix} 0.95 & 0 & 0 \\ 0 & 0.78 & 0 \\ 0 & 0 & 1.03 \end{bmatrix}$
$\sigma_{xy}^2$	0.08	2.50	0.08	
$\sigma_y^2$	25.41	24.65	25.41	
$\sigma_x^3$	-12.18	-12.03	-12.18	$[S_{33}] = \begin{bmatrix} 1.03 & 0 & 0 \\ 0 & 0.82 & 0 \\ 0 & 0 & 1.09 \end{bmatrix}$
$\sigma_{xy}^3$	0.05	2.45	0.05	
$\sigma_y^3$	29.33	26.79	29.33	
$\sigma_x^4$	-3.35	-1.79	-3.35	$[S_{44}] = \begin{bmatrix} 1.30 & 0 & 0 \\ 0 & 0.89 & 0 \\ 0 & 0 & 1.06 \end{bmatrix}$
$\sigma_{xy}^4$	0.53	1.96	0.53	
$\sigma_y^4$	39.79	37.52	39.79	
$\sigma_x^5$	-1.28	1.08	-1.28	$[S_{55}] = \begin{bmatrix} 0.84 & 0 & 0 \\ 0 & 0.92 & 0 \\ 0 & 0 & 1.07 \end{bmatrix}$
$\sigma_{xy}^5$	1.28	-2.34	1.28	
$\sigma_y^5$	-80.56	-75.03	-80.56	
$\sigma_x^6$	3.35	4.07	3.35	$[S_{66}] = \begin{bmatrix} 0.97 & 0 & 0 \\ 0 & 0.85 & 0 \\ 0 & 0 & 1.07 \end{bmatrix}$
$\sigma_{xy}^6$	2.19	-0.33	2.19	
$\sigma_y^6$	-49.23	-45.61	-49.23	

## Appendix C

### Influence of rotational speed on the damage of the hole surface

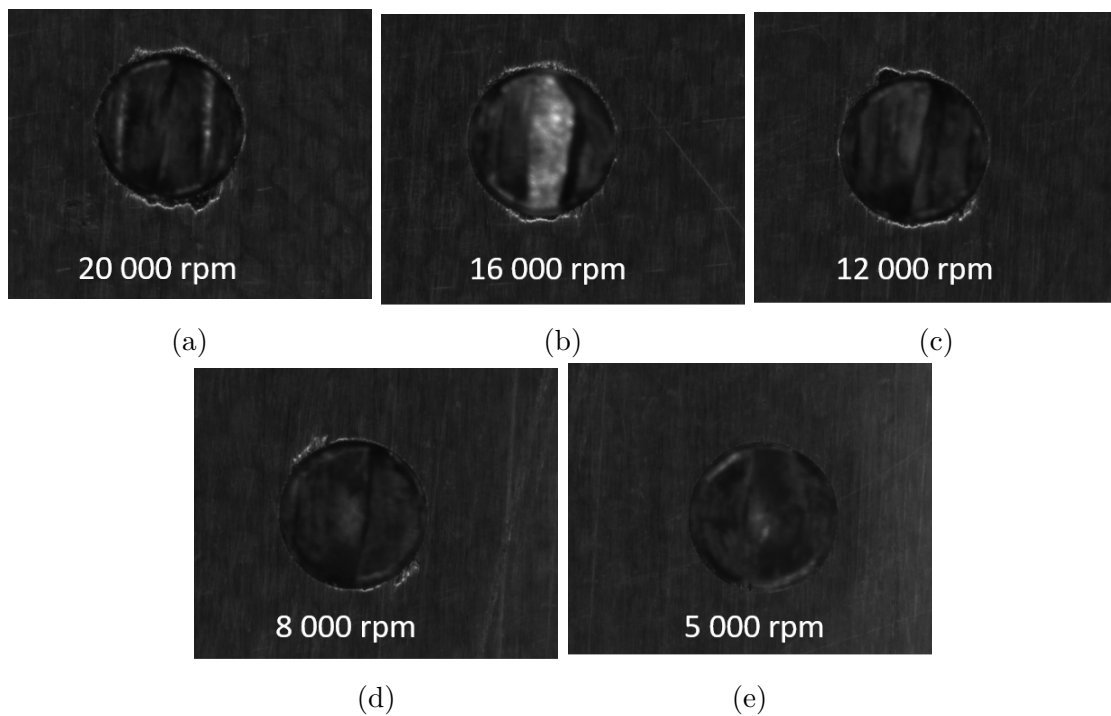


Figure C.1 – Damage on the surface of the hole as function of the rotation speed: (a) 20000 rpm , (b) 16000 rpm, (c) 12000 rpm, (d) 8000 rpm, (e) 5000 rpm

One can observe that the damage on the surface of the composite is minimal for 5000 rpm. From these observations, one can conclude that (in terms of surface damage) the optimal rotation speed is 5000 rpm.



# Appendix D

## Influence of the withdrawal speed of the milling cutter on the shape of the raw acquisition data

The withdrawal speed of the milling cutter (after the drilling of an increment) is varied from 0.1 mm/s to 10 mm/s in the same test in order to study its effect on the raw acquisition data of the relaxation strains. One can observe that the withdrawal speed of the milling cutter has no significant effect on raw acquisition data. Therefore, a high withdrawal speed is considered to limit the duration of the experimental measurement of the relaxation strains by the IHDM.

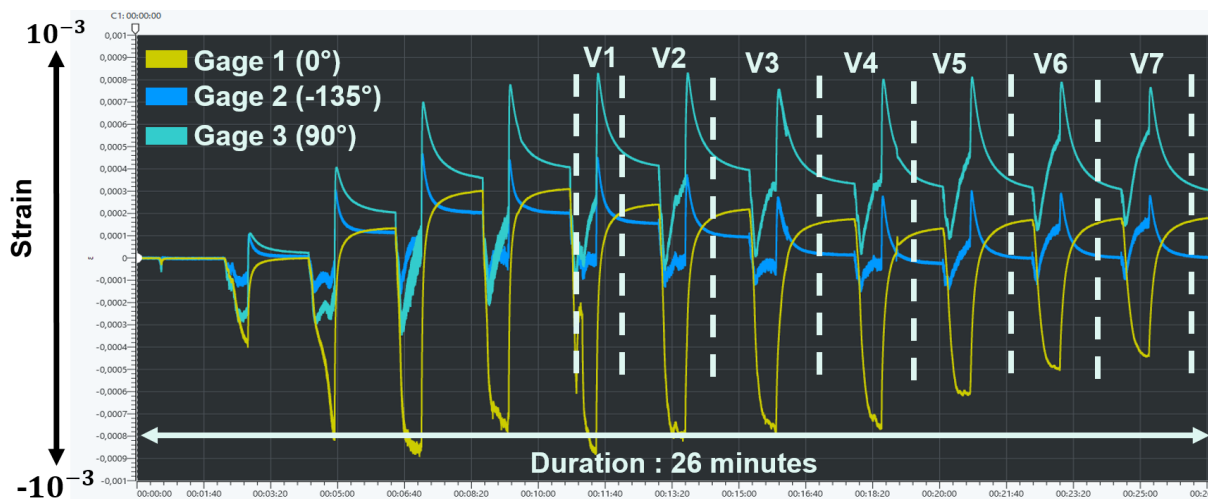


Figure D.1 – Study of the influence of the withdrawal speed on the raw acquisition data:  $v_1 = 5$  mm/s,  $v_2 = 1$  mm/s,  $v_3 = 0.5$  mm/s,  $v_4 = 0.1$  mm/s,  $v_5 = 10$  mm/s,  $v_6 = 2$  mm/s and  $v_7 = 5$  mm/s





# Appendix E

Calibration coefficients used to calculate the residual stresses in section 4.5.2 of chapter 4

$$\begin{bmatrix} -0.094 & 0 & 0.0187 \\ -0.0302 & -0.278 & -0.149 \\ -0.0139 & 0 & -0.336 \end{bmatrix} \begin{bmatrix} -0.112 & 0 & 0.0252 \\ -0.0382 & -0.335 & -0.182 \\ -0.0246 & 0 & -0.420 \end{bmatrix} \begin{bmatrix} -0.0257 & 0 & 0.0213 \\ -0.0114 & -0.206 & -0.105 \\ -0.0212 & 0 & -0.263 \end{bmatrix}$$



